EVALUATION OF COUPLED HYDRO-MECHANICAL (H-M) BEHAVIOUR OF IN SITU SHAFT SEALING COMPONENTS FOR USED NUCLEAR FUEL

by

Chang Seok Kim

A Thesis
Submitted to the Faculty of Graduate Studies
In Partial Fulfillment of the Requirements for the Degree of

DOCTOR OF PHILOSOPHY

Department of Civil Engineering
University of Manitoba
Winnipeg, Manitoba, Canada

ABSTRACT

This thesis examines hydraulic-mechanical performance of a full-scale 5-m diameter by 12-m long shaft seal installed at Canada's Underground Research Laboratory (URL). This installation spans a major water-bearing fracture zone located at a depth of 275 m and is intended to isolate two hydrogeochemcial regimes.

Performance of the hydraulic-mechanical behaviour of the shaft seal was examined using a Finite Element Method (FEM) program, CODE_BRIGHT (Vaunat and Olivella 2002). Coupled H-M constitutive models were developed using CODE_BRIGHT (Vaunat and Olivella 2002). An elastoplastic constitutive model was used to describe the behaviour of the unsaturated soil. Hydraulic-mechanical parameters of the shaft seal components were determined using laboratory test data. By matching van Genuchten's model (van Genuchten 1980) to the experimental laboratory data, hydraulic parameters of the clay component were determined. The relationship between unsaturated hydraulic conductivity and degree of saturation for the clay component was developed and used in this numerical modelling. The Basic Barcelona Model (BBM) proposed by Alsonso et al. (1990), an elastoplastic constitutive model, was used and the BBM's mechanical parameters of the clay component were determined using laboratory test data.

Three numerical models were simulated. The first model assumed fracture zone 2 (FZ2) to be horizontal, the second model assumed FZ2 to be inclined 16 degrees from the horizontal plane and the last model applied seepage of groundwater into the system based on the first model.

The numerical results were compared with field readings regarding water uptake and development of total pressure in the system. Numerical prediction from the three models showed that the hydration process of the clay seal was dominantly affected by the groundwater flow from FZ2. Overall, numerical prediction showed reasonably good agreement with field readings; however, it underestimated evolution of total stresses. The possible reason could be that the simplified groundwater flow system did not take into account radial groundwater flow toward the perimeter of the clay seal.

Prediction models of swelling pressure and swelling pressure estimates of the unsaturated clay seal have been discussed. The first model using crystalline and osmotic swelling mechanisms estimated a swelling pressure of 0.86 MPa, which was close to what was expected (0.8 MPa) in the field. The second model applying confined conditions estimated a swelling pressure of 0.41 MPa. This difference in swelling pressure prediction could be attributed to different microstructures developed under different confining conditions. The model predictions were then verified in terms of the water retention capacity of the unsaturated clay seal. Although the first model showed some deviation, overall predictions using the two models showed reasonably good agreement with the measured data.

Sensitivity analyses were conducted to assess effects of variations of H-M parameters on evolution of hydraulic-mechanical behaviour of the sealing components. Several sets of hydraulic and mechanical parameters of the clay seal were determined using available laboratory test data. The numerical results were compared in terms of changes in suction, degree of saturation and hydration time of the sealing components. The numerical prediction indicated that the hydraulic behaviour of the clay seal was sensitive to variations of the water retention parameters P_0 and β_1.

From sensitivity analyses of the BBM mechanical parameters, numerical simulation showed the development of compressive horizontal and vertical stresses. Different sets of the BBM parameters were obtained for the same clay material in this study and they resulted in slightly different predictions of mechanical behaviour of the clay seal. For this reason, sensitivity analysis of the parameters and validation of the predictions were required to improve the possibility to match field and modelled behaviour.

ACKNOWLDEGEMENTS

I wish to give my sincerest thanks to my supervisor, Dr. Marolo C. Alfaro for his patience, guidance, support and encouragement throughout this study. I also wish to acknowledge my co-advisor, Dr. James Blatz for helping me in all aspects.

I would like to sincerely thank Dr. Jim Graham and Dr. David Dixon for their valuable time to review this thesis and provide valuable suggestions and discussions. Valuable discussions with Dr. Deni Priyanto about numerical modelling concepts are acknowledged.

Most importantly, I would like to express sincere thanks and love to my parents (Hojoo Kim and Junghyee Choi) and my family members (Michelle Lee, Chloe Kim and Claire Kim) for their love, continuous encouragement, and tremendous support. All that I have achieved is truly because of them.

TABLE OF CONTENTS

LIST OF TABLES

LIST OF FIGURES

LIST OF SYMBOLS AND ABBREVIATIONS

AECL	Atomic Energy of Canada Limited
BBM	Basic Barcelona Model (Alonso et al. 1990)
BCE	Buffer Container Experiment
BSM	Bentonite-Sand Mixture
CMS	Constant Mean Stress
CV	Constant Volume
DGR	Deep Geological Repository
e	void ratio
E	Young's modulus of elasticity
EBS	Engineered Barrier System
EDZ	Excavation Damage Zone
EMDD	Effective Montmorillonite Dry Density
ESP	Enhanced Sealing Project
FEM	Finite Element Method
FDM	Finite Difference Method
FLAC	Fast Lagrangian Analysis of Continua (Itasca 2000)
FOPZ	Fibre Optic Piezometer
FZ2	Fracture Zone 2
G	shear modulus
G_s	specific gravity/ relative density of soil solids.
g	potential function
H-M	Hydro-Mechanical
ITT	Isothermal Test
K	bulk modulus
K_w	water bulk modulus
k	slope of k-line (BBM)
k_{sat}	saturated water permeability

k_w	water permeability coefficient
k_w^{sat}	water permeability at air saturated conditions
k-line	cohesion line (BBM)
LC-curve	loading collapse curve (BBM)
LY-line	load yield line (BGM)
M	slope of the critical state line that is constant (BBM)
MCC	Modified Cam-Clay
OCR	Over Consolidation Ratio
n	porosity
n_e	effective porosity
P_0	threshold pressure or air entry value (van Genuchten 1980)
p	mean net stress
p_1	reference mean stress (BBM)
p_o^*	mean stress at zero suction located on LC-line (BBM)
p_s	mean stress at corresponding suction s located on k-line (BBM)
q	deviator stress
r	BBM parameter for LC-curve
R	universal gas constant (8.31432 J/mol K),
RH	Relative Humidity
RH_{ret}	Relative Humidity according to retention curve
S_e	effective degree of saturation (water)
S_{max}	maximum degree of saturation
S_r	residual degree of saturation
S_w	degree of (water) saturation
SI-line	suction increase line (BBM)
SWCC	Soil Water Characteristic Curve
SWCS	Soil Water Characteristic Surface
s	total suction
s_o	suction limit defining SI-line (BBM)

T	absolute temperature (K)
TDR	Time Domain Reflectometry
TDS	Total Dissolved Solid
T-H-M	Thermo-Hydro-Mechanical
T-line	tension line (BGM)
TPC	Total Pressure Cell
URL	Underground Research Laboratory
u_a	pore air pressure
u_w	pore water pressure
$\bar{u}_v$	partial pressure of pore water vapour (kPa)
$\bar{u}_{v0}$	saturation pressure of water vapour (kPa)
v	specific volume
v_{w0}	specific volume of water (m^3/kg)
WRC	Water Retention Curve
w	gravimetric water content
w_{max}	maximum gravimetric water content
V	volume of reference soil
V_s	volume of solid particles
VWPZ	Vibrating Wire Piezometer
v_0	initial specific volume
z	depth from the ground surface (m)
ω_v	molecular mass of water vapour (18.016 kg/kmol)
β	BBM parameter for LC-curve
χ	Bishop's effective stress parameter
Δv	specific volume increment
ε	volumetric strain
κ	slope of ln p versus v within elastic range
κ_s	slope of ln s versus v within elastic range
λ	slope of ln p versus v when plastic strain occurs

λ_s	slope of ln s versus v when plastic strain occurs
ν	poisson's ratio
π	osmotic suction
θ_w	volumetric water content
ρ	bulk density
ρ_{dry}	dry density
ρ_w	water density
σ	total stress
σ'	effective stress
σ_i	principal stresses (i= 1,2,3)
σ_n	net effective normal stress
ψ	total suction

CHAPTER 1

INTRODUCTION

1.1. General

The Government of Canada has accepted recommendation of Adaptive Phased Management (APM) as the long-term management approach for Canada's used nuclear fuel, provided by the Nuclear Waste Management Organization (NWMO) (NWMO 2005). APM ultimately involves the isolation and containment of used nuclear fuel in a deep geological repository (DGR). A Canadian DGR would be constructed at a depth of approximately 500 m below the ground surface in either geologically suitable crystalline or sedimentary rock, and would consist of a network of placement rooms for the used fuel. A schematic of a generic DGR is shown in Figure 1-1.

Since construction of shafts and tunnels in a DGR create many pathways for water flow through the repository, these pathways would be required to be sealed in order to limit or control groundwater flow into the shaft. Shaft seals should be installed at strategic locations such as where significant fracture zones (FZs) are located after completion of operations for nuclear wastes or during repository closure (Dixon et al. 2009). These shaft seals are normally composed of both clay-based and concrete-based sealing components. The primary function of a shaft seal is to limit short-circuiting of the groundwater flow regime via the shaft.

As part of the closure of Atomic Energy of Canada Limited's (AECL) Underground Research Laboratory (URL), a full-scale shaft seal that is a composite concrete-clay-concrete seal has been constructed at the intersection of a low dipping thrust fault with the access shaft. The project is called the Enhanced Sealing Project (ESP) (Dixon et al. 2009).

The hydrogeology of the URL site is largely controlled by an ancient thrust fault (FZ2), shown in Figure 1-2. This feature is approximately 3 to 4 m in thickness in the locations where it was intersected at 273 m in the main shaft and 265 m in the ventilation shaft (Everitt et al. 1990). FZ2, shown in Figure 1-2 marks the boundary between the different groundwater zones (i.e., less saline groundwater than 2 g/L TDS (total dissolved solids content) near the surface and more saline groundwater up to ~90 g/L TDS below FZ2) (Dixon et al. 2009). The excavation and over 25 years of ongoing operation of the URL created a hydraulic draw down cone, where the water table was artificially lowered in the vicinity of the vertical openings. This is a situation similar to what would occur in an actual repository site.

Controlling water movement from FZ2 into the URL excavations is required for both isolating the two hydrogeochemical regimes and facilitating construction of the seals at that location. Since the shafts penetrate FZ2, they provide a possible route for the shallow-sourced, less saline groundwater and the deeper, higher salinity groundwater to mix more quickly than would occur in the absence of these openings naturally (Dixon et al. 2009). In this way, the goals of the URL shaft seals are the same as what is desired in an actual repository.

The composite seal consists of a 6-m-thick clay component and two concrete components (Figure 1-3). The clay component of the seal consists of an in situ compacted mixture of 40% Wyoming bentonite and 60% local quartz sand. This material is rigidly confined between two 3-m-thick low-heat high-performance concrete (LHHPC) components. This type of multiple component seal is similar in general concept to seal types proposed by various waste management agencies for sealing emplacement rooms and access tunnels in deep geologic repositories for nuclear materials. Compacted bentonite-aggregate mixtures have been chosen as engineered barriers (e.g., buffer and backfill materials) used in the construction of deep geological repositories for high-level radioactive wastes. The bentonite-aggregate mixtures have beneficial properties such as low permeability, high swelling potential, good self-sealing capacity and high radionuclide retardation capacity.

The ESP consists of the instrumentation and monitoring of the access shaft seal. A suite of 68 instruments, comprising a total of 100 sensors were installed in and around the shaft seal (refer to construction report by Martino et al. 2010 for more details).

The composite concrete-clay-concrete seal constructed in the main shaft at FZ2 represents a real field demonstration and application of conceptual designs. More importantly, the experimental results obtained from this seal will provide valuable information on performance of a repository seal system as well as a valuable opportunity to calibrate numerical models and evaluate what environmental parameters are critical in the hydration process.

This research program was designed to develop a numerical tool and examine the hydro-mechanical performance of the shaft sealing system, compared to the field measurements. The numerical results were specifically directed toward a better understanding of the interplay of the various phenomena between the sealing materials.

1.2. Hypotheses

Using in situ experimental data and boundary conditions from the ESP, numerical simulation of the shaft sealing system can improve understanding of (1) unsaturated bentonite-sand soil behaviour and (2) long-term performance of the shaft sealing system. This research will examine the following hypotheses:

1. Hydraulic-mechanical (H-M) model parameters calibrated from laboratory tests can improve prediction of the coupled H-M behaviour of the clay seal.
2. Numerical modeling can provide a better understanding of the evolution of swelling pressures generated by the clay seal.
3. Inclination of the fractured zone (FZ2) in simulated field conditions can affect the H-M performance of the clay seal, compared to more simplified use of a horizontally-oriented FZ2.
4. Available experimental methods have limitations in explaining the long-term H-M equilibrium processes, and so well-calibrated numerical modeling can provide better understanding of the long-term performance of clay seal component.

1.3. Objectives

The overall objective of this research program is to develop a numerical tool and assess the performance of the shaft sealing system. As such, the objectives can be listed as follows:

1. To determine representative H-M parameters of clay seal and rock components for the constitutive models.

2. To develop a parameter estimation method for the constitutive model parameters using laboratory test data.
3. To develop numerical design tools to predict the performance of the shaft sealing system.
4. To perform numerical simulation using the H-M parameters determined to examine the H-M performance of the shaft sealing components and compare the numerical results with field measurements.
5. To improve mechanical and hydraulic predictions by variations of H-M parameters.

1.4. Organization of Thesis

This thesis is organized as follows. Chapter 2 reviews literature relevant to this research project and the literature review provides a fundamental basis for the concepts and work presented in this thesis. Soil suction, mineralogy and structure of natural bentonite are briefly discussed. The mechanism of the swelling of bentonite and the water retention curve of bentonite are discussed. This chapter also introduces brief aspects of large-scale experiments carried out for assessing seal performance in Canada and other international countries.

Chapter 3 provides Hydro-Mechanical (H-M) performance of the shaft sealing system based on field measurements. Chapter 4 begins with a description of theoretical aspects of thermo-hydraulic-mechanical coupling. Three general balance equations for mass, energy density and momentum are described. Development of a numerical simulation tool to evaluate H-M performance of the shaft sealing system is described in Chapter 5, including determination of H-M model parameters for the shaft sealing components.

Chapter 6 introduces two methods used to estimate development of swelling pressure of the clay seal component during water uptake. Different swelling pressure estimates were found for different confining conditions. Chapter 7 describes sensitivity analysis of H-M parameters for the shaft sealing components. This sensitivity analysis focuses on assessing effects of variations of H-M parameters on evolution of hydro-mechanical behaviour of the sealing components. Several sets of hydraulic and mechanical parameters of the clay seal component were determined using laboratory test data. Chapter 8 summarizes the research program and outlines conclusions, contributions from the research and recommendations for future research.

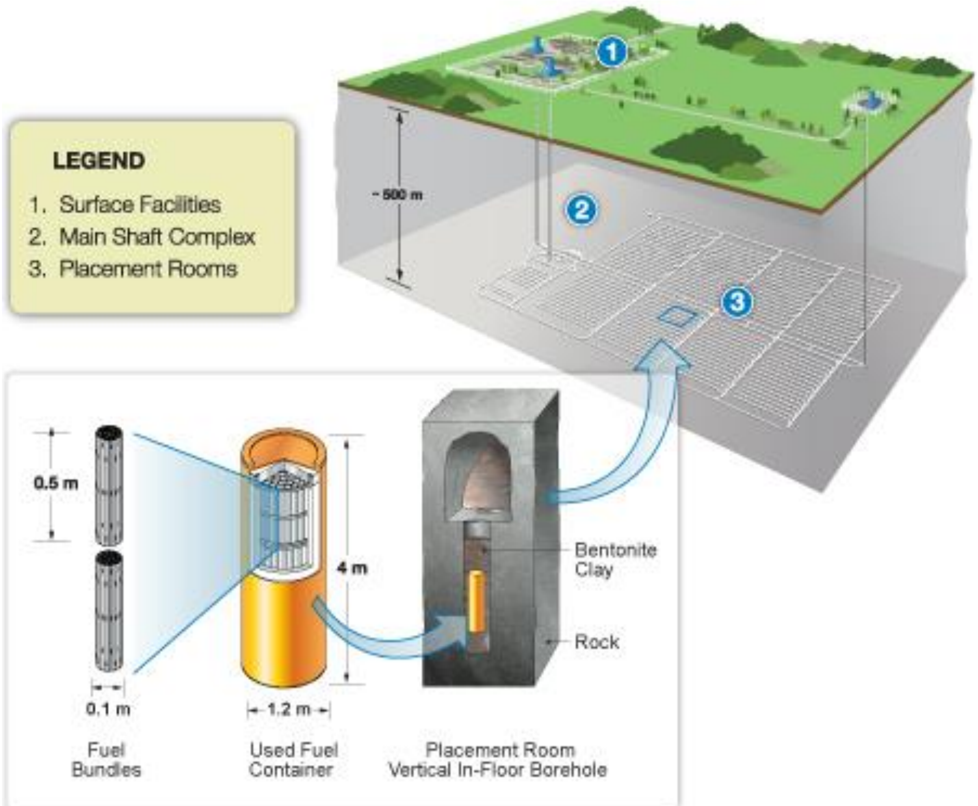

Figure 1-1. A schematic of genetic deep geological repository (NWMO 2005)

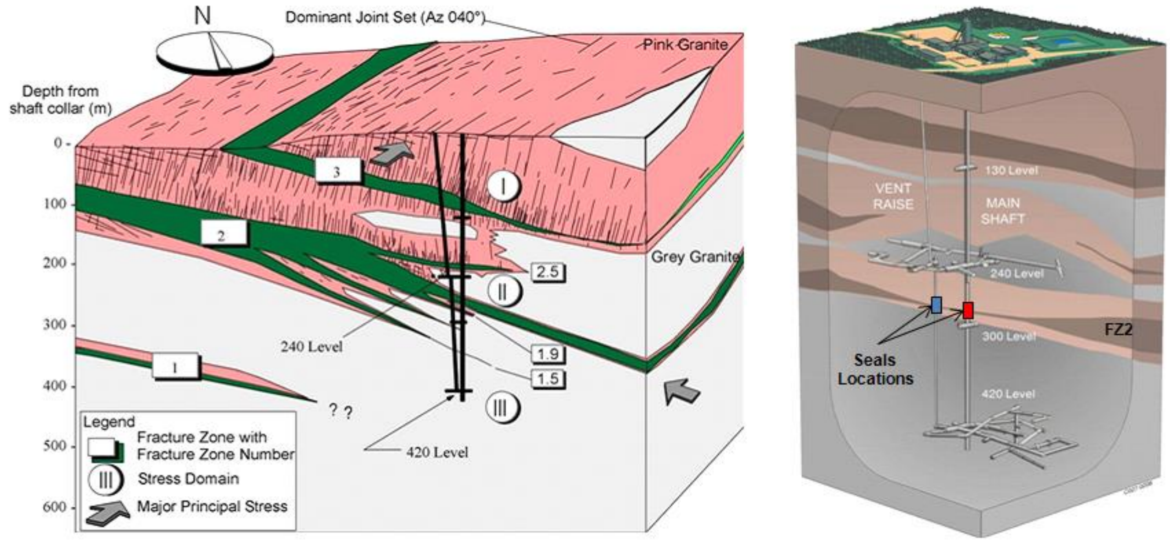

Figure 1-2. Arrangement of excavations and geology of the URL (after Dixon et al. 2010) (note that features are not shown to scale)

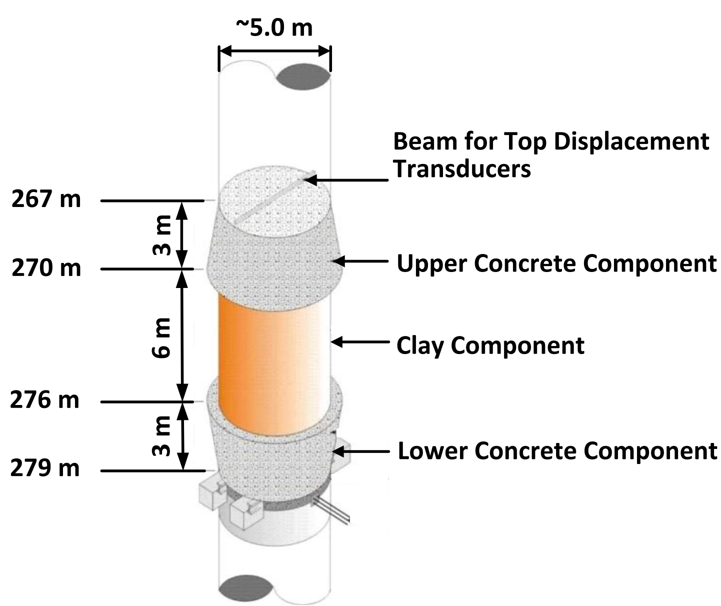

Figure 1-3. Conceptual shaft seals at fracture zone 2 (after Dixon et al. 2009)

CHAPTER 2

LITERATURE REVIEW

2.1. Soil Suction

Richards (1974) defined the soil suction as the water potential in a soil-water system. This soil suction consists of three components in unsaturated soils, capillarity, adsorption of water on the surface of the clay minerals, and osmotic phenomena. In engineering studies only two components are generally considered: matric and osmotic suctions. Matric suction is generated by capillary action caused by surface tension forces associated with the meniscus at the air-water interfaces within the pores of the soil. Osmotic suction is generated by pore fluid chemistry and water adsorption (Fredlund and Rahardjo 1993, Wan 1996). In general, matric suction is considered as the dominant component of total suction in soil, while osmotic suction is insensitive to changes in water content (as long as pore fluid chemistry remains constant). Thus any changes in total suction in unsaturated soils can be generally attributed to changes in matric suction (Fredlund and Rahardjo 1993). In this research, 'suction' refers to total suction, indicating that changes in suction reflect changes in matric suction since there is no change in the pore fluid chemistry during the experiment.

Using thermodynamics the relationship between soil suction and the partial vapour pressure of the soil water can be written as follows (Fredlund and Rahardjo 1993):

$$\psi = -\frac{RT}{v_{w0}\,\omega_v}\ln\left(\frac{\bar{u}_v}{\bar{u}_{v0}}\right) \qquad (2\text{-}1)$$

where ψ is total soil suction, R is the universal gas constant (8.31432 J/mol K), T is the absolute temperature (K), v_{w0} is the specific volume of water (m^3/kg), ω_v is the molecular mass of water vapour (18.016 kg/kmol), $\bar{u}_v$ is the partial pressure of pore water vapour (kPa) and $\bar{u}_{v0}$ is the saturation pressure of water vapour (kPa). Given that $\bar{u}_v/\bar{u}_{v0}$ is equal to the relative humidity (RH), Equation 2-1 can be simplified, at a temperature of 15°C, as:

$$\psi \text{ (in kPa)} = -132285 \ln (\text{RH in } \%/100) \qquad (2\text{-}2)$$

Measuring the partial vapour pressure of the pore water using thermocouple psychrometers can allow for indirect measurement of a soil's water content (Fredlund and Rahardjo 1993). Because the vapour pressure of soil water is a function of the soil's moisture content, when the soil is very wet, the vapour pressure is close to that of free water.

Yong (1999) distinguished the terms of soil suction and soil-water potential to describe suction in expansive clays and reported that soil-water potential consisted of matric, osmotic, gravitational, pneumatic, and pressure potential. In the case of no external pressure applied on the clay (i.e., unconfined condition), only the matric and osmotic potentials control the water holding capacity of the clay and the pressure potential is equal to zero. On the other hand, under confined conditions, the pressure potential is not equal to zero because the matric and osmotic potentials are balanced by pressure potential or swelling pressure at saturation condition. Swelling pressure is the pressure exerted by the hydrated clay under confined conditions. Therefore, the soil suction of the clay is considered to be equal to swelling pressure. Under unsaturated conditions, Agus et al. (2010) indicated that capillarity would control the water potential of the air space. In short, the matric suction comes from effects of the hydration forces and the capillary component, and osmotic suction comes from dissolved solute in the pore water of the soil.

2.2. Soil Mineralogy and Structure

Natural bentonite is a type of clay that contains large quantity of montmorillonite and expands when it is in contact with water due to the mineralogical composition of the structural unit of the montmorillonite. Bentonite also contains non-swelling minerals such as quartz, feldspars, micas and carbonate, void and sand.

The structure of montmorillonite is a silica tetrahedral-alumina octahedral-silica tetrahedral (T-O-T) unit layer (Mitchell 1993). The alumina octahedral structure consists of aluminum atom and six hydroxyls in an octahedral coordination, while the silica tetrahedral is composed of a silicon atom and four oxygen atoms in a tetrahedral coordination (Van 1977) as described in Figure 2-1.

A particle (platelet or crystal) is made by the structural unit layers stacked together. In dry conditions, bonding between the unit layers is provided by van der Waals attractive forces and exchangeable cations. This bonding becomes weak and broken when water penetrates between the layers (Mitchell 1993).

The number of structural unit layers in a particle depends on the moisture conditions and the type of exchangeable cation (Pusch et al. 1990, Mitchell 1993). Saiyouri et al. (2004) indicated that the number of structural unit layers in a particle was dependent on the compaction. For suctions greater than 3 MPa, the sodium-dominated and calcium-dominated bentonites showed different numbers of the structural unit layers, however the numbers were similar for suction lower than 3 MPa.

An aggregate is composed of particles like those just described. These features (i.e., structural unit layers, particles and aggregates) create two types of pores such as micropores and macropores in the bentonites (Gens and Alonso 1992). The micropores are defined as pores within the aggregates (between the structural unit layers and between the particles), which are also called intra-aggregate pores. By contrast, the macropores are defined as pores existed between the aggregates, which are also called inter-aggregate pores. Figure 2-2 shows the sketch of the micropores and macropores of bentonites (Yong 1999).

Yong and Warkentin (1975) reported three general classes of structure: macrostructure, microstructure, and ultra-microstructure. Microstructure and ultra-microstructure are commonly termed microstructure. Ahmed et al. (1974) found a bimodal distribution of clay specimens using mercury intrusion porosimetry testing. Wan et al. (1990) also found that the pore size distribution of the compacted sand-bentonite buffer was likely bimodal due to a microstructure in the soil structure. The microstructure is composed of the pore spaces between clay platelets that form in aggregates of clay mineral particles. The macrostructure is the framework of these aggregates and the pore spaces between them. The size of the micropores is influenced by the water content and pressure, and compactive effort determines the size of the macropores (Wan et al. 1990). The pore distribution has an effect on suction that can be developed in buffer and on the movement of water and air during external load application.

Wan (1996) conducted comprehensive studies on the mineralogy and structure of compacted sand-bentonite buffer and its constituents. The bentonite is a clay mineral that possesses a net negative charge on the mineral surface, while the sand component is angular quartz sand, which has little ability to react. The negative charge on the clay mineral surface exerts electrostatic forces on water and other nearby cations (Dixon and Miller 1995). Due to the chemical ability of the clay mineral, changes in suction or water content is dominated by the bentonite for the mixture of bentonite and sand.

2.3. Swelling Mechanism and Behaviour of Bentonite-Sand Mixtures

2.3.1. Swelling Mechanism of Bentonite-Sand Mixtures

The swelling mechanism of bentonite-sand mixtures is identical to that of natural bentonites (Mollins et al. 1996). Komine and Ogata (1996) provided a swelling mechanism of compacted bentonite as illustrated in Figure 2-3. Evolution of the swelling pressure of bentonites can be explained into three major steps such as before, during and after water uptake. Initially, the compacted bentonite consists of a mixture of montmorillonite, non-swelling minerals, sand particles and voids as shown in Figure 2-3. Before water uptake, the voids are occupied by air and free water. During a wetting stage, montmorillonite will absorb water and start swelling. Swelling montmorillonite will gradually occupy the voids and consequently the volume of montmorillonite will increase and swelling behaviour will occur in this wetting stage. After water uptake, all voids will be filled by montmorillonite and swelling pressure can be measured if there is access for further free water in the system.

2.3.2. Swelling Behaviour of Bentonite-Sand Mixtures

Laird (2006) showed that the swelling of montmorillonite is composed of 6 separate swelling processes and the basic mechanisms and forces that control each of the processes are different. They were crystalline swelling, osmotic swelling, breakup and formation of montmorillonite particles, de-mixing of exchangeable cations, co-volume swelling and Brownian swelling.

Madsen and Müller-Vonmoos (1989) and Yong (1999) reported that co-volume and Brownian swelling would not be important in determining the swelling pressure of compacted bentonites or bentonite-aggregate mixtures. Laird (2006) also indicated that among these swelling processes, the major mechanisms of the swelling were crystalline swelling, osmotic swelling and breakup of montmorillonite particles. The rest of the swelling processes were the secondary effect of these major mechanisms. Following sections briefly describe the mechanisms of crystalline and osmotic swelling and more details on their mechanisms will be provided in Chapter 6.

Crystalline Swelling

The crystalline swelling occurs as the montmorillonite absorbs water. This crystalline swelling is a process where 0 to 4 layers of water molecules are inserted between the structural unit layers in a sodium-dominated montmorillonite particle (Madsen and Müller-Vonmoos 1989). Yong (1999) reported that the crystalline swelling was controlled by the layer charge, interlayer cations, properties of adsorbed liquid and particle size. Madsen and Müller-Vonmoos (1989) found that in an unconfined condition, the volume of montmorillonite could increase two times larger than its initial volume due to crystalline swelling. By contrast, under confined conditions, the swelling pressure resulting from crystalline swelling could reach greater than 100 MPa. More details of the difference in swelling pressure for different confining conditions will be discussed in Chapter 6.

During a hydration process, several forces control the crystalline swelling. The dominant force is the hydration of the interlayer cations and the clay surface. The van der Waals attraction or the Born repulsion are also acting on the clay during hydration.

Crystalline swelling increases the distance between the unit layers of montmorillonite. This results in an increase of the volume of the montmorillonite and consequently, the swelling pressure occurs. By contrast, in dry condition, the exchangeable cations are located on the surface of the layers to balance the negative charge of the clay surface.

The studies conducted by Saiyouri et al. (2000) and Saiyouri et al. (2004) reported that the sodium-dominated bentonite (MX-80) had four water layers developed between the structural unit layers and the hydration process broke up the particles to unit layers. After development of up to four water layers between the structural unit layers, water molecules started to diffuse toward the surface to equalize ion concentrations. This occurs inside the external surfaces of particles. However, the studies also indicated that osmotic swelling, which is described in the following section, might already start after the formation of the second water layer in the interlayer space in highly compacted bentonites. The osmotic swelling might dominate over crystalline swelling after the formation of one or two water layers.

<u>Osmotic swelling</u>

Osmotic swelling is the second swelling mechanism that appears when montmorillonite absorbs water. Mitchell (1993) explained the osmotic swelling mechanism using the well-known model of diffuse double layer (DDL), where the decay of electrical potentials is modelled as a one-dimensional exponential function. The DDL is composed of three (3) parts such as (1) the negatively charged surface of clay particle, (2) the Stern layer which consists of only cations and (3) the Gouy layer which consists of both cations and anions (Mitchell 1993). Figure 2-4 shows a conceptual distribution of ions near a clay mineral surface which is naturally negatively charged.

Since the clay layers are negatively charged, a repulsive force between layers is produced. However, the attraction for hydrated cations is greater at the clay mineral surface, and cations are therefore concentrated near the surface to equilibrate the charge fields. The exchangeable cations are not too strong by the external surfaces and therefore tend to diffuse from regions of high concentration to the surface toward regions of low concentration as distance from the clay mineral surface increases. This mechanism is called diffuse electric double layer. As a result, a repulsive force among the overlapping double layers of the clay particles appears.

2.4. Soil Water Characteristic Curve (Water Retention Curve)

The soil water characteristic curve (SWCC), also known as water retention curve is the relationship between water content (degree of saturation) and suction (Fredlund and Rahardjo 1993). This SWCC is a very important relationship to assess unsaturated soil behaviour because suction strongly affects the hydraulic behaviour of unsaturated soil. The SWCC represents two curves with drying and wetting paths. Suction increases as water content decreases following a drying path. For a wetting path, it is the reverse process where the water content of soil increases as suction decreases.

Specimens with the same texture and mineralogy can have different water retention curves due to different initial water content, void ratio, stress history and compaction energy. The studies from Gens et al. (1995) and Delage and Graham (1996) showed that specimens compacted at different water contents resulted in different fabric of the soil. Blatz (2000) and Tang et al. (2002) confirmed that suction in compacted soils was a function of the hydrating water content used to prepare the specimen, the current water content of the specimen, and the drying/wetting history of the specimen. This finding originally came from Wan (1990).

Agus et al. (2010) focused on investigating suction characteristics of bentonite-sand mixtures. Total suctions were measured for various ratios of bentonite-sand mixture specimens (e.g., 30%, 50%, 70% and 100% bentonite) with initial dry density of 1.28 Mg/m^3 - 1.85 Mg/m^3 and initial water contents from 14% to 40%. In this study, Calcigel, calcium-dominated bentonite (60%-70% montmorillonite) and quartz sand were used. Two specimens were compacted using different compaction techniques and one specimen was obtained under loose condition (powder form). The retention curves for the specimens indicated that compaction had no significant impact on the magnitude of total suction. Total suction was a function of water content and bentonite content. The higher the percentage of bentonite in the mixture, the higher the total suction for the same water content. It also indicated that the total suction was strongly controlled by the bentonite water content (water content of mixture / the bentonite content in the mixture).

Agus et al. (2010) also suggested that the difference in the total suction for mixtures with different bentonite contents at the same mixture water content could be due to the difference in the sum of osmotic suction and sorptive forces whereas surface tension or capillary action had no significant influence.

2.5. Experiments Simulating Deep Geological Repository Concepts

Many experiments focused on seal performance as part of Deep Geological Repository (DGR) concepts have been carried out internationally. They provided useful information for advancing the design of seals. This section introduces brief aspects of experiments carried out for assessing seal performance in Canada and other international countries.

2.5.1. Tunnel Sealing Experiment (TSX) in Canada

Atomic Energy of Canada Limited (AECL) performed a full-scale Tunnel Sealing Experiment (TSX) to assess potential issues on construction and performance of seals for potential application in DGRs (Chandler et al. 2002, Martino 2008). The TSX focused on investigating the functionality of the sealing system, which was the main goal of the ESP. The only difference between the two experiments is that the ESP focused on hydraulic-mechanical (H-M) behaviour of the sealing system while the TSX considered thermal influences besides H-M behaviour of the sealing system (i.e., T-H-M). The experiment was installed at a depth of approximately 420 m at AECL's URL and consisted of the construction and monitoring of two types of seals (bulkheads); one comprised entirely of concrete and the other of highly compacted bentonite (HCB) blocks (Chandler et al.

2002). The seals confined a sand section that was injected with heated and pressurized water. The general layout of the TSX is shown in Figure 2-5(a).

The experiment operated for 64 months under varying thermal and hydraulic conditions until 2004 and its final decommissioning was completed in 2005. The experiment included tunnel pressurization phases up to 4 MPa with and without heating of the injected water. The water was heated to produce 50°C and 65°C temperatures at the concrete-sand and bentonite-sand interfaces.

The concrete bulkhead was keyed 1.75 m into the surrounding rock (Figure 2-5(b)). The bulkhead was an unreinforced concrete structure comprised of low heat, high performance concrete (Chandler et al. 2002). The concrete mix used had many desirable attributes such as low shrinkage, high strength, low permeability and good workability. The concrete bulkhead was sealed along the concrete-rock interface using bentonite sealing strips and grout injection. A total of 133 instruments were installed in the concrete bulkhead and at the concrete-rock interface. The instruments contained sensors for monitoring strain, interface water pressures, interface total pressures, excavation damaged zone (EDZ) pore water pressure, temperature, interface displacement, bulkhead displacement and micro-seismic events. Eighty-two (82) temperature sensors installed in and around the concrete bulkhead measured the thermal rise due to initial concrete hydration. The maximum temperature recorded was 45.1°C near the centre of the bulkhead. This indicated a maximum temperature rise of roughly 20°C above the ambient air temperature during the concrete pour.

Strains in the concrete were monitored continuously using vibrating wire strain gauges and fibre optic strain gauges. The total displacement of the outer concrete bulkhead face was 0.2 mm during pressurization and 0.7 mm during heating, indicating that thermal effects had a greater influence on the concrete displacement than tunnel pressurization. A substantial reduction in seepage was observed during the heating phase, since the aperture at the concrete-rock interface decreased in size due to thermal expansion of the bulkhead.

The clay bulkhead was 2 m long, and was keyed 1 m into the surrounding rock (Figure 2-5(b)) to provide a cut-off of the interconnected fractures around the tunnel's perimeter. The bulkhead was restrained on its downstream face by a steel support plate and the upstream face was in contact with the sand chamber as shown in Figure 2-5(a). The clay bulkhead was constructed of pre-compacted bentonite-sand blocks comprised of 70% Kunigel V1 bentonite and 30% silica sand (Figure 2-5(c)), with shot-clay applied along the clay-rock interface.

A total of 234 instruments were installed in and around the clay bulkhead. These instruments monitored the moisture content, swelling pressure, clay pore water pressure, EDZ pore water pressure, and displacement of the bulkhead at various locations.

The moisture content of the clay bulkhead was monitored using thermocouple psychrometers, hygrometers and time domain reflectometry (TDR) probes. A total of 132 psychrometers, 14 hygrometers, and 12 TDRs were installed. The psychrometers provided the distribution of soil suction (i.e., water content) throughout the bulkhead. A maximum swelling pressure of approximately 1 MPa was measured by the pressure sensors. It was found that the total pressure at the interface of clay-steel support increased linearly with the applied tunnel pressure. The total pressure measured was a sum of pore water pressure, pore air pressure and swelling pressure. The pressurization system was installed in parallel with the seal construction and supplied the pressurized water in the tunnel to a maximum of 4 MPa. The swelling clay bulkhead demonstrated the ability of self-sealing. Considering similar hydraulic conditions in both the TSX and the ESP (i.e., water uptake in the clay seal controlled by groundwater seepage from host rock), the self-sealing potential of the clay seal installed in the ESP is also expected.

The displacement of the clay bulkhead was monitored at its top, interior, upstream interface and downstream interface. A total displacement of 54 mm was recorded at the upstream (clay-sand) face of the bulkhead, and was primarily attributed to compression due to the applied load. Only about 3 mm of displacement was recovered after tunnel depressurization, indicating that non-recoverable compression of the clay mass had occurred.

Seepage rates passing through the clay bulkhead were dependent upon the tunnel pressures and showed that most of seepage occurred along the clay-rock interface. At the end of the test, the system was still moving toward an equilibrium state and it would take a few more years to reach full saturation with equilibrium of hydraulic and mechanical pressures.

2.5.2. Tunnel Sealing Test in Sweden

Swedish Nuclear Fuel and Waste Management Company (SKB) carried out a tunnel sealing experiment as part of the Stripa Project in the 1980s. The main focus of this experiment was to assess the performance of a tunnel seal designed for eliminating radial inflow from a fracture zone while still permitting through-traffic during DGR construction and operation (Pusch et al.

1987, Gray 1993). A saturated sand-fill chamber was employed as an analog to a water-bearing fracture zone as shown in Figure 2-6(a). The general layout of the tunnel sealing experiment is shown in Figure 2-6(b). The water in the chamber was pressurized up to 3 MPa during the test. Highly Compacted Bentonite (HCB) was used for two O-ring seals installed at both ends and two concrete plugs were used in confining the sand-filled chamber and bentonite O-rings.

Throughout the experiment, seepage, swelling pressure of bentonite, pore water pressure, displacement of the concrete plugs and displacement of the sand-bentonite interface were measured and monitored. The displacement of the sand-bentonite interface was measured and monitored by Plexiglas tubes installed through the concrete plugs and bentonite into the sand fill. During decommissioning, it was found that the HCB was expanded outward and around the corner of the concrete bulkhead with a range of 5-7 mm. That demonstrated the sealing potential of bentonite.

At the beginning of the experiment, the total pressures increased irregularly with respect to time and location due to the fact that the unsaturated system resulted in non-uniform contact and erroneous readings for total pressure at the concrete-bentonite interface. After 18 months, the total pressure at the rock-bentonite interface stopped increasing, indicating that a high degree of saturation had been achieved. The swelling pressure (total pressure minus pore water pressure) at the rock-bentonite interface measured was in the range between 0.8 MPa and 5.2 MPa at the end of the test.

Seepage was measured by monitoring the amount of water injected into the sand-filled chamber and the amount of water seeping past the concrete plugs. It was found that water mainly flowed through the EDZ immediately adjacent to the ends of the plug. At the initial stage of pressurization, there was a rapid water leak observed along the bentonite-rock interface and decreased after several hours, indicating that as the bentonite became hydrated, it swelled and sealed the gap. As a result, leakage dropped by 60% during the 10-month test period from approximately 4800 litre/day to 1800 litre/day at pressure of 3 MPa.

2.6. Constitutive Modeling of Soil Behaviour

Elastic-plastic models have been selected for the coupled relationship between strength and deformation of soils. Those models consist of two components, the elastic and plastic components. In general, the elastic component models recoverable soil behaviour at pressures lower than the yield stress. Elastic deformations are recovered after removal of the load. On the other hand, the second component is the non-recoverable component, which consists of both elastic and plastic deformations. Plastic deformations are not recoverable after load is removed, resulting in permanent change in soil structure that needs to be rearranged to equilibrium with the applied load.

The Modified Cam Clay (MCC) model (Roscoe and Burland 1968) can represent elastic-plastic behaviour of soil and therefore this model is used for predicting the elastic-plastic behaviour of saturated soft clays based on assumptions such as isotropic elasticity of the soil and semi-logarithmic elasticity of the soil (Roscoe and Burland 1968). The definition of the state variables for saturated soils are described with three variables mean effective stress (p' = p (total stress) - u (pore water pressure)), deviatoric stress (q) (stress state) and specific volume (V) (volume state) and these variables form the orthogonal axes of the model.

Since there are insufficient physical laboratory data to show the response of volume change to changes in suction when external stress is applied, general numerical models for behaviour of unsaturated soil have been conceptualized using elastic-plastic behaviour (Alonso et al. 1990, Gens and Alonso 1992, Delage and Graham 1995, Wheeler and Sivakumar 1995, Blatz and Graham 2003). These models with an elastic-plastic framework are related to the saturated Cam-Clay framework. Five state variables are required: p, q, s, V and either water content or degree of saturation in order to properly describe the behaviour of unsaturated soils. With the use of these five variables, the model can be visualized as two 3-dimensional surfaces and a SWCC to relate suction to degree of saturation or water content.

The Basic Barcelona Model (BBM) that was first proposed by Alonso et al. (1990) was used for the mechanical constitutive models. The reason to choose the BBM is because a finite element method program, CODE_BRIGHT (Vaunat and Olivella 2002) designed to incorporate the BBM was used for numerical modelling in this study.

The BBM, Figure 2-7(b), is known as the first comprehensive critical state model for unsaturated clays and is an extension of the MCC model into the area of unsaturated soils. The BBM (Alonso et al. 1987, Alonso et al.1990) presents three features: (1) yield surface, (2) critical state surface and (3) stress-volume relationships. The yield surface in p-s space is limited by three lines as follows: the LC-curve (Loading Collapse), the k-line (tension, parameter k), and the SI-line (Suction Increase, parameter s_o). The parameter, k is the slope of k-line and s_o is the suction limit defining SI-line in the BBM. The LC-curve is determined by six parameters (κ, $\lambda(0)$, r, β, p_0*, and p^c). Parameters κ and $\lambda(0)$ are the coefficient of soil compressibility corresponding with the changes in mean stress (p). Parameter κ is the slope of ln(p) versus V within the elastic range. Parameter $\lambda(0)$ is the slope of ln(p) versus V when plastic strain occurs at saturated conditions. Parameters p_0^* is the mean stress at zero suction located on LC-line. This parameter is the same as the preconsolidation pressure in the MCC model for saturated clay (Roscoe and Burland 1968). The parameter p^c is the reference mean stress that defines the LC-curve. The parameters r and β are the other fitting parameters that define the LC-curve.

Similar to the MCC model, the BBM assumes an ellipse for the yield surface in p-q space. This ellipse increases its size with increasing suction due to increasing shear strength of clay material when drying occurs. In the BBM, the critical state slope M is independent of the suction (constant) and therefore when the soil becomes fully saturated, the ellipse becomes the MCC ellipse for saturated soil (Roscoe and Burland 1968) (Figure 2-7 (a)).

Figure 2-7(c) illustrates deformations due to changes in mean stress (p) in V – ln(p) space with parameters κ and $\lambda(s)$. In the BBM, the parameter $\lambda(s)$ is a function of suction. This function is developed from coupling of the LC-curve with the stress-volume relationship. The parameter κ in the BBM is independent of suction. However, some laboratory test results report that the parameter κ decreases with increasing suction (s) (Al-Mukhtar et al. 1993, Priyanto et al. 2004).

Figure 2-7(d) shows parameters κ_s and λ_s, the coefficient of compressibility parameters, controlling deformation of the soil due to changes in suction. The parameters κ_s and λ_s are the slopes of ln(s) versus specific volume (V) in the elastic range and plastic range, respectively. In the BBM, these two parameters κ_s and λ_s are independent of suction changes (Alonso et al. 1990).

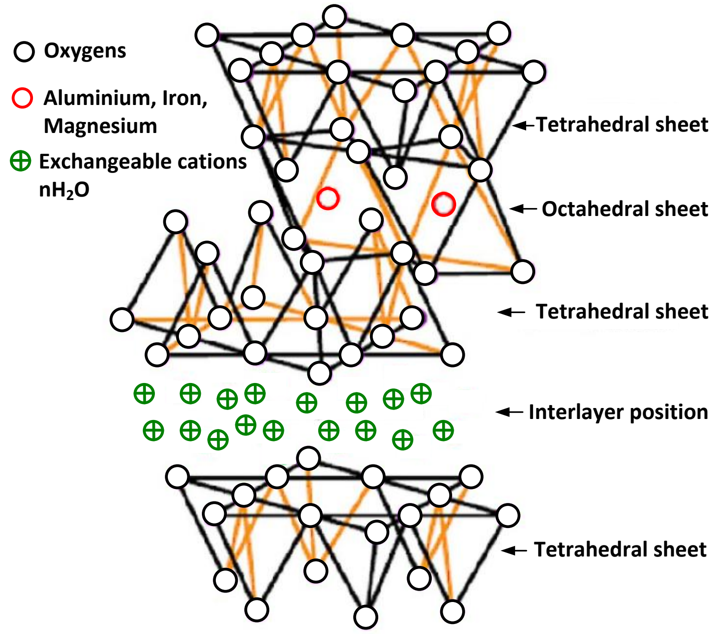

Figure 2-1. Sketch of the montmorillonite structure (revised from Mitchell 1993)

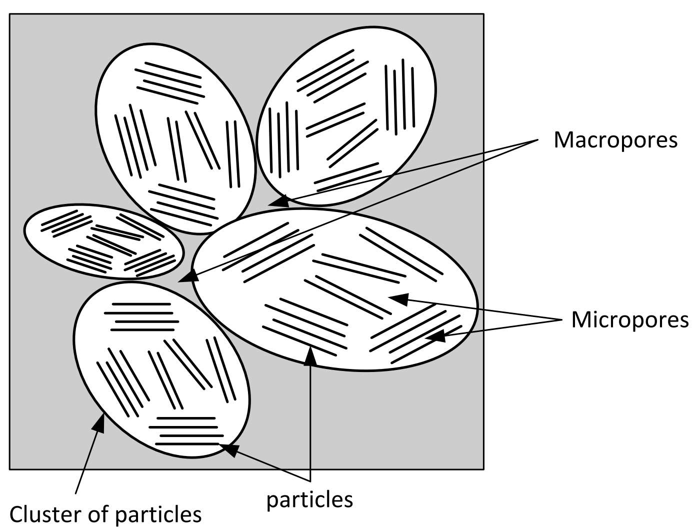

Figure 2-2. Sketch of microstructure of bentonite (revised after Yong 1999)

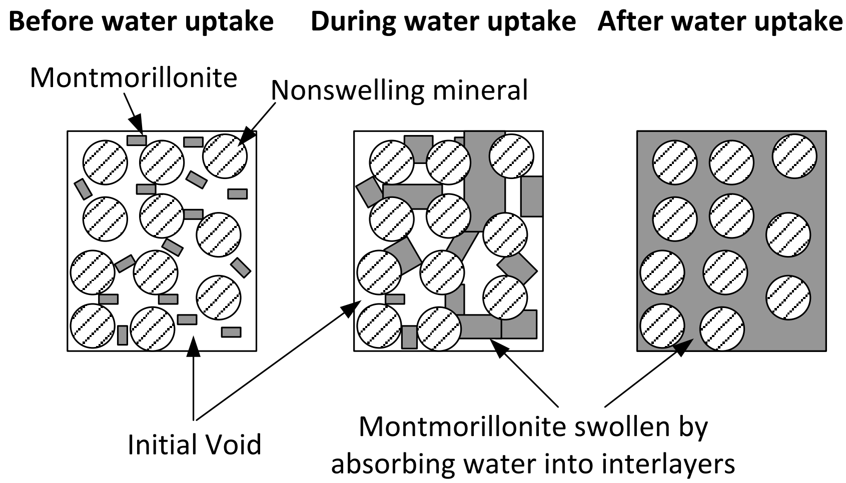

Figure 2-3. Mechanism on the swelling pressure of compacted bentonite (revised after Komine and Ogata 1996)

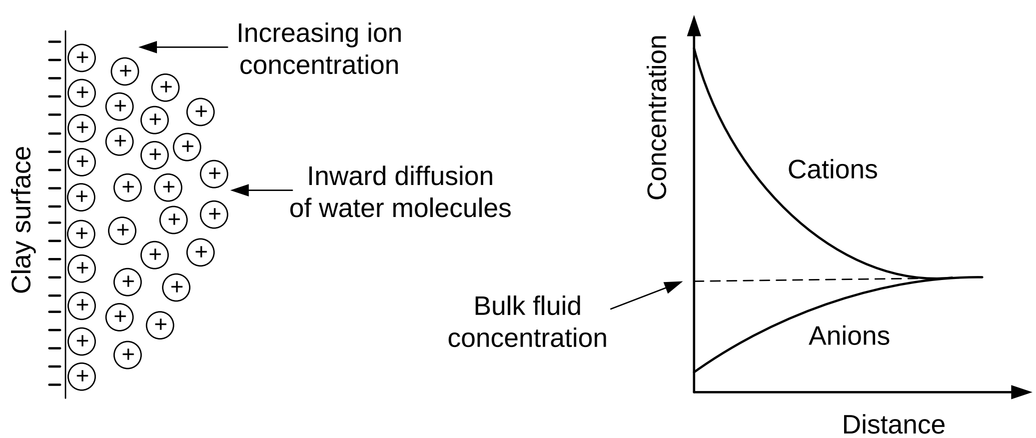

Figure 2-4. Conceptual distribution of ions and a negatively charged clay mineral surface (Mitchell 1993)

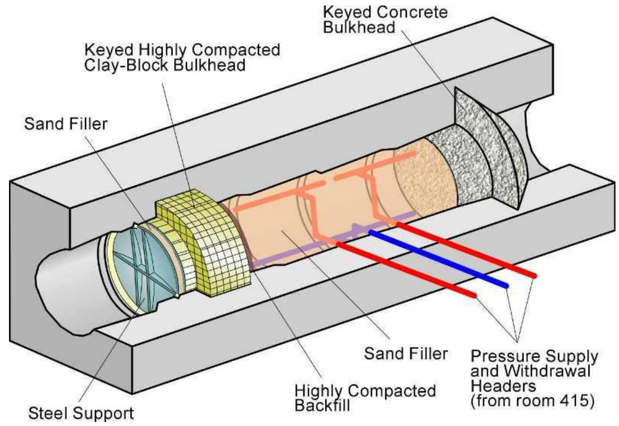

(a)

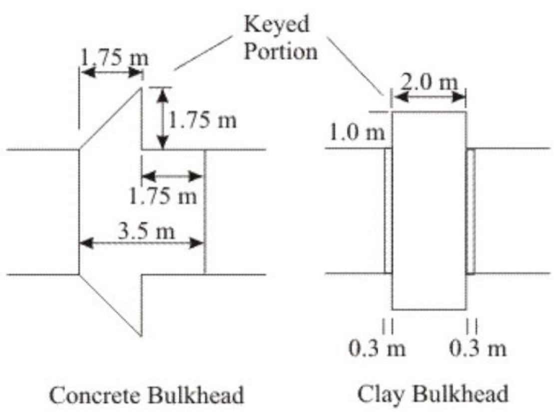

(b) (c)

Figure 2-5. Total pressures recorded in the clay component (Martino et al. 2008)

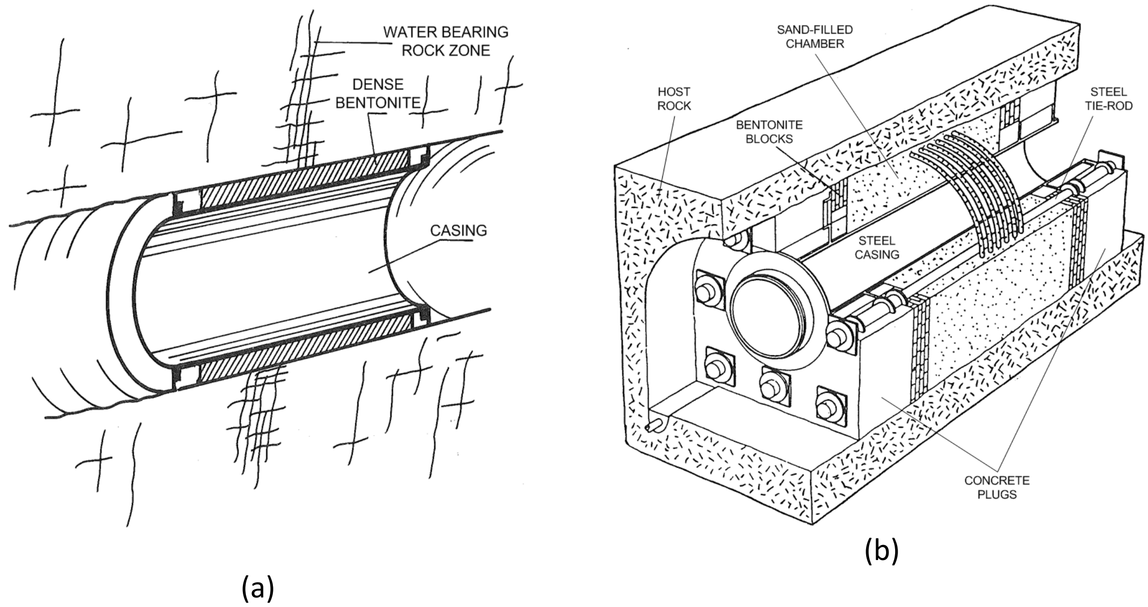

Figure 2-6. Conceptual layout of the Stripa tunnel seal (Pusch et al. 1987)

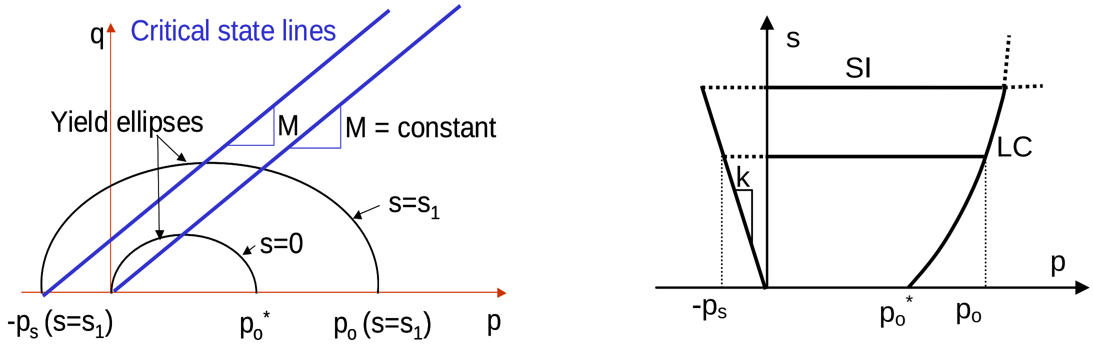

(a) p-q Space

(b) p-s Space

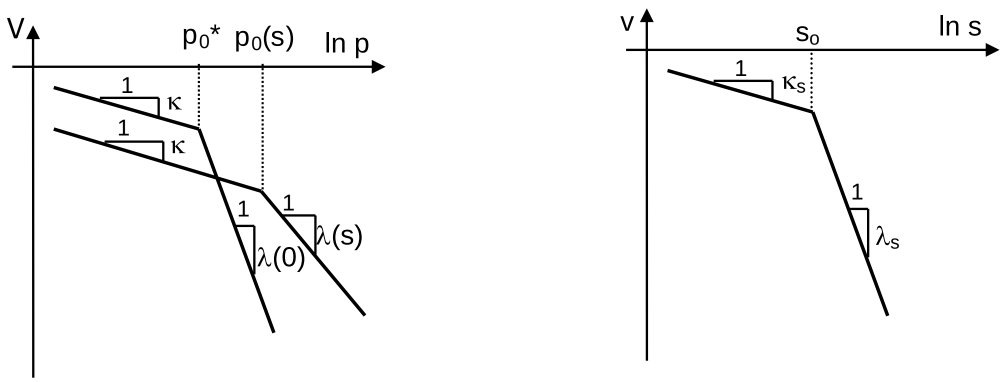

(c) ln p-V Space

(d) ln s – V Space

Figure 2-7. Relationship in p-s-q-V spaces used in the Basic Barcelona Model (after Alonso et al. 1990)

CHAPTER 3

INTERPRETATION OF ESP DATA

3.1. Introduction

Construction of the shaft seal was completed in late 2009 and the system has been allowed to passively flood since that time. As of 31 December 2015, a total of 25 sensors (5 of vibrating wire total pressure sensors, 15 of vibrating wire piezometer sensors, 4 of time domain reflectometers (TDR) and 1 of fibre-optic displacement transducer), were fully functional and indicated that the saturation of the seal was still evolving. Most of the perimeter regions of the clay component have reached saturation, but saturation of the core of the clay component is still progressing. Recovery of the local groundwater table from the drawdown conditions induced by the URL shafts and tunnels is slowly progressing (Priyanto et al. 2014).

3.2. Water Uptake by the Clay Seal Using Psychrometers and TDR Sensors

Two different types of sensors were installed to monitor water uptake in the clay seal component. A total of 14 thermocouple psychrometers and 4 time domain reflectometries (TDRs) were installed in the clay component. All psychrometers provided useful information on the conditions of the clay component of the seal while they were functional. The psychrometer sensors were connected to data logger, DL64 which was located at the 240 level of the URL.

The data logger ceased functioning and psychrometer monitoring was lost when the water reached the 240 level of the URL in the middle of 2013. The sensors were still not showing saturation until that time.

Psychrometers operate by measuring the partial vapour pressure within the pore spaces of the bentonite-sand material. These partial pressure readings can be converted into total soil suction using a thermodynamic relationship as described in Equation 2-1. Soil suction is an indicator of the stage of saturation of an unsaturated soil. In the ESP, a suction of approximately -6 MPa indicates initial conditions, which relates to a gravimetric water content of approximately 12% (degree of saturation of 65-70%). As soil wets up, the suction will decrease until it reaches approximately -0.5 - -1 MPa. These values are considered as the osmotic suction at the soil at full saturation (Dixon et al. 2011). Values smaller than -500 kPa are generally associated with flooded sensors. Therefore, locations in the seals with such readings are assumed to be at 100% saturation.

Figure 3-1 shows the evolution of suction in the clay seal component from all the psychrometer readings up to the mid of 2013. They were plotted based on their relative position below and above the mid-height of the clay seal region. Figure 3-1(a) shows the sensor readings above the mid-height and Figure 3-1(b) shows those below the mid-height. As of mid-2013, the data readings indicate that unsaturated conditions remained only in the upper region near the core of the clay-filled region. This is consistent with the data readings obtained from the TDR sensors indicating that the core of the clay component was not fully saturated. The data readings obtained around the perimeter of the clay seal show a slowly saturating system.

The TDR probes were installed closer to the centre of the clay seal region than the psychrometers because of their anticipated greater longevity and the greater time required for groundwater to reach the central portions of the clay component (Dixon et al. 2011). The TDR, as a second moisture sensor, allows for longer term monitoring of the clay seal past the flooding of the psychrometer data logger.

As seen in Figure 3-2, the monitoring TDR data collected from 2009 to 2014 showed only a very gradual increase in the water content of the clay component, however, in 2015 all of the sensors indicated discernible changes in regional saturation. The lowermost TDR1 has moved to almost 100% water saturation for a 9-month period (from March to December 2015). The volumetric water content of ~34% corresponds to 100% saturation. The other TDR sensors (TDR2-4) located at or above the mid-height of the clay component also show increases in water content during 2015, moving on average to approximately 85-90% saturation. Based on this rate of water content increase shown in 2015, it is anticipated that the clay component region would likely reach full water saturation in 2016 - 2017.

3.3. Piezometric Pressure in Clay Component

The pore water pressure in the clay component was monitored by a total of 8 piezometers, 3 above and 5 below the mid height of the clay seal, respectively as shown in Figures 3-3(a) and 3-3(b). The piezometric head differential across the seal was monitored using two vibrating wire piezometers (VWPZ10 and VWPZ02) as shown in Figure 3-3. These two piezometers were located at the top and bottom of the shaft seal. In order to represent piezometric heads at the elevations at the upper and lower concrete-clay interfaces, the data for the piezometers used in this comparison are elevation–adjusted to the lower concrete-clay contact and the upper concrete-clay contacts (Dixon et al. 2011).

The piezometer data show substantial changes in piezometric pressure across the 6-m-thick clay seal component with time (Figure 3-3(a)). The hydrostatic pressure difference between the lower and upper shaft under an open shaft condition is approximately 60 kPa, which would be seen if there was an ineffective shaft seal present. As of September 2011, the pressure differential across the clay seal component was approximately 410 kPa. The piezometric pressure in the lower region of the clay seal gradually decayed after September 2011 and started increasing from July 2012. The pressure differential across the clay seal was approximately 260 kPa as of the end of December 2012 and 157 kPa as of December 2015. The pressure increase in both regions above and below the clay seal from the end of June 2014 to the end of December 2015 was approximately 600 kPa and 725 kPa, respectively. These increases were not equal. This can indicate that there was no hydraulic connection between the upper and lower shaft regions, and the clay seal was effectively isolating the upper and the lower portions of the shaft. The dominant mechanism here was that the clay seal became saturated, swelled and formed a tight contact with rock (i.e., clay-rock interfaces and fractures).

The pressure readings in the clay seal component indicate the existence of a hydraulic connection which has likely been established through the rock, around the periphery of the clay component. This path would likely be through the shaft EDZ and through FZ2 since these are the regions of higher conductivity between the measurement points (Dixon et al. 2012).

During 2015, the vibrating wire piezometer (VWPZ) sensors closest to the clay-concrete and clay-rock contacts (VWPZ04, VWPZ06), and a fibre optic piezometer sensor (FOPZ05) continued to show substantial pressure increases and closely track the pressure changes being observed in the open shafts, however the magnitude of the values was not the same (Figures 3-3(a) and 3-3(b)). These similar trends but having different magnitudes can be due to the existence of a poor hydraulic connection between the upper shaft and FZ2 and the lower shaft and FZ2 and therefore a substantial pressure differential cannot be attributed to elevation differences.

Once regional groundwater conditions are re-established, the hydraulic pressure above and below the clay seal should come to equilibrium and the pressure difference across the clay seal should be approximately ~60 kPa, static head (elevation) difference. The different evolution of the hydraulic pressures around the upper and the lower concrete components clearly indicates that a substantial hydraulic disconnect continues to be present between these two regions, providing evidence of the continuing functional effectiveness of the clay seal.

3.4. Piezometric Pressure in Rock Adjacent to the Shaft Seal

The pore water pressure in the rock immediately adjacent to the shaft seal (EDZ) was measured at three horizontal distances into the rock (i.e., 0.5 m, 1.0 m and 1.85 m) at a height of 4.5 m above the base of the clay component. The sensors were therefore located 1.5 m below concrete-clay contact, as shown in schematic of Figure 3-4.

Figure 3-4 shows the data collected from the VWPZR instruments installed in the rock wall above FZ2, along with the water elevation in the shaft above and below the seal for comparison. The piezometric pressure in the rock immediately adjacent to the clay seal increased rapidly until early 2011, when a pressure decay extending into early 2012 was observed. For most of 2012 the hydraulic pressures in each of these monitoring locations were essentially stable. In late 2012 through to mid 2014, the rock piezometric pressures recovered slowly, following a pattern that was intermediate to the upper and lower shaft regions (Figure 3-4).

In the course of the more rapid flooding of the upper shaft, since September 2014 a substantial change in the pressures in the EDZ has developed and measured values are now closely tracking the pressure changes observed in the open shaft. These observations are strong evidence that the EDZ in the rock volume between FZ2 and the upper clay-contact is likely saturated and weakly interconnected. This interconnection does not seem to extend to the region below FZ2.

3.5. Total Pressure in Clay Seal Component

Based on swelling pressure of the same material estimated from laboratory testing, it is anticipated that on achieving saturation and completion of shaft flooding, the swelling pressure component of total pressure will be of the order of 800 kPa and the piezometric pressure component will be approximately 2500 kPa. This will result in a total pressure of approximately 3300 kPa that should be measured by the total pressure sensors (TPCs). As of the end of December 2015, under the existing piezometric pressures, a saturated system should see total pressures of the order of 2050 kPa at the lower concrete-clay interface (i.e., piezometric pressure of 1250 kPa and swelling pressure of 800 kPa). This value was not observed by any of the sensors. This is interpreted as indicating that the clay component has not been saturated yet.

Figure 3-5(a) shows the total pressure data obtained in the region of the clay seal component and the piezometric pressures at both upper and lower clay-concrete interfaces. These data clearly show that the clay seal is not in equilibrium and water saturation of the clay component has not yet been achieved. The data shown in Figure 3-5(a) is presented as smaller regional groupings in Figure 3-5(b) and Figure 3-5(c) as the regions at the rock-clay interface and the vertical centerline of the clay filled region, respectively.

As seen in Figures 3-5(a), 3-5(b) and 3-5(c), the total and piezometric pressure data show the pattern of decaying pressure in the clay seal during the period September 2011 to September 2012. Dixon et al. (2012) suggested that this phenomenon was associated with some form of degassing event where the excess gas pressure in the unsaturated region induced gas breakthrough along the clay-concrete and concrete-rock interfaces. This gas breakthrough would tend to increase the hydration process of the clay seal because air was allowed to escape rather than being forced to dissolve into pore fluid. After September 2012, the total and piezometric pressures were gradually increased in most part of the clay component. This can be indicative of further development of swelling pressure by the clay.

Total pressures measured along the rock-clay interface were much higher than those along the vertical centreline of the clay seal region as of December 2015 (Figures 3-5(b) and 3-5(c)). This is related to the recovering pressure below the seal and the rapidly increasing piezometric head in the upper shaft. Based on these readings the regions at the rock-clay interface were saturated and water was moving from the regions toward the core of the clay seal component. The TPCs located in the central portions of the clay-filled volume have continued to show that total pressures in these regions are also increasing. The magnitude of the responses is lower than those observed in the region of the rock-clay interface, as would be expected in those regions that have not yet achieved water saturation (Figure 3-5(c)).

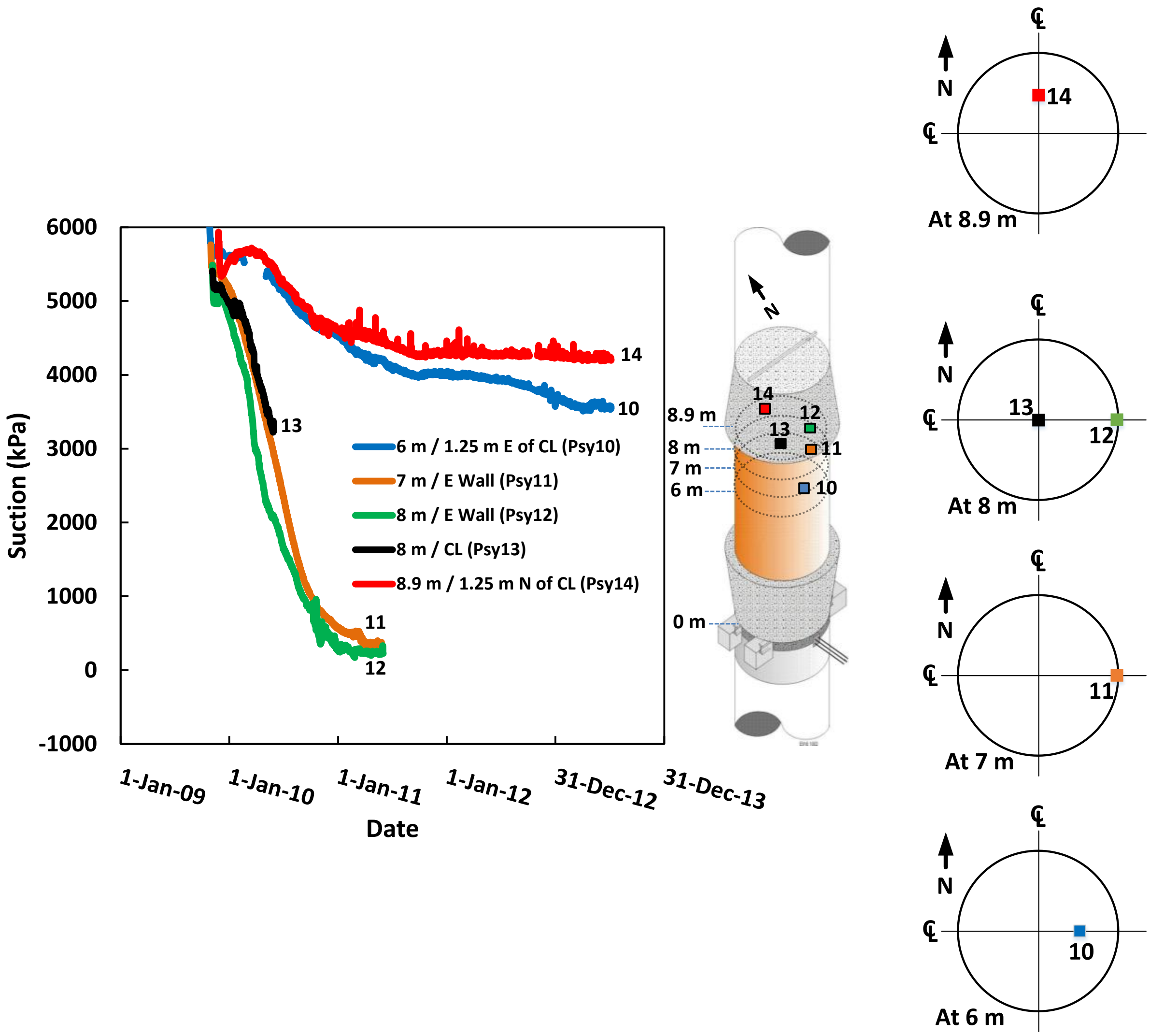

(a) Psychrometer readings above the mid-height of the clay seal

Figure 3-1. Psychrometer readings installed in the clay seal (after Priyanto et al. 2014)

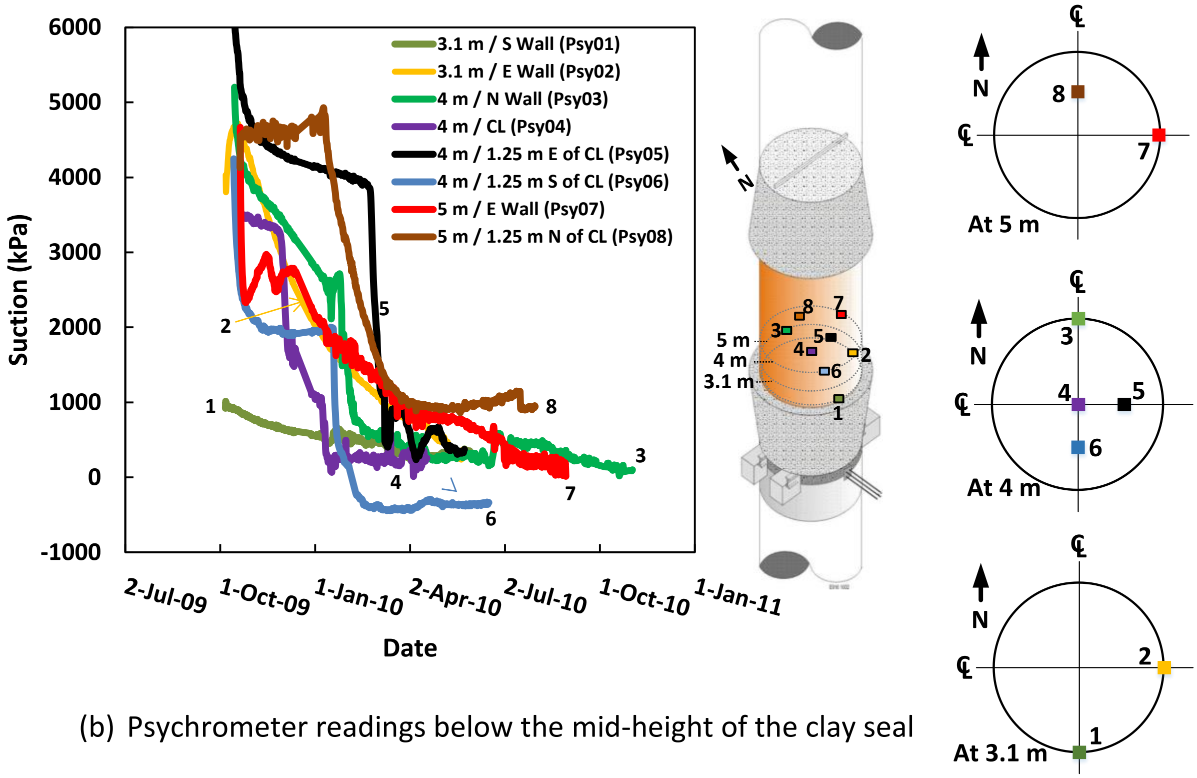

(b) Psychrometer readings below the mid-height of the clay seal

Figure 3-1. Psychrometer readings installed in the clay seal (after Priyanto et al. 2014) (Cont'd)

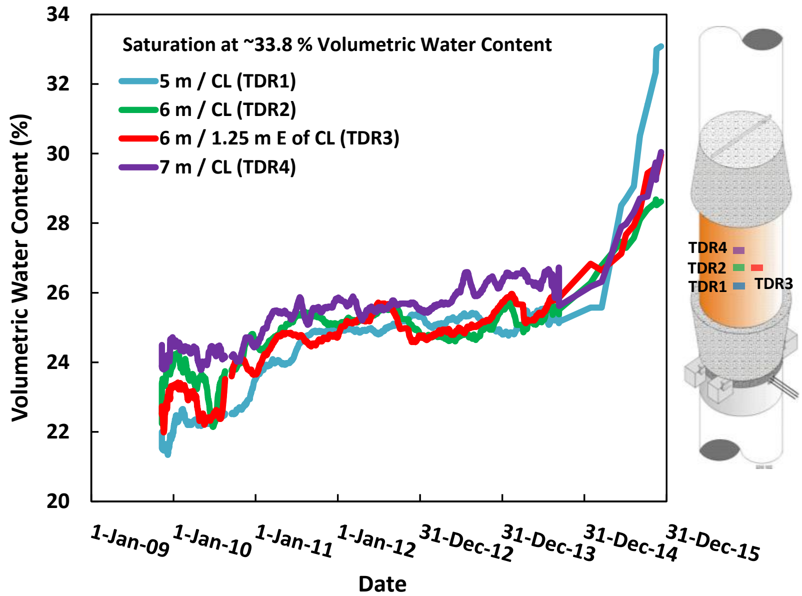

Figure 3-2. Volumetric water content in the clay seal measured by TDR sensors (after Priyanto et al. 2014)

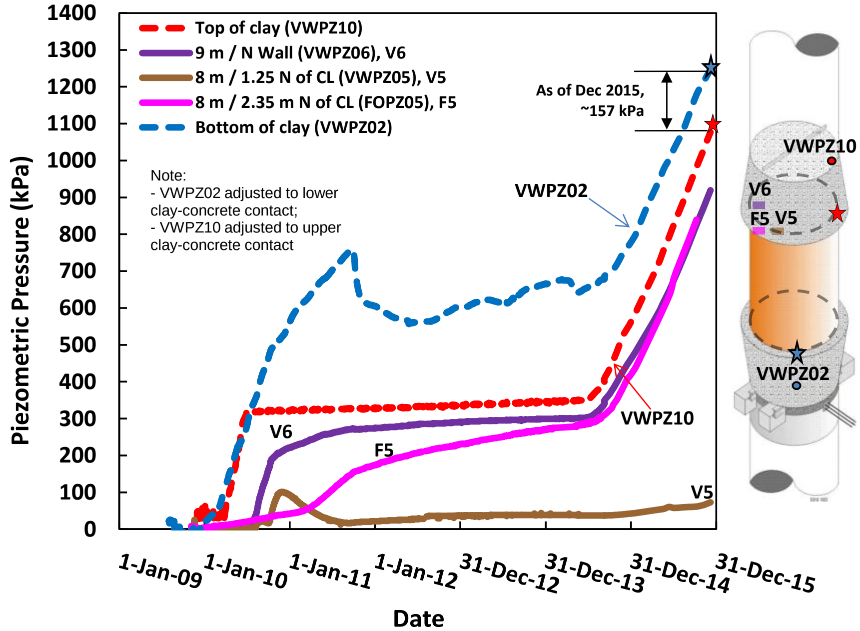

(a) Piezometric pressure 3 m above the mid-height of the clay seal

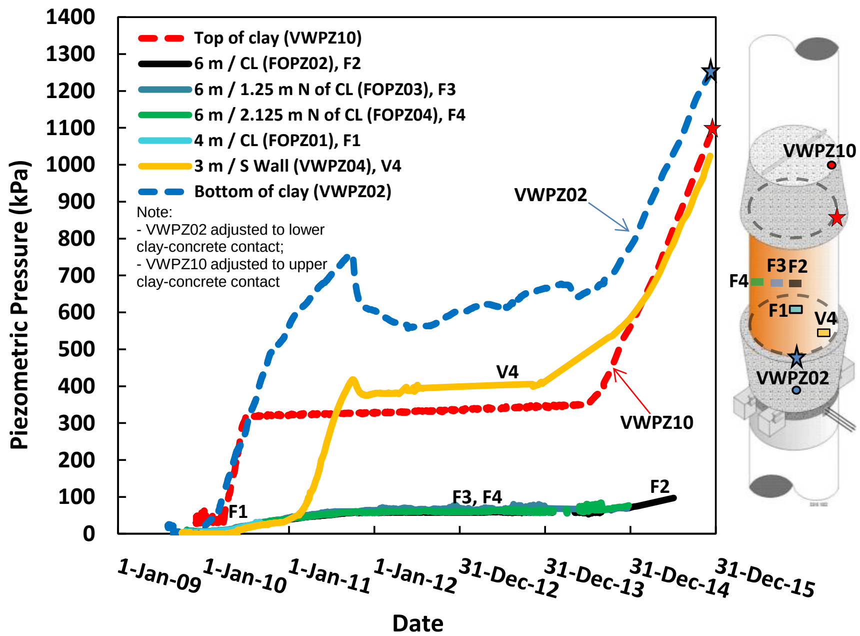

(b) Piezometric pressure 3 m below the mid-height of the clay seal

Figure 3-3. Piezometric pressures above and below the clay seal (after Priyanto et al. 2014)

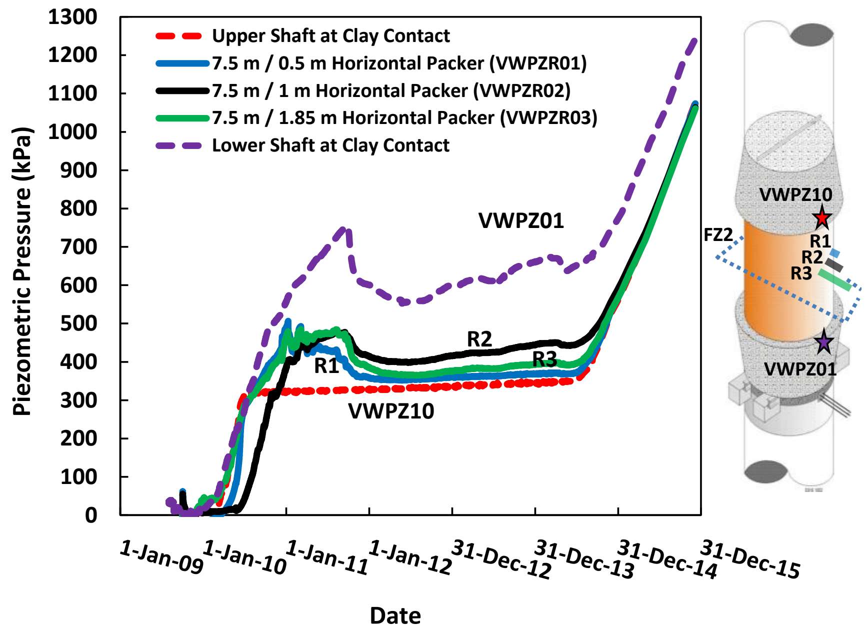

Figure 3-4. Piezometric pressure in the rock near the clay seal (after Priyanto et al. 2014)

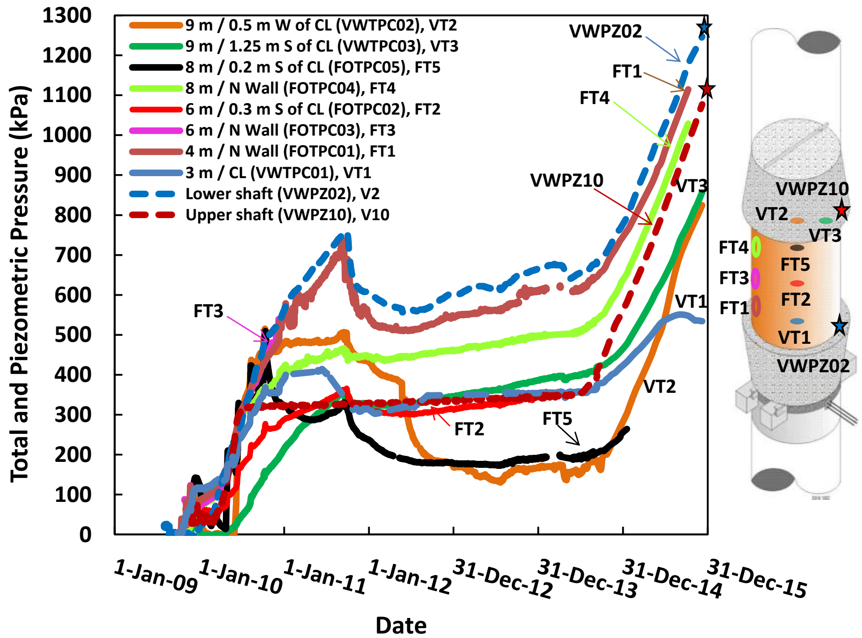

(a) Total pressures in the clay seal

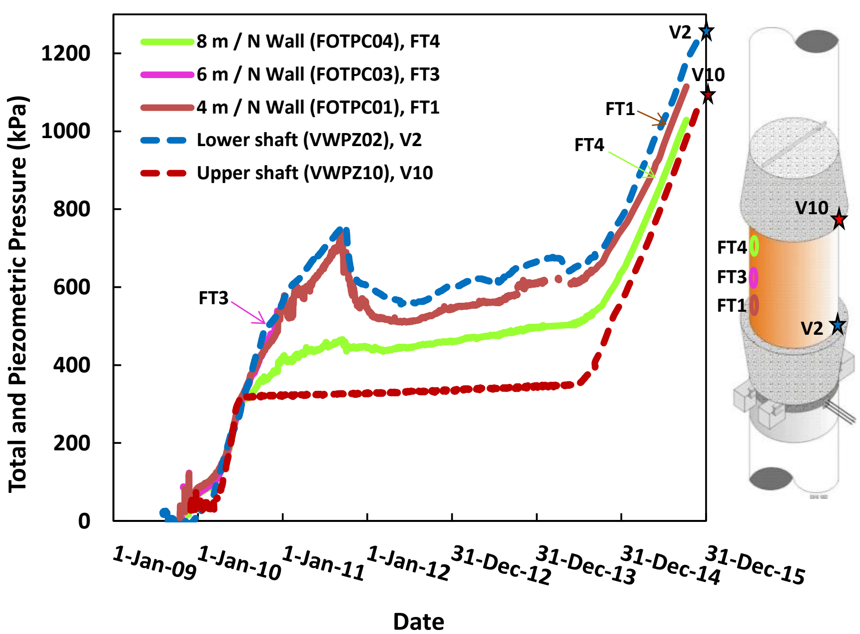

(b) Total pressures at the rock-clay seal interface

Figure 3-5. Total pressures recorded in the clay seal (after Priyanto et al. 2014) (cont'd)

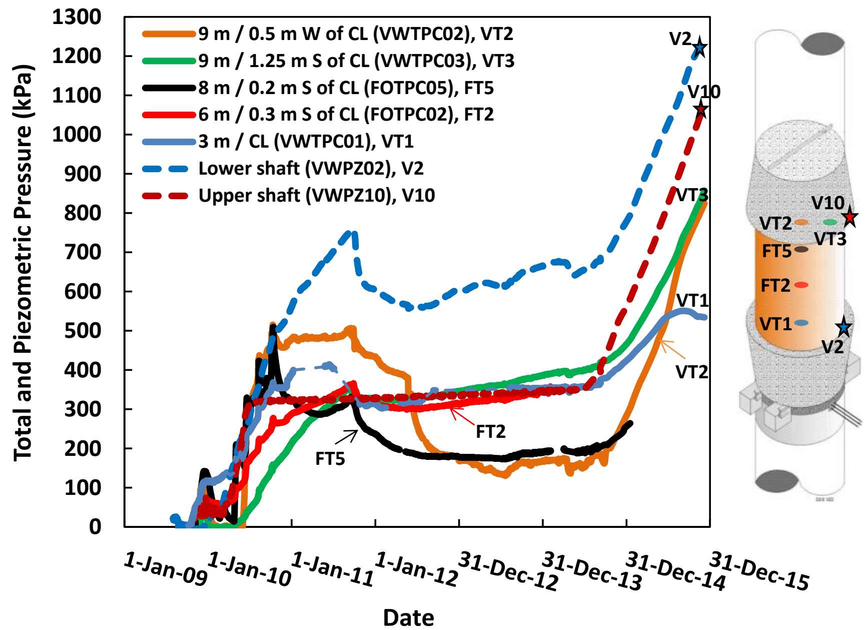

(c) Total pressures at the vertical centerline of the clay seal

Figure 3-5. Total pressures recorded in the clay seal (after Priyanto et al. 2014)

CHAPTER 4

THERORETICAL ASPECTS OF T-H-M COUPLING

4.1 Governing Thermal-Hydraulic-Mechanical (T-H-M) Balance Equations

A macroscopic balance equation of an extensive thermodynamic process consists of three sets of governing equations: mass balance equations, internal energy balance equations and momentum balance equations. This section presents derivations of the balance equations for mass, energy density and momentum. The procedures described by Rutqvist et al. (2000) are followed in these derivations.

The starting point is the general thermodynamic balance equation given by:

$$\frac{\partial}{\partial t} M_{\psi}^{\kappa} + \nabla \cdot q_{\psi}^{\kappa} - Q_{\psi}^{\kappa} = 0 \tag{4-1}$$

where, M_{ψ}^{κ} represents the mass or energy per unit volume. κ represents the mass component (e.g., solid, water or dry air) or the heat component and ψ represents a phase. In the following derivations three different phases (i.e., solid (s), liquid (l) and gas (g)) are considered. Q_{ψ}^{κ} represents a production rate of component κ in phase ψ. For example, Q_{l}^{a} represents a production of the dry air mass component per unit volume in the liquid phase. This term can represent a physical process like the dissolution of air into water. The term q_{ψ}^{κ} in Equation 4-1 represents a flux density (vector) with respect to a fixed coordinate system. Equation 4-1 is a general fundamental equation that allows for the following basic equations for hydraulic, thermal and mechanical processes.

4.1.1 Mass Conservation Equations

The individual contributions of Equation 4-1 for flowing fluids are the mass, M_{ψ}^{κ}, and mass flux, q_{ψ}^{κ} of a component (κ = a for air or w for water) in a phase (ψ = g for gas or l for liquid). The mass, M_{ψ}^{κ} can be expressed as:

$$M_{\psi}^{\kappa} = \phi S_{\psi} \rho_{\psi}^{\kappa} \tag{4-2}$$

where, ϕ is porosity and S_{ψ} is saturation phase (ψ = g for gas or l for liquid), ρ_{ψ}^{κ} is mass of component (kg/m^3) (κ = a for air or w for water) in a phase (ψ = g for gas or l for liquid).

The flux vector, q_{ψ}^{κ} can be expressed as:

$$\mathrm{q}_{\psi}^{\kappa} = \mathrm{i}_{\psi}^{\kappa} + \phi S_{\psi} \rho_{\psi}^{\kappa} \mathrm{v}_{\psi} \tag{4-3}$$

In which $\mathrm{i}_{\psi}^{\kappa}$ represents non-advective (diffusion/dispersion) mass flux of component κ in phase λ. The velocity vector v_{ψ} in the advective term represents the physical velocity of the fluid phase.

The fluid mass balance can be expressed after inserting Equations 4-2 and 4-3 into 4-1:

$$\frac{\partial(\phi S_{\psi} \rho_{\psi}^{\kappa})}{\partial t} + \nabla \cdot (i_{\psi}^{\kappa} + \phi S_{\psi} \rho_{\psi}^{\kappa} \mathrm{v}_{\psi}) - \mathrm{Q}_{\psi}^{\kappa} = 0 \tag{4-4}$$

The term, Q_{ψ}^{κ} can represent the movement of a component between phases due to dissolution, evaporation or condensation. An equation similar to Equation 4-4 can be derived for the solid. There is no source term for the solid mass per unit volume since it is assumed that the solid will not be dissolved in the fluid.

$$\frac{\partial}{\partial t}((1-\phi)\rho_S) + \nabla \cdot ((1-\phi)\rho_S \mathrm{v}_s) = 0 \tag{4-5}$$

The velocity vector, v_{ψ}, in Equation 4-3 can be divided into two vectors: one for the solid v_s and the other for the fluid velocity relative to the solid $\mathrm{v}_{r\psi}$.

$$\mathrm{v}_{\psi} = \mathrm{v}_s + \mathrm{v}_{r\psi} \tag{4-6}$$

Inserting Equation 4-6 into Equation 4-4 and applying the product rule provides:

$$\frac{\partial}{\partial t}\left(\phi S_{\psi}\rho_{\psi}^{\kappa}\right) + \phi S_{\psi}\rho_{\psi}^{\kappa}\,(\nabla \cdot \mathrm{v}_s) + \mathrm{v}_s \cdot \nabla\left(\phi S_{\psi}\rho_{\psi}^{\kappa}\right) + \nabla \cdot (\mathrm{i}_{\psi}^{\kappa} + \phi S_{\psi}\rho_{\psi}^{\kappa}\mathrm{v}_{r\psi}) - \mathrm{Q}_{\psi}^{\kappa} = 0 \tag{4-7}$$

The material derivative following the solid can be changed from its Eulerian form (i.e., observed from a fixed coordinate system) into its Lagrangian form (i.e., co-moving coordinate system) by using the material derivative given in Equation 4-8:

$$\frac{D}{D^s t} = \frac{\partial}{\partial t} + \nabla \cdot \mathrm{v}_s \tag{4-8}$$

With this definition, Equation 4-7 can be written in a more convenient form:

$$\phi\frac{D\left(S_{\psi}\rho_{\psi}^{\kappa}\right)}{D^s t} + S_{\psi}\rho_{\psi}^{\kappa}\frac{D\phi}{D^s t} + \phi S_{\psi}\rho_{\psi}^{\kappa}\,(\nabla \cdot \mathrm{v}_s) + \nabla \cdot (\mathrm{i}_{\psi}^{\kappa} + q_{r\psi}^{\kappa}) - \mathrm{Q}_{\psi}^{\kappa} = 0 \tag{4-9}$$

where,

$$q_{r\psi}^{k} = \phi S_{\psi} \rho_{\psi}^{\kappa} \mathrm{v}_{r\psi} \tag{4-10}$$

Equation 4-9 is the Lagrangian form of the relative mass balance equation.

A similar procedure can be applied to the solid mass balance equation in Equation 4-5. Applying the product rule yields:

$$\frac{\partial}{\partial t}((1-\phi)\rho_s) + \mathrm{v}_s \cdot \nabla\big((1-\phi)\rho_s\big) + (1-\phi)\rho_s(\nabla \cdot \mathrm{v}_s) = 0 \tag{4-11}$$

Again Equation 4-11 can be transformed from its Eulerian form into its Lagrangian form by using the material derivative given in Equation 4-8.

$$\frac{D(1-\phi)\rho_s}{D^s t} + (1-\phi)\rho_s(\nabla \cdot \mathrm{v}_s) = 0 \tag{4-12}$$

After applying the production rule, this equation can be used to express in terms of porosity variation, $\frac{D\phi}{D^s t}$, that appears in Equation 4-9.

$$\frac{D\phi}{D^s t} = \frac{(1-\phi)}{\rho_s}\frac{D\rho_s}{D^s t} + (1-\phi)(\nabla \cdot \mathrm{v}_s) \tag{4-13}$$

The divergence of the solid velocity $\nabla \cdot \mathrm{v}_s$ can be expressed in terms of skeleton volume strain ε_{v}:

$$\nabla \cdot \mathrm{v}_s = \frac{D\varepsilon_{\mathrm{v}}}{Dt} \cong \frac{\partial \varepsilon_{\mathrm{v}}}{\partial t} \tag{4-14}$$

Assuming that $\mathrm{v}_s \cdot \nabla S_\psi \rho_\psi^\kappa$ and $\mathrm{v}_s \cdot \nabla \rho_s$ are negligible due to small strain, plugging Equation 4-14 into Equation 4-12 and Equation 4-13 leads to:

$$\phi \frac{\partial \left(S_\psi \rho_\psi^\kappa\right)}{\partial t} + S_\psi \rho_\psi^\kappa \left[\frac{\partial \varepsilon_\mathrm{v}}{\partial t} + \frac{(1-\phi)}{\rho_s}\frac{\partial \rho_\mathrm{s}}{\partial t}\right] - \mathrm{Q}_\psi^\kappa = -\nabla \cdot (\mathrm{i}_\psi^\kappa + q_{r\psi}^\kappa) \tag{4-15}$$

The total mass balance of each component can be derived from relevant contributions in each phase (ψ = g for gas or l for liquid) to give expression of air and water relative mass balance.

$$\phi \frac{\partial \left(S_l \rho_l^a + S_g \rho_g^a\right)}{\partial t} + (S_l \rho_l^a + S_g \rho_g^a) \left[\frac{\partial \varepsilon_\mathrm{v}}{\partial t} + \frac{(1-\phi)}{\rho_s}\frac{\partial \rho_\mathrm{s}}{\partial t}\right] = -\nabla \cdot (\mathrm{i}_l^a + q_{rl}^a + \mathrm{i}_g^a + q_{rg}^a) \tag{4-16}$$

$$\phi \frac{\partial \left(S_l \rho_l^w + S_g \rho_g^w\right)}{\partial t} + (S_l \rho_l^w + S_g \rho_g^w) \left[\frac{\partial \varepsilon_\mathrm{v}}{\partial t} + \frac{(1-\phi)}{\rho_s}\frac{\partial \rho_\mathrm{s}}{\partial t}\right] = -\nabla \cdot (\mathrm{i}_l^w + q_{rl}^w + \mathrm{i}_g^w + q_{rg}^w) \tag{4-17}$$

Note that the production term, Q_ψ^κ was eliminated in Equations 4-16 and 4-17. Since Q_ψ^κ represents the movement of a component between the two liquid phases, the sum of Q_l^κ *and* Q_g^κ must be zero due to mass conservation.

4.1.2 Energy Conservation Equations

A similar procedure was applied to derive equations for energy balance. The internal energy content and the energy flux for each fluid phase can be defined as:

$$M_\psi^h = \emptyset S_\psi \rho_\psi e_\psi \tag{4-18}$$

$$q_\psi^h = \mathrm{i}_\psi^h + e_\psi^a q_{r\psi}^a + e_\psi^w q_{r\psi}^w + \phi S_\psi \rho_\psi e_\psi \mathrm{v}_s = \mathrm{i}_\psi^h + q_{r\psi}^h + \phi S_\psi \rho_\psi e_\psi \mathrm{v}_s \qquad (4\text{-}19)$$

where i_ψ^h represents a diffusive energy flux described by Fourier's law and e_ψ^κ represents the internal energy per unit mass of component κ in phase ψ. e_ψ^a and e_ψ^w are the specific energies of air and water component per unit mass of respective component. The remainder of Equation 4-19 represents an advective flux of energy. The velocity term in the advective flux is again divided into two parts: one for the solid velocity and the other for the fluid velocity relative to the solid. The internal energy content and energy flux density of the solid can be described as:

$$M_s^h = (1 - \emptyset)\rho_s e_s \qquad (4\text{-}20)$$

$$q_s^h = \mathrm{i}_s^h + (1 - \emptyset)\rho_s e_s \mathrm{v}_s \qquad (4\text{-}21)$$

Local thermal equilibrium is assumed in this equation. This means that the temperature of the solid, liquid and gas phases at a certain point is considered to be equal. This can be a good approximation when the flow velocity is small because the phases can have sufficient time to equilibrate. This assumption allows for a single energy equation. Substituting Equations 4-18 – 4-21 into the Equation 4-1 for general thermodynamic balance and summing the energy balance contributions from the solid, liquid and gas phases under the assumption that v_s is small gives:

$$\frac{\partial\left(\phi S_l \rho_l e_l + \phi S_g \rho_g e_g + (1-\phi)\rho_s e_s\right)}{\partial t} - Q^h = -\nabla \cdot (\mathrm{i}_m^h + q_{rl}^h + q_{rg}^h + q_{rs}^h) \qquad (4\text{-}22)$$

where i_m^h is an equivalent heat conduction over all the phases and Q^h is the total energy production in all of the phases. Using such an equivalent heat conduction is only justified under the assumption of uniform temperature. If these three phases have different temperatures, the equations will be more complex. If thermal equilibrium is not assumed, this energy exchange between phases can be integrated in the production terms Q for each phase's energy balance equation. The heat exchange between the phases at a specific point should be examined and properly applied since it affects the temperature of each of the phases individually. In this case, three energy balance equations should be used instead of Equation 4-22. One for each phase and each equation would require an expression for its own heat conduction and energy production. However, since local thermal equilibrium is assumed, the single Equation 4-22 is sufficient and an equivalent heat conduction, i_m^h is used. It depends on the volume fractions of the different phases (through porosity and saturation) and their specific thermal conductivities.

4.1.3 Momentum Conservation Equation

The last balance equation is the law of conservation of linear momentum. Each phase is assumed to be present at every point with volume fractions adding up to unity. This allows techniques from continuum mechanics (Rutqvist et al. 2000). Fung and Tong (2001) show the equation of motion, which is one of the most fundamental equations.

$$\rho \frac{D\mathrm{v}}{D\mathrm{t}} = \nabla \cdot \sigma + \mathrm{X} \tag{4-23}$$

In which σ is the stress tensor and X represents a body force. In the absence of electromagnetic forces, the body force reduces to the weight of the material (i.e., static stress equilibrium) and Equation 4-23 becomes:

$$\nabla \cdot \sigma + \rho_m g = 0 \qquad (4\text{-}24)$$

where s is the total stress tensor, g is a vector for the acceleration resulting from gravity, and ρ_m is the average density of the mixture (i.e., adding the weight contributions of the solid, liquid and gas phases):

$$\rho_m = (1-\phi)\rho_s + \phi S_l \rho_l + \phi S_g \rho_g \qquad (4\text{-}25)$$

The total stress σ in Equation 4-24 can be divided into an effective stress and a pressure term according to Bishop's method.

$$\sigma = \sigma' + \big(\chi p_w + (1-\chi)p_g\big)\mathrm{I} \qquad (4\text{-}26)$$

Inserting Equation 4-26 into Equation 4-24 gives:

$$\nabla \cdot \Big(\sigma' + \big(\chi p_w + (1-\chi)p_g\big)\mathrm{I}\Big) + \rho_m g = 0 \qquad (4\text{-}27)$$

The governing balance Equations 4-16, 4-17, 4-22 and 4-24 contain a large number of unknown parameters. Rutqvist et al. (2000) suggested that additional general equations and constraints were needed for defining the complete T-H-M state in a porous continuum and reducing the number of unknown parameters.

4.2 Theoretical Aspects of CODE_BRIGHT

CODE_BRIGHT is a finite element program for analyzing Thermal-Hydraulic-Mechanical (T-H-M) problems in geological media. This program couples the thermal (multiphase heat transport in porous media), hydraulic (two phase flow of liquid and gas in porous media) and mechanical (unsaturated soil mechanics) problems. These problems require a number of constitutive laws accordingly (Olivella et al. 1994, Vaunat and Olivella 2002). This section presents formulations and numerical approaches that are adopted in CODE_BRIGHT.

4.2.1 Basic Formulation Features

Geological and geotechnical materials like rocks and buffer materials are porous media. In general, a porous medium consists of solid grains, water and gas and is distributed in the medium in three phases such as solid, liquid and gas. Figure 4-1 illustrates the problem formulated in a multiphase and mulitispecies approach (CODE_BRIGHT manual 2015). The three phases considered in CODE_BRIGHT are:

- Solid phase (s): mineral
- Liquid phase (l): water, air dissolved and solute
- Gas phase (g): mixture of dry air and water vapour

The three species considered in the program are as follows:

- Solid: the mineral coincident with solid phase
- Water (w): as liquid or evaporated in the gas phase
- Air (a): dry air, as gas or dissolved in the liquid phase

The following assumptions and aspects are taken into account in the CODE_BRIGHT program for the formulation of the problem (Vaunat and Olivella 2002 and CODE_BRIGHT user's guide 2015):

- Dry air is considered a single species and it is the main component of the gaseous phase. Henry's law is used to express equilibrium of dissolved air.
- Thermal equilibrium between phases is assumed. This means that the three phases are at the same temperature.
- Vapour concentration is in equilibrium with the liquid phase. Psychrometric law expresses its concentration.
- State variables (also called unknowns) are: solid displacements, u (three spatial directions); liquid pressure, P_l; gas pressure, P_g; and temperature, T.
- Balance of momentum for the medium as a whole is reduced to the equation of stress equilibrium together with a mechanical constitutive model to relate stresses with strains. Strains are defined in terms of displacements.
- Small strains and small strain rates are assumed for solid deformation. Advective terms due to solid displacement are neglected after the formulation is transformed in terms of material derivatives (in fact, material derivatives are approximated as eulerian time derivatives). In this way, volumetric strain is properly considered.
- Balance of momentum for dissolved species and for fluid phases are reduced to constitutive equations (Fick's law and Darcy's law).
- Physical parameters in constitutive laws are function of pressure and temperature. For example: concentration of vapour under planar surface (in psychrometric law), surface tension (in retention curve), dynamic viscosity (in Darcy's law), strongly depend on temperature.

4.2.2 Governing Equations

Olivella et al. (1994) presents the governing equations for non-isothermal multiphase flow of water and gas through porous deformable saline media, which are adopted in CODE_BRIGHT. The governing equations of this program are categorized into three main groups: (1) balance equations, (2) constitutive equations and (3) equilibrium relationships. For balance equations, a detailed derivation was given in Section 4.1 and therefore only a brief description is provided in this section.

The total mass flux of a species in a phase (e.g., flux of air present in gas phase) is the sum of the following three terms (Olivella et al. 1994):

- The non-advective flux: i_g^w, diffusive/dispersive.
- The advective flux caused by fluid motion: $\theta_g^w\ q_g$, where q_g is the Darcy's flux.
- The advective flux caused by solid motion: $\phi S_g \rho_g^w du/dt$, where *du/dt* is the vector of solid velocities, S_g is the volumetric fraction of pores occupied by the gas phase and ϕ is porosity.

The total mass flux can be expressed as the sum of the non-advective and fluid motion advective fluxes minus the advective flux caused by solid motion.

Mass Balance of Solid

Equations for mass balance are established using the compositional approach. Volumetric mass of a species in a phase is the production of the mass fraction of that species and the bulk density of the phase. For example, water in gas phase θ_g^w is the product of the mass fraction of that species (ω_g^w) and the bulk density of the phase (ρ_g), (i.e., $\theta_g^w = \omega_g^w \rho_g$).

Similar to the equations in Section 4.1.1, mass balance of solid in the medium is expressed as:

$$\frac{\partial}{\partial t}\big((1-\phi)\theta_s\big) + \nabla \cdot (j_s) = 0 \tag{4-28}$$

where, θ_S is the mass of solid per unit volume of solid and j_S is the flux of solid.

Applying the material derivative for solids, an expression for porosity variation is expressed as:

$$\frac{D_s(\phi)}{Dt} = \frac{1}{\theta_s}\left[(1-\phi)\frac{D_s\theta_s}{Dt}\right] + (1-\phi)\nabla\frac{du}{dt} \tag{4-29}$$

Equation 4-29 expresses the variation of porosity caused by volumetric deformation and solid density variation.

Mass Balance of Water

Remembering that water is present in both the liquid and gas phases, the total mass balance of water is expressed as:

$$\frac{\partial}{\partial t}\left(\theta_l^w S_l \phi + \theta_g^w S_g \phi\right) + \nabla \cdot \left(j_l^w + j_g^w\right) = f^w \tag{4-30}$$

where f^w is an external supply of water. Applying the material derivative to Equation 4-30 leads to:

$$\phi\frac{D_s\left(\theta_l^w S_l+\theta_g^w S_g\right)}{D_t}+\left(\theta_l^w S_l+\theta_g^w S_g\right)\frac{D_s\phi}{Dt}+\left(\left(\theta_l^w S_l+\theta_g^w S_g\right)\phi\right)\nabla\cdot\frac{du}{dt}+\nabla\left(j_l^w+j_g^w\right)=f^w \quad (4\text{-}31)$$

The equations have several unknowns that are related to the dependent variables in some way. For instance, degree of saturation will be computed by using a soil-water characteristic curve that expresses it in terms of temperature, liquid pressure and gas pressure.

Mass Balance of Air

The mass balance equation of air takes into account air in the gas and liquid phases and is written as:

$$\phi\frac{D_s\left(\theta_l^a S_l+\theta_g^a S_g\right)}{D_t}+\left(\theta_l^a S_l+\theta_g^a S_g\right)\frac{D_s\phi}{Dt}+\left(\left(\theta_l^a S_l+\theta_g^a S_g\right)\phi\right)\nabla\cdot\frac{du}{dt}+\nabla\cdot\left(j_l^w+j_g^w\right)=f^a \quad (4\text{-}32)$$

Momentum Balance for the Medium

As mentioned in Section 4.1.3, the momentum balance reduces to the equilibrium of stresses if the inertial terms are neglected:

$$\nabla\cdot\sigma+b=0 \quad (4\text{-}33)$$

where σ is the stress tensor and b is the vector of body forces.

This assumption is acceptable because both velocities and accelerations are small, and can be considered negligible, compared to the stress term. A possible decomposition of strains is:

$$\dot{\varepsilon}=\dot{\varepsilon}^e+\dot{\varepsilon}^{vp}+\dot{\varepsilon}^c+\dot{\varepsilon}^o \quad (4\text{-}34)$$

Where $\dot{\varepsilon}^{e}$ is the elastic strain rate due to stress, $\dot{\varepsilon}^{vp}$ is the viscoplastic strain rate (except creep), $\dot{\varepsilon}^{c}$ is the creep strain rate and $\dot{\varepsilon}^{o}$ is the deformation due to temperature or fluid pressure changes. $\dot{\varepsilon}$ is the total strain rate which is related to solid velocities and can be expressed by:

$$\dot{\varepsilon} = \frac{1}{2}(\nabla\dot{u} + \nabla\dot{u}t) = 0 \tag{4-35}$$

Internal Energy Balance for the Medium

Assuming thermal equilibrium between phases, the temperature is the same in all phases and only one equation of total energy is required (Olivella et al. 1994). Adding the internal energy of each phase, the total internal energy per unit volume of porous medium is expressed as:

$$E_s\rho_s(1-\phi) + E_l\rho_l S_l\phi + E_g\rho_g S_g\phi \tag{4-36}$$

where E_s, E_l, and E_g are specific internal energy corresponding to each phase, which is internal energy per unit mass of phase. Bear et al. (1991) reported that the most important processes of energy transfer in a porous medium were conduction, advection (due to mass flux) and phase change.

Using the species specific internal energies and their mass fluxes, the energy fluxes due to mass motions in phases can be expressed as:

$$j_{Es} = j'^{h}_{s}E^{h}_{s} + j'^{w}_{s}E^{w}_{s} + E_s\rho_s(1-\phi)\dot{u} = j'_{Es} + E_s\rho_s(1-\phi)\dot{u} \tag{4-37}$$

$$j_{El} = j'^{h}_{l}E^{h}_{l} + j'^{w}_{l}E^{w}_{l} + j'^{a}_{l}E^{a}_{l} + E_l\rho_l S_l\phi\dot{u} = j'_{El} + E_l\rho_l S_l\phi\dot{u} \tag{4-38}$$

$$j_{Eg} = j'^{w}_{g}E^{w}_{g} + j'^{a}_{g}E^{a}_{g} + E_g\rho_g S_g \phi \dot{u} = j'_{Eg} + E_g\rho_g S_g \phi \dot{u} \tag{4-39}$$

where j'_{Es}, j'_{El} and j'_{Eg} are advective energy fluxes with respect to the solid phase. With these definitions, the equation of internal energy balance for the porous medium takes three phases into account and is expressed as:

$$\frac{\partial}{\partial t}\left(E_s\rho_s(1-\phi) + E_l\rho_l S_l\phi + E_g\rho_g S_g\phi\right) + \nabla \cdot \left(i_c + j_{Es} + j_{El} + j_{Eg}\right) = f^{Q} \tag{4-40}$$

where i_c is energy flux due to conduction through the porous medium and j_{Es}, j_{El}, and j_{Eg} are advective fluxes of energy caused by mass motions and f^Q is an internal/external energy supply.

In the case of solving problems involving geological materials, this equation usually reduces to the balance of enthalpy because temperature variations cause very large variations of enthalpy compared to the energy variations supplied from deformation work (Olivella et al. 1994).

The fluxes in the divergence term include conduction of heat and advection of heat caused by the motion of every species in the medium. A non-advective mass flux can cause an advective heat flux because a species inside a phase moves and transports energy. However, this term is usually neglected because, with respect to the movement of a containment in a groundwater system, the diffusive term for heat transport (i.e., conduct of heat) is much larger than the non-advective flux caused by the velocity of fluids (Olivella et al. 1994).

4.2.3 Constitutive Theories and Equilibrium Restrictions

The constitutive equations provide the relationship between the independent variables (or unknowns) and the dependent variables. The problem lies with complexity where they are related to the unknowns. The relationships between these variables are also seen in the equilibrium restrictions.

Non-Advective Fluxes of Different Species

In CODE_BRIGHT, non-advective fluxes for only vapour and air are considered (i.e., i_g^w and i_l^a) (Vaunat and Olivella 2002). Pinder and Abriola (1986) and Pruess (1987) suggested that the non-advective (dispersive) fluxes of species inside the fluid phases could be estimated through Fick's law in terms of gradients of mass fraction of species through a hydrodynamic dispersion tensor:

$$\mathrm{i}_\alpha^i = -D_\alpha^i \nabla w_\alpha^i \quad (i = h,\ w \text{ and } \alpha = l \text{ or } I = w,\ a \text{ and } \alpha = g) \tag{4-41}$$

where D_α^i is the dispersion tensor and this dispersion tensor contains non-advective flux caused by molecular diffusion and by hydromechanical dispersion.

Advective Fluxes of Different Fluid Phases

Advective fluxes of fluid phases (i.e., q_l and q_g) can be estimated using a generalized Darcy's law (Bear and Bachmat 1986) expressed as:

$$q_\alpha = -K_\alpha(\nabla P_\alpha - \rho_\alpha g) \qquad \alpha = l, g \tag{4-42}$$

Where $K_\alpha = \mathrm{k}(k_{r\alpha}/\mu_\alpha)$ is the permeability tensor and P_α is fluid pressure of α phase. The intrinsic permeability (tensor k) is dependent of the porous structure of the porous medium. For geological and geotechnical materials, variations of void volume are important and therefore intrinsic permeability can be considered a function of porosity.

Phase and Interphase Physical Properties

The properties of phases are density, viscosity, surface tension and enthalpy. They are shown in the balance equations and as parameters in constitutive laws. In general, these properties are likely to be dependent on the composition of the phase and on the independent variables (e.g., temperature and pressure) (Olivella et al. 1994).

The soil-water characteristic curve represents the equilibrium between suction (P_g – P_l) and capillary forces (surface tension) in the meniscus. This curve is an empirical relationship that is related to the inter-dependence of fluid saturation and suction. Several models for the soil-water characteristic curve are available in the literature. The van Genuchten (1980) curve is used in CODE_BRIGHT (Vaunat and Olivella 2002).

Equilibrium Restrictions

The assumption of equilibrium reduces the number of equations of mass balance. This assumption is adequate because phase change processes (i.e., chemical processes) are faster than the processes (flow and deformation) in porous media (Olivella et al. 1994). In this way, the concentrations of species in phases are considered dependent variables. These species are air dissolved in the liquid phase and water dissolved in the gas phase. Henry's law and psychrometric law are used to explain this equilibrium. Henry's law expresses a linear relationship between the concentration of air in dissolution and the partial pressure of air in the gaseous phase (Olivella et al. 1994). However, since air dissolved in the general problem has only a small influence, this law is kept as an approximation.

Psychrometric law describes the variation of vapour density or partial vapour pressure in the gas phase due to the surface of the liquid phase and the temperature.

$$\theta_g^w = (\theta_g^w)^o \exp\left(\frac{-(P_g - P_l)M_w}{RT\rho_l}\right) \tag{4-43}$$

where $(\theta_g^w)^o$ is the vapour density in the gas phase in contact with planar surface (i.e., $P_g - P_l = 0$) and depends on temperature. The ambient relative humidity measured by a psychrometer is considered to be vapour in contact with pure water.

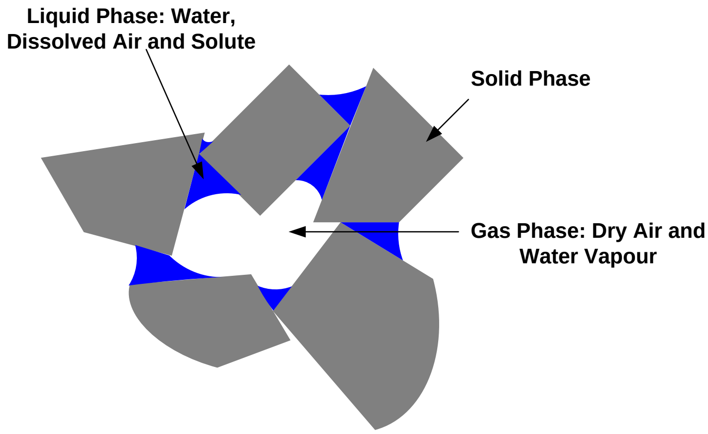

Figure 4-1. Schematic representation of an unsaturated porous material (CODE_BRIGHT user's guide 2015)

CHAPTER 5

NUMERICAL MODELLING OF A SHAFT SEALING SYSTEM

5.1. Introduction

Numerical modelling of the behaviour of clay-based sealing systems is very important for repository engineering design. Since the shaft seal is made up of compacted highly swelling clay, the coupling between hydraulic and mechanical phenomena should be explicitly considered. The interaction with the host rock also plays an important role in the evolution of the sealing system and should be included in the numerical analysis. The constitutive laws selected for numerical modelling consider the hydraulic-mechanical behaviour of the sealing components in both the saturated and unsaturated regimes. Performance of numerical analyses in connection with well instrumented in situ experiments provides a valuable opportunity to assess the evolution of sealing system components and allows for longer-term performance assessment than could be achieved by any physical experiment.

In this research study, a Finite Element Method (FEM) program, CODE_BRIGHT (Vaunat and Olivella 2002) has been used to examine the hydraulic-mechanical (H-M) behaviour of the sealing system. CODE_BRIGHT is a finite element program for the analysis of coupled thermo-hydraulic-mechanical (T-H-M) phenomena in geological media and was developed by University of Cataluña, Barcelona (Vaunat and Olivella 2002). Details of the numerical approach and theoretical formulation are described in Chapter 4. In order to accomplish pre-processing and post-processing of the CODE_BRIGHT input and output data, a universal, adaptive and user-friendly graphical user interface known as GiD (Ribó et al. 2000) has been used. GiD allows for geometrical modelling, data input and visualization of results for all types of numerical simulation programs (Ribó et al. 2000).

Coupled H-M constitutive models have been developed using the CODE_BRIGHT program (Vaunat and Olivella 2002). An elastoplastic constitutive model was used to describe the behaviour of the unsaturated soil and the Basic Barcelona Model (BBM) (Alsonso et al. 1990) was used to determine a set of behavioural parameters for use in describing the mechanical behaviour of the sealing system components. The hydraulic behaviour of the sealing components was defined through the use of van Genuchten's (1980) Soil-Water Characteristic Curve (SWCC) and Wan's (1996) soil-water retention relationship.

As mentioned earlier, the overall behaviour of the shaft sealing system is controlled mainly by coupled hydro-mechancial effects. In this case, the mass balance of water (Equation 4-30) and stress equilibrium (Equation 4-33) are solved simultaneously in the computer program. This means that flow of the vapour phase and air flow are not considered. As a consequence, no diffusive flux is considered.

Baroghel-Bouny et al. (1999) indicated that transport of gases could have significant effect on the saturation-desaturation process in cement-based materials. For clayey materials, Olivella and Gens (2000) reported that the build-up of gas pressure in presence of vapour phase depended on the ratio between material tortuosity and intrinsic permeability. Intrinsic permeability is affected by microstructural changes that depend themselves on the type of pore fluid.

Consequently, it is likely that gas pressure build-up will be low in the early stages of system wetting and will increase only at the very end of the process when degree of saturation is close to unity. Omitting consideration of two flows of vapour and air may reduce the reliablity of the numerical results, however it will be seen in this section that numerical predictions of this study capture field readings quite well.

5.2. Development of Numerical Modelling

5.2.1. Model Geometry, Boundary and Initial Conditions

A two-dimensional view of the axisymmetric model of the ESP is shown in Figure 5-1(a). The domain in the numerical model has 100-m radius and 200-m height. This domain size was determined after performing scale effect analysis using different domain sizes (more details are provided in Section 5.3.1). The bottom of the shaft seal is placed at 97 m above the bottom of the model, corresponding to a depth of 276 m below surface.

To complete a numerical simulation of the ESP's evolution a series of initial state and boundary conditions must be defined. These are so far as possible based on measured initial conditions and then the evolution of the system is modelled using a series of previously established behavioural relationships. The initial and boundary condition assumptions are as follows:

1. The actual URL shafts were open for approximately 26 years, the period of ongoing facility operation. This resulted in a hydraulic draw-down cone in the vicinity of the shafts and URL excavations. This situation would also occur in an actual repository site. For this reason, the groundwater flow around the empty shaft prior to installation of the shaft

seal was numerically simulated first. Pore water pressure in the rock due to the open shaft was modelled for 26 years.

2. Initial pore water pressure (u_w) was applied in the rock based on the measurement of the groundwater pressure at AECL's URL and calculated using the following equation (Chandler 2000):

$$u_w = \rho_w \bullet g \bullet (z+80) \text{ for } z \leq -80 \text{ m } (0 \text{ for } z > -80 \text{ m}) \quad (5\text{-}1)$$

where z is the depth (m) from the ground surface.

3. At the time the shaft seal was installed, a linear change in pore water pressure in the surrounding rock mass was assumed and values of 0.9 MPa and 2.9 MPa were applied at the top (depth -173 m) and bottom (depth -373 m) respectively of the model.
4. It was assumed that there was no fluid flow across the boundary that corresponded to the centre of the axisymmetric model at the coordinate x = 0 m.
5. The in situ compacted bentonite-sand (clay seal) had an average bulk unit weight of 19.9 kN/m^3, which would lead to a passive overburden pressure of ~120 kPa for the 6-m-thick bentonite-sand component. An initial stress from 0 to 120 kPa was linearly applied across the clay seal due to its bulk unit weight.
6. The concrete segments did not contribute to the initial vertical stresses since the concrete was mechanically fixed in place through keying into the rock above and below the clay seal component.
7. Assuming pore air pressure was constant and equal to zero (atmospheric pressure) in the clay seal, suction would be equal to negative pore water pressure (i.e., $s = -u_w$). Initial

suction of 12.8 MPa in the clay seal was applied, corresponding to an initial degree of saturation of 67%. This value was calculated using the soil-characteristic curve and degree of saturation for the clay seal material provided by Wan (1996).

8. For mechanical boundary conditions, the top and bottom boundaries of the model were fixed in the Y-direction and the outside boundary of the model was fixed in the X-direction.

Figure 5-1(b) illustrates the dimensions of the model with initial boundary conditions as described above. Fuchsia-coloured rectangles shown in Figure 5-1(b) indicate geometry surfaces generated.

5.2.2. Discretization of the Model

Three different numerical simulations were performed as part of this study:

- Case 1: Couple H-M modelling with horizontal fracture zone 2 (FZ2)
- Case 2: Coupled H-M modelling with FZ2 inclined at 16 degrees to the horizontal plane
- Case 3: Coupled H-M modelling with horizontal FZ2 and seepage applied along the edges of the clay seal above and below FZ2 as well as at top and bottom of it

Before performing numerical modelling of these three cases, potential scale effects on numerical results were examined using different model domain sizes (i.e., small, medium and large domain sizes). The numerical results indicated that it was reasonable to choose the medium domain size defined in Section 5.3.1 to be used for this numerical study (more details in Section 5.3.1). Case 1 assumed FZ2 to be horizontal to simplify the conceptual model. Case 2 assumed FZ2 to be inclined 16 degrees from the horizontal plane. It should be noted that the actual inclination of the FZ2 at the URL is 20 - 25 degrees (Everitt et al. 1990). Selection of the lower angle was required due to limitations in modelling geometry and 16 degrees is the maximum inclined angle the model can handle. Case 2 is just a comparative model to Case 1 and does not represent the actual physical conditions. Numerical modelling conditions of Case 3 were identical to Case 1, except for applying seepage of water into the system at the top and bottom of the clay seal component as well as the edges of the clay seal above and below FZ2. The rate of groundwater seepage flow was measured to be approximately 3.0 m^3 per day. Case 3 simulated groundwater seepage through the interfaces between rock and concrete cap toward the clay seal component.

The discretization of the axisymmetric model in the 2-D representation is illustrated in Figure 5-2. There were 2844 nodes and 2,730 elements and more elements were generated near the shaft seal location, which is the focus of this study.

5.2.3. Determination of Material Parameters for Numerical Modelling

The modelled domain consisted of three different materials: the clay seal (60% sand-40% bentonite), the granite and the concrete. The clay seal was assumed to be an elastoplastic material and the granite rock and concrete were assumed to be a linear elastic material in this study.

The hydraulic and mechanical parameters and values used in the study are the result of extensive studies conducted on unsaturated bentonite-sand mixtures (50% - 50% dry mass) during the period from 1988 to 2006. Although the data obtained from these studies were slightly dated, it is believed that they are the best available information to describe the materials installed in the ESP.

It is noted that the clay seal installed in the shaft seal consists of a bentonite/sand ratio of 40%/60%, while the laboratory test data used to generate many of the behavioural parameters has a bentonite/sand ratio of 50%/50%. A key characteristic of the bentonite-sand mixture (BSM) is that when the bentonite content exceeds approximately 30%, the material is considered to have a clay-dominated behaviour (Graham et al. 1992), which means that the fundamental behaviour of these two materials should be similar and existing laboratory-generated test data can be used to estimate the properties of the bentonite-sand mixture.

Hydraulic Parameters of Clay Seal Material

The clay seal was compacted in situ with initial gravimetric water content of 12.1% and an average dry density of 1.81 Mg/m^3. Initial porosity of the clay seal was 0.33 and the initial degree of saturation of the clay seal was 67%, corresponding to the initial suction of 12.8 MPa for the clay seal. Effective Montmorillonite Dry Density (EMDD) of the clay seal was calculated to be 1.04 Mg/m^3.

The relationship between water content and suction for the unsaturated buffer was derived from the results of three different types of free swell tests (Wan 1996). Wan (1996) described the psychrometer, vapour equilibrium and filter paper tests used to define the soil-water retention relationship in Figure 5-3. Wan (1996) defined suction in terms of gravimetric water content (i.e., 1%-11% and 11%-25%) as shown, but was unable to define suction uniquely as a function of degree of saturation. The relationship between degree of saturation (S_r) and gravimetric water content (w) also depends on dry density (γ_d), as defined in the following equation:

$$S_r = \frac{w}{\frac{\gamma_w}{\gamma_d} - \frac{1}{G_s}} \tag{5-2}$$

where γ_w is the density of water (1 Mg/m^3) and G_s is the specific gravity of the clay seal material, taken to be 2.7 (Chandler 2000).

The suction versus water content relationship for water content of 11% - 25% in Figure 5-3 can be rewritten as follows:

$$w = \frac{1.983 - \log s}{0.074} \tag{5-3}$$

The soil-water retention curve for constant volume (i.e., dry density unchanged at 1.81 Mg/m^3) by substituting Equation 5-3 into Equation 5-2 was estimated (Figure 5-4). The suction-saturation relationship can be fitted to van Genuchten's equation that is used in CODE_BRIGHT:

$$S_{re} = \left[1 + \left(\frac{s}{P_0}\right)^{1/(1-\beta_1)}\right]^{-\beta_1} \tag{5-4}$$

where s is suction in MPa, β_1 is a fitting parameter and P_0 is the air entry value determined using regression analysis. From this matching process, P_0 and β_1 were determined to be equal to 11 MPa and 0.48, respectively (Figure 5-4). The effective degree of saturation (S_{re}) takes into account all water that is not removed during oven-drying of buffer at a temperature of 110°C (van Genuchten 1980) and is expressed as follows:

$$S_{re} = \frac{S_r - S_{rres}}{S_{max} - S_{rres}} \tag{5-5}$$

where S_r is the absolute degree of saturation, S_{rres} is the degree of residual saturation representing the remaining mass of retained water at a temperature of 110°C and S_{rmax} is the degree of maximum saturation.

Using existing experiment data for bentonite-sand (50-50) mixtures compacted to dry density of ~1.67 Mg/m^3 (Wiebe 1996, Tang 1999, Blatz 2000, Anderson 2003), the fitting parameters of P_0 and β_1 were also estimated in plots between suction and degree of saturation. By matching to the experimental data, P_0 = 12 MPa and β_1 = 0.36 were determined (Figure 5-5). These two methods provided P_0 values ranging from 11 MPa to 12 MPa, and values of β_1 ranging from 0.36 to 0.48.

The hydraulic conductivity of the unsaturated clay seal was determined using the following empirical equation (5-6) presented by Gens et al. (1998), which was described as a function of saturation. Gens et al. (1998) suggested this equation for clay-sand buffer materials with over 40% degree of saturation, which is applicable to the clay seal (initial degree of saturation of 66.7%).

$$K = K_0 \cdot {S_{re}}^{\frac{1}{2}} \cdot \left(1 - \left(1 - {S_{re}}^{\frac{1}{\beta}}\right)^{\beta}\right)^2 \tag{5-6}$$

where K is the hydraulic conductivity of the unsaturated buffer in m/s, K_0 is the saturated hydraulic conductivity. The hydraulic conductivity (K) is a function of the properties of the medium (soil) and the fluid (water) whereas the intrinsic permeability depends only the soil properties. The saturated hydraulic conductivity (K_0) of the clay seal material was determined by using the relationship between Effective Montmorillonite Dry Density (EMDD) and hydraulic conductivity of bentonite-sand mixtures shown in Figure 5-6. These data shown are laboratory permeability data, except for the data from Kim et al. (2009), which was obtained from 1D consolidation tests. Pfeifle (1987), Bucher et al. (1986), and Radhakrishna and Chan (1985) used Wyoming bentonite-sand mixtures (45% - 45%, 50% - 50%, 70% - 30% dry mass, respectively). Dixon (2000) and Kim et al (2009) used Wyoming bentonite-sand mixtures (50% - 50% dry mass). EMDD is an important normalizing parameter with respect to being able to predict the hydraulic conductivity and swelling pressure when mixed clay:aggregate systems when aggregate content is less than approximately 70% are used (Dixon et al. 2002). At installation, the EMDD for the clay seal was 1.04 Mg/m^3, corresponding to a saturated hydraulic conductivity in order of 10^{-12} m/s. This saturated hydraulic conductivity value (K_0) was used in Equation 5-6 and for the regression parameter (β), a typical value of 0.3 for sand-bentonite mixtures was used (Gens et al. 1998). Figure 5-7 shows the relationship between unsaturated hydraulic conductivity and degree of saturation, which was developed using Equation 5-6 and used in the numerical modelling. Values of hydraulic parameters determined for the clay seal are summarized in Table 5-1.

Mechanical Parameters of Clay Seal Material

The Barcelona Basic Model (BBM), an elastoplastic model for unsaturated soil was used to simulate the mechanical behaviour of the clay seal component. The following equations proposed by Alonso et al. (1990) were used to determine mechanical parameters of the clay seal material. The equation for the yield curve in p-s space is:

$$\left(\frac{P_0}{P^c}\right) = \left(\frac{P_0^*}{P^c}\right)^{[\lambda(0)-\kappa][\lambda(s)-\kappa]} \tag{5-7}$$

where P_0 is preconsolidation stress at varying suction (s), P_0^* is preconsolidation stress for saturated conditions, p^c is reference stress, and $\lambda(s)$ is the stiffness parameter at a given suction (s).

In the numerical study completed in this thesis, preconsolidation stress, P_0^* of 1.0 MPa for saturated condition was used (Blatz and Graham 2003). The stiffness parameter related to suction, $\lambda(s)$ is calculated by the following equation:

$$\lambda(s) = \lambda(0)[(1-r)\exp(-\beta s) + r] \tag{5-8}$$

where $\lambda(0)$ is the stiffness parameter for changes in net mean stress at saturation, r is a parameter defining the maximum soil stiffness; s is suction and β is a constant describing the rate of increase in soil stiffness with suction.

A value of $\lambda(0)$ was determined using experiment data from Lingnau et al. (1995). Lingnau (1995) conducted a series of undrained triaxial tests on saturated buffer specimens composed of 50% bentonite and 50% sand, and calculated a value of 0.12 for $\lambda(0)$ from the plot of ν_c versus σ'. With the value of $\lambda(0)$ calculated, the elastic stiffness parameter (κ) for changes in net mean stress was estimated using the relationship between hardening parameter (Λ) and $\lambda(0)$ (Lingnau et al. 1995). Lingnau (1995) estimated the hardening parameter (Λ) value of 0.79 for the bentonite-sand mixture at room temperature and therefore a value of the elastic stiffness parameter (κ) for changes in net mean stress for the clay seal material was calculated to be 0.0256.

$$\Lambda = 1 - \frac{k}{\lambda(0)} \tag{5-9}$$

In addition, P_0 and s values were obtained from laboratory testing of a 50:50 bentonite:sand mixture (Blatz and Graham 2003). These values were then used to determine values of reference stress (p^c). Parameters r and β were determined using Equations 5-7 and 5-8. The following values were determined and used in this study:

r = 0.65 $\quad\quad$ $\beta = 5 \times 10^{-7}$ Pa^{-1} $\quad\quad$ $p^c = 1.8 \times 10^5$ Pa.

Thomas et al. (2002) estimated a value of the stiffness parameter (κ_s) for changes in suction in the elastic region, using laboratory data from Blatz and Graham (2003). Thomas et al. (2002) reported a value of 0.0111 for κ_s and this value was used in this numerical simulation. He also estimated a value of 0.111 for λ_s, the stiffness parameter for changes in suction in the plastic region based on suggestion provided by Volckaert et al. (1996), which λ_s would be ten times greater than κ_s.

The slope of the critical state line (M) of 0.526 was used for the clay seal material (Graham et al. 1989, Lingnau et al. 1995). Values of mechanical parameters determined are summarized in Table 5-2.

Hydraulic-Mechanical Parameters of Granite Rock

Equation 5-4 from van Genuchten (1980) was used again for soil-water retention curve of the granite rock. Gens et al (1998) suggested a value of 0.33 for β_1 for granite rock. A value of the air entry value (P_0) was taken as 0.7 MPa for granite (Thomas et al. 2002).

Hydraulic conductivities (K) of the granite rock were estimated using measurements previously done at the AECL's URL (Chandler 2000, Martino 2000, Dixon et al. 2002). The hydraulic conductivity for intact granite rock typically ranged from approximately 10^{-12} to 10^{-13} m/s and could increase up to 10^{-9} m/s in the region of the Excavation Damage Zone (EDZ) (Martino 2000). Based on these data, the hydraulic conductivity for the intact rock is assumed to be 4 x 10^{-13} m/s. For the purpose of numerical simulation, the FZ2 feature is defined as being uniform in hydraulic character, 4 m thick and its hydraulic conductivity is assumed to be 1 x 10^{-9} m/s. Table 5-1 shows a summary of hydraulic parameters assumed for the granite rock. The granite rock was assumed to be linearly elastic. Its Young's modulus was set as 60 GPa and its Poisson's ratio was set as 0.22 as suggested by Graham et al. (1997).

Hydraulic-Mechanical Parameters of Concrete Component

The concrete components were assumed to be linearly elastic. Its mechanical and hydraulic parameters were assumed to be the same values as those for the granite rock. Martino et al. (2008) measured the hydraulic conductivity of 1 x 10^{-12} m/s for the concrete cap in the Tunnel Sealing Experiment. Low Heat High Performance Concrete (LHHPC) was used for both the concrete cap (Chandler et al. 2002) and the ESP concrete segments (Dixon et al. 2009).

Schneider et al. (2012) reported a value of 5.7 x 10^{-13} for the hydraulic conductivity of concrete seal in a deep geological repository from laboratory testing. Schneider et al. (2012) tested concrete specimens whose constituents were the same as the LHHPC except for calcium carbonate (limestone fumes) used instead of silica fume. These two additives are commonly used to improve workability of the cement mix and develop early strength of concrete. Although a slight difference between silica fume and limestone fume may influence the hydraulic conductivity of concrete, it is assumed that the influence of the difference between these two fumes would be minor.

5.3. Discussion of Numerical Results

This section presents results of coupled hydraulic-mechanical (H-M) simulation of a shaft seal at AECL's Underground Research Laboratory. As mentioned in Section 5.2.2, the first coupled H-M simulation was conducted to assess potential scale effects on numerical results and Section 5.3.1 presents the results. Section 5.3.2 and Section 5.3.3 show comparisons of results from three different numerical models with physically measured ESP experimental data with regard to changes in suction, degree of saturation, pore water and total pressures. Section 5.3.3 also presents prediction of displacements within the clay seal.

5.3.1. Verification of Scale Effect in Numerical Modelling

Three different domain scales were modelled numerically. The first domain had 50 m radius and 200 m thickness (smaller scale), the second domain had 100 m radius and 200 m thickness (medium scale), and the last domain had 150 m radius and 200 m thickness (larger scale). Note that only a radius size was changed in the numerical modelling without changing the elevation of the shaft seal and the number of elements.

Possible scale effects on suction prediction in the clay seal was assessed first. Figure 5-8 shows changes in suction with time for the three different domain scales modelled. The results indicate that there was little effect of using different scales on the hydraulic behaviour of the clay seal component.

After installation of the clay seal, the small and medium scale models show slightly higher pore water pressures of the rock near the clay seal than the larger domain model (Figure 5-9(a)) and slightly lower pore water pressures of the rock in the region between 25 m and 50 m (e.g., the smaller model: 1.7 MPa, the medium model: 1.8 MPa and the large model: 1.87 MPa at 50 m). The difference in pore water pressure between the smaller and larger scale models is 0.17 MPa at 50 m during this period. After 900 days the difference between the two models becomes smaller, about 0.16 MPa, and distribution of pore water pressure using the medium scale model is similar to that using the larger scale model. It also indicates that the difference shown in pore water pressure near the clay seal is minimized with time (Figure 5-9(b)).

Overall, the three scale models show slight difference in pore water pressure near the clay seal after installation of the clay due to numerical scale effects. However, the difference is relatively small and is minimized with time. It would not likely affect greatly interaction with the clay seal component. It is likely that the medium scale represents the average pore water pressure of the other two scales. Based on the results, it would be reasonable to conclude that the medium domain scale is sufficient to minimize model boundary influence on the numerical results. Therefore, all numerical models were conducted using the medium scale in this study.

5.3.2. Hydraulic Behaviour of Clay Seal

Suction Prediction of Clay Seal Compared with ESP Data

Changes in moisture conditions (and hence suction) in the clay seal component of the ESP were measured by psychrometers and TDRs. It is noted that the initial suctions measured by all psychrometers were approximately 6 MPa, which was the upper limit of suction the psychrometers measured. The actual initial suction within the clay seal would actually have been 12.8 MPa based on the known as-placed material's properties. This required that the monitoring data values needed to be adjusted to match with the known initial state and final, saturated conditions measured.

As mentioned in Section 5.2.2, three different numerical simulations were carried out (1) coupled H-M models with horizontal FZ2 (Case 1), (2) coupled H-M simulation with 16-degree-inclined FZ2 (Case 2) and (3) coupled H-M simulation with horizontal FZ2 and seepage applied at the top and bottom and the edge of the clay seal (Case 3).

Numerical results were generated for three different vertical locations in the clay seal component; the bottom, centre, and top, corresponding to 0.1 m, 3 m and 5.9 m from the bottom of the clay seal, respectively. In each vertical location, three horizontal points were taken such as x = 0 m, 1.25 m, and 2.5 m from the centre of the clay seal. These numerical results are compared with the measured data and presented in this section.

Figure 5-10 shows suction predictions of three models at the bottom of the clay seal (y = 0.1 m), compared with field psychrometer readings (Psychrometer 02). Numerical predictions, labelled with NM, obtained from Cases 1 and 2 show similar trends and underestimate field-observed changes in suction at the edge of the clay seal (x = 2.5 m) (Figures 5-10(a) and 5-10(b)). Despite differences in suction between the measured data and numerical results, slopes of the suction prediction for these cases are similar to that of the measured data.

The possible explanation for the underestimation in suction for Cases 1 and 2 could be that the numerical model simplified the groundwater flow system surrounding the clay seal component. In other words, the numerical simulation considers only two directions (horizontal and vertical) of groundwater flow from FZ2 while in the real condition of the shaft, groundwater flows radially toward the perimeter of the clay seal. As a result, saturation at the location of the sensor was anticipated to occur more quickly than that of numerical simulation.

Another possible reason can be that the time of beginning of hydration for the sensor (psy 02) installed in the bottom region is different from the hydration starting time in numerical simulation. In the real field, the hydration process of the clay around the sensor started as soon as completion of installation of the clay in the region, while numerical analysis did not consider installation of the clay seal component with time intervals. Therefore, the underestimation of the field readings can be attributed to these different starting times for hydration. The bottom outer region will be more affected by the different starting times than the top regions as there is a small time-gap between hydration starting time and completion of the clay installation in the top regions. As seen in Figure 5-11 and Figure 5-12, numerical prediction in upper regions captures the field psychrometer readings reasonably well, compared to that in the bottom region.

Figure 5-10(c) clearly demonstrates the effect of applying groundwater seepage in the bottom and outer regions on the hydraulic behaviour of the clay seal. As expected, Case 3 shows a dramatic decrease in suction in the outer region in the initial stage of system wetting. Applying groundwater seepage in the region results in reducing the initial suction from 12.8 MPa to 8.5 MPa and consequently accelerates the rate of decrease in suction, compared to the rates of Case 1 and Case 2.

The three curves of Case 3 indicate similar slopes of suction prediction through the hydration process (Figure 5-10(c)). When suction becomes close to zero, the curves become closer after approximately 2000 days (5.5 years). This means that the additional wetting process in the region affects changes in suction at a very early stage of system wetting, but does not significantly affect the rate of decrease in suction after the early stage. The possible explanation for this phenomenon is that once the edge regions become hydrated and start to swell, the swelling mechanism becomes dominant to control its hydraulic behaviour. In other words, due to the swelling of the clay in the outer region at the earlier stages, its hydraulic conductivity will be lowered and therefore the hydration process then controlled by the lower hydraulic conductivity of the clay, but not by the additional seepage applied.

Figures 5-11 and 5-12 show good agreement between suction prediction in the centre and top of the clay and the field readings (psychrometers 10 and 14, 1.25 m East and North from the centre and 5.9 m from the bottom, respectively). Suction prediction in the centre region for all cases is very close to the experimental data as shown in Figure 5-11. This is likely because of the close match of field to numerically-assumed conditions in this region with the centre region being directly affected by groundwater flow from FZ2. Numerical results of Case 1 and Case 2 in the top region, 5.9 m from the bottom of the clay seal show a reasonably good match with the measured data as shown in Figures 5-12(a) and 5-12(b). However, the predicted suction in Case 3 is slightly overestimated, compared to the measured data (psy14). The top outer region shows a similar pattern of suction changes to that observed in the bottom outer region.

Comparing the numerical prediction of Case 2 with that of Case 1 indicates a similar or slightly faster hydration rate observed in the regions. The effect of groundwater flow from inclined FZ2 (Case 2) seems to be minor in hydraulic behaviour of the clay seal, compared to numerical prediction of Case 1 with perfectly horizontal FZ2. However, the effect becomes noticeable in comparing predicted total pressures, which will be presented later in Section 5.3.3. The possible reason for the influence of inclined FZ2 on hydraulic-mechanical behaviour of the clay seal will be provided in the same section.

Longer-Term Suction Prediction in the Clay Seal Component

Figure 5-13 shows modelled evolution of suction in the clay seal with different times for Case 1. This predicted evolution of suction confirms that the hydration process of the clay seal is dominantly affected by the groundwater flow from FZ2. The centre region is not fully saturated for 17 years and full saturation of the centre region appears for 19 years. The suction (negative pore water pressure) of the clay seal will come to equilibrium after 19 years.

Figure 5-14 shows predicted suctions of the clay seal along a horizontal centre line, 3m from the bottom of the clay seal for all cases. They show a similar pattern of suction prediction, indicating the outer region from 2 m to the edge of the clay seal is significantly affected by the groundwater flow from FZ2 while the inner regions far from the edge respond very slowly. The suction prediction for Case 3 shows a slightly faster rate of decrease in suction with time (Figure 5-14(c)) than the other cases (Figures 5-14(a) and 5-14(b)) due to the seepage applied. The estimated time required for the core of the clay component to achieve full saturation is approximately 18 years for Case 3 and approximately 19 years for Case 1 and Case 2.

These different hydration times can be because more water supply is available along the edge of the clay seal due to seepage applied along the surface of the clay seal so that the outer regions becomes hydrated more rapidly than the same regions for the other cases. The clay seal in the outer regions starts to swell and consequently its dry density is decreased. The swelling of the clay seal in the outer regions compresses the adjacent regions (toward the centre) and therefore results in increasing the dry density of the adjacent inner regions. In turn, the adjacent inner regions start to swell and compresses the outer regions, resulting in increasing the dry density of the outer regions. This process can be continued until the clay seal becomes fully saturated. As a result of this process, the outer regions can be denser and consequently its hydraulic conductivity can be reduced, which means that less groundwater can be available from outside boundary toward the clay seal. This mechanism would occur in the outer regions within a relatively short period of approximately up to 5 years in this numerical simulation.

Degree of Saturation of Clay Seal Compared with ESP TDR Data

The degree of saturation present in the clay seal was estimated using measured TDR data, based on the assumption that the dry density of the clay seal was constant and that the calibration curves for the TDRs prior to installation are representative of what is present in the field installation. A total of 4 TDRs was installed in the clay seal and their locations are shown in Figure 3-2. The degree of saturation of the TDRs in each location was estimated and then compared with numerical results in this section.

Figure 5-15 shows numerical results of the three simulated cases at 2 m from the bottom of the clay seal, compared with the measured readings of TDR1. The numerical results match the measured data reasonably well with respect to trend, but substantially underestimates the measurement from the beginning up to 5 years after start of wetting. However, after 5 years, the prediction of the degree/rate of saturation for all cases becomes closer to the experimental data and shows a similar slope. The TDR1 sensor then shows a substantial increase in degree of saturation (water content) after 6 years. The numerical results cannot capture its evolution during that period.

As shown in Figure 5-15, all cases do not show any discernible difference in the pattern of the predicted degree of saturation. Since the hydration process of the clay in this region is directly affected by the groundwater flow from FZ2, the numerical prediction obtained from all cases indicates little effect of applying either inclined FZ2 or seepage on the hydration process. This similar prediction is also observed in the other regions of the clay seal.

The other TDR sensors show a similar evolution pattern after 6 years. As shown in Figure 5-16, predicted degrees of saturation at the mid-height of the clay seal show good agreement with the measured readings of TDR2 and TDR3. TDR2 was installed at the centre of the clay seal and TDR3 was installed at 1.25 m from the centre of the clay seal. Again the reason for this good match can be that this centre region is likely the most homogenous region and is being affected by only groundwater flow from FZ2. Similar to what was previously observed at a depth of 2 m from the bottom of the clay, all three cases underestimate evolution of degree of saturation in these regions at earlier stages of system wetting, however they capture the measurement well after 3 years in the centre region and 1 year in the region 1.25 m from the centre of the clay. All cases show no noticeable difference in the pattern of the predicted degree of saturation.

Figure 5-17 illustrates another reasonably good match with experimental readings of TDR4 that was installed at 4 m from the bottom of the clay seal. Numerical prediction for all cases shows similar underestimation of the evolution of degree of saturation during the initial period of water uptake and becomes closer to the experimental data after 5 years.

Based on the comparison of the numerical results with the field readings provided by the TDR sensors, it would appear that the numerical simulations provide a reasonable simulation of the trend in water uptake behaviour of the clay seal for the period beyond initial wetting stages (1 - 4 years). The models slightly underpredict early-stage water uptake and appear to slightly overpredict the time required for the core of the clay component to achieve water saturation. The numerical results and the TDR readings available up to December 2015 indicate that the clay seal in the centre region has not been fully saturated.

Pore Water Pressure in near Rock

Pore water pressure in the rock immediately adjacent to the shaft seal (Excavation Damage Zone (EDZ)) was measured at three horizontal distances into the rock (0.5 m, 1.0 m and 1.85 m) at the height of 4.5 m above the base of the clay seal component.

Pore water pressure in the rock near the clay seal was numerically simulated and the results are compared with measured piezometric data as shown in Figure 5-18. The numerical results indicate that discernible changes in the pore water pressure of the rock are occurring within approximately 20 m from the centre of the clay seal. This can be interpreted as indicating influence of the clay seal on the pore water pressure of the rock within this distance. Note that these vibrating wire piezometer sensors installed are capable of measuring only positive pore water pressure, which means that the effect of suction developed by the unsaturated clay seal on evolution of pore water pressure of the rock near the clay is not able to be examined by the sensors. For this reason, only positive pore water pressure readings are provided for comparison with numerical prediction in this section.

Numerical prediction obtained from the three cases indicates that pore water pressure of the rock near the clay seal is directly affected by the clay seal. After installation of the clay seal, the pore water pressure of the rock near the clay immediately decreases and the initial pore water pressure values range from -0.25 MPa to -0.3 MPa. Figure 5-18 also shows that after an immediate decrease in pore water pressure, the pore water pressure of the rock starts rapidly increasing as observed for Cases 1 and 2. This early-stage phenomenon can be due to the dry perimeter regions of the clay becoming saturated by the initial influx of water and, as a result, this newly saturated clay then provides resistance to further water influx. Case 3 shows a relatively gradual increase in pore water pressure compared to the other cases. This gradual decrease in pore water pressure for Case 3 can be attributed to seepage applied along the edge of the clay seal. This additional wetting process is like to accelerate the clay's hydration process in the edge region and consequently reduce its suction potential at the early stage.

After this early stage of the system becoming wetter, the numerical prediction indicates a gradual decrease in pore water pressure of the rock near the clay seal for 845 days. This gradual decrease in pore water pressure in the region is associated with the effect of suction of the clay seal installed. Similar results have been reported by several numerical studies (Thomas et al. 2002, Guo and Dixon 2005, Priyanto et al. 2011). After 845 days, pore water pressure in the area has slowly recovered toward its hydrostatic equilibrium, with the clay-filled region becoming more extensively saturated and allowing for the generation of increasing pore water pressures. Numerical prediction for the three cases underestimates the evolution of pore water pressure of the rock in the region for 845 days and 2300 days. As mentioned before, the discernible difference can be attributed to the limitation of groundwater flow modelling compared to the real shaft conditions.

The numerical results show pore water pressures ranging of -0.25 MPa to -0.3 MPa in the rock nearest to the clay seal after installation of the clay seal. These initial negative pore water pressures are likely attributed to desaturation of the rock adjacent to the shaft seal being exposed to the air for over 25 years of operation. Desaturation of the rock at the region (EDZ) would decrease the hydraulic conductivity of the rock toward the shaft seal (Chandler 2000, Thomas et al. 2002), during the initial stages of system wetting. It was estimated by Chandler (2000) and Thomas et al. (2002) that the initial pore water pressure of the rock in the region immediately adjacent to the shaft (EDZ) ranged from -0.3 MPa to -0.4 MPa. These values were used for their numerical modelling of the isothermal experiment conducted at the 240 level of the AECL's URL in order to investigate the effect of a reduction in relative humidity. Based on the pore water pressures estimated from the studies, the computed pore water pressures ranging of -0.25 MPa to -0.3 MPa in this numerical analysis are reasonable.

In this study, the initial conditions of the region (EDZ) adjacent to the shaft seal is reasonably well captured by numerical modelling with regard to changes in pore water pressure. In the numerical simulation, the suction of 12.8 MPa applied by the clay seal caused the pore pressure in the fractures to become negative and desaturation of the EDZ (i.e., reduction in relative humidity) could affect the hydraulic conductivity of the rock adjacent the clay seal. However, desaturation of the EDZ was not observed from field readings of three piezometers located in the EDZ as shown in Figure 5-18. The readings indicated positive values, which were indicative of some recharge. This could be attributed to a relatively high initial degree of saturation (~67%) of the clay seal and therefore the suction corresponding to the degree of saturation was not high enough to withdraw water from the EDZ. Another possible reason could be that during water uptake the clay seal expanded into the EDZ region and effectively sealed the micro-cracks and pores in the EDZ. Numerical modelling using CODE_BRIGHT (Vaunat and Olivella 2002) could not simulate this phenomenon and consequently there was a discrepancy found between numerical prediction and field readings.

5.3.3. Mechanical Behaviour of the Clay Seal

Total Pressure Prediction Compared with ESP TPC Data

The hydration process in the clay seal results in an increase of degree of saturation, a tendency to swelling of the clay, and consequently an increase of total pressures. As such, the development of total pressures in the clay seal is a consequence of the progressive development of the swelling potential under conditions of complete confinement as hydration proceeds.

Horizontal and vertical pressures in the clay seal component were estimated numerically and compared with measured TPC data. An initial stress from 0 to 120 kPa was linearly applied from the top to the bottom of the clay seal due to its bulk unit weight of 19.9 kN/m^3.

Figure 5-19 shows the simulated horizontal and vertical pressures at the top of the clay seal, 6 m from the bottom of the clay seal. The numerical results obtained from the three cases show a similar pattern in predicting the vertical pressure in the top region. The measured TPC data in the region (i.e., VWTPC02 (VT2) and VWTPC03 (VT3)) show no discernible difference in vertical pressure until approximately 200 days and then gradual increases after 200 days. Rapid increases in vertical pressure occur after approximately 1800 days. The numerical predictions underestimate the evolution of vertical pressures in the top region, indicating a slow increase in vertical pressure until approximately 7000 days (~19 years) and a rapid increase after that time. In Section 5.3.2, Figure 5-13 indicates that suction of the clay seal will be dissipated after approximately 19 years. This means that the clay seal will be fully saturated after ~19 years and start generating significant swelling pressure that consequently increases the total pressure as shown in Figure 5-19. As explained in Section 5.3.2, the possible reason for this underestimation is that the simplified groundwater flow system surrounding the clay seal does not take into account radial groundwater flow toward the perimeter of the clay seal. That is likely to result in slower saturation than observed in the sensors.

The similar trends can be seen in other depths of the clay seal. Figures 5-20 to 5-23 present comparisons of numerical results with the measured TPC data at different depths (5 m, 3 m, 1 m and 0 m from the bottom of the clay seal). Predicted vertical pressures of Case 1 and Case 3 in the regions seem to be similar. However, Case 2 shows slightly greater vertical pressures than the other cases and the pressure difference becomes more noticeable at the bottom of the clay (e.g., 2.7 MPa for Case 2 and 2.4 MPa for Case 1). The simulated horizontal pressures at these regions are in the range of 2.3 MPa to 2.6 MPa. The same phenomenon is also found in comparison of the predicted horizontal pressures.

The difference in predicted total pressures between Case 2 and the other cases can be attributed to the effect of groundwater flow from inclined FZ2. The quantity of groundwater flowing through a cross-sectional area of FZ2 can be defined by Darcy's equation (5-10) and depends on three things: (1) the pressure gradient across the length of FZ2, (2) the cross sectional area of FZ2 and (3) the hydraulic conductivity of FZ2.

$$Q = \frac{P}{L} \cdot K \cdot A \tag{5-10}$$

where Q is the quantity of groundwater, P is piezometric pressure, L is the length of FZ2, K is the hydraulic conductivity of FZ2 and A is a cross-sectional area of FZ2.

The model domain of Case 1 has 100 m radius and the radius of FZ2 is 97.5 m while the radius of FZ2 inclined to 16 degrees from the horizontal plane is 101.4 m. The radius difference of FZ2 between the two cases is 3.9 m.

In numerical modelling, pore water pressure in the rock is linearly applied from the top to the bottom and therefore pore water pressure increases with depth. In Case 1, the piezometric water pressure between two ends of FZ2 is the same because they are located on the same horizontal plane. The piezometric pressure of FZ2 for Case 1 is 1.89 MPa at a depth of 273 m from the ground surface. By contrast, in Case 2, the piezometric water pressure between two ends of FZ2 is different due to the inclination of FZ2 (i.e., each end of FZ2 has a different depth). This inclination of FZ2 results in the right end of FZ2 being located down to at a depth of 301 m from the ground surface and the piezometric pressure of 2.17 MPa, as shown in Figure 5-24. The pressure difference between Case 1 and Case 2 is 0.28 MPa. Considering the same hydraulic conductivity (K) and cross-sectional area (A) of FZ2, the quantity of groundwater flow (Q) can be influenced by a pressure gradient (i.e., 0.28 MPa/3.9 m), which can allow for more quantity of groundwater flowing toward the clay seal. As such, it is likely that Case 2 with inclined FZ2 can have more quantity of groundwater flowing to the clay seal than Case 1 with horizontal FZ2. Consequently, an increase in quantity of groundwater toward the clay seal can increase the clay seal's hydration process rate. The phenomenon showing slightly greater total pressures in Case 2 can result from the different pressure gradient.

Overall, numerical prediction for the three cases shows a similar pattern in total pressure and underestimates the evolution of the total pressure. Case 2 with an inclined FZ2 indicates slightly higher total pressures that the other cases. The predicted vertical pressures from the three cases are in the range of 2.5 MPa to 2.7 MPa for 100 years, which are not far from the final vertical pressure of 3.3 MPa anticipated after the clay seal comes to equilibrium. On achieving saturation and completion of re-establishing the regional groundwater conditions, the swelling pressure of the clay seal should be approximately 0.8 MPa and the piezometric pressure at that level will be 2.5 MPa. This will result in a total pressure of approximately 3.3 MPa as measured by TPC sensors.

5.3.4. Predicted Pressures and Displacements of the Clay Seal

Displacement sensors were installed at the top of the upper concrete segment to monitor any net movements of the seal and since the concrete is assumed to be volumetrically stable, any displacements would be attributable to processes occurring within the clay-filled volume. The upper concrete segment showed essentially no displacement during the first 5 years of monitoring. Within the clay seal, there were no instruments installed to measure the internal displacements during the experiment. Only simulated displacements in the clay seal are therefore presented in this section. This section presents predicted horizontal (radial) and vertical pressures and displacements of the clay seal component.

Figure 5-25 and Figure 5-26 show distributions of the horizontal pressure and displacement along a vertical line, 1.25 m from the centre of the clay seal, respectively. Figure 5-25 clearly indicates that horizontal pressures are dominantly developed along the location of FZ2. Negative horizontal pressure means compressive horizontal pressure in this figure. Case 2 shows a more uniform distribution of horizontal pressure in the region above FZ2. As previously mentioned in

Section 5.3.3, this uniform distribution can be attributed to inclined FZ2 that supplies more groundwater flowing to the clay seal than the horizontal FZ2. Numerical prediction for all cases also shows a bit of expansion in the horizontal pressure at an early stage up to 50 days and then compression after 50 days. The maximum compressive horizontal pressure is approximately 2.5 MPa for all cases.

In Figure 5-26, Case 1 and Case 3 show a similar trend in the horizontal (radial) displacement, indicating that the clay seal at this vertical section was compressed (inward movement) because of the restraint of the rock wall of the shaft, the effects of water pressure at the perimeter and swelling of the clay at the perimeter. Note that the influence of displacement or volume change due to swelling does not affect the saturated hydraulic conductivity in this numerical analysis. Case 3 shows the largest inward radial displacement of about 10 mm at 3 m from the bottom of the clay seal, corresponding to the centre region of FZ2. By contrast, Case 2 shows that the top and bottom regions were compressed (inward movement) and the mid-height region was slightly expanded (outward movement). This may mean that the clay seal in this region is close to an equilibrium state due to more groundwater flow supplied to the clay seal. The importance of flow direction would increase with increasing hydraulic conductivity and consequently it can affect the behaviour of an unsaturated soil.

The prediction patterns observed from the three cases can be indicative of direct influence of groundwater flow from FZ2. Guo and Dixon (2005) and Chandler (2000) conducted numerical modelling of the Isothermal Test (ITT) using FLAC (Fast Lagrangian Analysis of Continua) (Itasca 2000) and CODE_BRIGHT (Vaunat and Olivella 2002) respectively, and reported similar patterns of horizontal and vertical displacements of the clay seal. Although the boundary conditions of the ITT numerical simulation are slightly different from those of the ESP, the mechanical behaviour of clay seal caused by groundwater flow is likely comparable for both models.

Figure 5-27 and Figure 5-28 show numerical prediction of vertical pressure and displacement along a vertical line, 1.25 m from the centre of the clay seal for the three cases. The numerical results show no discernible pattern in both vertical pressure and displacement found for the three cases (Figure 5-27). Similar to distribution of the horizontal pressure in the region, the three cases show compressive vertical pressures after 50 days and the maximum compressive vertical pressure is approximately 2.5 MPa observed in this region for Case 2.

Figure 5-28 clearly indicates that the clay in this region is moving toward equilibrium after 4900 days and close to an equilibrium state at 35900 days. Case 2 shows a more uniform distribution of the vertical displacement for 35900 days. The cases show a similar pattern in the vertical displacement, indicating upwards movement above mid-height and downwards movement below the clay mid-height. This phenomenon can be attributed to the initial conditions of groundwater flow applied in the domain where a higher groundwater pressure was set up at the bottom of the shaft seal, resulting in an upward groundwater flow from the bottom to the top. This may result in more groundwater accessible at the bottom of the clay seal and hence increase in the compressive upwards vertical displacement in the region.

Numerical prediction of total pressure and displacement is also examined along a horizontal line at the mid-height of the clay seal (y = 3 m) and presented in Figures 5-29 to 5-32. Figure 5-29 shows a similar distribution pattern of predicted horizontal pressures for all cases. The predicted horizontal pressure becomes compressive after 50 days and the maximum compressive horizontal pressure is 2.5 MPa for Case 2 in this region. Figure 5-30 shows a similar trend in horizontal displacement for all three cases. The maximum compressive horizontal displacement for each case is observed at 1.8 m from the centre of the clay seal and the maximum values of the horizontal displacement range from 6 mm to 10 mm.

Figure 5-31 and Figure 5-32 show respectively the distributions of vertical pressure and vertical displacement in the same region. A similar distribution pattern is observed for all cases and Case 2 shows the maximum compressive vertical stress of 2.7 MPa near the centre region. As seen in Figure 5-31, the predicted vertical pressures in the centre region are slightly higher than the outer region after 13900 days. It can result from differences in vertical pressure between the clay seal and the rock so that the outer region of the clay is influenced by the vertical pressure of the rock. In comparison of predicted vertical displacements for all cases, Case 1 and Case 3 show almost an identical pattern (Figure 5-32). However, Case 2 shows expansion up to 1.2 mm in the centre region until 13900 days (38 years) and compression after the time period. Although the distribution of the vertical displacement for Case 2 is different from the other cases, the displacement values of Case 2 are still very small.

5.4. Summary

Coupled H-M numerical simulation using an axisymmetric model in the 2-D representation was used to evaluate the shaft seal performance. The domain used in the numerical model had 100 m radius and 200 m thickness after performing scale effect analysis using different domain sizes. Three different numerical simulations were performed. Case 1 assumed FZ2 to be perfectly horizontal, Case 2 assumed FZ2 to be inclined 16 degrees from the horizontal plane, and Case 3 was identical to Case 1, except for applying seepage of water into the system at the top and bottom of the clay seal component as well as the edges of the clay seal above and below FZ2.

The hydraulic-mechanical parameters used in these models for the sealing components were calibrated using laboratory measurements. The hydraulic parameters of the sealing components were defined through use of van Genuchten's (1980) model and extensive laboratory test data related to the soil-water retention relationships (Wan 1996, Wiebe 1996, Tang 1999, Blatz 2000, Villar 2002, Anderson 2003, Kim et al. 2009). For the mechanical behaviour of the sealing components the Basic Barcelona Model (BBM), an elastoplastic constitutive model, (Alsonso et al. 1990) was used. Laboratory test results on bentonite-sand mixture materials (Graham et al. 1989, Lingnau et al. 1995, Volckaert et al. 1996, Thomas et al. 2002, Blatz and Graham 2003) were used to determine a set of BBM mechanical parameters.

For the host rock and concrete components, hydraulic conductivities (K) of the granite rock and the concrete were estimated using field measurements previously done at the AECL's URL (Chandler 2000, Martino 2000, Dixon et al. 2002). Both the host rock and concrete components were assumed to be linearly elastic and the same Young's modulus and Poisson's ratio were assigned (Graham et al. 1997).

Case 3 shows a dramatic decrease in suction in the outer region in the initial stage of system wetting due to groundwater seepage applied in the bottom and outer regions. However, the additional wetting process in the region affects only changes in suction at a very early stage of system wetting, but does not significantly affect the rate of decrease in suction after the early stage. The possible reason for this phenomenon is that once the edge regions become hydrated and start to swell, the swelling mechanism becomes dominant in controlling its hydraulic behaviour.

Numerical simulations from the three cases show a reasonable match with the field TDR readings for water uptake trends of the clay seal component although it slightly overpredicts the time required for the core of the clay component to achieve water saturation. The numerical results and the TDR readings available up to December 2015 indicate that the clay seal in the centre region was not fully saturated.

The predicted vertical pressures of the three cases are in the range of 2.5 MPa to 2.7 MPa for 100 years, which are not far from the final vertical pressure of 3.3 MPa anticipated after the clay seal comes to equilibrium. Predicted distributions of the horizontal pressure and displacement along a vertical line, 1.25 m from the centre of the clay seal are dominantly affected by groundwater flow from FZ2. In addition, Case 2 shows a more uniform distribution of displacements along the region, which likely mean that the clay is close to an equilibrium state.

Table 5-1. Hydraulic parameters for clay seal and granite rock/concrete materials

Material Parameters	Clay Seal	Granite Rock / Concrete
Water retention curve	$S_{re} = \left[1 + (\frac{s}{P_0})^{1/(1-\beta_1)}\right]^{-\beta_1}$ P_0 = 11.0 MPa, β_1 = 0.48	$S_{re} = \left[1 + (\frac{s}{P_0})^{1/(1-\beta_1)}\right]^{-\beta_1}$ P_0 = 0.7 MPa, β_1 = 0.33
Hydraulic conductivity (m/s)	$K = K_0 \cdot S_{re}{}^{1/2}(1-(1-S_r{}^{1/\beta})^{\beta})^2$ $K_0 = 1 \times 10^{-12}$, β = 0.3	$K = K_0 \cdot S_{re}{}^{1/2}(1-(1-S_r{}^{1/\beta})^{\beta})^2$ $K_0 = 4 \times 10^{-13}$, β = 0.33
Porosity	0.33	0.005
Dry density (Mg/m^3)	1.81	2.63
Initial saturation (%)	67.0	100

Table 5-2. Mechanical parameters for clay seal and granite rock materials

Material Parameters	Clay Seal	Granite Rock / Concrete
p_0^* (MPa)	1.0	-
$\lambda(0)$	0.12	-
k	0.0256	-
r	0.65	-
β (Pa^{-1})	$5x10^{-7}$	-
p_c (Pa)	$1.8x10^5$	-
λ_s	0.111	-
k_s	0.0111	-
M	0.526	-
s_0 (MPa)	12.8	-
E (GPa)	-	60
v	-	0.22

where,

p_0^*	preconsolidation stress at saturated condition (s = 0)
$\lambda(0)$	stiffness parameter for changes in net mean stress at saturation
κ	slope of the ln (p)-v within elastic range for constant s
r	parameter defining maximum soil stiffness
β	parameter controlling the rate of increase of soil stiffness with suction
p_c	reference stress
λ_s	slope of the ln (s)-v outside elastic range for constant p
κ_s	slope of the ln (s)-v within elastic range for constant p
M	slope of critical state line
v	specific volume
s_0	initial SI-yield line,
E	Young's modulus,
v	Poisson's ratio

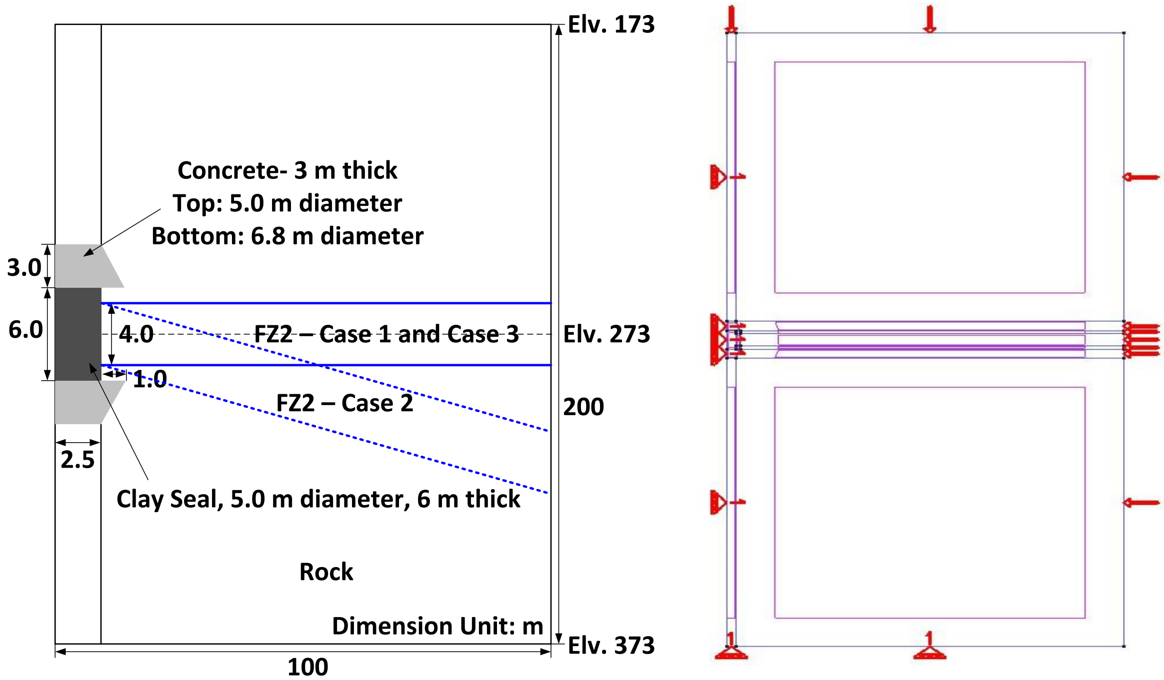

(a) Numerical Model Domain

(b) Initial Boundary Conditions

Figure 5-1. Dimensions of numerical model geometry and initial boundary conditions

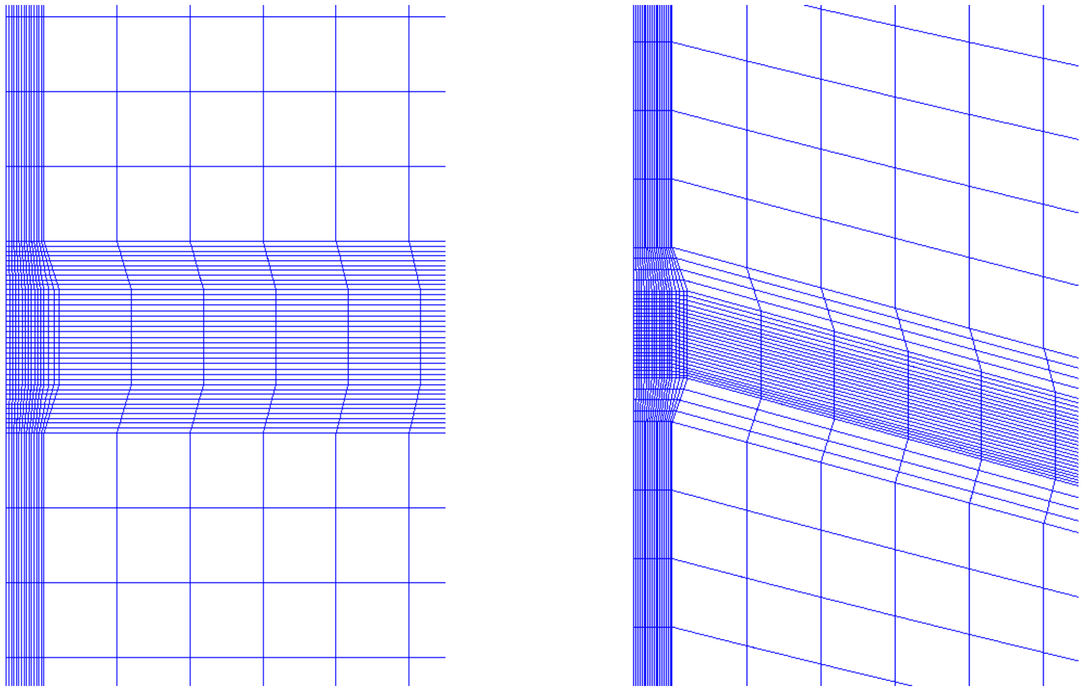

(a) Case (1) and Case (3) (b) Case (2)

Figure 5-2. Asymmetric four-nodes finite element mesh in 2-D representation

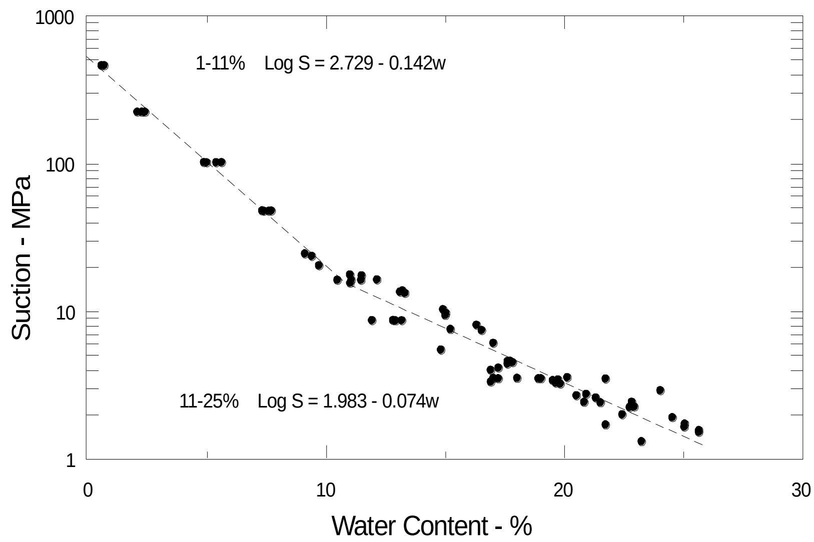

Figure 5-3. A Plot of suction versus water content for 50:50 bentonite:sand buffer materials compacted to an initial dry density of 1.67 Mg/m^3 (Wan 1996)

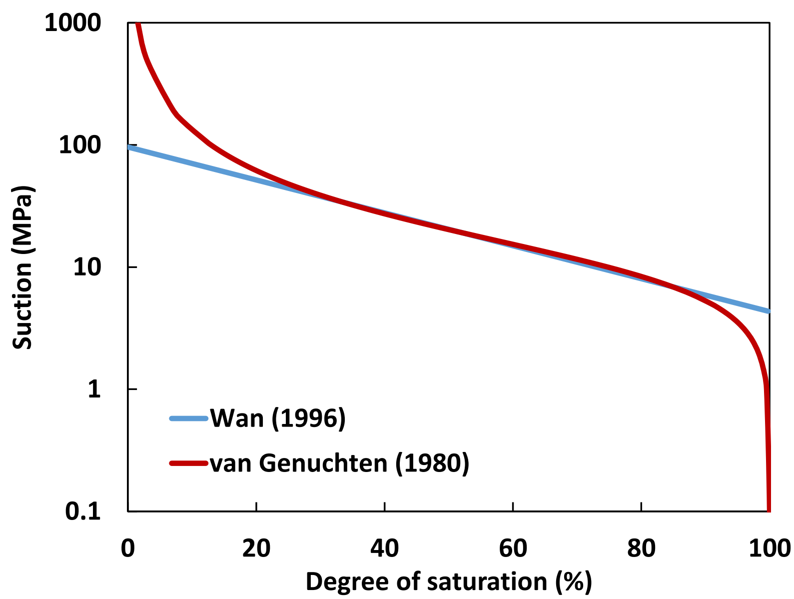

Figure 5-4. A plot of suction versus degree of saturation for clay seal material

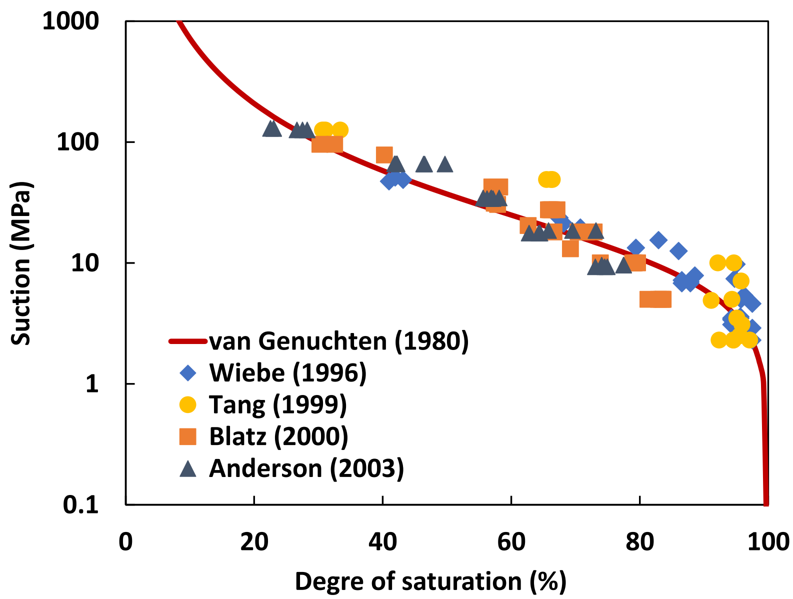

Figure 5-5. A Plot of suction vs. degree of saturation for clay seal material using experimental data

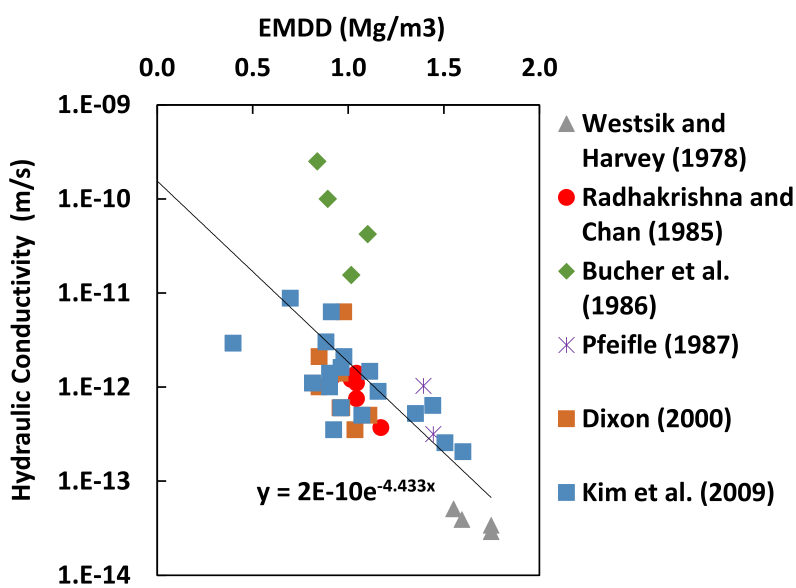

Figure 5-6. Relationship between EMDD and hydraulic conductivity of the clay seal

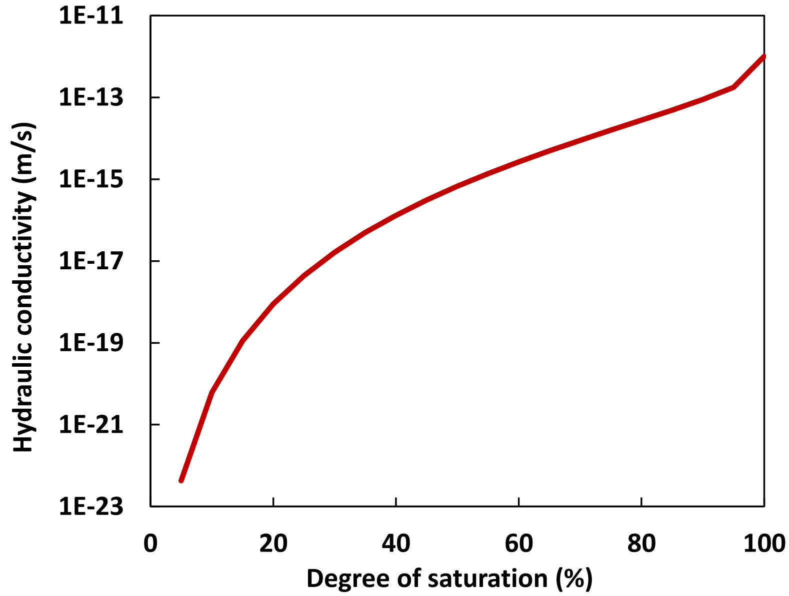

Figure 5-7. Hydraulic conductivity of the clay seal as a function of degree of saturation

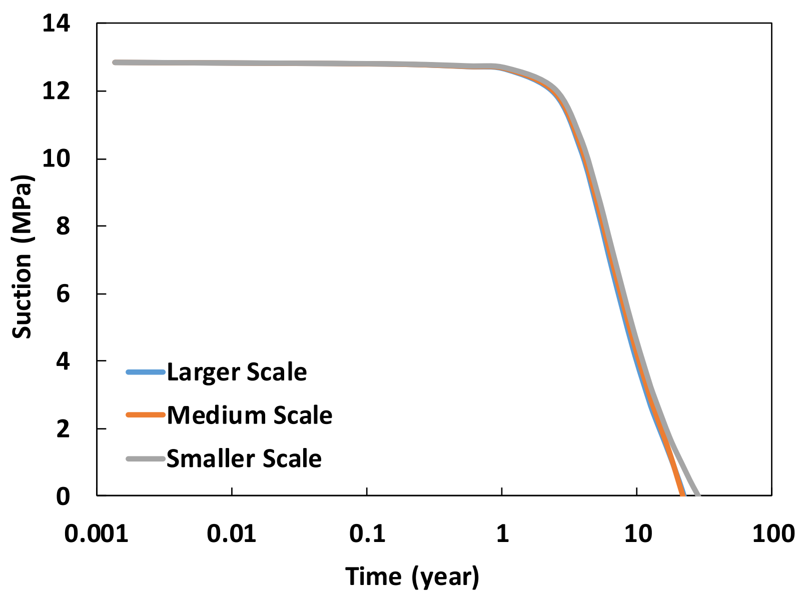

Figure 5-8. Comparison of changes in suction of the clay seal for three different domain scales

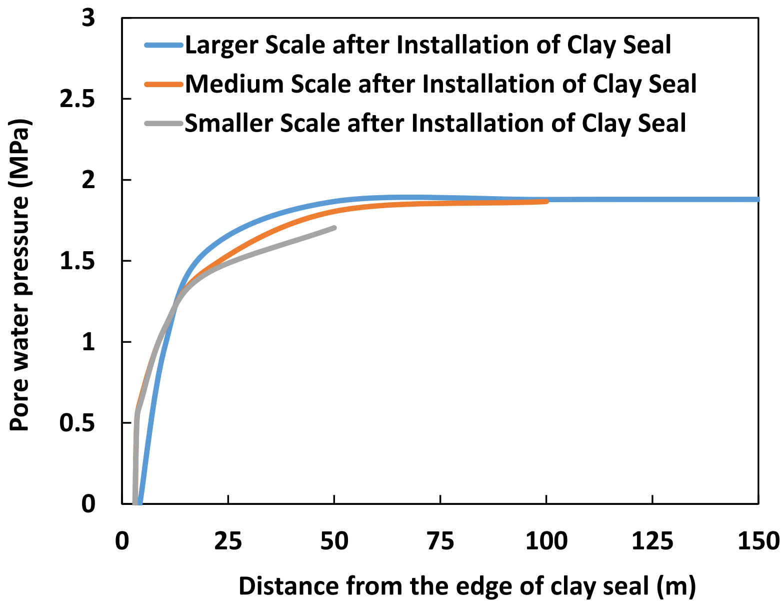

(a) Pore water pressure after installation of clay seal

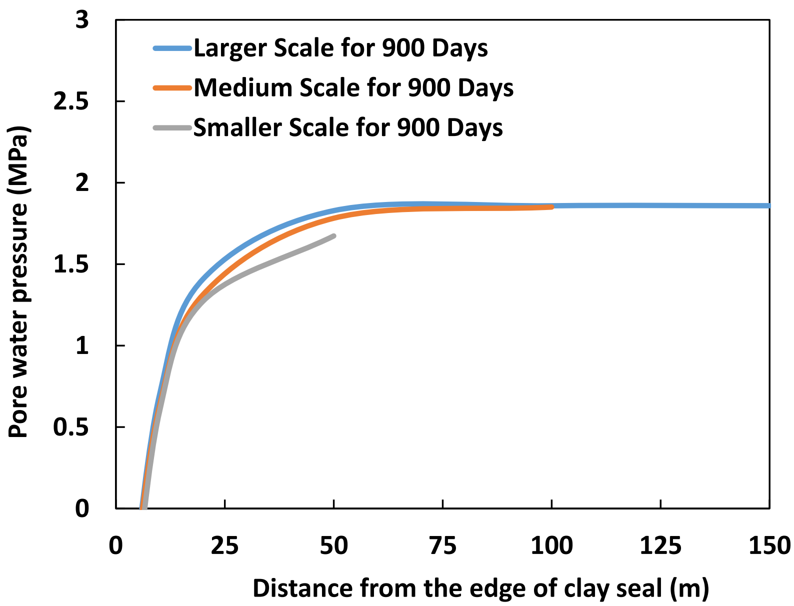

(b) Pore water pressure after 900 Days

Figure 5-9. Comparison of changes in pore water pressure for three different domain scales

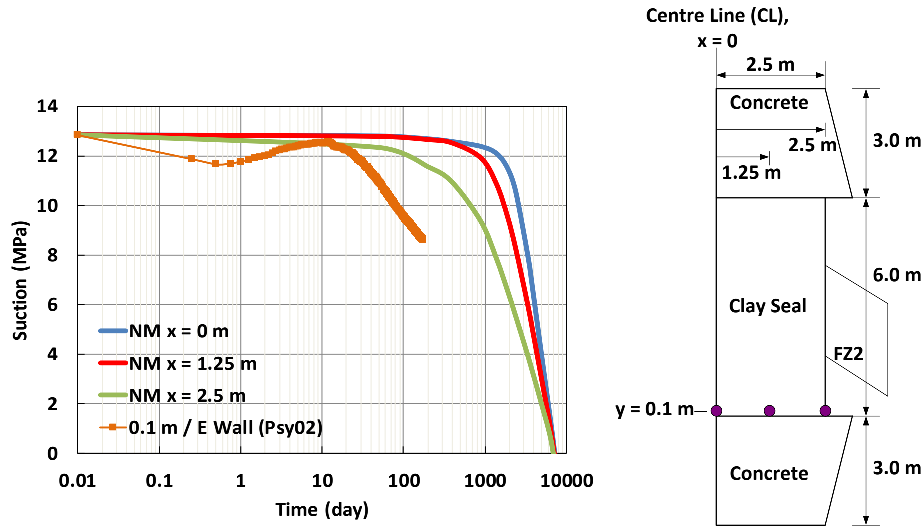

(a) Case 1

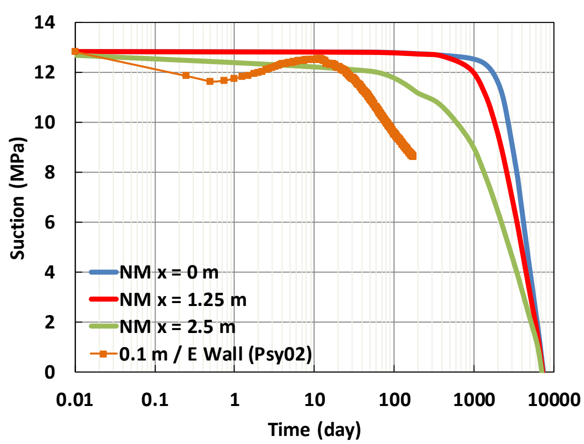

(b) Case 2

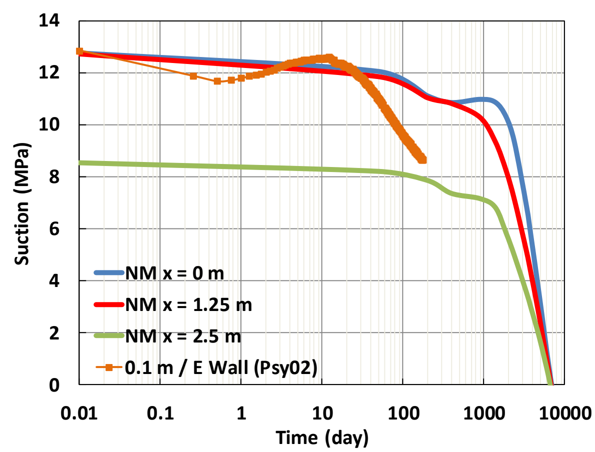

(c) Case 3

Figure 5-10. Comparison of changes in suction at y = 0.1 m with field psychrometer readings (note that NM shown in the figure means Numerical Modelling)

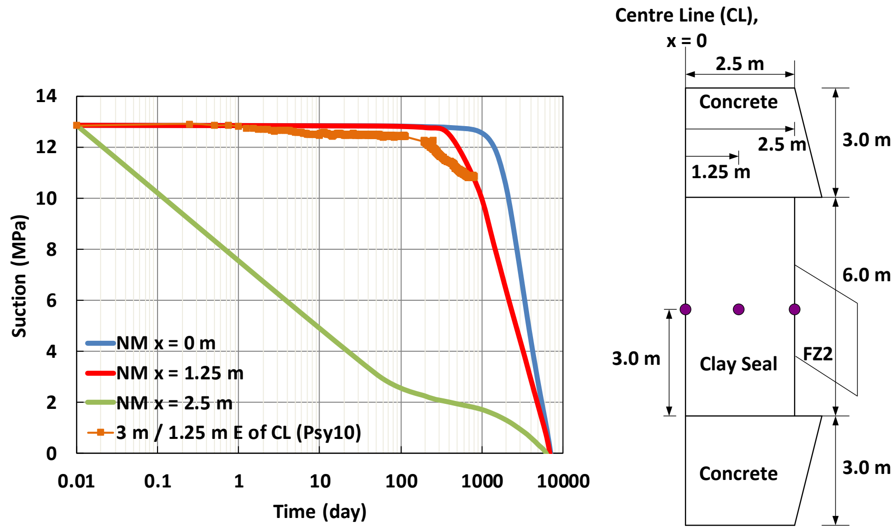

(a) Case 1

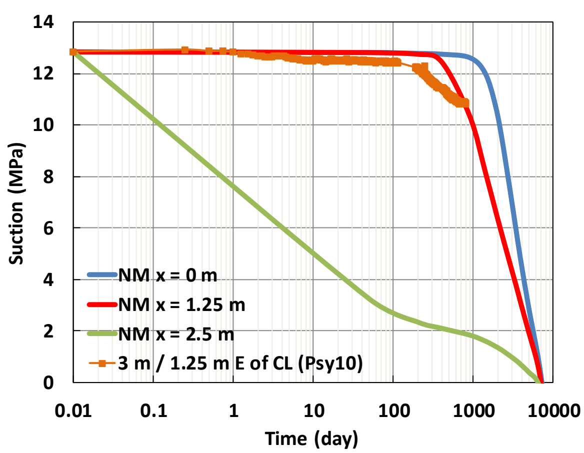

(b) Case 2

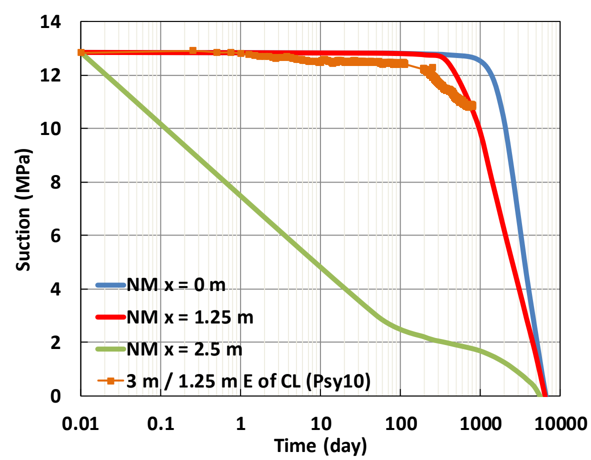

(c) Case 3

Figure 5-11. Comparison of changes in suction at 3 m with field psychrometer readings

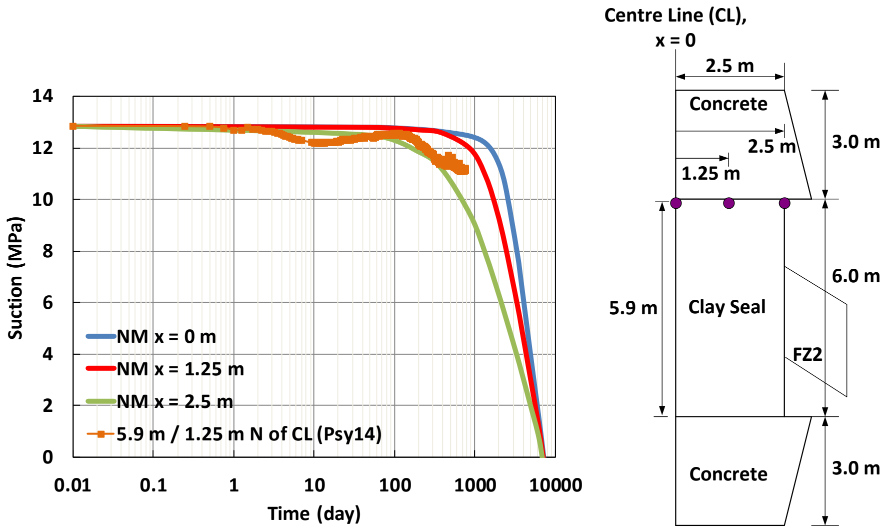

(a) Case 1

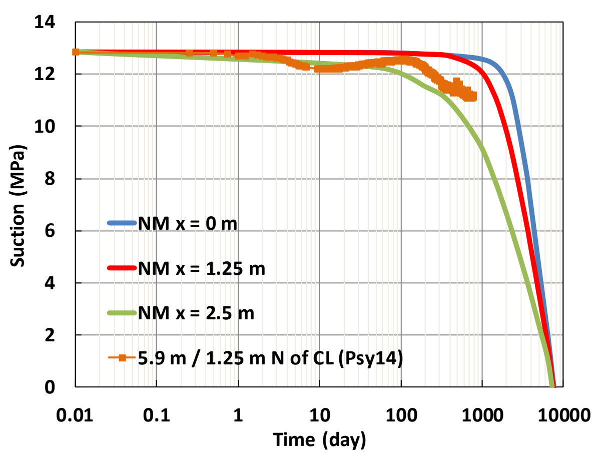

(b) Case 2

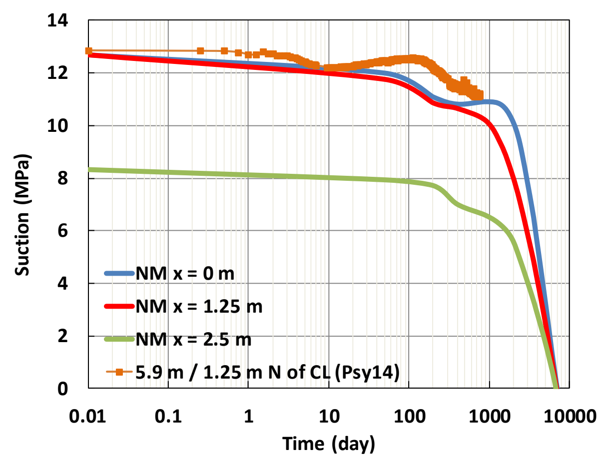

(c) Case 3

Figure 5-12. Comparison of changes in suction at 5.9 m with field psychrometer readings

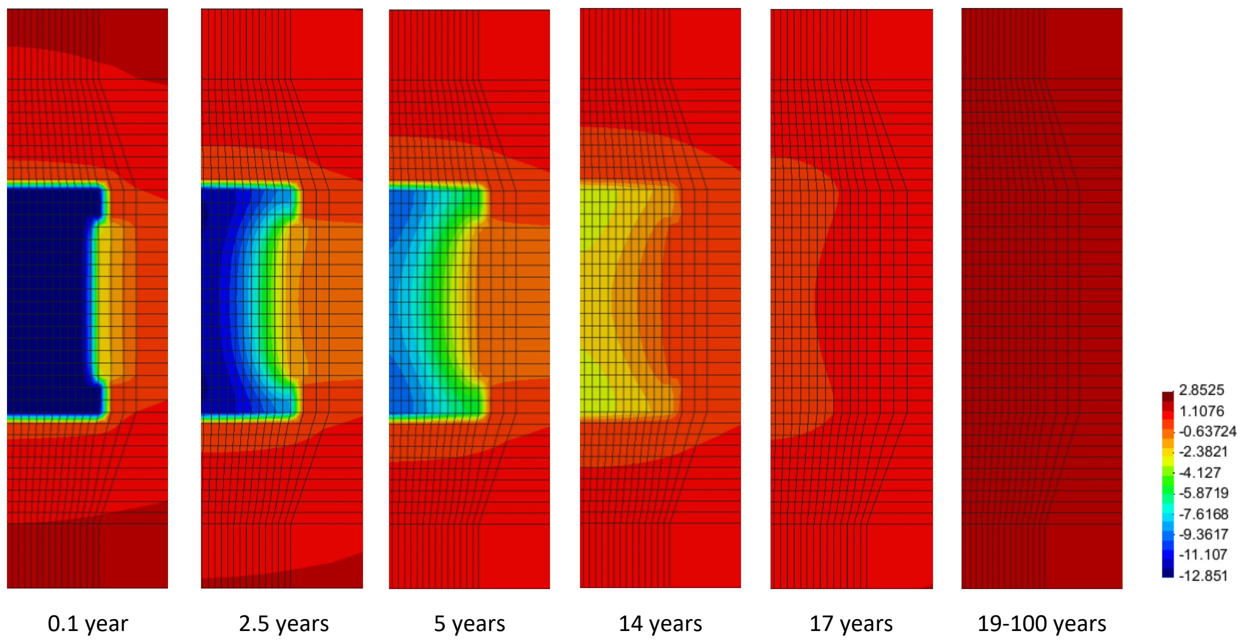

Figure 5-13. Suction prediction in the clay seal with time for Case 1 (note that predicted suction is shown as negative liquid pressure in CODE_BRIGHT when pore air pressure is constant).

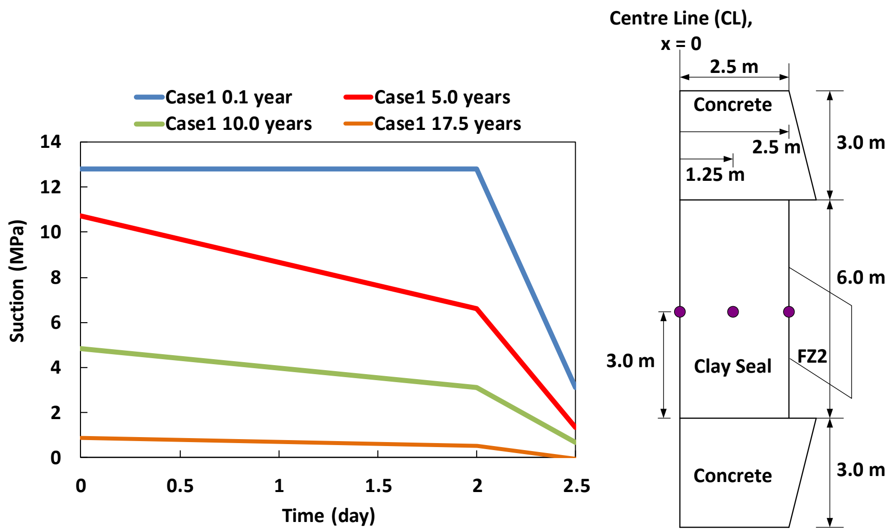

(a) Case 1

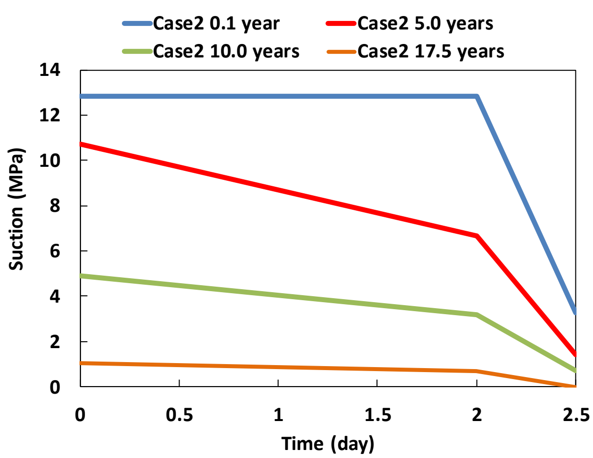

(b) Case 2

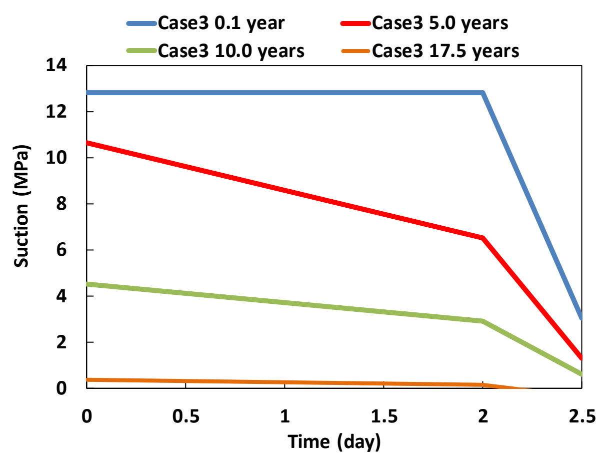

(c) Case 3

Figure 5-14. Comparison of suction prediction with time for all cases

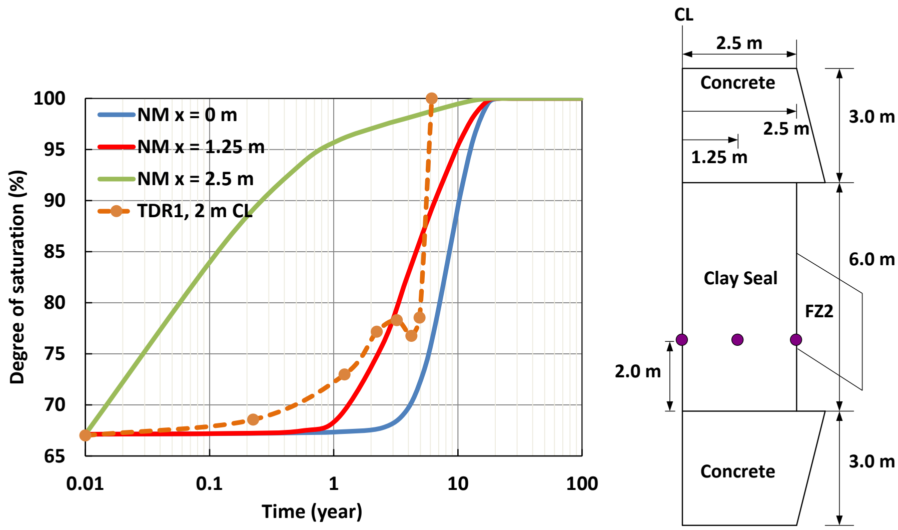

(a) Case 1

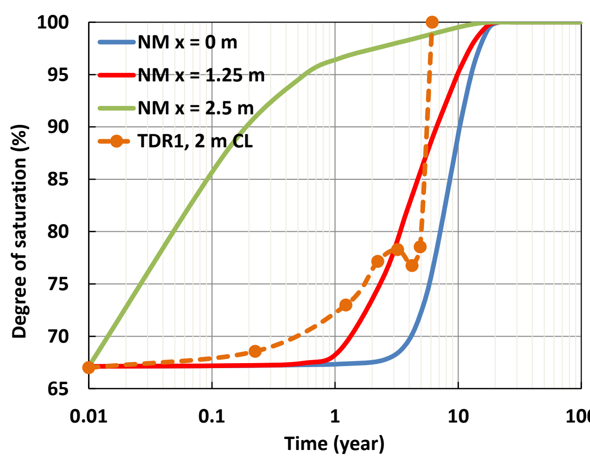

(b) Case 2

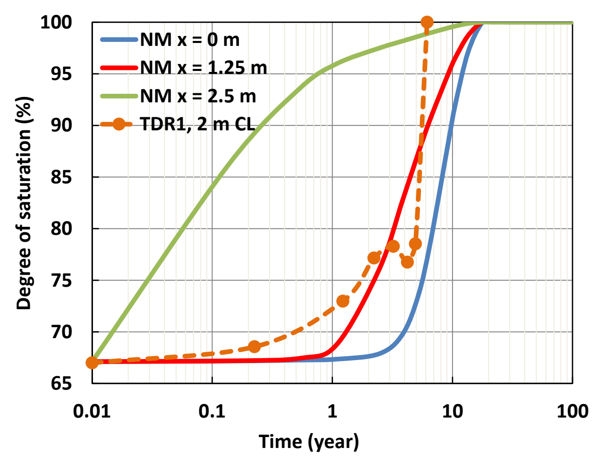

(c) Case 3

Figure 5-15. Comparison of predicted degree of saturation with TDR1 readings at 2 m from the bottom of the clay seal

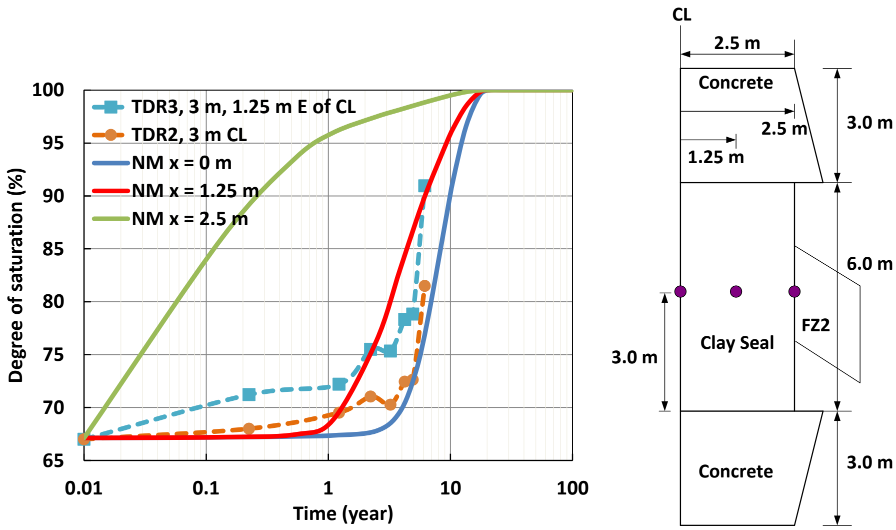

(a) Case 1

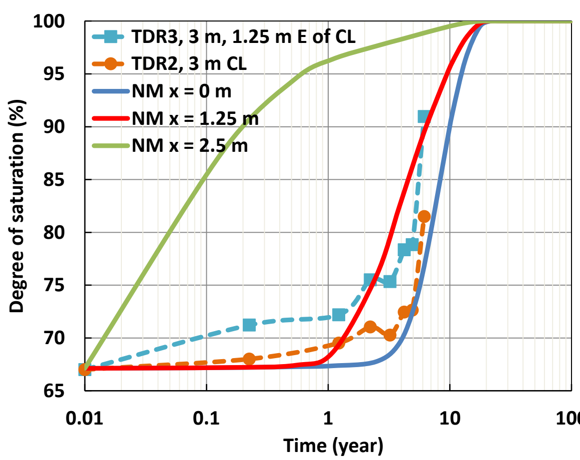

(b) Case 2

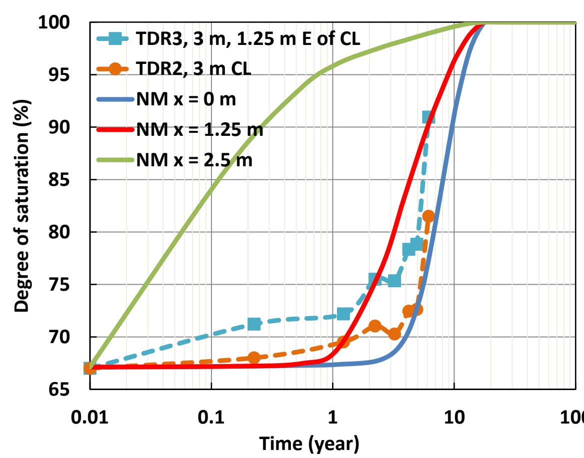

(c) Case 3

Figure 5-16. Comparison of predicted degree of saturation with TDR2 and TDR3 readings at 3 m from the bottom of the clay seal (mid-height)

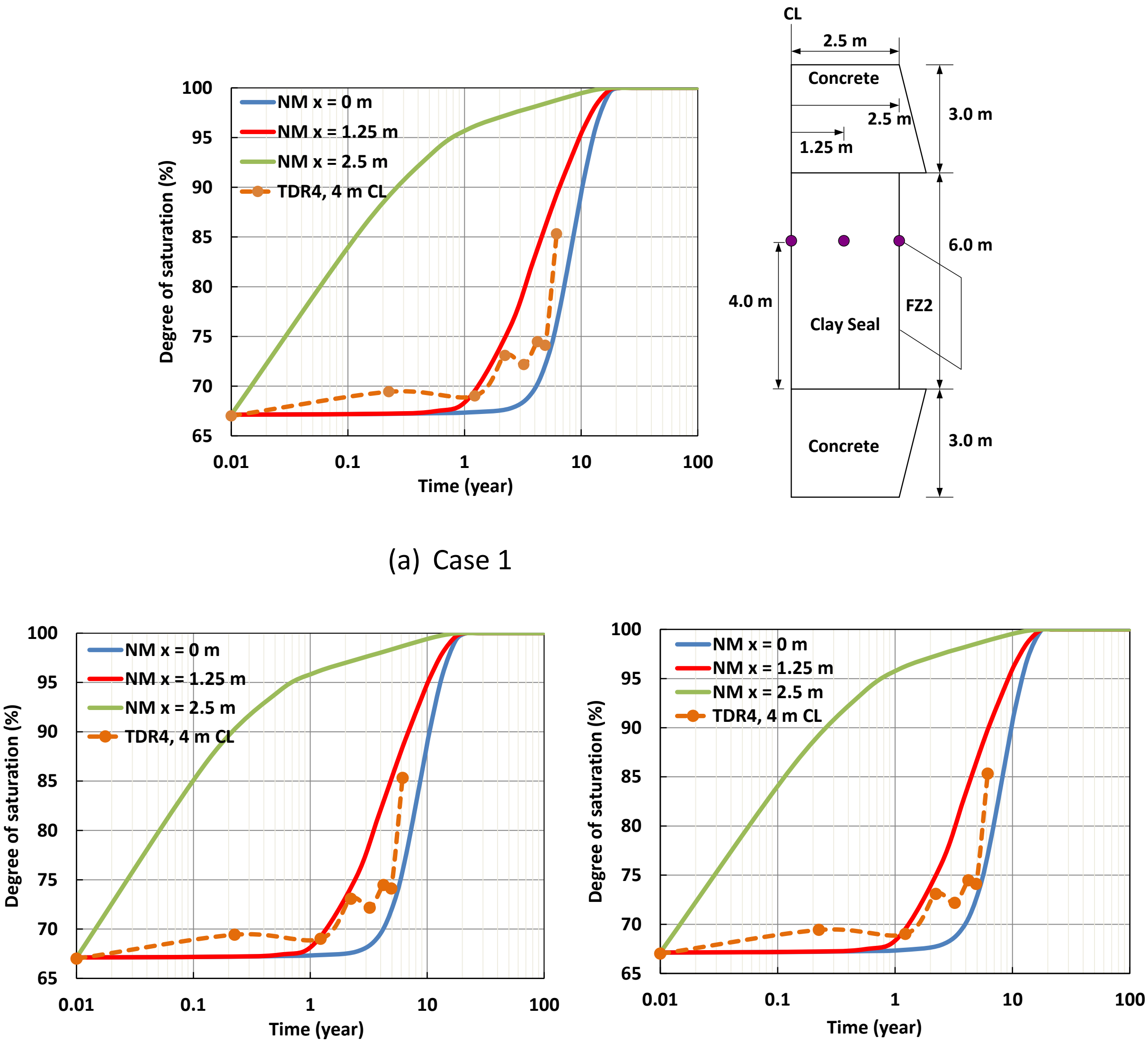

(a) Case 1

(b) Case 2

(c) Case 3

Figure 5-17. Comparison of predicted degree of saturation with TDR4 readings at 4 m from the bottom of the clay seal

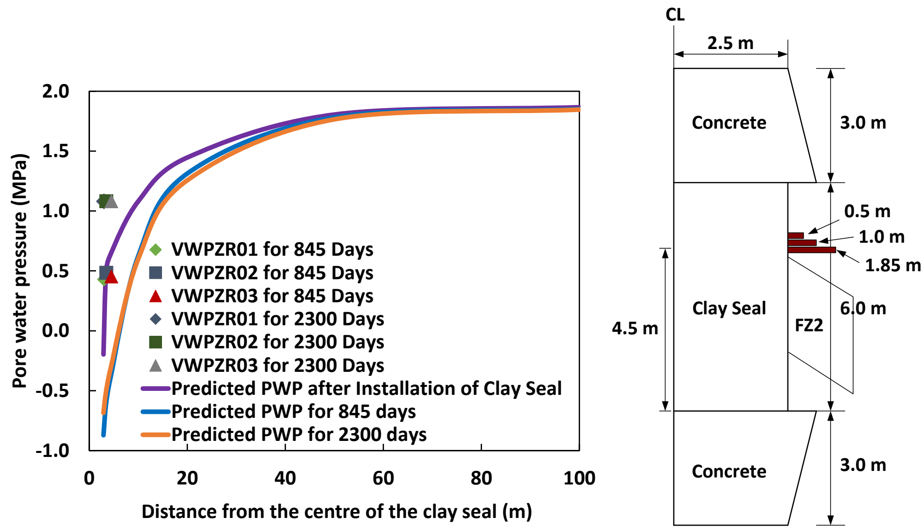

(a) Case 1

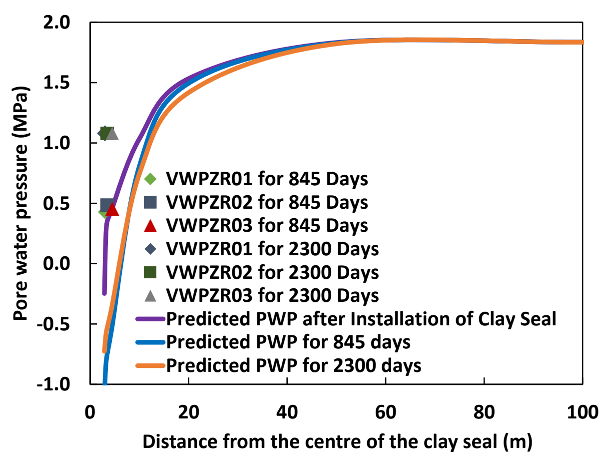

(b) Case 2

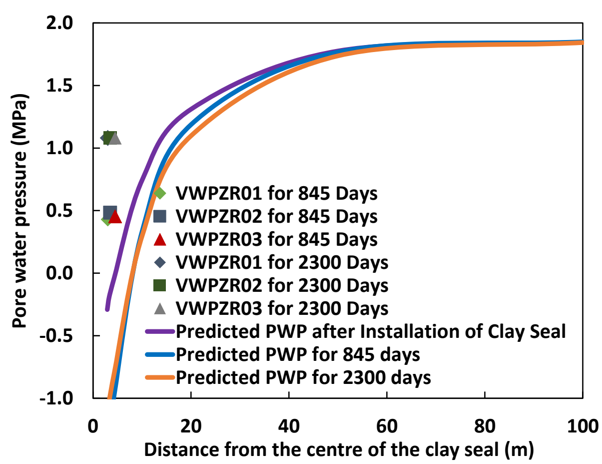

(c) Case 3

Figure 5-18. Simulated pore water pressure in near Rock

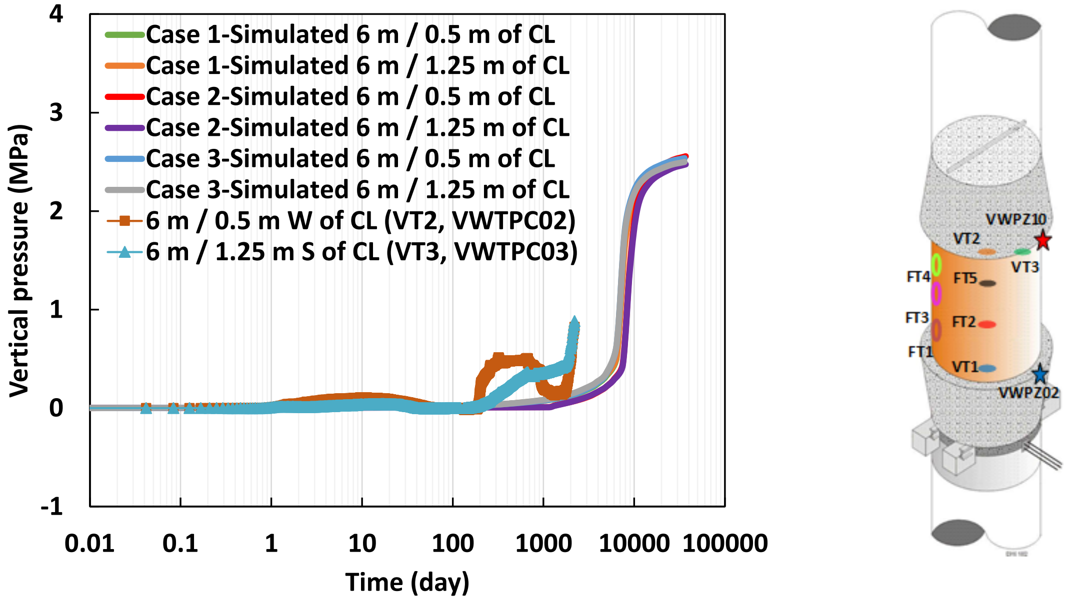

Figure 5-19. Predicted total pressures compared with TPC readings at 6 m from the bottom of the clay seal

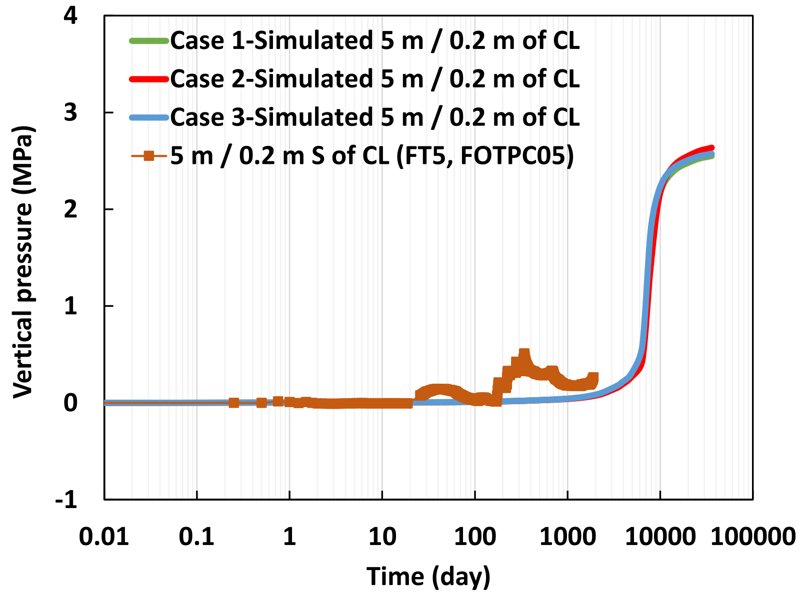

(a) Vertical pressure

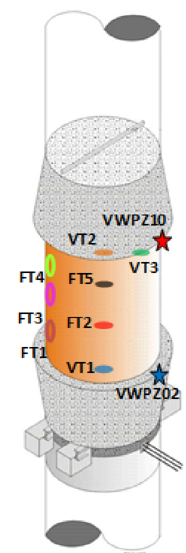

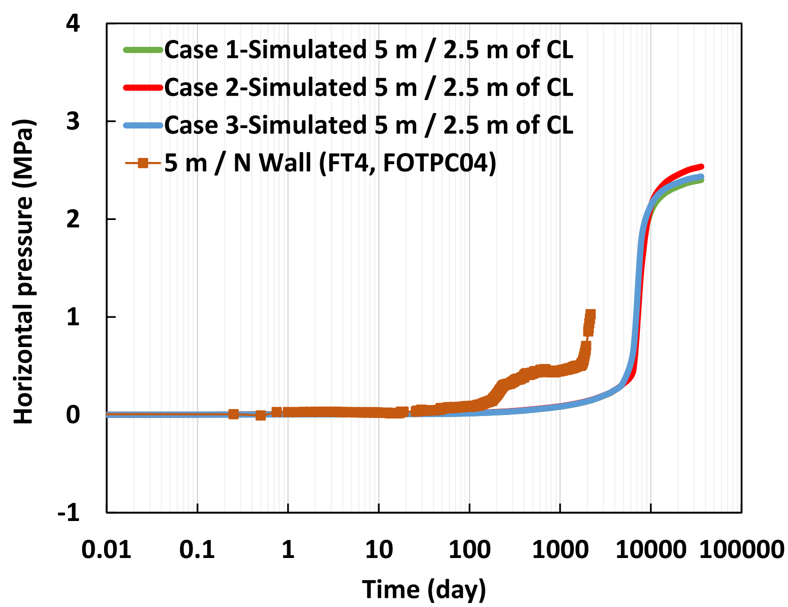

(b) Horizontal pressure

Figure 5-20. Predicted total pressures compared with TPC readings at 5 m from the bottom of the clay seal

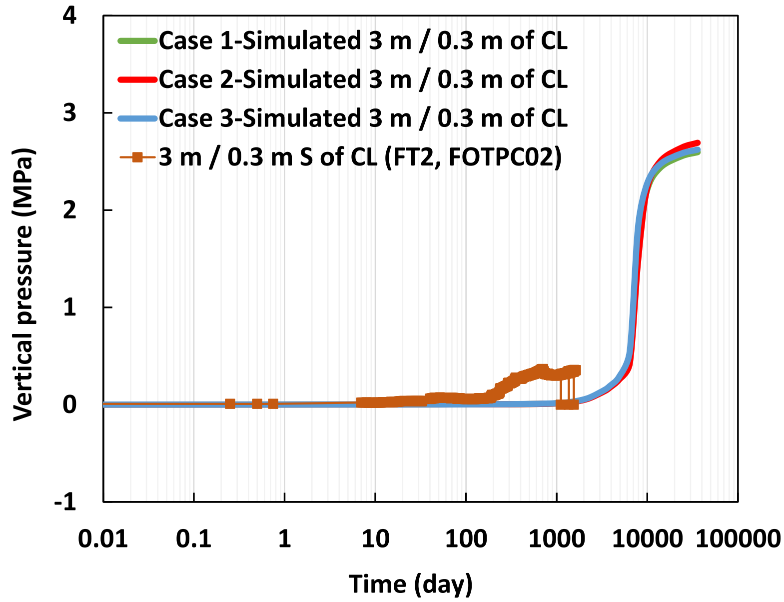

(a) Vertical pressure

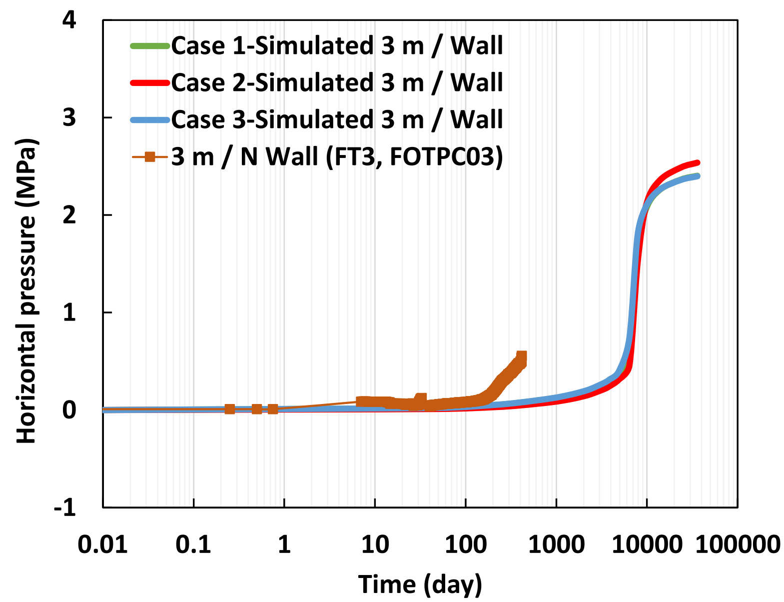

(b) Horizontal pressure

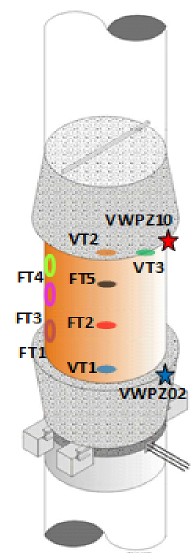

Figure 5-21. Predicted total pressure compared with TPC readings at 3 m from the bottom of the clay seal

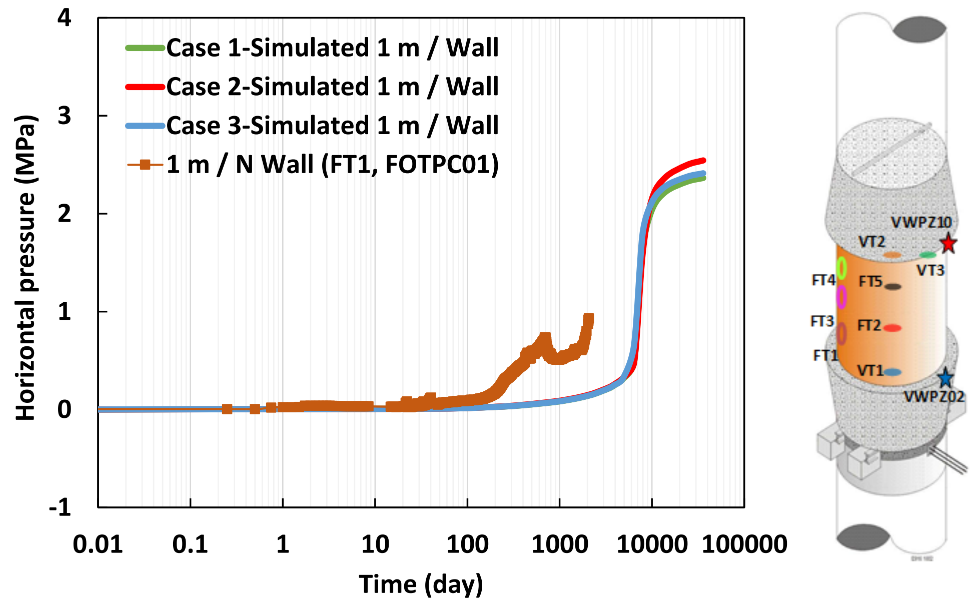

Figure 5-22. Predicted total pressure compared with TPC readings at 1 m from the bottom of the clay seal

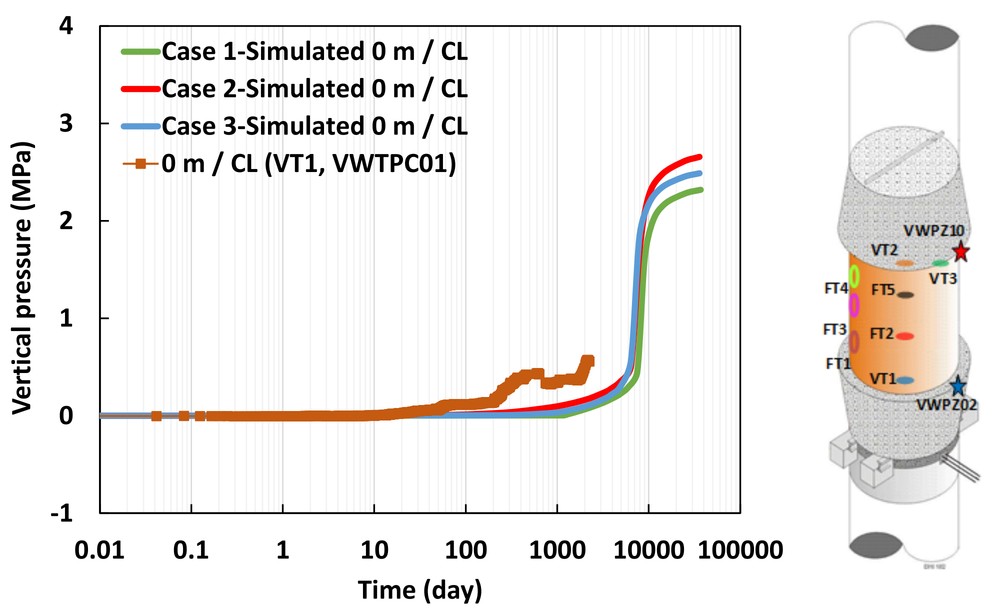

Figure 5-23. Predicted total pressure compared with TPC readings at the bottom of the clay seal

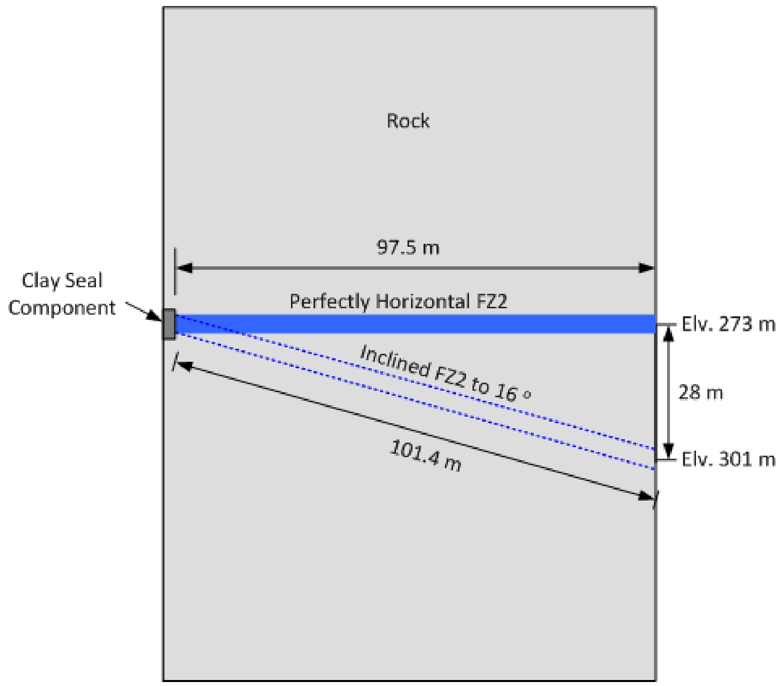

Figure 5-24. Difference between perfectly horizontal FZ2 and FZ2 inclined to 16 degrees from the horizontal plane

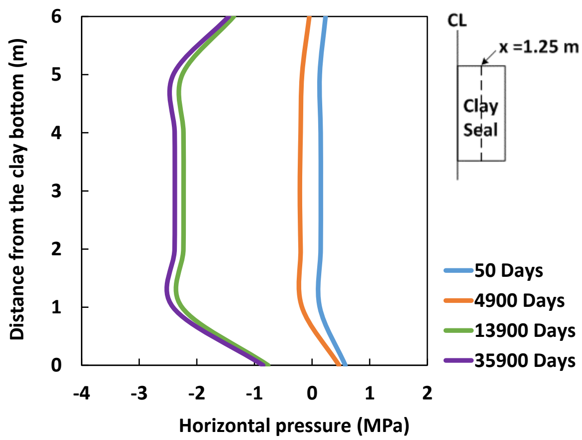

(a) Case 1

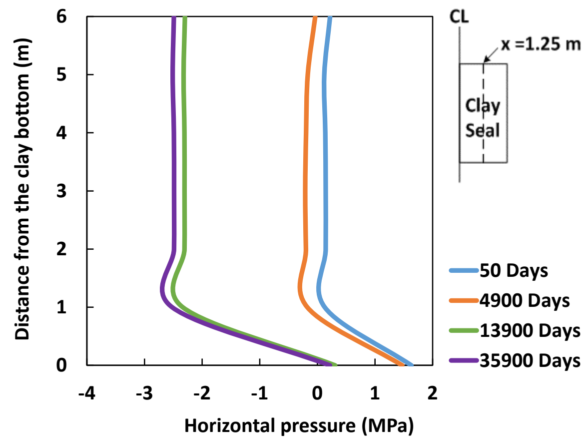

(b) Case 2

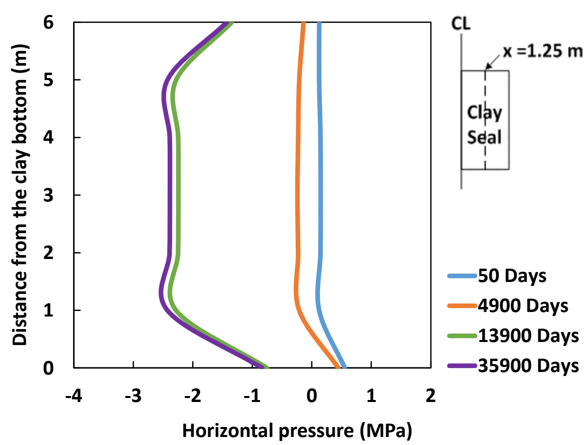

(c) Case 3

Figure 5-25. Prediction of horizontal (radial) pressures within the clay seal along a vertical line, 1.25 m from the shaft centerline

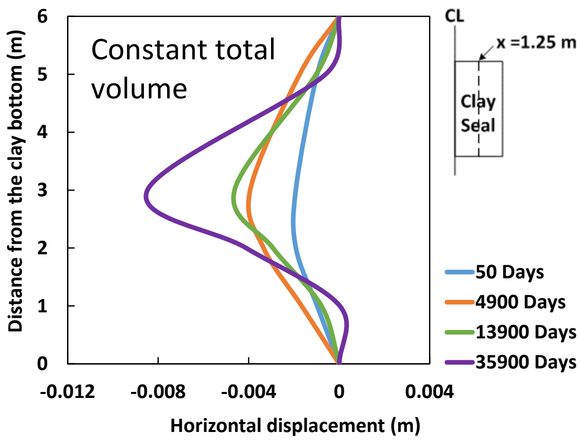

(a) Case 1

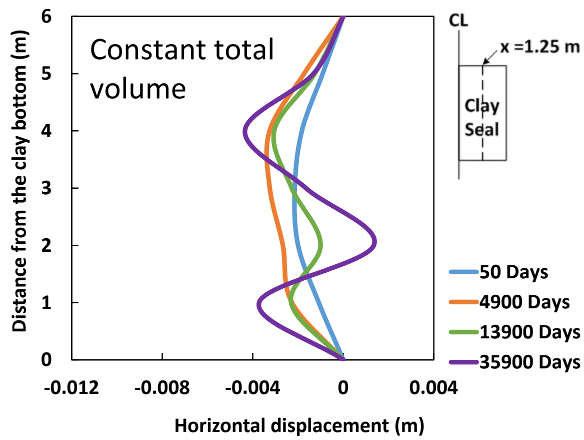

(b) Case 2

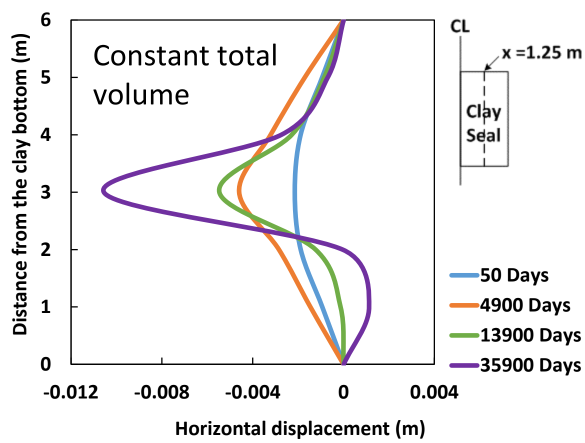

(c) Case 3

Figure 5-26. Prediction of horizontal (radial) displacements within the clay seal along a vertical line, 1.25 m from the shaft centerline

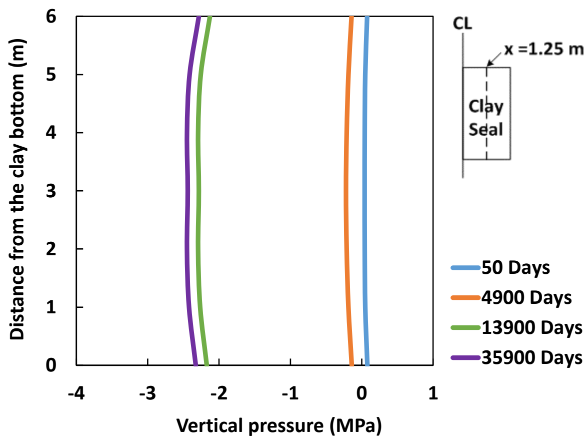

(a) Case 1

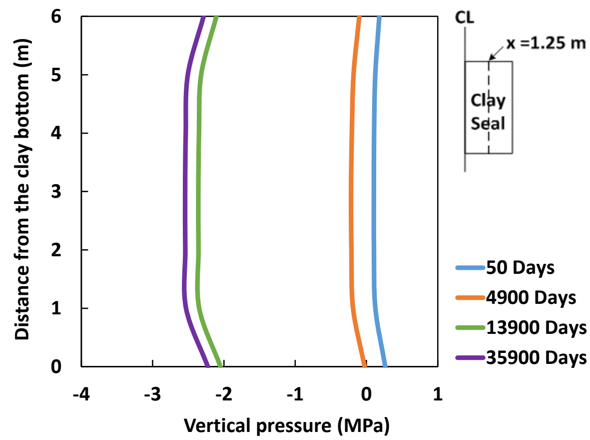

(b) Case 2

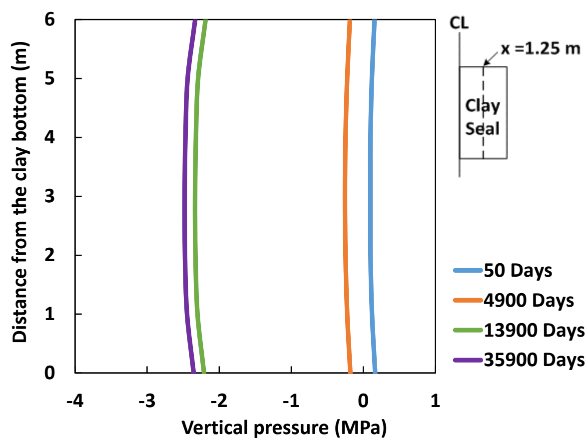

(c) Case 3

Figure 5-27. Prediction of vertical pressures within the clay seal along a vertical line, 1.25 m from the shaft centerline

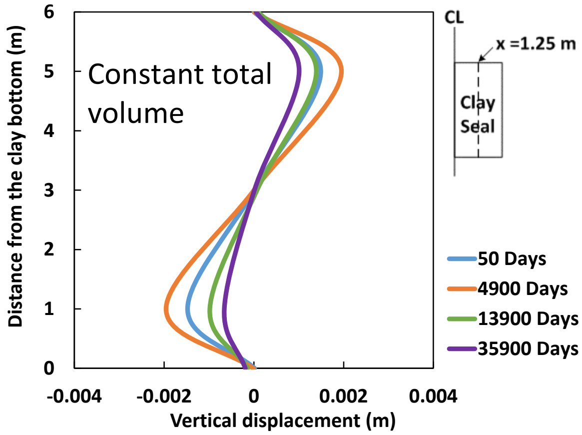

(a) Case 1

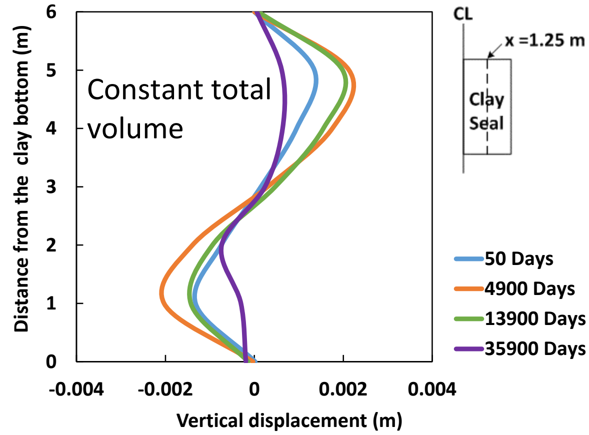

(b) Case 2

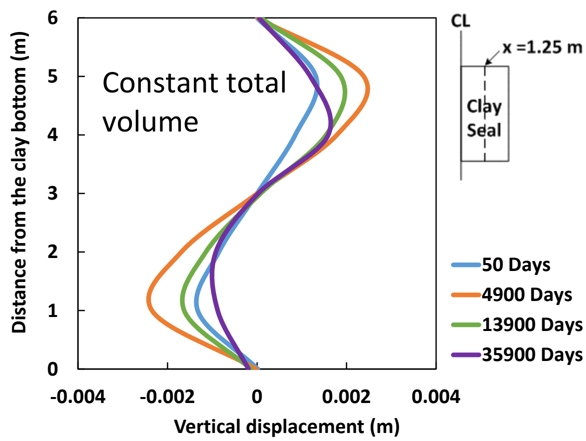

(c) Case 3

Figure 5-28. Prediction of vertical displacements within the clay seal along a vertical line, 1.25 m from the shaft centerline

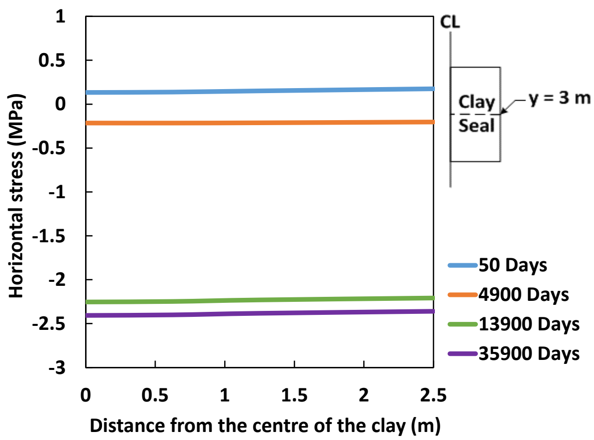

(a) Case 1

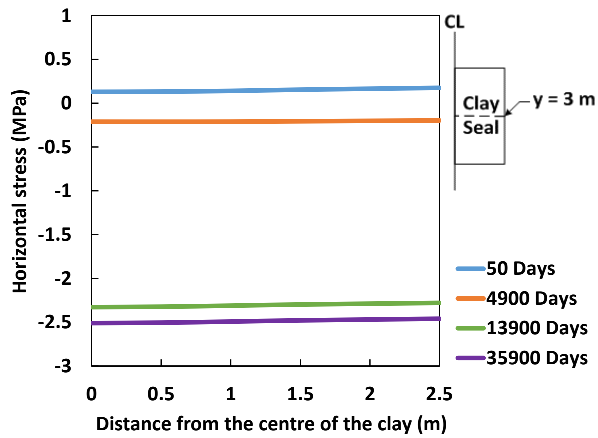

(b) Case 2

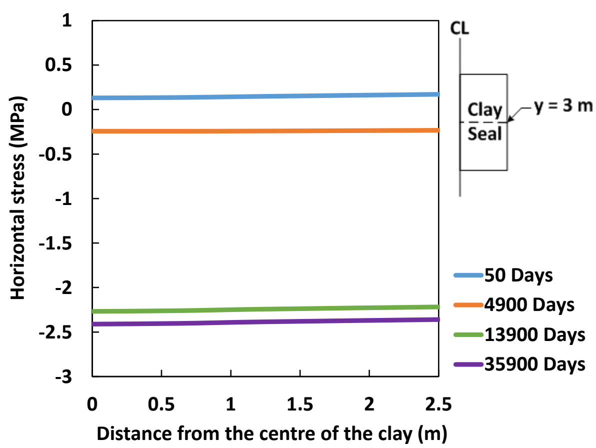

(c) Case 3

Figure 5-29. Prediction of horizontal (radial) stresses within the clay seal along a horizontal line, 3 m from the bottom of the clay seal

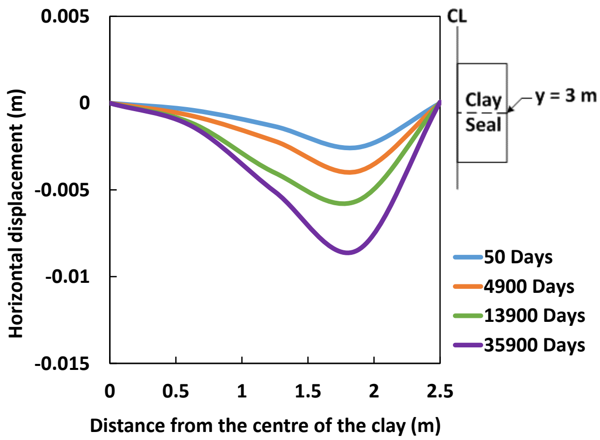

(a) Case 1

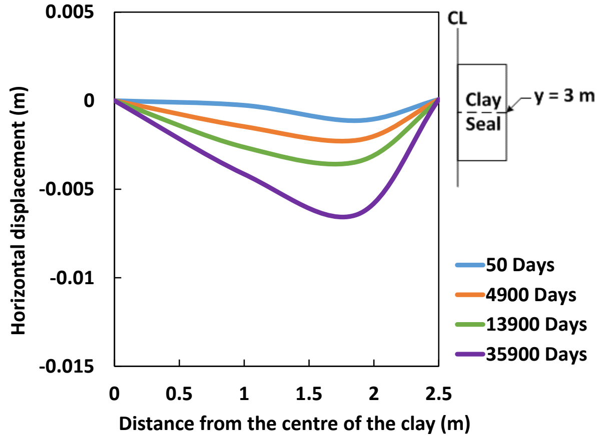

(b) Case 2

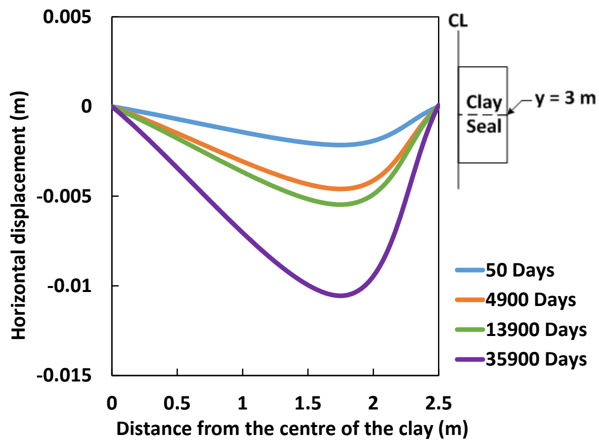

(c) Case 3

Figure 5-30. Prediction of horizontal (radial) displacements within the clay seal along a horizontal line, 3 m from the bottom of the clay seal

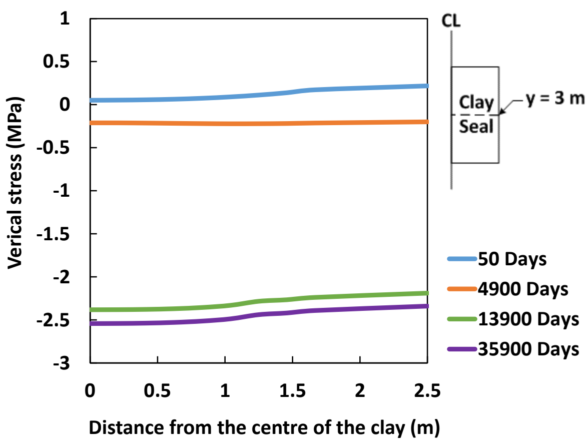

(a) Case 1

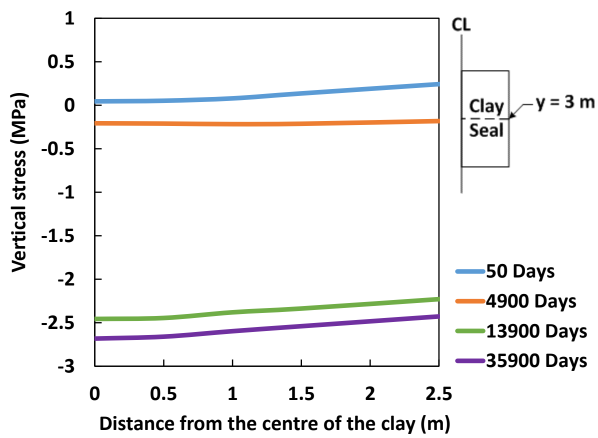

(b) Case 2

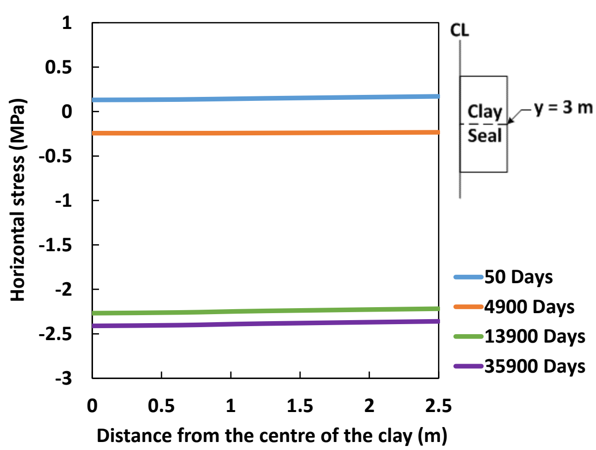

(c) Case 3

Figure 5-31. Prediction of vertical stresses within the clay seal along a horizontal line, 3 m from the bottom of the clay seal

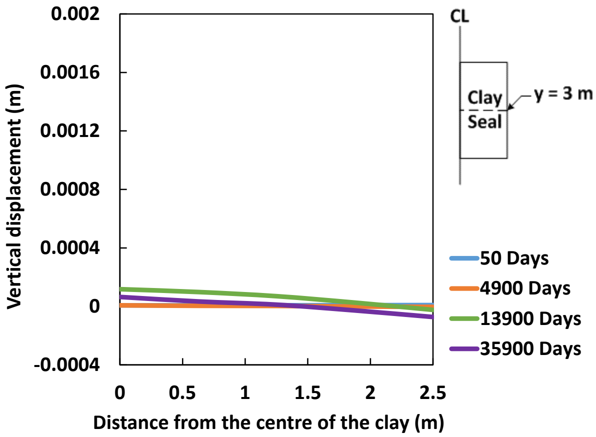

(a) Case 1

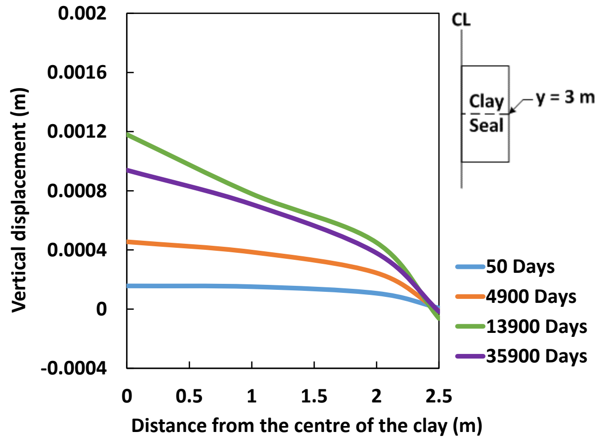

(b) Case 2

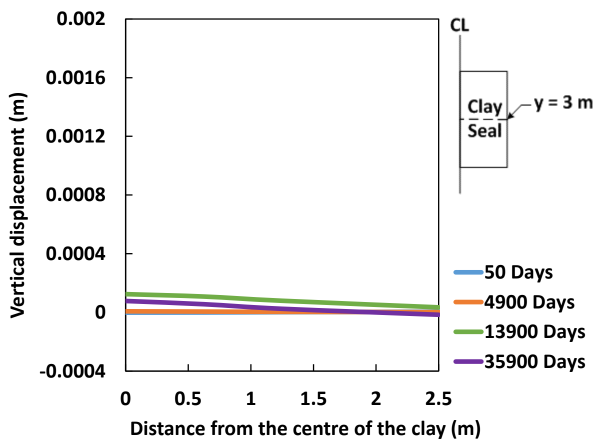

(c) Case 3

Figure 5-32. Prediction of vertical displacements within the clay seal along a horizontal line, 3 m from the bottom of the clay seal

CHAPTER 6

EVOLUTION OF SWELLING PRESSURE IN THE CLAY SEAL

6.1. Introduction

Compacted bentonite-aggregate mixtures have been chosen as engineered barriers (e.g., buffer and backfill materials) used in the construction of deep geological repositories for high-level radioactive wastes. The bentonite-aggregate mixtures have beneficial properties such as low permeability, high swelling potential, good self-sealing capacity and high radionuclide retardation capacity.

In the ESP, the clay seal component is composed of a blend of 40% Wyoming sodium-dominated bentonite (200 mesh gradation) and 60% local quartz sand (Dixon et al. 2009). The clay seal was installed at the location where the shaft passed through a major hydrogeological feature (Fracture Zone 2 (FZ2)) to limit the potential for mixing of deeper saline groundwater and shallower, less saline groundwater (Dixon et al. 2009). The bentonite swells as it hydrates and when confined produces a swelling pressure that effectively reduces groundwater movement.

Extensive studies have been focused over the years on thermal-hydraulic-mechanical behaviour of different types of bentonites or bentonite-aggregate mixtures in both distilled water and saline solutions. The main objectives of these studies were to determine swelling pressures and hydraulic conductivities in order to qualify them for use as buffer and backfill materials. The results have indicated that montmorillonite is the key component controlling the water uptake and swelling processes. The swelling mechanism of bentonite-based materials is the same as that of natural bentonite (i.e., montmorillonite) (Komine and Ogata 1996, Mollins and Stewart 1996, Saiyouri et al. 2000, Saiyouri et al. 2004, Dueck and Börgesson 2007, Ferrage et al. 2007, Cui et al. 2012, Liu 2013).

In the ESP, the functioning and performance of the shaft seal mainly depend on swelling and hydraulic properties of the clay seal (bentonite-sand mixtures (BSM)). The field data obtained from instrumentation sensors have indicated that the shaft seal is functioning as designed, which means swelling pressure of the unsaturated clay seal has been gradually developed.

This section presents evolution of swelling pressure of the unsaturated clay seal during water uptake. Two methods were used to estimate development of swelling pressure. Liu (2013) developed a mechanistic model using a thermodynamic relationship between the swelling pressure and suction and the DLVO theory (Derjaguin and Landau 1941, Verwey and Overbeek 1948) to describe the behaviour of crystalline swelling, while using a diffuse double-layer theory to explain the behaviour of osmotic swelling and van der Waals swelling. Derjaguin, Landau, Verwey, and Overbeek (DLVO) developed a theory of colloidal stability that currently represents interactions between colloidal particles and their aggregation behaviour (Derjaguin and Landau 1941, Verwey and Overbeek 1948). This DLVO theory was used to explain forces acting between interfaces. The other model suggested by Dueck and Börgesson (2007) was based on empirical relationships between the swelling pressure, the water content and the actual suction (or relative humidity) under confined conditions. The following sections explain details about each model and present predictions of swelling pressure using the models for the clay seal component.

6.2. Development of Swelling Pressure by Crystalline and Osmotic Swelling

6.2.1. Crystalline Swelling and Osmotic Swelling

In unsaturated conditions, there are exchangeable cations located on the surface of the unit layers of clay minerals. The unit layers lie very close together and the distance (d_m) (also called basal spacing) between the bottom of a unit layer to the bottom of another layer directly over it is approximately 0.95 - 1.0 nm (Ferrage et al. 2007). The negatively charged unit layers are held together by the interlayer cations and the van der Waals attraction. During water uptake, the cations hydrate and crystalline swelling can extend the basal spacing (d_m) up to between 1.25 and 1.9 nm, depending on the degree of saturation and the exchange cation capacity (Liu 2013). Ferrage et al. (2005) reported that hydration initially occurred on the montmorillonite surface and around the exchangeable cations in the interlayer space inside the particles (Figure 6-1). The water molecules were found to be inserted between the unit Si-Al-Si layers of montmorillonite, layer after layer up to 4 layers for sodium-dominated bentonites and 3 layers for calcium-dominated bentonites. In short, crystalline swelling occurs as 0 - 4 discrete layers of water molecules are inserted between the unit layers of montmorillonite.

The hydrated cations are separated from the outer surfaces of the montmorillonite particles moving into the interparticle pores (Liu 2013). This process results in formation of the electrical diffuse double-layers, which is directly related to osmotic (interparticle) swelling. The swelling beyond four layers of water for sodium-dominated montmorillonite is associated with the interactions of the diffuse double-layers due to the osmotic phenomenon (Yong 1999). The osmotic swelling is mainly resulted from the difference in concentration between the ions electrostatically held close to the surface of the unit layers and the ions in the pore water (Madsen and Müller-Vonmoos 1989). As a result, the repulsive force between the overlapping double-layers of the particles at a given separation distance depends on the concentration of electrolytes in the pore water and the valence and the radius of the ions in the diffuse double-layer (Madsen and Müller-Vonmoos 1989, Liu 2013). However, some studies indicated that osmotic swelling might start after the formation of the second water layer in the interlayer space for highly compacted bentonite (Saiyouri et al. 2000, Saiyouri et al. 2004). This means that osmotic swelling is dominant over crystalline swelling as the crystalline swelling is confined to the first two layers of water and then osmotic swelling occurs from the third water layer. This phenomenon that showed higher osmotic swelling pressure than crystalline swelling pressure at the initial hydration stage could be due to the diffuse double-layers that might develop within the interlayer space and consequently broke the montmorillonite particles into individual layers as more water was taken up after the crystalline swelling had fully developed (Madsen and Müller-Vonmoos 1989, Liu 2013).

In contrast to sodium-dominated bentonite, calcium-dominated bentonite can have the diffuse double-layers formed on the outer surface of the montmorillonite so that the particles are more difficult to break into individual layers. As a result, significantly less osmotic swelling pressure is generated for Ca-dominated bentonite (Liu 2013).

6.2.2. A Mechanistic Model for Estimating Swelling Pressure

Liu (2013) suggested a mechanistic model to estimate swelling pressure of bentonite and bentonite-aggregate mixtures under saturated conditions. This model considered major mechanisms of both crystalline swelling and osmotic swelling that resulted from the effects of cation demixing and the consequences of disintegration of the montmorillonite particles into small stacks of unit layers from unsaturated condition to saturated condition. However, this model did not take account of the change of the microstructures of bentonite during hydration. This section presents the model concept developed by Liu (2013) for predicting swelling pressure of bentonite-aggregate mixture.

Figure 6-2 shows conceptualization of the bentonite-sand mixture suggested by Komine and Ogata (1996) and Liu (2013). As can be seen in the figure, before water uptake the volume of solid (V_{solid}) is the sum of montmorillonite volume (V_m), volume of non-swelling minerals (V_{nm}) and volume of sand particles (V_{sand}) as shown in Equation 6-1 (Liu 2013).

$$V_{solid} = V_m + V_{nm} + V_{sand} \tag{6-1}$$

With water uptake, the volume of montmorillonite increases and swells. The volume of water (V_w) is a sum of volume of void and an increase in volume of montmorillonite (ΔV). Therefore, the total volume of the mixture becomes a sum of volume of solid and volume of water as described in Equation 6-2 (Liu 2013).

$$V = V_{solid} + V_w \tag{6-2}$$

Since montmorillonite is the key component of the mixture for water uptake and swelling processes, the void ratio of montmorillonite (e_m) is used to describe the behaviour of the bentonite-sand mixture for both confined and unconfined conditions as shown in Equation 6-3 (Liu 2013).

$$e_m = \frac{V_w}{V_m} \tag{6-3}$$

The void ratio of montmorillonite at saturation can be defined using the final void ratio of the system (Equation 6-4).

$$e_m = e\,\frac{\rho_m}{\rho_s \cdot \alpha \cdot C_m} \tag{6-4}$$

where e is the final void ratio, ρ_m and ρ_s are the density of montmorillonite and solid in mixture, respectively. C_m and α are the content of montmorillonite and bentonite, respectively. The density of solid in mixture (ρ_s) can be defined using the average density of solids in bentonite (ρ_b) and the density of sand (ρ_a) (Liu 2013).

$$\rho_s = \frac{1}{\frac{\alpha}{\rho_b} + \frac{(1-\alpha)}{\rho_a}} \tag{6-5}$$

where the average density of solids in bentonite (ρ_b) is given by (Liu 2013):

$$\rho_b = \frac{1}{\frac{C_m}{\rho_m} + \frac{(1-C_m)}{\rho_n}} \tag{6-6}$$

where ρ_n is the density of non-swelling minerals in bentonite.

Final dry density of montmorillonite ($\rho_{dry,\,b}$) can also be used to describe the behaviour of the bentonite-sand mixture for both confined and unconfined conditions as shown in Equations 6-7 and 6-8 (Liu 2013).

$$\rho_{dry,\,b} = \frac{1}{\frac{C_m}{\rho_{dry,\,m}} + \frac{(1-C_m)}{\rho_n}} \quad (6\text{-}7)$$

where,

$$\rho_{dry,\,m} = \frac{\rho_m}{1 + e_m} \quad (6\text{-}8)$$

These relationships ($\rho_{dry,\,b}$, $\rho_{dry,\,m}$, and e_m) allow for describing the behaviour of the bentonite-sand material with water uptake. Several assumptions are made for this model and are as follows (Liu 2013):

- Montmorillonite particles are uniformly distributed in the bentonite-aggregate-water system.
- Montmorillonite particles are made up of stacked unit layers.
- The number of stacked unit layers depends on the montmorillonite content, the type and amount of the exchangeable cations in the interlayers and the final density of bentonite.
- Osmotic swelling and van der Waals swelling are generated after crystalline swelling pressure has been fully developed. Additional interaction in the Stern layer is not considered.

The model proposed by Liu (2013) did not consider interaction in the Stern layer. However, Liu (2013) compared measured swelling pressures at various interparticle distances (h) between the unit layers with the proposed model and some diffuse double-layer models. The comparison showed that the proposed model provided better predictions than DLVO theory and the Gouy-Chapman model that was corrected by accounting for interaction in the Stern layer (Yong and Mohamed 1992).

Crystalline Swelling Component

The mechanism of crystalline swelling is hydration of the interlayer cations and the clay surface and therefore crystalline swelling pressure (P_{ccs}) depends only on the separation distance (h). It is assumed that crystalline swelling has just started when adsorption of water molecules into interlayer spaces dominates over all other interactions such as the van der Waals attraction and the diffuse double-layer repulsion. This assumption leads to the separation distance (d) between the unit layers has not reached d_m, but increases the separation distance (h) between the particles.

The swelling pressure exerted in crystalline swelling mechanism can be defined as (Liu 2013):

$$P_{CCS} = \kappa \cdot e^{\frac{-h}{l}} \tag{6-9}$$

where κ and l are two constants, the pre-exponential factor and the decay length, respectively.

Osmotic Swelling and van der Waals Swelling Components

It is assumed that after crystalline swelling has fully developed, osmotic swelling has also been developed, which means that interaction with water in the interlayers (between the unit layers) is complete. In this stage, the electrostatic, repulsive force caused by overlapping of diffuse double-layers and van der Waals attractive force are the only forces operating between particles (stacks) (Liu 2013).

Montmorillonite particles (stacks) consist of a number of unit layers (n_s) and these unit layers are separated by a fixed distance of d_m as shown in Figure 6-3. The fixed distance (d_m) is dependent on the types of exchangeable cation and can be defined as (Liu 2013):

$$d_m = \frac{1}{CEC} \sum_i EXC_i d_i \tag{6-10}$$

where d_i is the fixed distance between the unit layers of montmorillonite for the i^{th} exchangeable cation. CEC is the cation exchange capacity of bentonite and EXC_i is the exchange capacity of the i^{th} exchangeable cation.

The separation distance (h) between the montmorillonite particles can be determined using the void ratio of montmorillonite (e_m) as shown in Equation 6-11 (Liu 2013).

$$h = n_s \delta_s e_m - (n_s - 1) d_m \tag{6-11}$$

where δ_s is the thickness of the unit layer of montmorillonite. The diffuse-double layer (DDL) model determines half-spacing between the two platelets using specific surface based on assumption that all montmorillonite particles are equally spaced (Komine and Ogata 1996).

Electrostatic swelling pressure can be defined using the Gouy-Chapman theory as:

$$P_{DDL} = 2\ c\ R\ T\ (\cosh y^m - 1) \tag{6-12}$$

where R is the gas constant, T is the absolute temperature in Kelvin and y^m is the scaled potential at the mid-point between montmorillonite particles. The scaled potential at the mid-point (y^m) can be determined by Equations 6-13 – 6-17 (Liu 2013).

$$y^m = \sinh^{-1}\left[2\sinh y_\infty^m + \frac{4}{\kappa h}\sinh\left(\frac{y_\infty^h}{2}\right)\right] \tag{6-13}$$

$$y_\propto^m = 4\tanh^{-1}\left[\tanh\left(\frac{y_\infty^0}{4}\right)\exp\left(\frac{-\kappa h}{2}\right)\right] \tag{6-14}$$

$$y_\propto^h = 4\tanh^{-1}\left[\tanh\left(\frac{y_\infty^0}{4}\right)\exp(-\kappa h)\right] \tag{6-15}$$

$$\kappa = \left(\frac{2c\nu^2F^2}{\varepsilon_0\varepsilon_r RT}\right)^{1/2} \tag{6-16}$$

$$y_\infty^0 = 2\sinh^{-1}\left(\frac{\upsilon F\sigma^0}{2\varepsilon_0\varepsilon_r\kappa RT}\right) \tag{6-17}$$

where ε_0 is the permittivity of vacuum, ε_r is the relative dielectric constant of the pore solution, F is the Faraday constant, and σ_0 is the surface charge density.

Swelling pressure from van der Waals can be defined by the following equation (Liu 2013):

$$P_{vdW} = \frac{A_H}{6\pi}\left\{\frac{1}{h^3} - \frac{2}{\left(h+D_p\right)^3} + \frac{1}{\left(h+2D_p\right)^3}\right\} \tag{6-18}$$

where A_H is the Hamaker's constant and D_p is the thickness of the montmorillonite particles as shown in Equation 6-19.

$$D_p = n_s\delta_s + (n_s\text{-}1)d_m \tag{6-19}$$

Based on the thermodynamic relation and the DLVO theory, the swelling pressure of the bentonite-sand mixture can be determined as (Liu 2013):

$$P = P_{CCS} + P_{DDL} - P_{vdW} \tag{6-20}$$

Physical constants used in this method are shown in Table 6.1. Constants used in the determination of the pressure of crystalline swelling are shown in Table 6.2. The number of stacked unit layers (n_s) of 1.25 was used because a range of n_s from 1 to 1.5 was the best fit for experiment data of bentonite-sand mixtures (MX80-sand) (Liu 2013). Fixed separation distance (h) between unit layers was determined using Equations 6-11.

6.2.3. Results and Discussion

Numerical results obtained from CODE_BRIGHT have provided evolution of total stress and effective stress across the clay seal with no swelling pressure. The effective stress is the difference between the total stress and maximum of liquid and gas pressure in unsaturated condition in CODE_BRIGHT. The gas pressure was constant and therefore the liquid (pore water) pressure became negative due to suction applied initially in the clay seal. For unsaturated condition, the effective stress was identical to the total stress ($P_g = 0 > P_w$), while for saturated condition the effective stress was calculated using Terzaghi's equation (CODE_BRIGHT user's guide 2015).

The numerical analysis using CODE_BRIGHT has provided changes in porosity of the clay seal from the initial system wetting to full saturation. That allowed for calculating values of void ratio of montmorillonite at each time step and the calculated void ratios of montmorillonite were then used in the model to estimate development of swelling pressure with time.

Figure 6-4 clearly shows that during the process of water uptake, the swelling pressure increases while the void ratio of montmorillonite decreases because the montmorillonite particles swell and occupy the voids of the bentonite as described in Figure 2-3 (Komine and Ogata 1996) in Chapter 2. The maximum swelling pressure estimated in this method (Liu 2013) indicates approximately 0.86 MPa, which is close to what is expected (0.8 MPa) in the field. The expected swelling pressure of 0.8 MPa was estimated based on laboratory test data under rigidly confined conditions.

Figure 6-4 also presents other laboratory results to compare with the predicted swelling pressure. Laboratory data obtained from Mollins et al. (1996) and Studds et al. (1998) used Wyoming bentonite (100%) or bentonite (20%)-sand mixtures for free swell tests, while Sun et al. (2009) used Kunigel bentonite (100%) and bentonite (30% and 50%)-sand mixtures for free swell tests. Kunigel bentonite was a sodium-dominated bentonite with about 40% montmorillonite content. The swelling prediction shows good agreement with the experimental data. A slight deviation is observed from specimens composed of 20% Wyoming bentonite-80% sand (Mollins et al. 2009). For the possible reason for this deviation, Graham et al. (1986) reported that these specimens contained a low percentage of bentonite and therefore sand became dominant in its mechanical behaviour, not montmorillonite as in the other specimens.

Since swelling pressure generated from both the diffuse double layer and van der Waals interactions depends on the properties of electrolytes and the separation distance (h), a relationship between the swelling pressure and the separation distance (h) between the unit layers is examined. Figure 6-5 clearly shows greater swelling pressures at smaller interparticle distance. It also indicates that swelling pressures become more sensitive at interparticle distances smaller than 2.4 nm.

6.3. Predictions of Swelling Pressure under Confined Conditions

Some studies focused on hydraulic-mechanical (H-M) properties under different confining conditions have reported different H-M behaviour of bentonite or bentonite-sand mixtures between confined and unconfined conditions (Yahia-Aissa et al. 2001, Cui et al. 2002, Chen et al. 2006, Dueck and Börgesson 2007, Ye et al. 2009). Cui et al. (2002) conducted swelling tests on Kunigel bentonite-sand mixtures (70%:30% dry mass) under constant volume conditions to investigate changes in microstructure of the mixtures using mercury intrusion porosimetry and scanning electron microscopy. This study found different infiltration rates between constant volume and free-swell conditions. The bentonite aggregates started swelling during wetting and then reduced the volume of macro-pore space under constant volume conditions. By contrast, in free swelling conditions, swelling of aggregates could increase the volume of macro pore space and consequently increase the water flow rate or hydraulic conductivity.

A microstructure change occurs due to combined hydraulic (suction) and mechanical (swelling pressure) effects. During wetting, suction decreases and this separates the bentonite sheets in aggregates and deforms the aggregates. As a result, the macro pores are progressively closed to finally reach a homogeneous structure at zero suction. The micro pores seemed not to be affected by the hydration for higher suctions. However, when the suction is close to zero, the generated swelling pressure can compress the soil structure, reducing the size of the micro pores (Cui et al. 2002, Cui et al. 2012).

Water retention curves of bentonite-based materials are also different from different confining conditions. Chen et al. (2006) found that water retention curves under confined and unconfined conditions were similar for suction greater than 4 MPa, however for suction lower than 4 MPa, differences in confining conditions became significant as suction increased. Under unconfined conditions, the water content increased quickly with increasing suction and availability of water.

To assess potential differences in swelling pressure from different confining conditions, another method for estimating swelling pressure under confined conditions was considered. The following section describes details about a second prediction model that applies confined conditions.

6.3.1. A Model for Predicting Swelling Pressure under Confined Conditions

At the URL, the unsaturated clay seal (40% bentonite- 60% sand mixture) would undergo a decrease in suction and an increase in swelling pressure during water uptake if volume change was restricted. Dueck and Börgesson (2007) focused on the influence of confinement on water uptake and swelling pressures during water uptake. Based on laboratory test results, Dueck and Börgesson (2007) provided a relationship between water content, swelling pressure and suction. The material used in the study was Wyoming bentonite (MX-80) with about 80% montmorillonite content. This relationship was based on a thermodynamic relationship and included the water retention curve for free swelling conditions.

Dueck (2004) determined the retention curve using the relationship between relative humidity (RH) and water content (w) as described in Equation 6-21.

$$w = \left[a \ln\left(\frac{RH_{ret}}{100}\right)\right]^{b} \tag{6-21}$$

where, RH is relative humidity (%) referring to the condition in the air near the soil sample, RH_{ret} is relative humidity corresponding to the retention curve for free swelling samples and w is a gravimetric water content (%). The constants a and b can be found for absorption from an initial water content and the final relative humidity 100%.

Based on thermodynamic equilibrium of water potential, the swelling pressure can be estimated from the free energy of the water in a clay-water system and the free energy in pure water (Low and Anderson (1958), Sposito (1972)).

$$- P_s \cdot \nu_w = \frac{R \cdot T}{\omega_v} \ln\left(\frac{p}{p_s}\right) \tag{6-22}$$

where P_s is swelling pressure at saturation (kPa), R is the universal gas constant (j/(mol K)), T is temperature (K), ν_w is specific volume of water (m^3/kg) and ω_v is a molecular mass of water vapour (kg/kmol). Using Equation 6-22 can calculate swelling pressure at saturation from the water content by using the water retention curve expressed in terms of relative humidity.

For unsaturated conditions, the swelling pressure can be calculated by the following equation.

$$P_s\,(RH, w_f) = -\frac{R \cdot T}{\nu_w \omega_v} \ln\left(\frac{RH_{ret}(w_f)}{RH}\right) \tag{6-23}$$

In this equation, RH_{ret} is relative humidity according to the retention curve (%), w_f is final water content measured after the test (%). RH_{ret} is the relative humidity taken from the retention curve corresponding to the measured final water contents of the unsaturated samples under no load conditions. RH is the actual relative humidity applied in the specimen. This equation is basically identical to Equation 6-22, however the reference relative humidity (RH=100%) is replaced by an actual RH applied to the specimen. This equation was proposed to estimate development of swelling pressure during a constant volume under unsaturated conditions (Dueck and Börgesson 2007).

Figure 6-6 shows different suction behaviours resulting from different confining conditions (Dueck and Börgesson 2007). The initial water content, w_D corresponds to suction s_D (point D) on the unconfined retention curve. When suction decreases to s_E as hydration proceeds under unconfined conditions, the water content will increase to w_E (point E) on the unconfined retention curve. By contrast, water uptake occurs under confined conditions, the decrease of suction to s_E will correspond to the water content w_F (point F) on the confined retention curve due to the effect of load. The water content, w_F also corresponds to suction s_G on the unconfined retention curve. Therefore, the difference in suction between suction s_G (point G) and suction s_F (point F) is the swelling pressure. In other words, the swelling pressure is considered by the difference in suction between free swelling specimens and constrained specimens for the same water content.

To determine the constants a and b in Equation 6-21 for free swelling specimens, laboratory data on bentonite-sand mixtures (50%-50% dry mass) for free swell tests were used. Wang et al. (1995), Tang (1999) and Blatz et al. (2006) determined retention curves between suction and water content for Wyoming bentonite-sand mixtures (50%-50% dry mass) with an initial dry density of 1.67 Mg/m^3 and initial water content of 19.4% (corresponding to degree of saturation of 85%). The suction values measured in their studies were converted to values of relative humidity using Kelvin's law as described in Equation 6-24.

$$s = -10^{-6}\,\frac{R\cdot T}{V_w}\,\ln\left(\frac{RH}{100}\right) \quad \text{(MPa)} \tag{6-24}$$

where R is the universal constant of gases (8.3143 J/mol·K), T is the absolute temperature and V_w is the molar volume of water (1.80·10-5 m^3/mol).

Figure 6-7 shows a relationship between suction and water content determined for the bentonite-sand (50%-50% dry mass) mixture specimens with an initial water content of 19.4% (Wang et al. 1995, Tang 1999, Blatz et al. 2006). The measured suction values were used to estimate relative humidity values corresponding to the measured values of water content. Figure 6-8 shows a clear relationship between relative humidity and water content for the same specimens. The solid green line is referred to as the best fit line on the data. This relationship allowed for estimation of the clay seal's relationship with an initial water content of 12.1%. By adjusting the two constants a and b in Equation 6-21, the location of the estimated curve (shown as the red dashed line in the figure) was determined to be below the green curve that was the best fit for an initial water content of 19.4%. This relationship estimated for the clay seal was considered for free swelling under unconfined conditions.

Estimation of swelling pressure using Equation 6-23 required changes in actual relative humidity values of the clay seal during water uptake. As presented in Chapter 3, there were four (4) time-domain reflectometer (TDR) sensors installed in the centre region of the clay seal that monitored the evolution of degree of saturation. The monitored degrees of saturation were then used to estimate suction values using the relationship between suction and degree of saturation suggested by van Genuchten (1980). Again, suction values were converted to relative humidity values using Equation 6-24.

Figure 6-9 shows changes in degree of saturation with time, which were measured by TDR sensors in the clay seal. According to the TDR readings, the centre region at 2 m from the bottom of the clay seal (TDR1) reached 100% saturation at 2250 days (~6.2 years). Figure 6-10 shows a relationship between suction and relative humidity estimated using the measured degrees of saturation.

Equation 6-23 also required determination of a final water content of the clay seal. Since the clay seal is still evolving toward the saturation state, numerically computed porosity values were used again to estimate the final water content of the clay seal. Numerical simulation using CODE_BRIGHT (Vaunat and Olivella 2002) was performed for 100 years and the final void ratio of the clay seal after 100 years was estimated using computed porosity values. The final water content was calculated using the following equation:

$$w_{final} = \left(\frac{S \times e_f \times \rho_w}{\rho_s}\right) \quad (\%) \tag{6-25}$$

where ρ_s is the density of Wyoming bentonite (2705 kg/m^3) and ρ_w is the density of water (1000 kg/m^3). The estimated final water content of the clay seal for 100 years was 19.0 % when the clay seal became fully saturated (degree of saturation S = 100%). In addition, changes in water content of the clay seal during water uptake were also estimated using the computed void ratios obtained from CODE_BRIGHT. Table 6-3 summarizes estimated values of both water content and relative humidity during water uptake. As noted in the table, initial relative humidity values of the clay seal are high - over 90% - corresponding to a degree of saturation of 67%. Changes in relative humidity during water uptake are small because the clay seal was initially installed at a relatively high degree of saturation (67%).

6.3.2. Results and Discussion

Swelling pressure was estimated after applying all parameters in Equation 6-23. Predicted swelling pressure values are summarized in Table 6-3. The TDR2 sensor installed at the centre and 3 m from the bottom of the clay seal indicates a swelling pressure of 0.41 MPa under confined conditions, which corresponds to the degree of saturation of 81.5% measured at 2250 days (~6.2 years). As mentioned earlier, TDR1 at the centre and 2 m from the bottom of the clay seal became fully saturated and it indicates that a swelling pressure of 0.43 MPa should have developed during the same period. Based on the use of the TDR readings, the prediction model proposed by Dueck and Börgesson (2007) estimates swelling pressures ranging from 0.38 MPa to 0.43 MPa under confined conditions. The predicted swelling pressures using the model are lower than what is expected (0.8 MPa) in the field. Note that the second prediction model is very sensitive to the value of RH_{ret} / RH (relative humidity according to the retention curve / the actual relative humidity applied in the specimen). Dueck and Börgesson (2007) reported that 1% of the relative error would cause an error equal to ± 1.35 MPa in the calculated swelling pressure. Since the initial relative humidity values of the clay seal were over 90%, this relative error might not significantly affect the predicted swelling pressure. However, underestimation of the predicted swelling pressure using the second model might be attributed to determination of values of RH_{ret} and RH.

Figures 6-11 and 6-12 show relationships between predicted confined swelling pressures and suction, and between predicted confined swelling pressure and degree of saturation, respectively. As expected, swelling pressure increases as a result of decreasing suction (increasing degree of saturation).

Another attempt was made to compare field readings of total pressure with predicted swelling pressures using the second model. In the central region of the clay seal, a total pressure cell (FT2) had been installed at 0.3 m south from the centre and 3 m from the bottom of the clay seal to monitor changes in total pressure. Development of total pressure in the unsaturated clay seal is a consequence of the progressive development of swelling pressure (potential), gas pressure and pore water (hydraulic) pressure as hydration proceeds. It will take considerable time to reach stress and density equilibrium of the clay seal. Since the clay seal has not yet been fully saturated, it is difficult to break down the measured total pressures into swelling pressure, gas pressure and pore water pressure components.

Full-scale experiments simulating a deep geological repository concept such as the RESEAL in situ shaft-seal test in the Boom clay (Barnichon and Volckaert 2003), Full Scale Engineered Barrier Experiment (FEBEX) (T-H-M testing of an engineered barrier in granite) (Gens et al. 1998), the Isothermal test in AECL's URL (Thomas et al. 2002) and the Tunnel Sealing Experiment (TSX) in AECL's URL (Chandler et al 2002), provided information on the evolution of total pressure and pore water pressure in clay-based sealing materials. They did not, however, provide measured breakdowns of the various components of the total pressures, principally because their systems did not reach either density or stress equilibrium. Breaking down the measured total pressures would require critical assumptions for unsaturated conditions. For instance, swelling pressure would be locally different if hydraulic pressures were not uniformly distributed through the clay seal. If there was a hydraulic gradient across the clay seal after full saturation (likely access for constant flow), estimation of swelling pressure would be difficult. These components of the total pressures might be individually estimated in saturated condition when the hydraulic gradient across the clay seal was very small enough that it would not affect uniform distribution of the hydraulic pressure in the clay seal.

Some of the full-scale experimental studies reported that during water uptake, a decrease in suction resulted in a development of total pressure which was equal to swelling pressure for unsaturated bentonite-sand mixtures (Thomas et al. 2002, Ballie et al. 2006).

Figure 6-13 shows the predicted swelling pressure using the second model compared with field readings of total pressure in the central region of the clay seal. Changes in total pressure from the FT2 sensor were plotted with time, while the swelling pressure prediction was plotted against degree of saturation. The total pressure cell (FT2) monitored for approximately 1630 days (4.5 years) and then stopped functioning. The field readings using the FT2 sensor indicate that total pressure in the centre region was gradually increasing again after 1000 days (2.7 years) and the final total pressure monitored was approximately 0.36 MPa, which is very similar to the predicted swelling pressure of 0.43 MPa in the region. In addition, the slope increment of the predicted swelling pressure is in good agreement with that of FT2's curve.

In this section, two prediction models have been used to estimate evolution of swelling pressure in the clay seal during water uptake. The first model used crystalline and osmotic swelling mechanisms to provide the maximum swelling pressure of 0.86 MPa in the centre of the clay seal, while for a confined condition the second model estimated the maximum swelling pressure of 0.41 MPa in the same region. Considering the confined condition (e.g., constant volume condition) where the clay seal is sandwiched by the concrete segments and surrounded by the host rock, development of the swelling pressure can be affected by the confined condition. The amount of infiltrated water can be minimized when swelling is prevented because volume change conditions significantly influence the hydraulic conductivity through microstructure changes.

The model predictions were verified for prediction of the water retention capacity of the unsaturated clay seal. Based on thermodynamic relationships between swelling pressure and suction (Vanapalli et al. 2012), the estimated swelling pressure values could be converted to suction values using the following equation:

$$P_s = \left(\frac{S_r}{1000}\right)^a \cdot \psi \tag{6-26}$$

where, P_s is swelling pressure (MPa), S_r is effective degree of saturation (%) and ψ is suction (MPa). Vanapalli et al. (2012) suggested Equation 6-26 provided reasonable prediction for the swelling behaviour of only bentonite-sand mixtures.

Suction values that were calculated from the predicted swelling pressures were plotted against computed degree of saturation using CODE_BRIGHT as shown in Figure 6-14. As can be seen in the figure, the suction prediction using the first model proposed by Liu (2013) shows some deviation from the measured data. By contrast, the suction prediction using the second model proposed by Dueck and Börgesson (2007) shows reasonably good agreement with the measured data.

6.4. Summary

Two prediction models of swelling pressure of the unsaturated clay seal have been discussed in this chapter. Since the clay is still evolved toward equilibrium, numerically computed porosity values from CODE_BRIGHT are used to estimate swelling pressure of the clay seal. The first model using crystalline and osmotic swelling mechanisms estimates a swelling pressure of 0.86 MPa, which is very close to what is expected (0.8 MPa) in the field. The second model applying confined conditions estimates a lower swelling pressure of 0.41 MPa. The model predictions are also verified in terms of the water retention capacity of the unsaturated clay seal. The suction prediction using the first model shows some deviation from measured data, while the second model shows reasonably good agreement.

Table 6-1. Physical constants used in the predictions (Liu 2013)

Parameter	Notation	Value
Faraday constant	F	9.64853×10^{4} C mol^{-1}
Gas constant	R	8.31446 JK^{-1} mol^{-1}
Temperature	T	298 K
Permittivity of vacuum	e_0	8.8542×10^{-12} Fm-^{1}
Relative dielectric constant of water	e_r	78.54
Density of water	ρ_w	1000 kg m^{-3}
Density of montmorillonite	ρ_m	2770 kg m^{-3}
Thickness of the unit layers	σ_s	0.96 nm
Fixed separation between the unit layers	di	1.2 nm
Hamaker constant	A_H	$2.2 \text{ X } 10^{-20}$ J

Table 6-2. Constants used in the crystalline swelling pressure (Liu 2013)

Types	Pre-exponential factor, κ (Pa)	Decay length l (nm)
Na-montmorillonite	5.8×10^{8}	0.2
K-montmorillonite	3.8×10^{8}	0.2
Mg-montmorillonite	9.0×10^{8}	0.25
Ca-montmorillonite	9.0×10^{8}	0.25

Table 6-3. Estimated values of swelling pressure using degree of saturation from TDR sensors

TDR1

Degree of saturation	Water content	Suction	Relative humidity	Swelling pressure
(%)	(%)	(MPa)	(%)	(MPa)
0	0	19828.0	0	0
15.0	2.8	134.5	52.9	0.25
30.0	5.7	62.6	74.8	0.30
50.0	9.5	20.5	85.9	0.35
67.0	12.2	12.8	91.0	0.38
68.6	12.5	12.2	91.3	0.38
73.0	13.2	10.7	92.4	0.39
77.2	14.0	9.4	93.3	0.40
78.3	14.2	9.0	93.5	0.40
76.8	13.9	9.5	93.2	0.40
78.5	14.2	8.9	93.6	0.40
100	19.0	0	100	0.43

TDR2

Degree of saturation	Water content	Suction	Relative humidity	Swelling pressure
(%)	(%)	(MPa)	(%)	(MPa)
0	0	19828.0	0	0
15.0	2.8	134.5	52.9	0.25
30.0	5.7	62.6	74.8	0.30
50.0	9.5	20.5	85.9	0.35
67.0	12.2	12.8	91.0	0.38
68.0	12.4	12.4	91.2	0.38
69.5	12.6	11.9	91.6	0.39
71.0	12.9	11.4	91.9	0.39
70.3	12.7	11.6	91.8	0.39
72.5	13.1	10.9	92.3	0.39
72.6	13.1	10.8	92.3	0.39
81.5	14.8	8.0	94.2	0.41

TDR3

Degree of saturation	Water content	Suction	Relative humidity	Swelling pressure
(%)	(%)	(MPa)	(%)	(MPa)
0	0	19828.0	0	0
15.0	2.8	134.5	52.9	0.25
30.0	5.7	62.6	74.8	0.30
50.0	9.5	20.5	85.9	0.35
67.0	12.2	12.8	91.0	0.38
71.2	12.9	11.31	92.0	0.39
72.2	13.1	10.98	92.2	0.39
75.5	13.7	9.90	92.9	0.40
75.3	13.6	9.95	92.9	0.40
78.3	14.2	9.00	93.6	0.40
78.8	14.3	8.85	93.7	0.40
91.0	16.5	5.05	96.3	0.42

TDR4

Degree of saturation	Water content	Suction	Relative humidity	Swelling pressure
(%)	(%)	(MPa)	(%)	(MPa)
0	0	19828.0	0	0
15.0	2.8	134.5	52.9	0.25
30.0	5.7	62.6	74.8	0.30
50.0	9.5	20.5	85.9	0.35
67.0	12.2	12.80	91.0	0.38
69.4	12.6	11.93	91.6	0.39
69.0	12.5	12.08	91.5	0.39
73.1	13.2	10.69	92.4	0.39
72.2	13.1	11.00	92.2	0.39
74.5	13.5	10.24	92.7	0.39
74.1	13.4	10.35	92.6	0.39
85.3	15.4	6.85	95.1	0.41

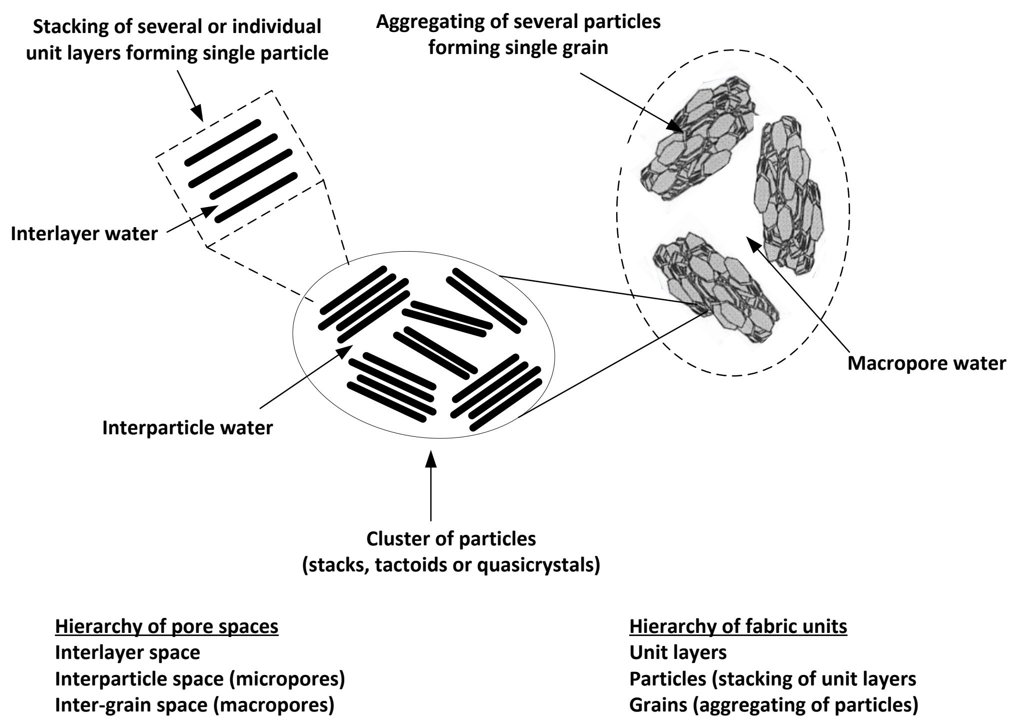

Figure 6-1. Fabric units and pore spaces of bentonite, adapted from Liu (2013)

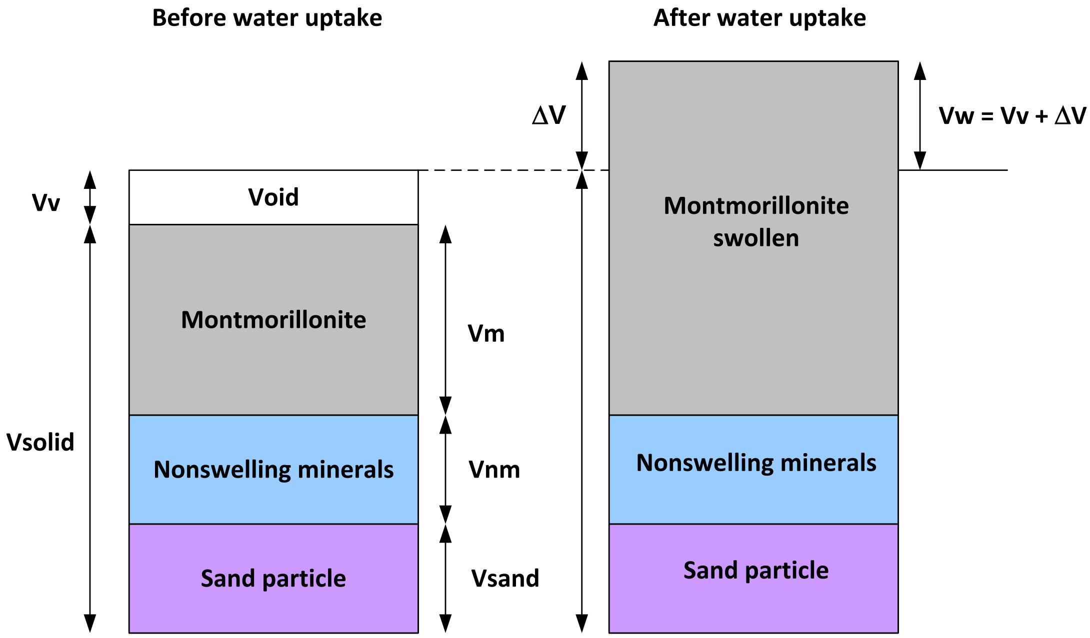

Figure 6-2. Conceptualization of the composition of the bentonite-sand mixture (revised after Liu (2013))

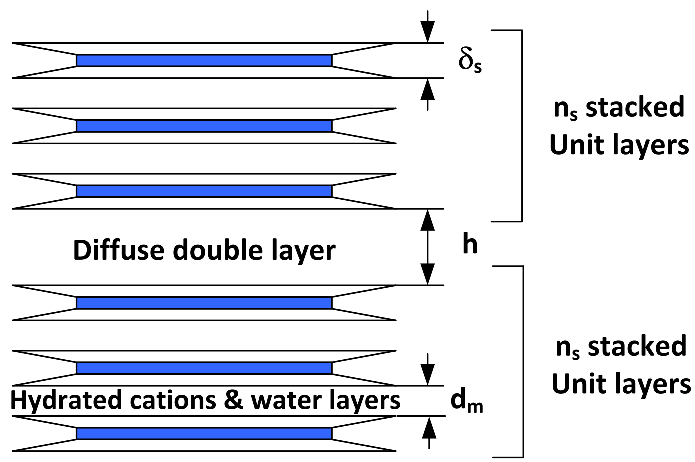

Figure 6-3. A schematic of the montmorillonite particles absorbed water layer and diffuse double-layer (Liu 2013)

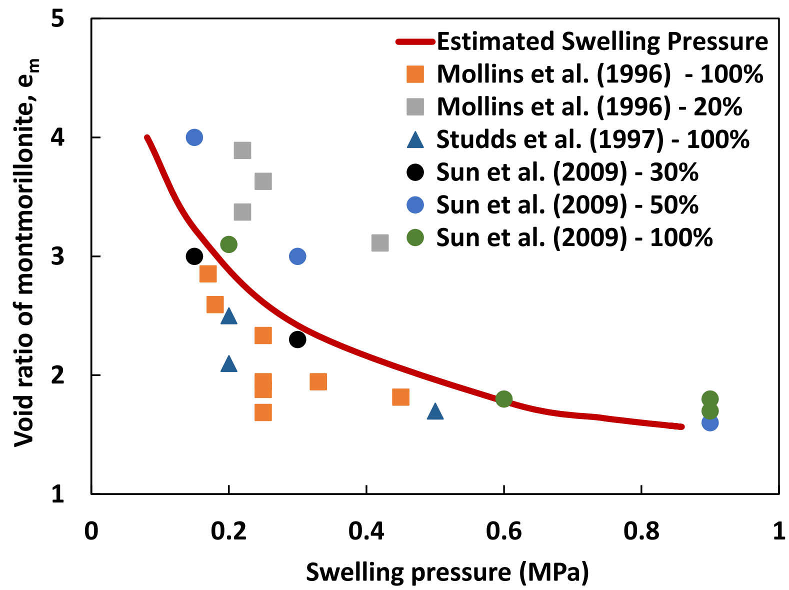

Figure 6-4. Estimated swelling pressure compared with laboratory test data for bentonite-sand mixtures

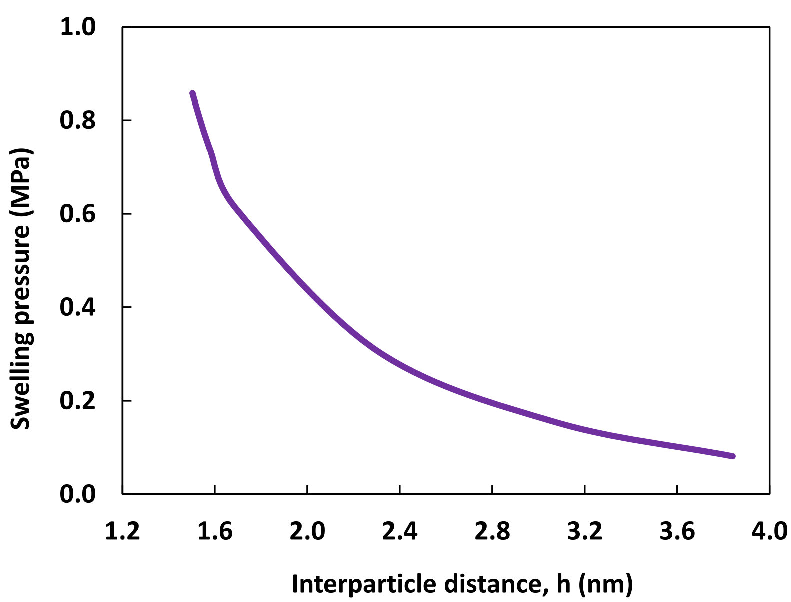

Figure 6-5. A relationship between swelling pressure and interparticle distance

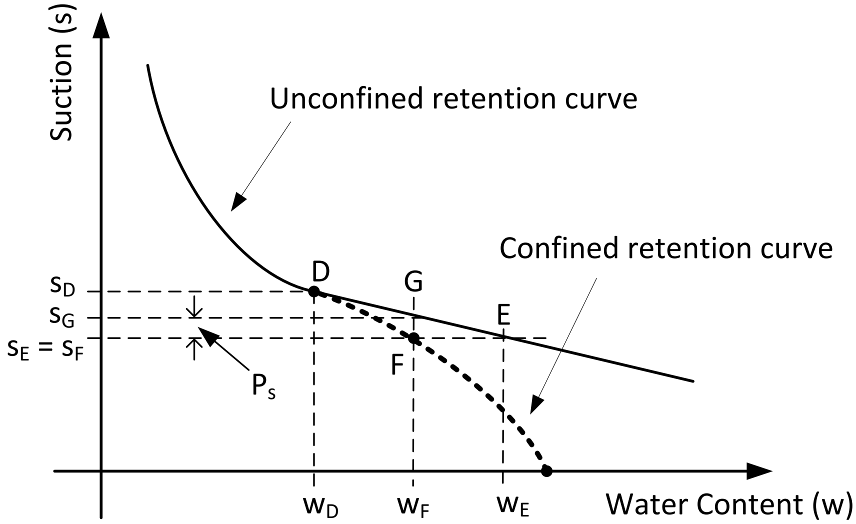

Figure 6-6. Estimation of swelling pressure P_s under unconfined condition (revised after Dueck and Börgesson (2007))

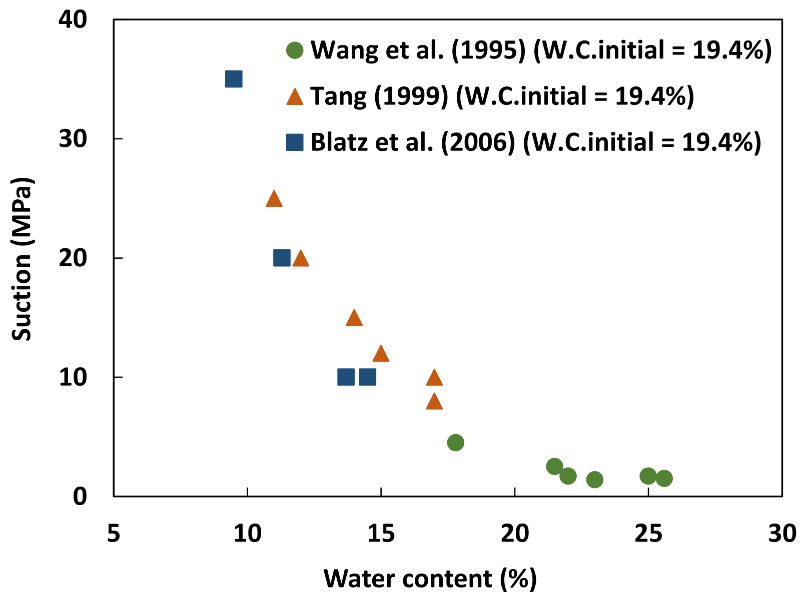

Figure 6-7. A relationship between suction and water content for bentonite (50)-sand (50) mixtures

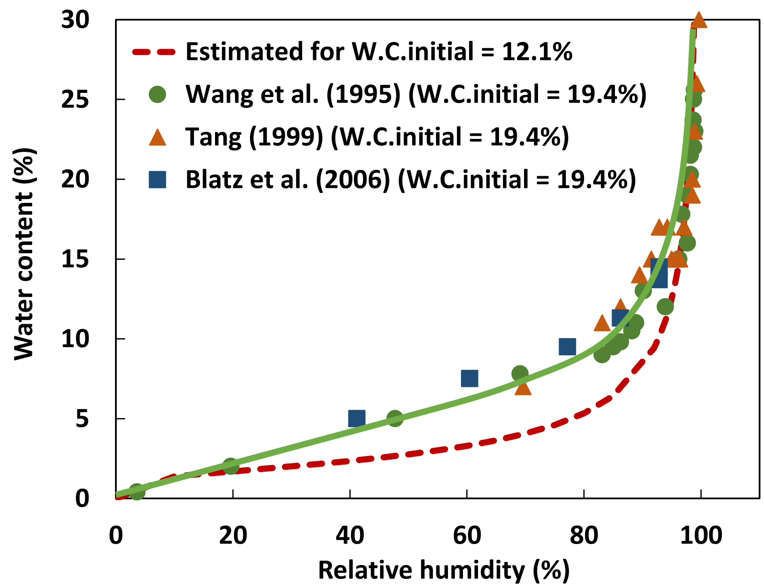

Figure 6-8. A relationship between relative humidity and water content for bentonite (50)-sand (50) mixtures

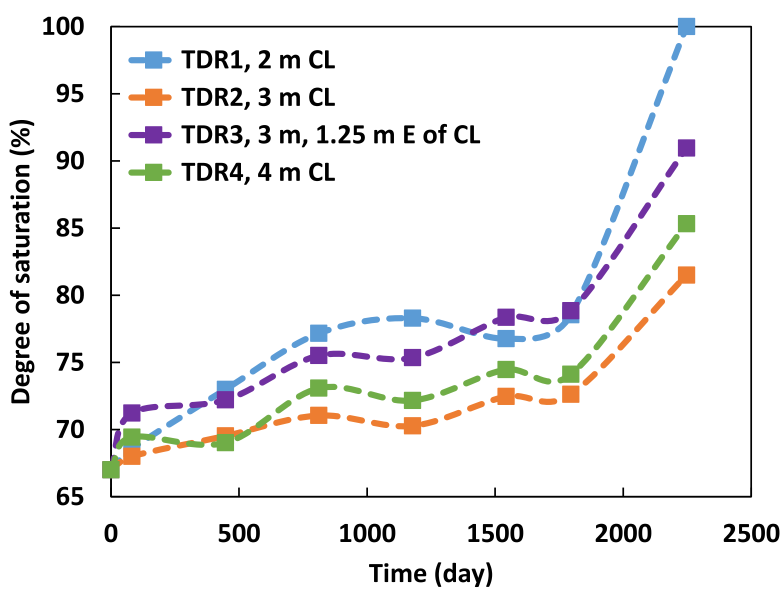

Figure 6-9. Measured degrees of saturation from 4 TDRs.

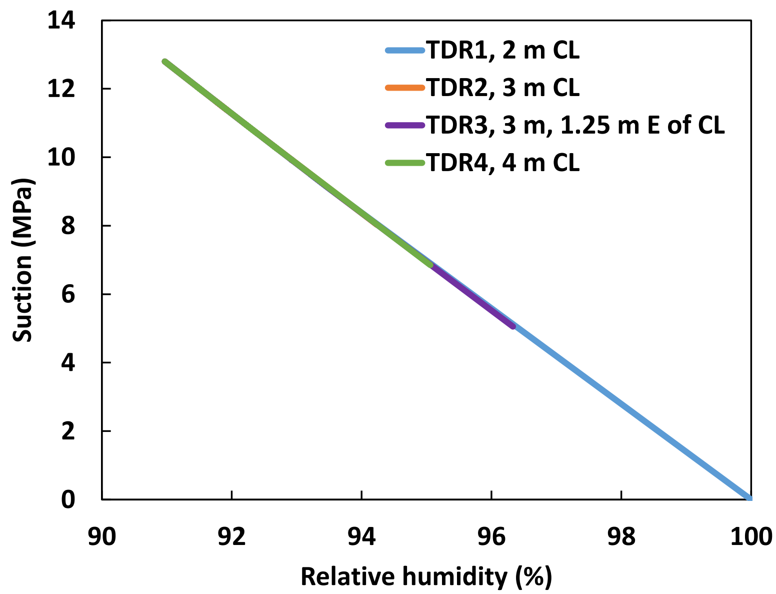

Figure 6-10. A relationship between suction and relative humidity for the clay seal

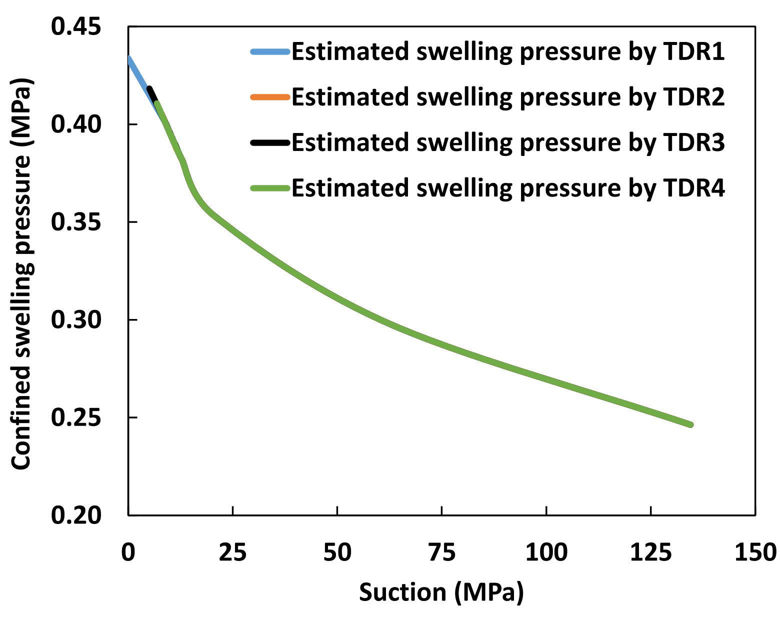

Figure 6-11. A relationship between predicted swelling pressure and suction for the clay seal

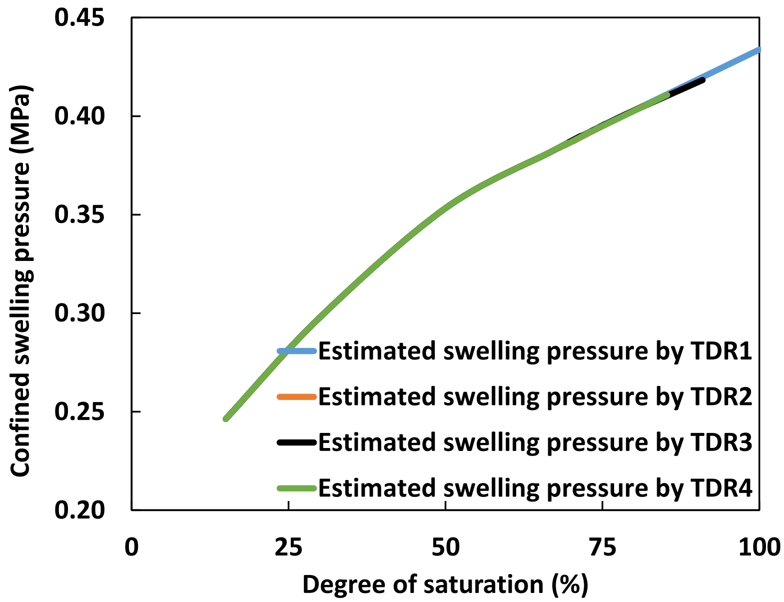

Figure 6-12. A relationship between predicted swelling pressure and degree of saturation for the clay seal

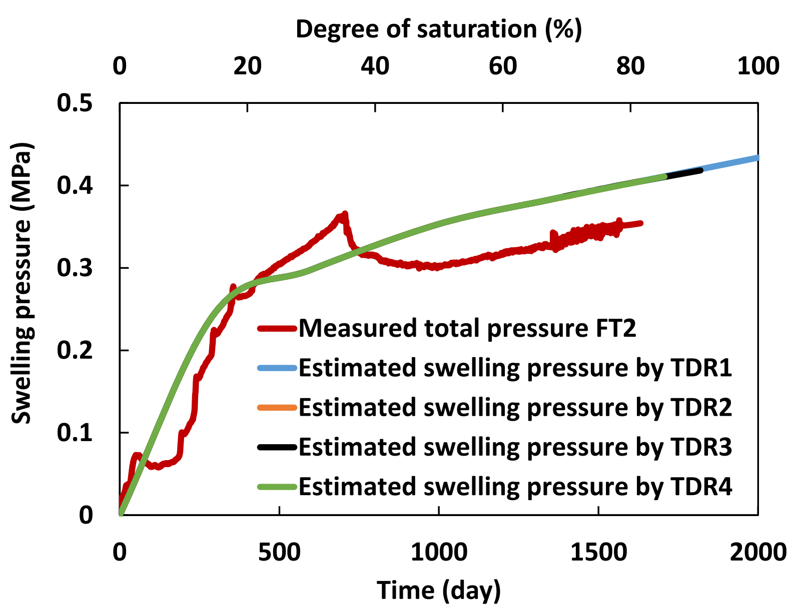

Figure 6-13. A comparison between predicted swelling pressure and measured total pressure

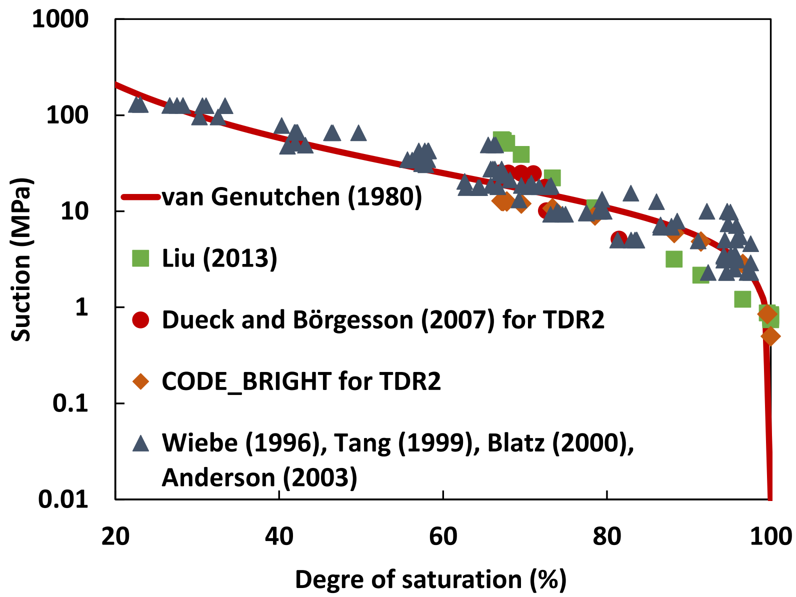

Figure 6-14. Estimated retention capacity for the clay seal compared with the measured data

CHAPTER 7

SENSITIVITY ANALYSIS OF H-M MODEL PARAMETERS

7.1. Introduction

Performing an analysis of the effect of critical Hydraulic-Mechanical (H-M) parameters and assessing the results can provide useful information with regard to the interplay of the various phenomena. Many numerical studies have used a set of H-M parameters estimated from laboratory test data or literature reviews, and assumed that these parameters were the most representative and the best to describe behaviour of unsaturated sealing materials. However, studies on sensitivity analysis of H-M model parameters have been limited.

This sensitivity analysis focuses on assessing effects of variations of H-M parameters on evolution of hydraulic-mechanical behaviour of the sealing components. Several sets of hydraulic and mechanical parameters of bentonite were determined using available laboratory test data obtained from extensive studies conducted at the University of Manitoba from the 1980's to 2006. From these different sets of the H-M parameters, a series of numerical modelling exercises was performed. The numerical results were compared to each other in terms of changes in suction, degree of saturation and hydration time of the sealing components.

This section presents (1) a sensitivity analysis of the clay seal's hydraulic (water retention) parameters and BBM mechanical parameters, (2) effects of the desaturation of the rock adjacent to the clay seal on the hydration process of the clay, and (3) effects of variations of the hydraulic conductivity of FZ2 on the hydration times of the clay seal.

7.2. Sensitivity Analysis of Hydraulic Parameters of the Clay Seal

7.2.1. Methods Used to Determine Water Retention Parameters of the Clay Seal

A sensitivity analysis of water retention parameters of the clay seal was conducted to examine the effects of changes in water retention parameters on the hydraulic behaviour of the clay. The water retention parameters were determined using different methods.

In using van Genuchten's model (van Genuchten 1980), two parameters, an air entry pressure (P_0) and a material parameter (β_1) are the key variables that affect the water retention behaviour of the clay. An air entry pressure (P_0) was defined by Corey (1977) and Fredlund and Rahardjo (1993) as the matric suction value that must be exceeded before air moves into the soil pores. This is the critical pressure head at which air starts to displace water in the soil pores. When the matric suction is greater than the air entry pressure then the soil starts to desaturate as illustrated in Figure 7-1 (Matsuoka 1999). The amount of water in soil decreases significantly with increasing suction in the transition stage. Eventually, as desaturation proceeds, a large increase in suction leads to a relatively small change in the water content and this is the residual stage where only absorbed water remains (Figure 7-1).

The first model (called Model 1) used the water retention parameters P_0 and β_1 estimated by matching two water retention curves. One water retention curve was generated using Wan's (1996) equation and the other curve was generated using van Genuchten's water retention model. As mentioned previously, Wan (1996) assessed a relationship between suction and gravimetric water content using psychrometer and filter paper tests. From this matching process, the parameters P_0 and β_1 were determined to be equal to 11 MPa and 0.48, respectively.

The second calibration method for the water retention parameters used extensive laboratory test data. Extensive studies on unsaturated bentonite-sand (50-50) buffer (BSB) materials were performed at the University of Manitoba and provided useful laboratory results for use in further calibration of parameters used in H-M constitutive models. Water retention trendlines were generated from distributions of each data set for drying cycles and wetting cycles, and then the van Genuchten's model was generated to match the trendlines by adjusting the water retention parameters P_0 and β_1.

Figure 7-2 shows Water Retention Curves (WRC), these are also known as Soil Water Characteristic Curves (SWCC) for laboratory test data of BSB materials obtained from Wiebe (1996), Tang (1999), Blatz (2000), Anderson (2003) and Siemens (2006). As clearly seen in Figure 7-2, and as expected, there is hysteretic behaviour in the WRC with respect to drying and wetting cycles. This hysteretic behaviour has been attributed to several mechanisms that act on both macro- and micro-structures (Lu and Likos 2004). Seiphoori et al. (2014) assessed the water retention behaviour of compacted MX-80 granular bentonite and found that a clear transition from a double-structured to a single-structured fabric, followed by a permanent change of the microfabric, was found after the first wetting of this clay. This microstructural evolution can result in the change in the water retention properties and consequently affects the macroscopic response of the bentonite in terms of water retention behaviour.

This hysteretic behaviour is one of the challenges in calibrating parameters for hydraulic constitutive models. To assess the hysteretic effect of the clay on its hydraulic behaviour, two sets of the water retention parameters of P_0 and β_1 were determined for each cycle. Figure 7-3(a) presents laboratory results obtained from shrinkage tests for drying cycles. An exponential best-fit trendline for this data was created based on the laboratory results and it generated a plot of suction versus degree of saturation (Figure 7-3(a)). The van Genuchten's water retention model generated a second trendline as shown in Figure 7-3(b). The van Genuchten's model trendline was then matched to the first trendline by adjusting the water retention parameters P_0 and β_1. This matching process utilized a built-in function, 'Solver' in MS-excel. This function allowed for defining the best-fit parameters through the matching process. For drying cycles the parameters of P_0 and β_1 were determined to be equal to 8.0 MPa and 0.28, respectively.

For wetting cycles, the infiltration test results obtained by Villar (2002) and Siemens (2006) were used. Siemens (2006) conducted infiltration tests on unsaturated BSB using a triaxial apparatus with controlled suction. All specimens were compacted to a target dry density of 1.67 Mg/m^3 with a gravimetric water content of 19.4%. Villar (2002) carried out infiltration tests on unsaturated bentonite using modified oedometric cells with controlled suction. These specimens were compacted to an initial dry density ranging from 1.60 Mg/m^3 to 1.70 Mg/m^3. The bentonite used by Villar (2002) was the Ca-dominated bentonite used for the Full Scale Engineered Barrier Experiment (FEBEX), which was performed at Grimsel underground facility in Switzerland.

The same matching process that was described previously for drying was then conducted for the wetting cycles. The infiltration test data generated a trendline and van Genuchten's model generated a set of data points in a plot of suction versus degree of saturation as shown in Figures 7-4(a) and 7-4(b). The same matching process was conducted for these two lines and determined the parameters of P_0 and β_1 to be equal to 3.1 MPa and 0.43, respectively for wetting cycles.

Table 7-1 summarizes values determined for the water retention parameters of P_0 and β_1. Note that Model 1, shown as M1 in following figures, used the parameters, P_0 and β_1 determined from both Wan's and van Genucheten's equations. Model 2 used the water retention parameters determined for drying cycles and Model 3 used the parameters for wetting cycles. In addition, Model 4 with P_0 = 11 MPa and β_1 = 0.28 was added to examine effects of changing the parameter value of either P_0 or β_1 on the clay's hydraulic behaviour.

7.2.2. Effects of Changes in Water Retention Parameters of P_0 and β_1

Coupled H-M modelling was conducted using different water retention parameters P_0 and β_1 determined, while keeping mechanical parameters unchanged. Numerical results were generated for locations taken vertically at the top, bottom and mid-height of the clay and horizontally at the centre (x = 0 m), 1 m from the centre (x = 1 m) and the edge of the clay (x = 2.5 m). The results were compared in terms of changes in suction and in degree of saturation with time.

Comparison of results of Model 1, Model 2 and Model 3 at the bottom of the clay

Figure 7-5 shows comparisons of the results obtained from three models (Model 1 (M1), Model 2 (M2) for drying, and Model 3 (M3) for wetting) in a plot of suction versus time at the bottom of the clay (y = 0.1 m). The results of Model 3 for wetting cycles show much longer time to reach zero suction in the clay (i.e., full saturation) than the other models for drying cycles (Model 1 and Model 2). For instance, at the centre of the clay (x = 0 m) (Figure 7-5(a)), zero-suction times for Model 2 and Model 3 are approximately 6400 days and 18400 days, respectively. It means that the full saturation time using the parameters for drying cycles is almost three times quicker than that using the parameters for wetting cycles. This comparison clearly demonstrates the effect of hysteretic behaviour of the clay on its water uptake times.

The water retention parameters used for Model 1 and Model 2 were estimated using different laboratory data for drying cycles. Model 2 shows slightly faster decreases in suction than Model 1. Suction starts decreasing after 100 days in the outer region (x = 2.5 m) (Figure 7-5(c)) and much later in the centre region (x = 0 m) after 400 days (Figure 7-5(a)). The time to reach zero suction in the center region is approximately 7100 days for Model 1 whereas approximately 6400 days for Model 2. This comparison indicates that different water retention parameters can be determined from the same clay material and consequently result in different predictions of the clay's hydraulic behaviour. For the reason, selection of the water retention parameters is fundamentally important for numerical modelling and sensitivity analysis of the parameters is required to obtain qualitative and representative results.

The numerical predictions of all models are also compared with field psychrometer readings (i.e., changes in suction). Figure 7-5(c) presents the psychrometer readings (psy 02) compared with the numerical results at the edge of the clay (x = 2.5 m). This psychrometer sensor (psy 02) had measured changes in suction for approximately 170 days and its final suction value was 8.6 MPa. The curve of Model 3 is close to the field readings until 500 days; however, it shows much longer time for zero suction than that of Model 1 and Model 2. The numerical prediction of Model 2 is closer to the field readings than that of Model 1. This indicates that further parameter calibration can improve prediction of hydraulic behaviour of the clay. This improvement in prediction is clearly observed in the other regions.

<u>Comparison of results of Model 1, Model 2 and Model 3 at the top and mid-height of the clay</u>

Similar trends of changes in suction are observed at the mid-height and top of the clay (Figure 7-6 and Figure 7-7). The numerical results obtained from Model 1 and Model 2 are compared with the measured psychrometer readings (i.e., psy10 and psy 14) that were located at 1.25 m from the centre of the clay and in the mid-height and top regions, respectively. Figure 7-6(b) and Figure 7-7(b) clearly demonstrate that Model 2 with further calibration of the water retention parameters P_0 and β_1 provides better prediction of the field readings, indicating good agreement with the measured psychrometer readings (psy10 and psy14), compared to the other models. Based on these comparisons, the water retention parameters used for Model 2 are more representative of the hydraulic behaviour of the clay.

In Figure 7-6(c), at the mid-height (y = 3 m) and the edge of the clay (x = 2.5 m) Model 1 shows a slower decrease in suction than Model 2 and Model 3 as hydration progresses, and the maximum suction difference is approximately 0.7 MPa at 200 days. Numerical patterns of the hydraulic behaviour in this mid-height region are different from what was observed in the other regions (top in Figure 7-7 and bottom in Figure 7-5). This may be due to the direct effect of groundwater flow from FZ2 in the outer region (x = 2.5 m). In addition, the suction curves of Model 2 and Model 3 are very similar during the hydration process. This means that hysteresis does not seem to be influencing the hydraulic behaviour of the clay in the outer region being directly affected by groundwater flow from FZ2. The time for reaching zero suction at the centre of the clay (x = 0 m) is approximately 7000 days for M1, 6300 days for M2, and 15200 days for M3.

In Figures 7-5, 7-6 and 7-7, the results obtained from Model 1, Model 2 and Model 3 have been compared with regard to changes in suction with time. These comparisons confirm that the hysteresis from drying and wetting cycles affects evolution of the hydraulic behaviour of the clay, except for the outer region where there appears to be a direct effect of groundwater inflow from FZ2. Further calibration made for water retention parameters improves predictions of the hydraulic behaviour of the clay. In addition, different methods for determining the water retention parameters of P_0.and β_1 can result in different predictions of the hydraulic behaviour of the clay seal. It should be pointed out that these comparisons are only valid for the hydraulic boundary conditions and the specific laws of variation of hydraulic conductivity with suction and retention curves used in the analysis.

Effects of changes in the material parameter β_1 (Model 1 versus Model 4)

Effects of the individual parameter of P_0 and β_1 of the clay seal were assessed as part of this sensitivity study. To examine effects of changes in the parameter of β_1 on the hydration mechanism of the clay seal, Model 4 with the water retention parameters of P_0 = 11 MPa and β_1 = 0.28 was simulated and its results were then compared with the results of Model 1 (P_0 = 11 MPa and β_1 = 0.48).

Figure 7-8 shows comparison of the results between Model 1 and Model 4 at three vertical and horizontal locations. Based on the same air entry pressure (P_0) of 11.0 MPa, the curves of Model 4 with a lower β_1 value show faster decreases in suction during hydration progress than those of Model 1. The time to reach zero suction for Model 4 is approximately 5100 days at the mid-height (y = 3 m) and the centre of the clay (x = 0 m) (Figure 7-8(b)), which is much faster than 7000 days for Model 1. At the top and bottom of the clay, numerical prediction of Model 4 shows a faster decrease in suction after 100 days (Figure 7-8(a) and Figure 7-8(c)). These comparisons clearly demonstrate the sensitivity of the hydraulic behaviour of the clay to the material parameter β_1.

At the bottom of the clay (y = 0 m), the predicted curve of Model 4 becomes closer to the measured psychrometer readings (psy02); however, it still underestimates the readings (Figure 7-8(c)). The predicted curves of Model 4 at the top and mid-height of the clay capture the field readings (psy10 and psy14) reasonably well, compared to those of Model 1 (Figures 7-8(a) and 7-8(b)).

Effects of changes in air entry pressure P_0 (Model 2 versus Model 4)

Influence of varying only an air entry pressure (P_0) on hydraulic behaviour of the clay seal was assessed, while keeping the material parameter (β_1) of 0.28 constant. The numerical results obtained from Model 2 and Model 4 were compared and presented in this section. The air entry pressure values of 8.0 MPa and 11.0 MPa were applied for Model 2 and Model 4, respectively.

Figures 7-9 to 7-11 show plots of suction versus time for the numerical results of Model 2 and Model 4. In all three vertical and all the horizontal locations, Model 4 with a higher air entry pressure of 11 MPa shows faster decreases in suction with time than Model 2 where the value of 8 MPa was used. For example, the times to reach zero suction at the mid-height (y = 3 m) and the centre of the clay (x = 0 m) for Model 2 and Model 4 are approximately 6300 days and 5100 days, respectively. This simple comparison indicates that the time for zero suction is reduced by 1200 days if the air entry pressure increases from 8 MPa to 11 MPa.

Many studies have examined the relationship between air entry pressure and suction (Fredlund et al. 1994, Gens et al. 1998, Iravanian and Bilsel 2009, Fredlund and Houston 2013). These studies focused on the effects of air entry pressure values on water retention curves in unsaturated soils. They reported that a decrease in air entry pressure of unsaturated soil increased the rate of desaturation and consequently decreased the unsaturated hydraulic conductivity. The numerical results in this thesis confirm the relationship between air entry pressure and suction provided by the experimental studies.

Figure 7-10(c) shows almost identical curves of Model 2 and Model 4 at the mid-height (y = 3 m) and the edge of the clay (x = 2.5 m). This simple comparison indicates that changes in the air entry pressure are not likely to affect the hydraulic behaviour of the clay in this edge region where groundwater flow from FZ2 applies directly. The results of Model 4 show a slight improvement in matching with the measured psychrometer readings, compared to the results of Model 2.

Predictions of degree of saturation of the clay compared with field TDR readings

As part of the sensitivity analysis of various water retention parameters P_0 and β_1, the results of all four numerical Models are compared with the field TDR readings in a plot of degree of saturation with time. It is assumed that the TDR readings measured have been representative of water uptake evolution of the clay component, and therefore comparisons of the numerical results with the TDR readings can show more clearly the effects of various water retention parameters on the water uptake evolution of the clay than comparisons made with psychrometer readings.

Figure 7-12 shows changes in degree of saturation with time for all four models, compared with the field readings of TDR4 that was installed in the centre region (x = 0 m) and 4 m from the bottom of the clay (y = 4 m). As seen in the figure, the curve of Model 4 (Figure 7-12(d)) shows the closest match with the field readings in this region, compared to Model 1 and Model 2. Note that these three models (Model 1, Model 2 and Model 4) were simulated using different water retention parameters determined for drying cycles. A comparison of the numerical predictions between Model 1 and Model 4 clearly demonstrates the effect of changing the material parameter of β_1 (i.e., 0.48 for Model 1 and 0.28 for Model 4). As observed in the comparison with the measured psychrometer data, a lower material parameter (β_1) reduces hydration time of the clay. The hydration times estimated for full saturation at the centre of the clay (x = 0 m) are approximately 20 years and 14 years for Model 1 and Model 4, respectively.

Figure 7-12 (b) and Figure 7-12 (c) indicate the effect of hysteresis of the clay. Model 3 for wetting cycles significantly underestimates the measure TDR readings. For example, the curve of Model

3 in the centre region (x = 0 m) indicates a much longer hydration time of approximately 55 years to be fully saturated than Model 2 for about 17 years. This difference is so significant that the hysteresis effect should be taken in account for selection of the water retention parameters of the clay-based sealing materials.

Figure 7-12(b) and Figure 7-12(d) show a comparison of the curves between Model 2 and Model 4, indicating the effect of changing the air entry pressure on the hydraulic behaviour of the clay. A higher air entry pressure value makes the prediction curves move more closely to the measured TDR data. The time for full saturation at the centre of the clay (x = 0 m) is approximately 17 years for Model 2 and 14 years of Model 4. The increase of 3 MPa in air entry pressure shortens hydration time by about 3 years.

In the mid-height region of the clay (y = 3 m), Model 1 and Model 2 show good agreement with the measured TDR data (Figures 7-13(a) and 7-13(b)) although numerical prediction for the models underestimates the evolution of degree of saturation for the initial period of water uptake. By contrast, the results of Model 4 overestimate the TDR data for times 1 year up to 6 years (Figure 7-13(d)). However, considering the rapid increase in degree of saturation observed in both TDR2 and TDR3 sensors during 2014-2015, the predicted curves for Model 4 will likely capture further evolutionary movement of water uptake in the regions.

The results of Model 3 using the water retention parameters for wetting cycles indicate much slower hydration processes and significantly underestimate the measured TDR data. In comparing Model 4 with Model 1 and Model 2, an increase of air entry pressure from 8 MPa to

11 MPa and a decrease of a material parameter β_1 from 0.48 to 0.28 result in shorter hydration times for the clay.

Surprisingly the lowermost TDR #1 sensor shows a very rapid increase in degree of saturation during the period of 2014-2015 and full saturation in the centre region (x = 0 m) and 2 m from the bottom of the clay (y = 2 m) (Figure 7-14). Numerical prediction for all models in this region does not capture the measured TDR#1 data well and considerably overestimates.

The times for reaching full saturation in this region are approximately 13 years for Model 4 whereas approximately 6 years for the TDR #1 sensor. The possible explanation for this considerable discrepancy is that the numerical model simplifies the groundwater flow system surrounding the clay seal, while in real shaft seal, groundwater flows radially toward the perimeter of the clay seal. In addition, pore water pressure has been developed from the bottom of the clay seal due to shaft flooding since the shaft seal components were installed in 2009. This gradual increase in pore water pressure can make the hydration process of the clay seal in this lowermost region quicker. Despite underestimation of the measured TDR#1 data, Model 2 and Model 4 provide improved predictions of the evolution of water uptake.

Relationship between hydration time and air entry pressure P_0 (Model 2, Model 4, Model 4-1 and Model 4-2)

Two additional numerical models (called Model 4-1 and Model 4-2) with higher defined air entry pressures of 16 MPa and 25 MPa were also simulated. These additional numerical simulations are an extension of the analysis focusing on the relationship between the air entry pressure and suction as discussed in the previous section. As mentioned previously, the numerical results have confirmed that an increase in air entry pressure increases the hydration rate of the clay and consequently reduces the time required for full saturation to be achieved.

Results of the two simulations (i.e., Model 4-1 (M4-1) and Model 4-2 (M4-2)) are compared with the results of Model 2 and Model 4 to examine the relationship between the hydration time and the air entry pressure. Air entry pressures of 16 MPa and 25 MPa were applied for Model 4-1 and Model 4-2, respectively while remaining the material parameter (β_1) value of 0.28 unchanged. The maximum air entry pressure (value) of 25 MPa was set up because Villar and Romero (2012) determined the water retention curves of Opalinus clay samples under wetting and drying paths and obtained the maximum air entry value of 28 MPa. The Opalinus clay was taken from the Opalinus claystone in Switzerland, which is considered as potential host rock in the Swiss radioactive waste disposal concept. The clay has up to 80% clay minerals of mixed layers of swelling illite and smectite.

Figure 7-15 shows a plot of suction versus time for all models (Model 2 (M2), Model 4 (M4), Model 4-1 (M4-1) and Model 4-2 (M4-2)). These curves are generated from the data point taken at the mid-height (y = 3 m) and the centre of the clay (x = 0 m). The numerical predictions clearly demonstrate that the hydration rate increases with increasing the air entry pressure of the clay. Hydration times for zero suction for all models are summarized in Table 7-2. The increase in air entry pressure from 8 MPa (Model 2) to 25 MPa (Model 4-2) reduces hydration time by about 3360 days (approximately 9 years) at the mid-height and the centre of the clay. The plot of the hydration time versus the air entry pressure indicates a curved relationship that can be approximated by a linear relationship as illustrated in Figure 7-16. Since expected hydration time of the clay seal is one of the main concerns during the initial design stage of a repository or experiment, this relationship between hydration time and air entry pressure can be a useful tool to estimate hydration time of the clay-based sealing material under similar hydrogeological conditions.

Based on the numerical results of this sensitivity study, the hydraulic behaviour of the clay seal is quite sensitive to variations of the water retention parameters P_0 and β_1. The hysteresis of the clay also affects the hydration process of the clay. The numerical simulations using the calibrated parameters improve predictions of hydraulic behaviour of the clay, showing reasonably good agreement with the measured data. Therefore, the numerical results confirm the first hypothesis listed at the beginning of the thesis that is "Hydraulic-mechanical (H-M) parameters calibrated from laboratory tests can be used to improve prediction of the coupled H-M behaviour of the clay".

7.3. Sensitivity Analysis of Mechanical Parameters of the Clay Seal

Effects of variations of mechanical parameters on mechanical behaviour of the clay seal were examined as part of the sensitivity study. In the Basic Barcelona Model (BBM) mechanical parameters for numerical modelling have been calibrated using some representative laboratory test data. This section describes methods used to calibrate the BBM mechanical parameters and presents the effects of variations of the BBM parameters on the mechanical behaviour of the clay seal.

7.3.1. Methods Used to Determine BBM Mechanical Parameters of the Clay Seal

As mentioned previously, extensive studies focusing on the H-M behaviour of the unsaturated BSM were conducted at the University of Manitoba (Tang 1999, Blatz 2000, Anderson 2003, Siemens 2006). Tang (1999), Blatz (2000) and Anderson (2003) conducted shrinkage tests to define the relationship between suction (s) and degree of saturation (S_w) (i.e., SWCC) and the suction (s)-volume (v) relationship. Initially, the BSM specimens were compacted to a target dry density of 1.67 Mg/m^3 and target gravimetric water content of 18.75%. In the shrinkage tests, the mass and dimensions of all specimens were recorded before the specimens were placed in sealed glass desiccators that contained ionic solutions. The sealed glass desiccators provided the relative humidity (suction) environments needed to generate the desired suction conditions and induce drying of the specimens. During drying, water was drawn from the specimens and into the vapour phase and the vapour was then transferred to the ionic solution. The concentration of the solution decreased with increasing water content of the ionic solution and therefore gradually reduced the applied suction in the system. During the shrinkage tests by keeping the mean stress (p) value of zero unchanged, the degree of saturation decreased with increasing suction. The target suctions were in the range of ~5 MPa to 125 MPa.

Figure 7-17 illustrates a stress path as a plot of mean stress versus suction. The drying process (path A-B) was applied to the specimens using triaxial testing apparatus before isotropic loading and unloading (path B-C-D) (Blatz 2000). During these loading and unloading processes, total mass and gravimetric water content of the specimens were constant. Blatz (2000) measured changes in suction during isotropic loading using psychrometers embedded into the specimens, and reported the relationship between changes both in suction and in mean stress. The ratio of changes in suction to changes in mean stress (Δs / Δp) was equal to be -0.83. Anderson (2003) and Priyanto (2007) used this relationship to define suction during isotropic compression.

Figure 7-18 illustrates results of shrinkage tests in a plot of suction (s) versus volume (v). The results indicate that increases in suction up to approximately 40 MPa result in decreases in volume, however for suction greater than 40 MPa, the slope (i.e., λ_s) is close to zero, which indicates little volume change. This result is different from the relationship between suction and volume in the BBM, which indicates that volume decreases with increasing suction (Alonso et al. 1990) as shown in Figure 2-7(d) in Section 2.6. Despite this difference, the BBM can still be applied in order to define mechanical parameters. The stiffness parameter (κ_s) due to changes in suction can be determined from the slope of ln(s) vs v and it is equal to 0.056 as shown in Figure 7-18.

This calibration of the BBM mechanical parameters combined values of an elastic stiffness parameter (κ) and a stiffness parameter related to suction ($\lambda(s)$). These parameters (κ) and $\lambda(s)$ were determined from 30 BSM specimens provided by Anderson (2003) and 8 BSM specimens (JB104 – JB111) provided by Blatz (2000). Anderson (2003) conducted isotropic loading tests on 30 BSM specimens (15 Wyoming and 15 Avonlea bentonite) with different suction levels and measured the relationships between mean stress (p) and volume (v). The laboratory data allowed for defining the relationship between suction (s) and volume (v) using the relationship between changes in suction and mean stress (i.e., Δs / Δp = -0.83).

The result of each specimen plotted in the mean stress (p) - volume (v) space allowed for defining a single set of κ and $\lambda(s)$ values (Priyanto 2007). For example, Figure 7-19 shows a loading and unloading path of the specimen DA-027 in the p-v space (Anderson 2003). The intersection between these two log-linear lines (i.e., B-p_0 and p_0-C) is equal to the preconsolidation pressure (p_o) at the corresponding suction.

Changes in total volume during isotropic compression is the sum of volume changes due to changes in both mean stress (p) and suction (s). Within the elastic range ($p < p_o$ and $s < s_0$), total volume is estimated using the following equation:

$$v = v_{in} + \kappa \ln\left(\frac{p}{p_{in}}\right) + \kappa_s \ln\left(\frac{s}{s_{in} + p_{at}}\right) \tag{7-1}$$

where p_{in},v_{in}, s_{in} represent the initial state and s_0 is the initial SI-yield line. For outside elastic range ($p > p_o$ and $s < s_0$) the total volume is estimated using the following equation:

$$v = v_{in} + \kappa \ln\left(\frac{p_0}{p_{in}}\right) + \lambda(s) \ln\left(\frac{p_0}{p_{in}}\right) + \kappa_s \ln\left(\frac{s}{s_{in} + p_{at}}\right) \tag{7-2}$$

When $s > s_0$, κ_s in Equations 7-1 and 7-2 are substituted with λ_s. Parameters κ_s and λ_s were determined from the shrinkage test results as shown in Figure 7-18 where $\kappa_s = 0.056$ and $\lambda_s \approx 0$, while values of the preconsolidation pressure (p_o) were determined graphically for individual specimens (Figure 7-19).

Substitutions of these known parameters (κ_s, λ_s and p_0) into Equations 7-1 and 7-2 meant that two unknown parameters κ and $\lambda(s)$ still remained. These two parameters (κ and $\lambda(s)$) could be determined by fitting the Equations 7-1 and 7-2 to the laboratory test results. As shown in Figure 7-19, a set of fitting data points (i.e., B, p_0 and C) was determined based on the loading-unloading data and a fitting line (B-p_0-C) was generated using the fitting data points (called 'fitting' in the figure). Using Equations 7-1 and 7-2 generated two linear lines based on the κ_s value of 0.056 (called 'simulation' in the figure). These simulation lines were matched to the fitting line (B-p_0-C) by changing the two parameters κ and $\lambda(s)$. Suction values were generated using the relationship between mean stress and suction ($\Delta s / \Delta p = -0.83$). This process was completed for each test using 'Solver' function built in MS-Excel to find the best match between the fitting and simulation lines.

Figure 7-20 and Figure 7-21 show distributions of the parameters κ and $\lambda(s)$ respectively plotted versus suction. The maximum, average and minimum values of each parameter are obtained from the distributions. These values of the parameters κ are 0.019, 0.010, and 0.001 (Figure 7-20), and 0.172, 0.075, 0.026 for the parameter $\lambda(s)$ (Figure 7-21), respectively. The maximum, average and minimum values of the parameter κ were then applied into the BBM equations to determine the remaining unknown parameters such as r, β and $\lambda(0)$ and p^c.

The calibration process for these unknown parameters (r, β and $\lambda(0)$ and p^c) required two relationships that needed to be simultaneously considered. One was the relationship between preconsolidation pressure and suction (p_0 - s) and the other one was the relationship between the stiffness parameter and suction ($\lambda(s)$ - s). These relationships of p_0 - s and $\lambda(s)$ - s were previously determined at the time when the parameters κ_s and λ_s were determined from the shrinkage test results. Figure 7-22 and Figure 7-23 show distributions of the parameters p_0 and

$\lambda(s)$ plotted versus suction. Based on the distributions of each parameter p_0 and $\lambda(s)$, a trend line (dashed green line) was generated as shown in Figure 7-22 and Figure 7-23. A BBM line was generated using BBM equations and then matched to the trend line by adjusting the four unknown parameters (i.e., r, β and $\lambda(0)$ and p^c). The preconsolidation pressure (p_0*) value of 1.0 MPa at saturated conditions was used throughout the process (Blatz and Graham 2003). The maximum, average and minimum values of the parameter κ produced three sets of the BBM mechanical parameters. Figures 7-22 and 7-23 show the matching lines between the two relationships for the average κ value of 0.010. Again this process was completed using 'Solver' function built in MS-Excel to find the best match between the trend line and BBM line.

Table 7-3 summarizes three sets of BBM mechanical parameters determined from the calibration processes. The BBM mechanical parameters determined for Model 2, Model 3 and Model 4 correspond to the minimum, average and maximum values of κ, which are 0.001, 0.010 and 0.019, respectively (see Figure 7-20). Table 7-3 also presents BBM mechanical parameters for Model 1 and details of the method to determine the parameters for Model 1 were described in Section 5.2.3.

The method of determining the BBM mechanical parameters for Model 1 is different from the method used for the other models (Model 2, Model 3 and Model 4). The method for Model 1 used laboratory test results to determine individual BBM mechanical parameters. For example, the stiffness parameter $\lambda(0)$ for changes in net mean stress at saturation and the elastic stiffness parameter (κ) were estimated based on laboratory test results reported by Lingnau et al. (1995). The rest of the parameters r, β and p^c were determined using three values of the preconsolidation pressure at varying suction, which were measured by Blatz and Graham (2003). The stiffness parameters κ_s and λ_s for changes in suction were estimated from values reported by Blatz and Graham (2003) and Volckaert et al. (1996), respectively. By contrast, the method used to determine BBM mechanical parameters for Model 2, Model 3 and Model 4 considered distribution patterns of laboratory data for the key parameters. The distribution patterns were then matched with the simulated BBM lines to obtain the rest of the mechanical parameters.

As clearly seen in Table 7-3, different calibration methods conducted using the same BSM formulation generate a wide range of the BBM mechanical parameters. This indicates that different model users can select different parameter sets for the same material, and therefore sensitivity analysis of H-M parameters and verification of numerical predictions should be performed to provide more reliable results.

Since these mechanical parameters are simultaneously computed in the BBM, it is difficult to examine which parameter is more sensitive to the mechanical behaviour. For this reason, this sensitivity analysis of the BBM mechanical parameters focuses on identifying differences in the mechanical behaviour of the clay seal by applying various sets of the mechanical parameters. Note that in this sensitivity analysis the hydraulic parameters used in Model 1 remain unchanged.

7.3.2. Effects of Changes in BBM Mechanical Parameters

This section presents predictions of total stresses and displacements for all models at the mid-height of the clay (y = 3 m) and 1.25 m from the centre of the clay (x = 1.25 m). Figure 7-24 and Figure 7-25 show the distribution of horizontal (radial) stresses and horizontal (radial) displacements for all models at the mid-height of the clay (y = 3 m) along its horizontal section. All models show similar distribution patterns of horizontal (radial) stresses. The horizontal compressive stresses in the clay region increase with time as the clay becomes more hydrated. These compressive horizontal stresses can be attributed to the swelling of the clay generated in this region causing compression of the clay next to it (under condition where the clay is rigidly confined by the concrete components and host rock).

Figure 7-24(a) shows a comparison of horizontal stresses for all models at 1.25 m from the centre of the clay. This figure indicates that numerical predictions of horizontal stress for Model 2, Model 3 and Model 4 are almost identical, which means that the horizontal stress of the clay seal is not significantly sensitive within the range of variations of the mechanical parameters. All four models show a slight expansion along the horizontal section at earlier stages of system wetting and then an increase in compressive horizontal stress with time after 50 days (Figures 7-24(b), 7-24(c) and 7-24(d)). Again this phenomenon can be attributable to the swelling of the clay generated in the region under the confined conditions of the ESP. Model 1 shows the greatest compressive horizontal stress of approximately 2.5 MPa and the other models show 2.0 MPa (Figure 7-24(a)).

All four models show a similar pattern of predicted horizontal (radial) displacements (Figure 7-25). Numerical predictions indicate that the maximum horizontal displacement occurs at 1.8 m from the centre of the clay. The displacement pattern can be attributed to the source of groundwater flow from FZ2 and the restraint of the rock wall of the shaft. The outer regions of the clay became hydrated more rapidly than the other regions and started swelling, reducing the local dry density. In turn, the adjacent inner regions will subsequently hydrate and start swelling and compressing the outer regions, resulting in maximum displacements located close to the outer region. Similar patterns of total stresses and displacements were reported by several numerical studies (Gens et al. 1998, Chandler 2000, Thomas et al. 2002, Guo and Dixon 2005). Chandler (2000), Guo and Dixon (2005) and Thomas et al. (2002) performed coupled T-H-M modelling for the full-scale Tunnel Sealing Experiment (TSX) in Canada using FLAC (Itasca 2000), CODE_BRIGHT (Vaunat and Olivella 2002) and COMPASS (Thomas et al. 1994), respectively. The first computer program was a finite difference method program and the other programs were finite element method programs. Gens et al. (1998) conducted coupled T-H-M modelling for a full-scale heating test (FEBEX) of an engineered barrier using CODE_BRIGHT. Despite different schemes of their numerical modelling, they focused on coupled hydro-mechanical interactions between bentonite-sand mixtures and the host rock and reported similar patterns of mechanical behaviour.

The results of Model 1 (Figure 7-25(b)) show greater horizontal displacements at each time step than the other models and indicate the maximum horizontal displacement of 8.5 mm, while the other models show approximately 6 mm in the same region (Figures 7-25(c), 7-25(d) and 7-25(e)). Figure 7-25(a) shows a comparison of values of the horizontal displacement at 1.25 m from the centre of the clay for all models. Numerical predictions of Model 2, Model 3 and Model 4 indicate little difference in the distribution of the horizontal displacement, which is similar to what was observed in the comparison of the horizontal stresses. Based on the numerical predictions in this region, it is likely that both horizontal stress and displacement of the clay seal is not significantly sensitive to changes in the fitting parameters r, β and $\lambda(0)$, p^c, and κ within the range of their variations.

All four Models show similar distributions of the predicted vertical stress and displacement at the mid-height of the clay along its horizontal section (Figures 7-26 and 7-27). The maximum values of the compressive vertical stress are approximately 2.5 MPa for Model 1 and approximately 2.0 MPa for the other models. The centre region for Model 1 and Model 2 shows a slightly greater vertical compression observed than the outer region after 13900 days (Figures 7-26(b) and 7-26(c)), however the difference is very small and is not observed in Model 3 and Model 4 (Figures 7-26(d) and 7-26(e)).

For predictions of vertical displacement in this region, all models show higher expansion in the centre regions and higher compression in the outer regions after 4900 days (Figures 7-27(b), 7-27(c), 7-27(d) and 7-27(e)). The models also indicate that the inner region starts to expand after 4900 days until 13900 days and compression starts after 13900 days.

Figure 7-27(a) clearly shows the gradual transition from expansion to compression for all models. Simulated values of the vertical displacement at 1.25 m from the centre of the clay are plotted with each time step in Figure 7-27(a). Similar to comparisons of the predicted horizontal displacements, variations of the mechanical parameters result in little difference in the vertical displacement for Model 2, Model 3 and Model 4.

Figure 7-28 and Figure 7-29 show distributions of simulated horizontal stresses and horizontal displacements at 1.25 m from the centre of the clay along its vertical section. Figure 7-30 and

Figure 7-31 show distributions of simulated vertical stresses and vertical displacements in the same region. Values of the horizontal (radial) and vertical stresses in this region are similar to those observed in the mid-height region, which are about 2.5 MPa for Model 1 and 2.0 MPa for the other models (Figure 7-28 and Figure 7-30). The horizontal and vertical stresses at 1.25 m from the centre of the clay along its vertical section are plotted with each time step for all models as shown in Figure 7-28(a) and Figure 7-30(a) to compare the evolution of the horizontal and vertical stresses.

Patterns of horizontal stress are shown for all models in Figures 7-28(b), 7-28(c), 7-28(d) and 7-28(e). They can be attributed to the direct influence of groundwater flow from FZ2, which is vertically located from 1 to 5 m, depending on location along the shaft wall (FZ intersects at an angle of approximately 20-25 degrees). As seen in these figures, numerical prediction for all four models indicates a very limited amount of expansion at the earliest stage and then compression after 50 days. They also show more expansion in the lowermost region of the clay than at the top region. This can be due to higher pore water pressure applied at the bottom, which can accelerate the hydration rate in the lowermost region.

Simulated horizontal (radial) displacements for all four models appear to be similar, indicating that the horizontal displacements are developed along the region where groundwater directly flows into (Figure 7-29). The maximum horizontal displacement is approximately 8 mm for Model 1 and 4 mm for the other models at the mid-height of the clay (y = 3 m). The predicted curves of all models show compressive horizontal displacements developed along the location of the groundwater flow applied (Figures 7-29(b), 7-29(c), 7-29(d) and 7-29(e)). The difference between

Model 1 and the other models is a slight compression observed in the bottom region for Model 1 and in the upper region for the other models.

All three models (Model 2, Model 3 and Model 4) show similar predictions of the horizontal stress and displacement at 1.25 m from the centre of the clay along its vertical section. Again this indicates that changes in the mechanical parameters within this range are unlikely to significantly affect evolution of the horizontal stress and horizontal displacement.

Figures 7-31 shows a similar pattern of the vertical displacement in the region for all models, indicating the upwards movement above the mid-height and the downwards movement below the mid-height of the clay. The predicted vertical displacements clearly indicate that the clay in this region is moving toward equilibrium after 13900 days (~38 years), except for Model 1 showing after 4900 days (~13.5 years). Prediction curves from Model 1 and Model 4 show a more uniform distribution of the vertical displacement at 35900 days (98 years). In addition, the predicted vertical displacement in the bottom region show a more uniform distribution than in the top region. This could be attributed to the initial conditions of groundwater flow applied in the domain where a higher groundwater pressure was set up at the bottom of the shaft seal, resulting in an upward groundwater flow from the bottom to the top. This means that more groundwater was accessible at the bottom of the clay and hence faster hydration time.

Sensitivity analyses of the BBM mechanical parameters have been performed and the numerical results obtained from all four models are compared in order to examine the sensitivity of the mechanical performance of the clay seal the material parameters. Numerical prediction for all models shows similar patterns showing the development of compressive horizontal and vertical stresses. Evolution of the horizontal stress and horizontal displacement is strongly affected by the groundwater flow from FZ2 because they are developed along the contact where groundwater flow is applied. The numerical predictions of Model 2, Model 3 and Model 4 indicate that mechanical behaviour of the clay is not significantly sensitive to variations of the BBM mechanical parameters within the range of their variations. Numerical prediction of Model 1 shows higher values of vertical stress and vertical displacement than those of the other models. This difference implies that the parameter calibration using laboratory test data on the same clay material allows for determining various sets of the mechanical parameters and consequently predicting different mechanical behaviours for the clay seal. Therefore, sensitivity analysis of the parameters and validation of the predictions are required to improve the possibility to match field and modelled behaviour.

In summary, sensitivity analyses of both hydraulic and mechanical parameters have established that the numerical results obtained using hydraulic-mechanical parameters calibrated from laboratory tests can improve prediction of the coupled H-M behaviour of the clay seal. By varying of the water retention parameters P_0 and β_1, numerical predictions have clearly demonstrated (1) the effect of hysteretic behaviour of the clay on it water uptake times of the clay, (2) the relationship between hydration process times and the water retention parameters P_0 and β_1, and (3) improvement in predicting the hydraulic behaviour of the clay. On the other hand, the numerical predictions using calibrated BBM parameters indicate that mechanical behaviour of the clay seal is not significantly sensitive to variations of the BBM mechanical parameters within the range of their variations.

7.4. Effects of Rock Desaturation on Hydration Time of the Clay Seal

Model 1 used the air entry pressure P_0 of 0.7 MPa for the host rock and 11.0 MPa for the clay seal. This low air entry pressure may lead to a significant desaturation of the rock adjacent to the clay seal that controls many of the aspects of behaviour of the shaft sealing system. The consequence of applying the low air entry pressure of the rock may be the formation of an unsaturated barrier that delays hydration process of the clay seal. This section focuses on examining the direct effect of potential desaturation of the host rock adjacent to the clay seal (or Excavation Damaged Zone (EDZ)) on hydraulic behaviour of the shaft sealing components. In this analysis, changes of the rock's hydraulic conductivity with porosity were not considered.

The air entry pressure suggested by Gens et al. (1988) was 0.1 MPa for granite in the FEBEX site, however, Thomas et al. (2002) thought this was too low for the granite in AECL's URL and defined the air entry pressure of 0.7 MPa from a plot of intrinsic permeability against threshold pressure (or air entry pressure) based on the intrinsic permeability of the granite provided by Graham et al. (1997). As seen in Table 7-1, Model 1 used the air entry pressure P_0 of 0.7 MPa for the host rock and 11.0 MPa for the clay. The air entry pressure value of the host rock is much lower than that of the clay. As a result, numerical simulation can predict a significant desaturation expected in the rock region in the close vicinity of the clay due to the adoption of the water retention curve of the rock.

Several field experiments have observed desaturation of the rock adjacent to the clay-based shaft seal during the initial stages of system wetting (Pusch 1989, Gens et al. 1998, Chandler 2000, Bock 2001). They reported that desaturation of the rock in the region close to the clay could also be attributed to factors such as suction and swelling potential of the clay. Suction developed by the unsaturated clay can draw more water from the surrounding rock (EDZ) and the clay at the edge region can then swell and seal the pores and micro-cracks in the EDZ. The suction and swelling potential of the clay will result in accelerating desaturation of the rock in the region close to the clay with its associate decrease of hydraulic conductivity. However, examination of the direct effects of changes in air entry pressure of the rock on hydraulic behaviour of the shaft sealing components are not included in this numerical study.

Figure 7-32 illustrates predicted degrees of saturation at various times for Model 1. As expected, the lower air entry pressure of the host rock results in a dramatic desaturation of the rock adjacent to the clay. This desaturation of the rock continues to be evident for 4900 days and the rock in this region is therefore not fully saturated for the period.

Since desaturation of the host rock adjacent to the clay seal could affect the hydration process in the clay, a sensitivity analysis was performed using a water retention curve for the host rock with much higher air entry pressures up to 500 MPa. Figure 7-33 shows the various water retention curves applied in this sensitivity analysis.

Figure 7-34 compares predicted degrees of saturation at different time intervals (Figures 7-34(a) for 50 days, 7-34(b) for 2400 days, 7-34(c) for 4900 days and 7-34(d) for 7900 days) using various air entry pressure values. The numerical results clearly demonstrate the dramatic effects of variations of the air entry pressure of the rock on hydraulic behaviour of both the clay and the surrounding rock. As seen in Figures 7-34(a), 7-34(b) and 7-34(c), numerical prediction with an air entry pressure of 0.7 MPa clearly shows desaturation of the rock in the region close to the clay and this desaturation continues to be present for 4900 days. By contrast, for a rock with greater air entry pressures, ranging from 100 MPa to 500 MPa shows full saturation in the region throughout the hydration process. An increase in air entry pressure decreases a desaturation rate.

The desaturation of the rock in the immediately adjacent to the clay seal directly affects the clay's hydration rate. A higher desaturation rate (or lower air entry pressure) of the rock decreases the saturation rate of the clay seal and increases hydration (water uptake) time of the clay. The main reason can be the hydraulic barrier surrounding the clay seal due to the desaturation of the rock. Figures 7-34(a), 7-34(b) and 7-34(c) clearly indicate the effect of the desaturation of the rock on hydration behaviour of the clay seal. Numerical prediction with a lower air entry pressure (P_0) of 0.7 MPa shows a dramatic decrease in degree of saturation in the outer region of the clay and the decrease in degree of saturation continues appearing for 4900 days. The clay in the outer region shows a 12% decrease in degree of saturation for 50 days, 17% for 2400 days and 7.5% for 4900 days due to the desaturation of the rock.

Numerical prediction with air entry pressures of the rock ranging from 0.7 MPa to 100 MPa indicates that the centre region of the clay is not directly affected by changes in air entry pressure of the rock and shows similar patterns of evolution of hydration process.

For 50 days after installation of the clay, the edge region of the clay is fully saturated for greater P_0 values (100 MPa and 500 MPa), while the lowest P_0 of 0.7 MPa shows the degree of saturation of 74%. The effect of the greatest air entry pressure of 500 MPa is more dramatic when it reaches 2400 days. Numerical prediction with the P_0 of 500 MPa indicates almost saturation (99%

saturation) in the centre of the clay, while showing less than 80% for lower air entry values. For 4900 days, the prediction using the lower air entry values (0.7 MPa and 10 MPa) still shows the centre region unsaturated.

The desaturation of the rock in the region close to the clay seal affects the saturation rate of the clay as shown in Figure 7-34. As a result, hydration times for 100% saturation of the clay are estimated based on the numerical results. Figure 7-35 presents a relationship between the air entry pressure of the rock and hydration time for full saturation at three different locations of the clay (e.g., the centre (x = 0 m), 1.25 m from the centre (x= 1.25 m) and the edge of the clay (x = 2.5 m)). As expected, the edge region (x = 2.5 m) of the clay is affected more dramatically by increasing the air entry pressure of the rock than the other areas. In the edge region, the hydration time for full saturation is less than approximately 0.2 year (70 days) at an air entry pressure greater than 200 MPa. The centre region (x = 0 m) indicates approximately 19 years for full saturation at an air entry pressure of 200 MPa and approximately 10 years at the pressure of 500 MPa.

In the ESP, interestingly the piezometer data located into the rock (EDZ) near the clay showed positive values during the monitoring period, which indicates some recharge was taking place. In other words, desaturation of the EDZ was not observed in the actual field conditions of the ESP. The possible reason for no desaturation in the EDZ could be a relatively high initial degree of saturation (~67%) of the clay seal. As a result, the suction corresponding to the degree of saturation was not high enough to withdraw water from the EDZ. Another possible reason could be that the outer region of the clay seal would have a relatively lower dry density achieved due to difficulty of compaction. That would result in higher voids inside the soil and consequently lower suction applied against the EDZ.

This sensitivity analysis simplified the water retention curve of the rock near the clay. The rock in contact with the clay contains a considerable EDZ and this EDZ contacts both FZ2 and the water-filled shaft above and below the seal. The EDZ is not open because a hydraulic channel between the upper and lower shaft has been disconnected by the clay seal. Therefore, the water retention curve used for the rock in this analysis may not be entirely representative of the actual field conditions. The effects of the EDZ on both the "global" water retention curve and water supply to the clay should be studied for future research.

This section examines the effects of desaturation of the rock on the hydraulic behaviour of the shaft sealing components. The sensitivity analysis used a water retention curve for the host rock with much higher air entry pressure values. Predictions of degree of saturation indicate that the rock with a lower air entry pressure should show significant desaturation in the region adjacent to the clay, resulting in slower hydration process in the clay. The slower hydration in the clay is likely due to a hydraulic barrier surrounding the clay as a result of desaturation of the rock. By contrast, the rock with a greater air entry pressure remains fully saturated throughout. Much quicker hydration times are obtained in this analysis with a greater air entry pressure of the rock, which means no desaturation takes place.

7.5. Effects of Changes in Hydraulic Conductivity of FZ2 on Hydration Times

In the Enhanced Sealing Project (ESP) hydration times of the clay is one of the critical features and requires special consideration as the times are directly related to fundamental design theories and expected performance. Since the groundwater flow from FZ2 directly affects evolution of hydraulic behaviour of the clay seal, an analysis focusing on effects of changes in the hydraulic conductivity of horizontal FZ2 on hydration times of the clay has been conducted as part of this sensitivity study. The hydraulic conductivity of FZ2 was assumed to be 1.0×10^{-9} m/s in this numerical study, while the hydraulic conductivity of the clay seal was assumed to be 1.0×10^{-12} m/s.

Hydration times of the clay depend on factors such as hydraulic conductivity, temperature and pore water pressure of the rock at the site. For instance, under confined conditions the hydraulic conductivity of the clay increases as temperature increases. The influence of temperature on the hydraulic conductivity is suction-dependent and it is related to both the water viscosity and the macro pores closing phenomenon (Dixon et al. 1992, Lingnau et al. 1994, Ye et al. 2012). Gens et al. (1998) studied the influence of different pore water pressures of the rock on hydration times of compacted bentonite and showed that hydration times were sensitive to the pore water pressure in the rock. In the ESP, the groundwater flow from FZ2 dominantly affects water uptake in the clay and therefore the consequences of adopting different hydraulic conductivities of the FZ can influence the hydration rate of the clay.

A sensitivity analysis was performed by varying the hydraulic conductivity of horizontal FZ2 up to four orders of magnitude (i.e., K of FZ2, 1.0×10^{-9} to 1.0×10^{-13} m/s), while keeping the hydraulic conductivity of the clay constant (i.e., K of clay, 1.0×10^{-12} m/s). Table 7-4 summarizes variations of the hydraulic conductivity of FZ2 for this analysis. Hydration times were measured at the mid-height (y = 3 m) and 1.25 m from the centre of the clay (x = 1.25 m) when the region reached 100% saturation. Note this sensitivity analysis used various hydraulic conductivities of horizontal FZ2 and therefore the head difference above and below FZ2 was not taken into account. In addition, the hydration times predicted indicate only local saturation, not the saturation of the whole clay-filled volume.

It should be expected that the hydraulic conductivity of the clay will control hydration times of the clay if the FZ2's hydraulic conductivity is higher than that of the clay. This is what is expected in the shaft sealing system. On the other hand, if the FZ2's hydraulic conductivity is sufficiently lower, it will control the amount of water released into the clay and therefore the rate of hydration will depend on the FZ2's hydraulic conductivity.

The numerical results shown in Figure 7-36 clearly demonstrate that there are two distinct hydraulic behaviour regions. It is apparent that at the ratio of the saturated hydraulic conductivity of the FZ2 to that of the clay (K_{FZ2} / K_{clay}) is higher than 100, hydration times are controlled by the clay's hydraulic conductivity. Interestingly for the ratio of 10 where the rock's hydraulic conductivity is still higher than the clay's, hydration time of the clay is not controlled by the clay, but by the rock. This indicates that if rock's hydraulic conductivity is equal or slightly higher than the clay's (K_{FZ2} / K_{clay} less than 100), hydration time of the clay is dominantly affected by the rock's hydraulic conductivity. In the ratio range of 100 to 1000, hydration times do not seem to be sensitive to changes in rock's hydraulic conductivity, indicating a relatively flat slope.

Hence for FZ2 hydraulic conductivities greater than the 10^{-9} m/s shown in Table 7-4, there would be little or no effect on the hydration time for the clay. In the ESP, the ratio of FZ2's hydraulic conductivity to the clay's hydraulic conductivity is 1000 and therefore, the clay's hydraulic conductivity controls the hydration time of the clay.

By contrast, the rock's hydraulic conductivity controls hydration times for the ratios lower than 100 and predicted hydration times are much longer. As also seen in Figure 7-36, within this ratio range, hydration times of the clay are quite sensitive to changes in rock's hydraulic conductivity because it controls the amount of water release into the clay.

Hydration times are naturally controlled by the permeability of the rock and clay components. This sensitivity analysis has allowed for distinguishing two hydraulic zones in which the hydration process is controlled by either the hydraulic conductivity of the rock or the hydraulic conductivity of the clay.

7.6. Summary

This chapter has discussed (1) the sensitivity of Hydraulic-Mechanical (H-M) parameters to H-M performance of the clay seal component, (2) effects of the desaturation of the rock adjacent to the clay seal during the hydration process of the clay and (3) effects of variations of the hydraulic conductivity of FZ2 on the hydration times of the clay. The numerical results have provided useful information on the interplay of the various phenomena.

Effects of critical hydraulic parameters on evolution of hydraulic behaviour of the clay seal component are investigated. By varying of the water retention parameters P_0 and β_1, numerical predictions have clearly demonstrated the effect of hysteretic behaviour of the clay on it water uptake times of the clay and the relationship between hydration process times and the water retention parameters P_0 and β_1. Numerical prediction using the water retention parameters of P_0 and β_1 obtained for drying cycles indicates almost three times quicker hydration time for full saturation than those for wetting cycles. A lower material parameter (β_1) results in faster decreases in suction during hydration progress, while a higher air entry pressure (P_0) causes faster decrease in suction. The time for zero suction is reduced by 1200 days with increasing an air entry pressure of 3 MPa.

Different values of the water retention parameters of P_0 and β_1 can be determined from the same clay material and consequently result in different predictions of the clay's hydraulic behaviour. For this reason, selection of the water retention parameters is fundamentally important for numerical modelling to obtain qualitative and representative results.

A series of numerical modelling exercises using different sets of BBM mechanical parameters determined has been performed to examine the sensitivity of the parameters to mechanical performance of the clay component. The numerical predictions using different BBM mechanical parameters indicate that mechanical behaviour of the clay seal is not significantly sensitive to changes in the parameters within the likely range of their variations.

The effects of desaturation of the rock on the hydraulic behaviour of the shaft sealing components are examined. The rock with a lower air entry pressure shows significant desaturation in the region adjacent to the clay and results in slower hydration process of the clay.

By contrast, the rock with a greater air entry pressure remains fully saturated throughout and much quicker hydration times are obtained with a greater air entry pressure of the rock.

Desaturation of the EDZ was not observed in the actual field conditions of the ESP. The possible reason for no desaturation in the EDZ could be a relatively high initial degree of saturation (~67%) of the clay seal and therefore the suction corresponding to the degree of saturation was not high enough to withdraw water from the EDZ.

As part of the sensitivity study, an analysis focusing on effects of changes in hydraulic conductivity of FZ2 on hydration times of the clay has been conducted. This analysis has identified two hydraulic conditions in which the hydration process is controlled by either the hydraulic conductivity of the rock or the hydraulic conductivity of the clay. When the ratio of the saturated hydraulic conductivity of the FZ to that of the clay (K_{FZ} / K_{clay}) is higher than 100, hydration times are controlled by the clay's hydraulic conductivity. By contrast, when the ratio is lower than 100, hydration time of the clay is dominantly affected by the rock's hydraulic conductivity. In the ESP, the ratio of FZ2's hydraulic conductivity to the clay's hydraulic conductivity is 1000 and therefore, the clay's hydraulic conductivity controls the hydration time of the clay.

Table 7-1. Summary of estimated hydraulic parameters P_0 and β_1

Model Type	P_0	β_1
Model 1	11.0	0.48
Model 2 for Drying Cycles	8.0	0.28
Model 3 for Wetting Cycles	3.1	0.43
Model 4	11.0	0.28

Table 7-2. A summary of hydration times for various air entry pressures of the clay seal

	Model 2	Model 4	Model 4-1	Model 4-2
Air Entry Pressure, P_0 (MPa)	8	11	16	25
Hydration time for zero suction (day)	6300	5100	3940	2940

Table 7-3. Various mechanical parameters determined from calibration processes

		Model 2	Model 3	Model 4		Model 1
Fitting Parameters	r	0.248	0.254	0.259		0.650
	β (MPa^{-1})	0.061	0.076	0.074		0.500
	$\lambda(0)$	1.657	0.156	0.708		0.120
	p^c (MPa)	0.974	0.752	0.965		0.180
Measured Parameters	κ	0.001	0.010	0.019		0.256
	P_0^* (MPa)	1.000	1.000	1.000		1.000
	κ_s	0.056	0.056	0.056		0.011

Table 7-4. Variations of the hydraulic conductivity of FZ2

	FZ2 (m/s)	Clay (m/s)	Ratio, K_{FZ2} / K_{Clay}
Saturated Hydraulic Conductivity (K)	1.0×10^{-13}	1.0×10^{-12}	0.1
	1.0×10^{-12}	1.0×10^{-12}	1
	1.0×10^{-11}	1.0×10^{-12}	10
	1.0×10^{-10}	1.0×10^{-12}	100
	1.0×10^{-09}	1.0×10^{-12}	1000

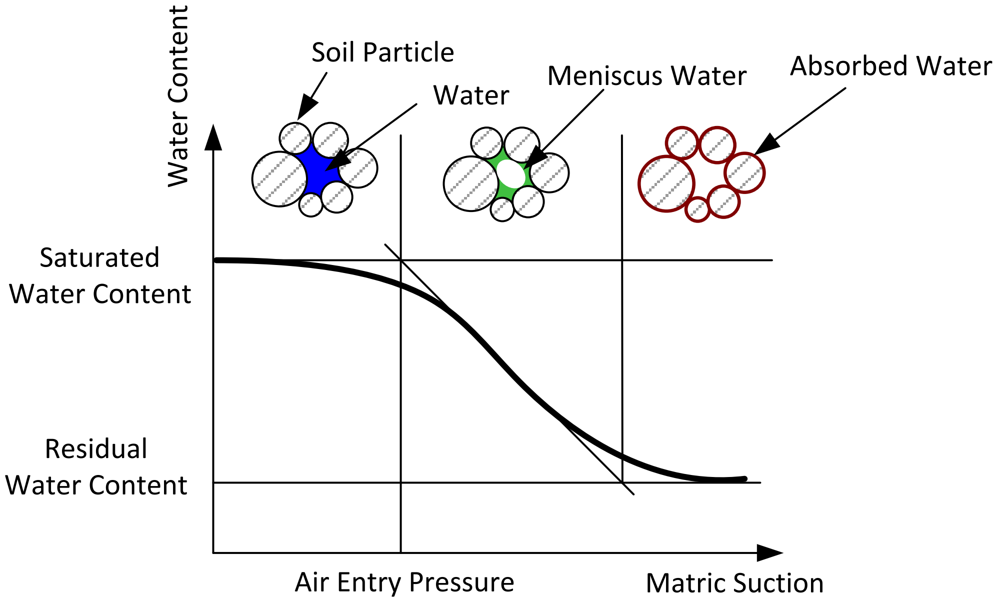

Figure 7-1. Relationship between air entry pressure and matric suction (Matsuoka 1999)

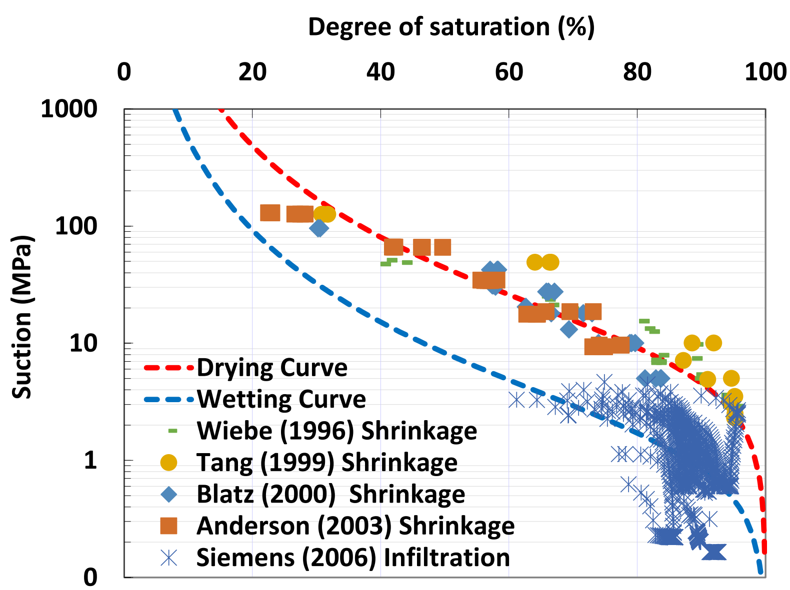

Figure 7-2. Water retention curves for drying and wetting for bentonite-sand buffer materials

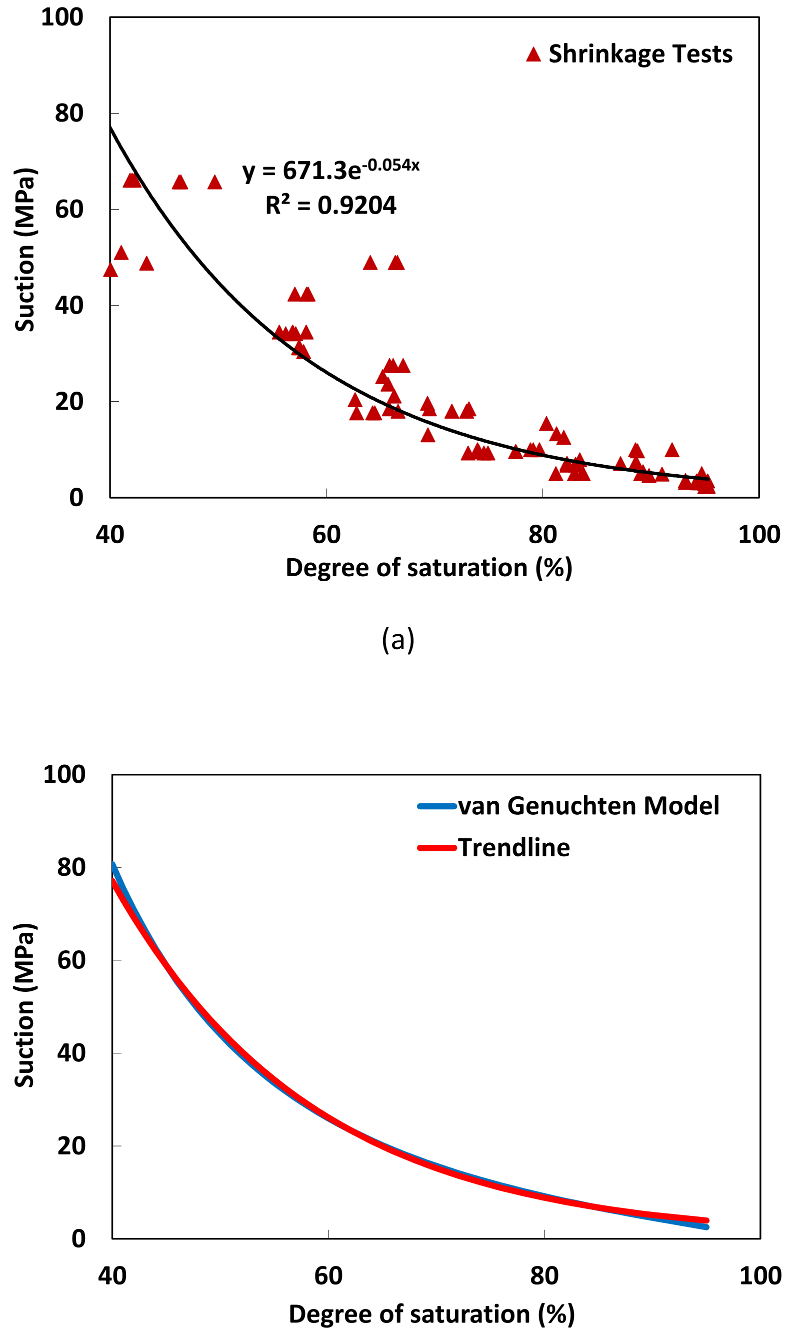

(a)

(b)

Figure 7-3. Determination of hydraulic parameters, P_0 and β_1 for drying cycles

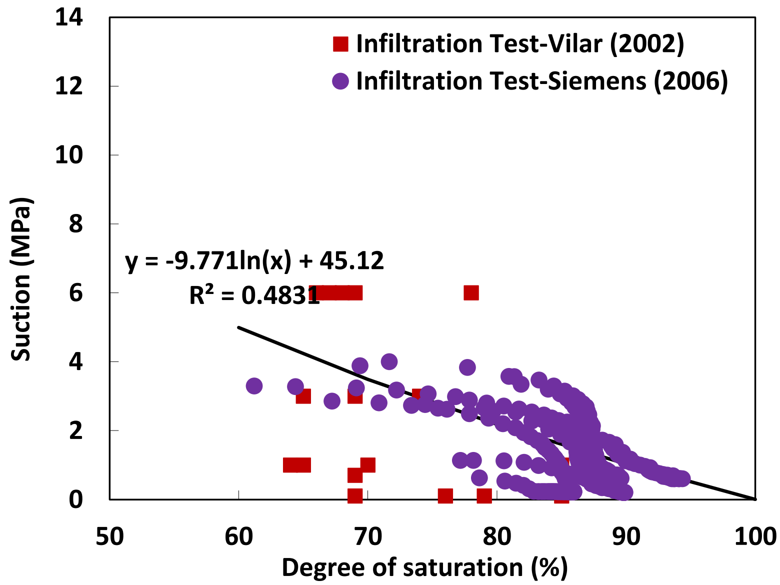

(a)

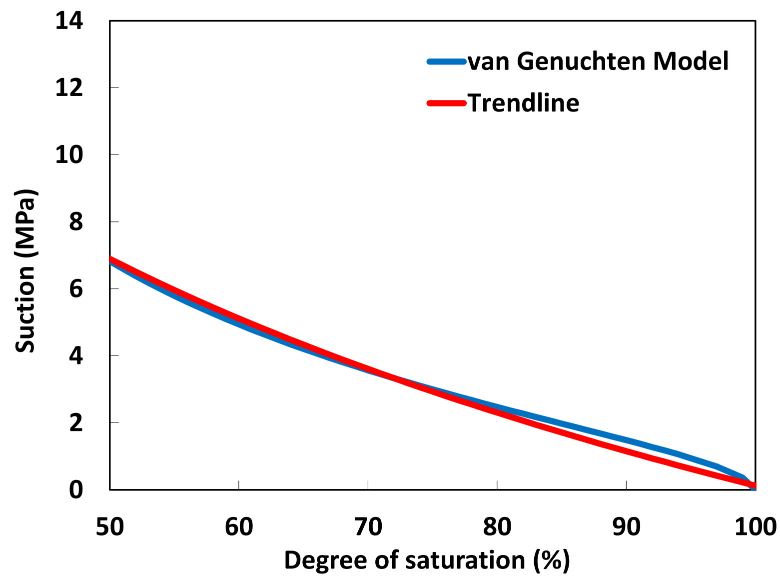

(b)

Figure 7-4. Determination of hydraulic parameters, P_0 and β_1 for wetting cycles

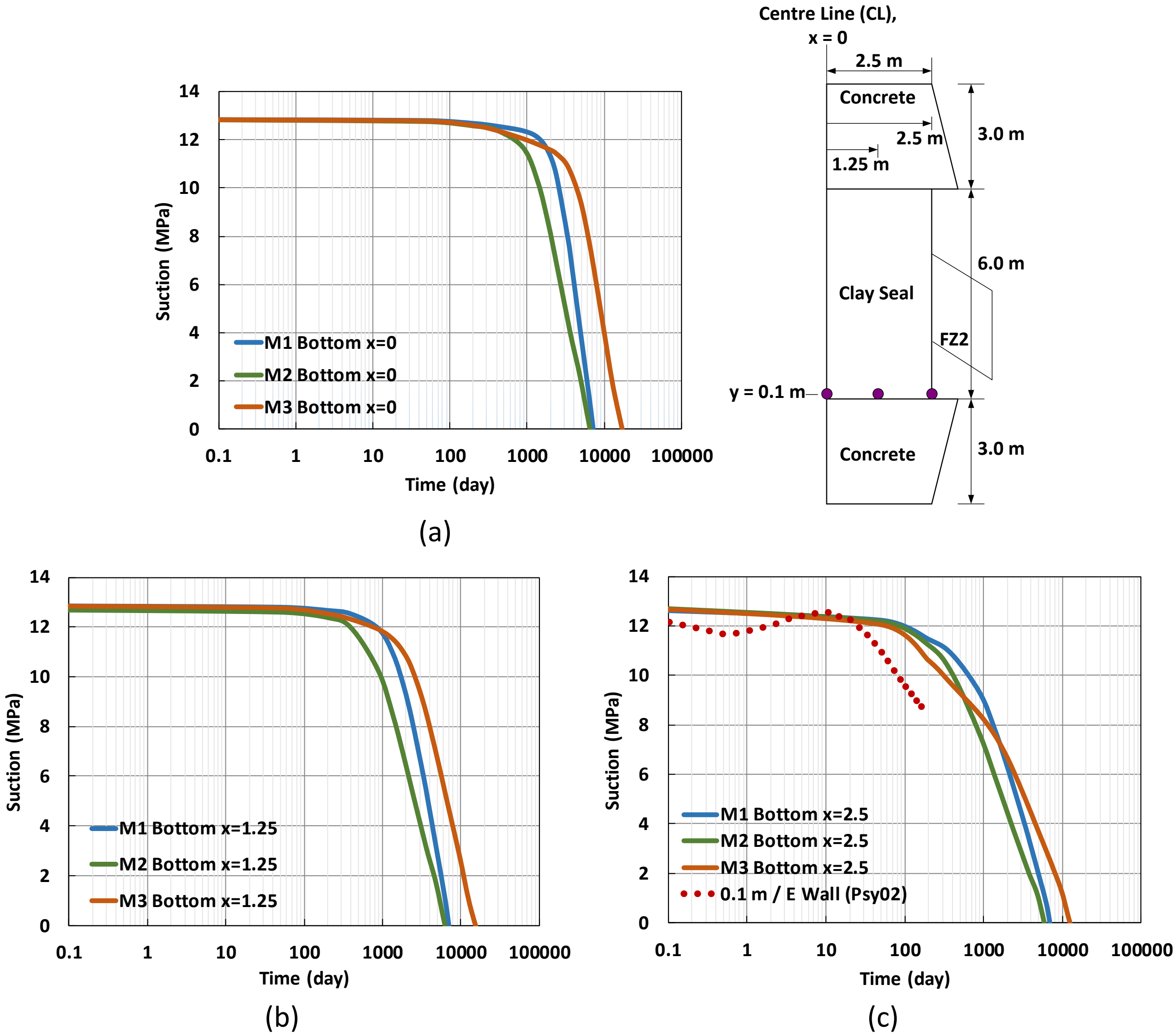

Figure 7-5. Comparison of changes in suction at the bottom of the clay (y = 0.1 m) for three models

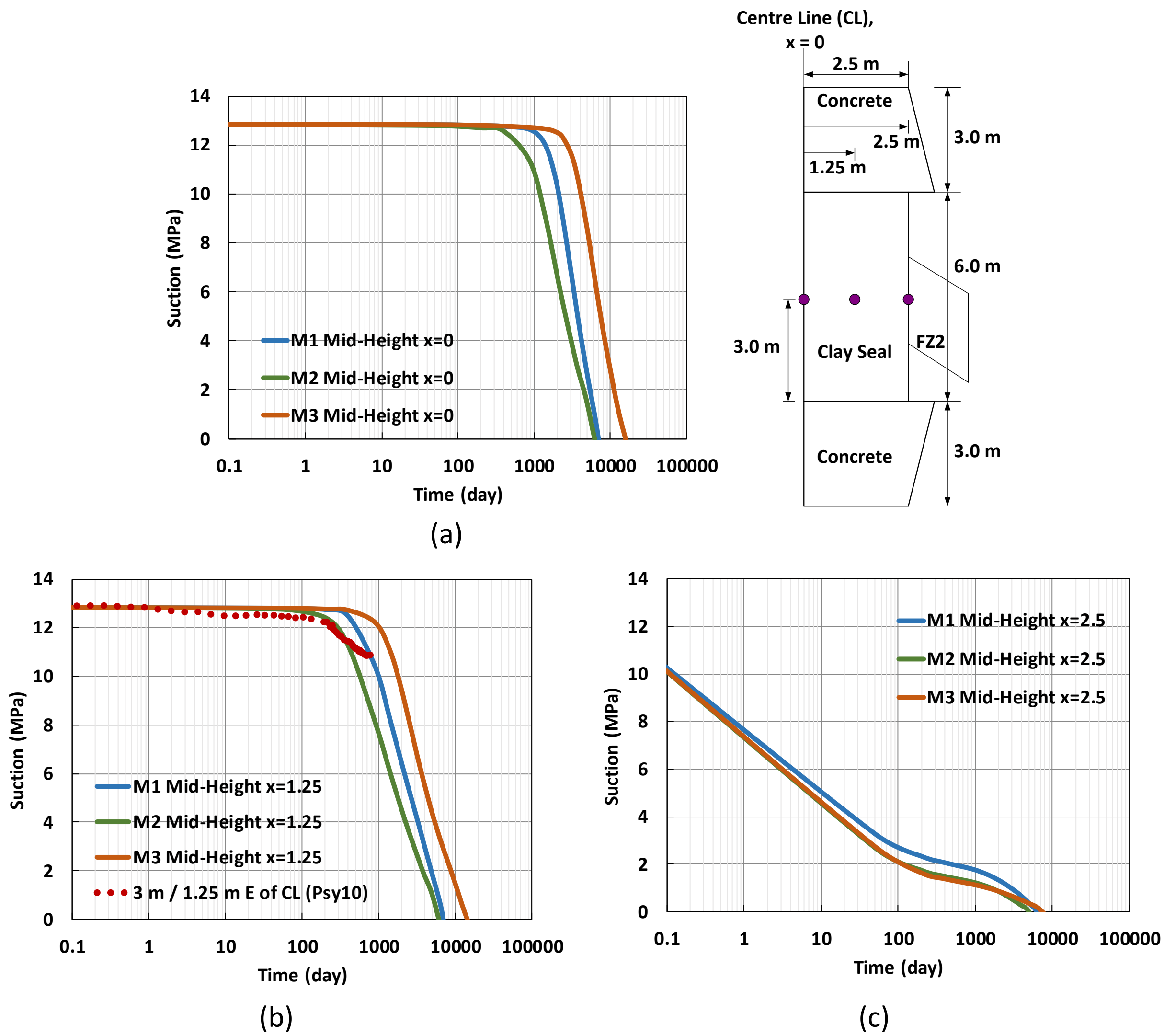

Figure 7-6. Comparison of changes in suction at the mid-height of the clay (y = 3 m) for three models

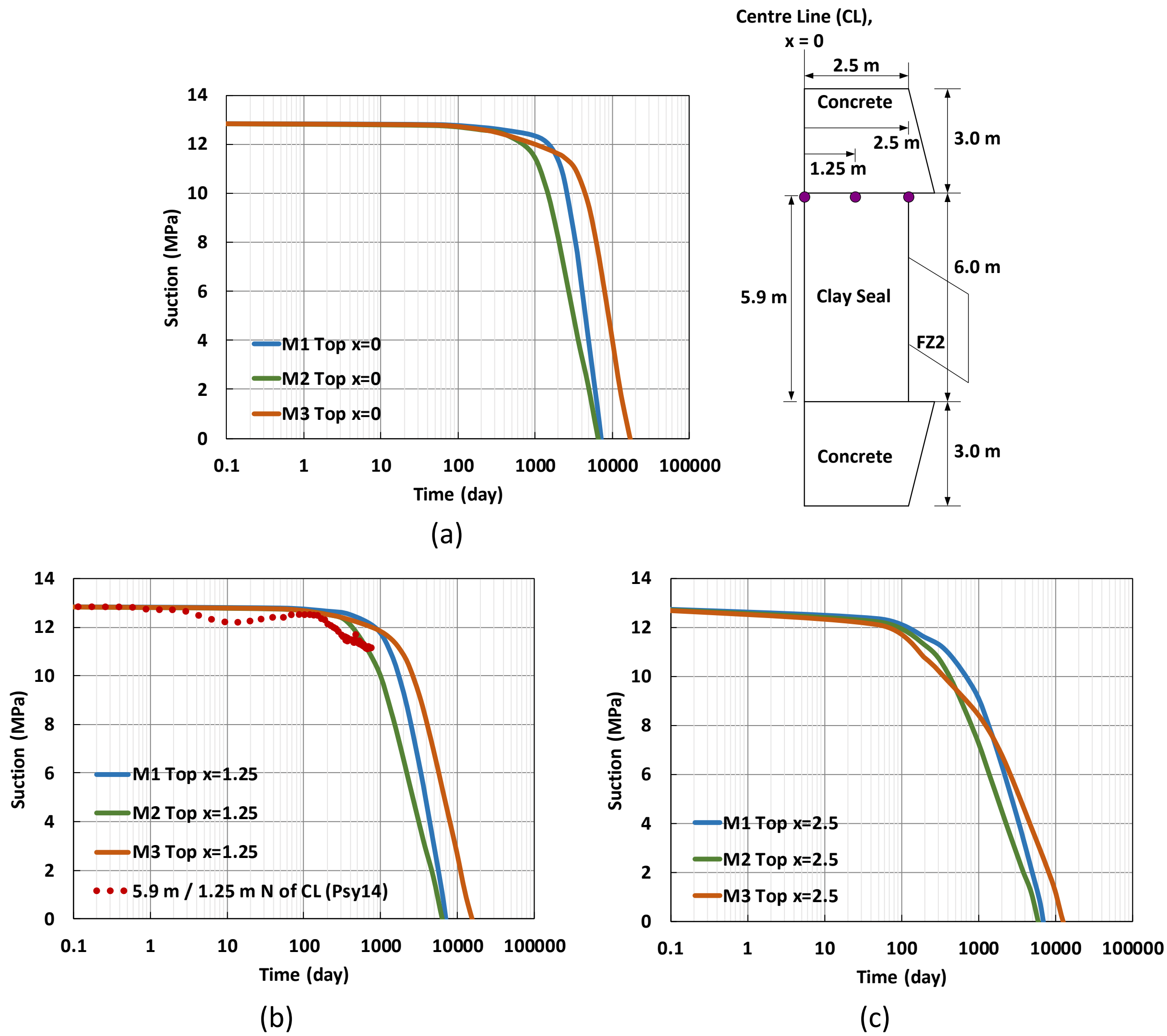

Figure 7-7. Comparison of changes in suction at the top of the clay (y=5.9 m) for three models

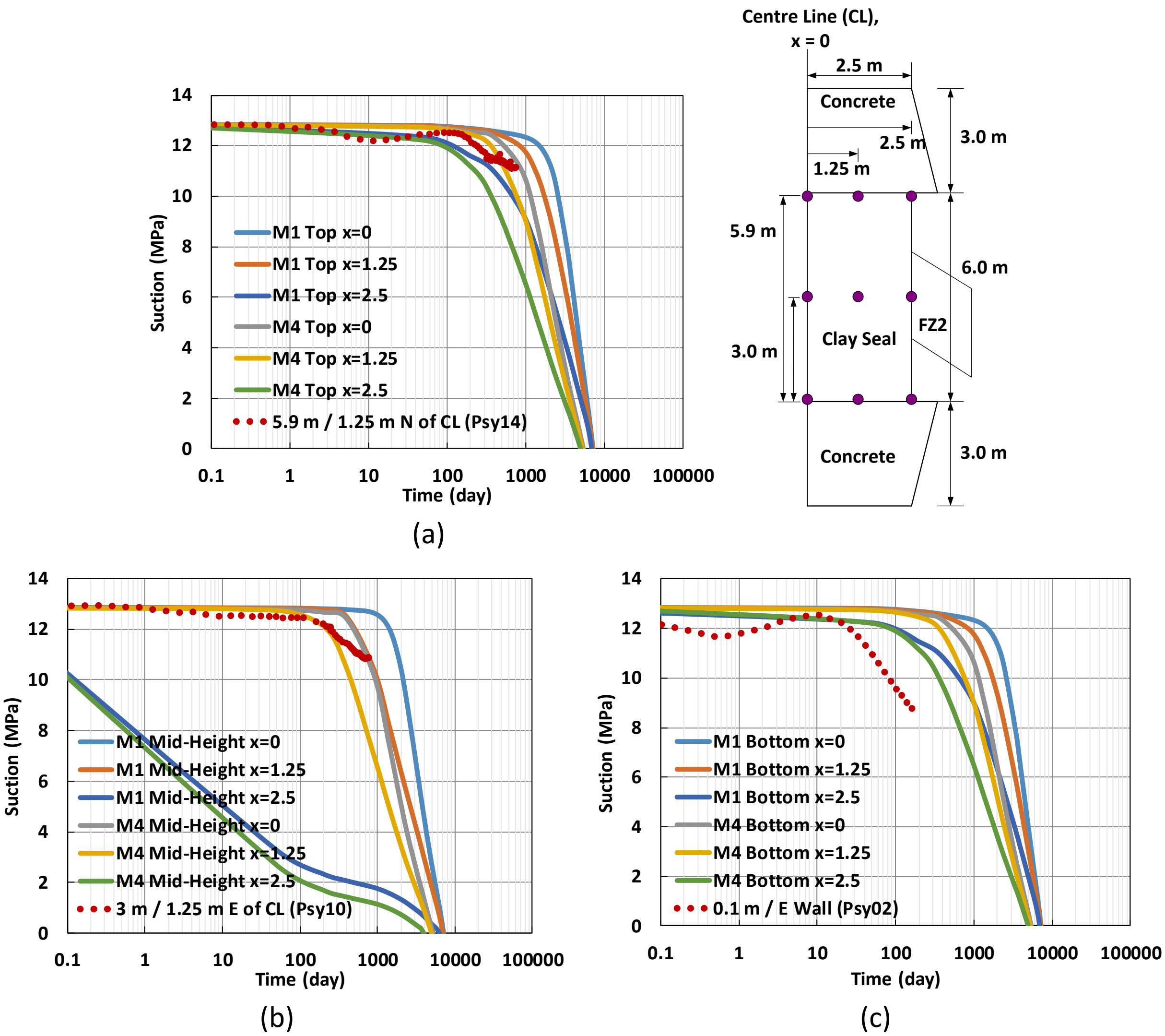

Figure 7-8. Comparison of changes in suction between Model 1 and Model 4

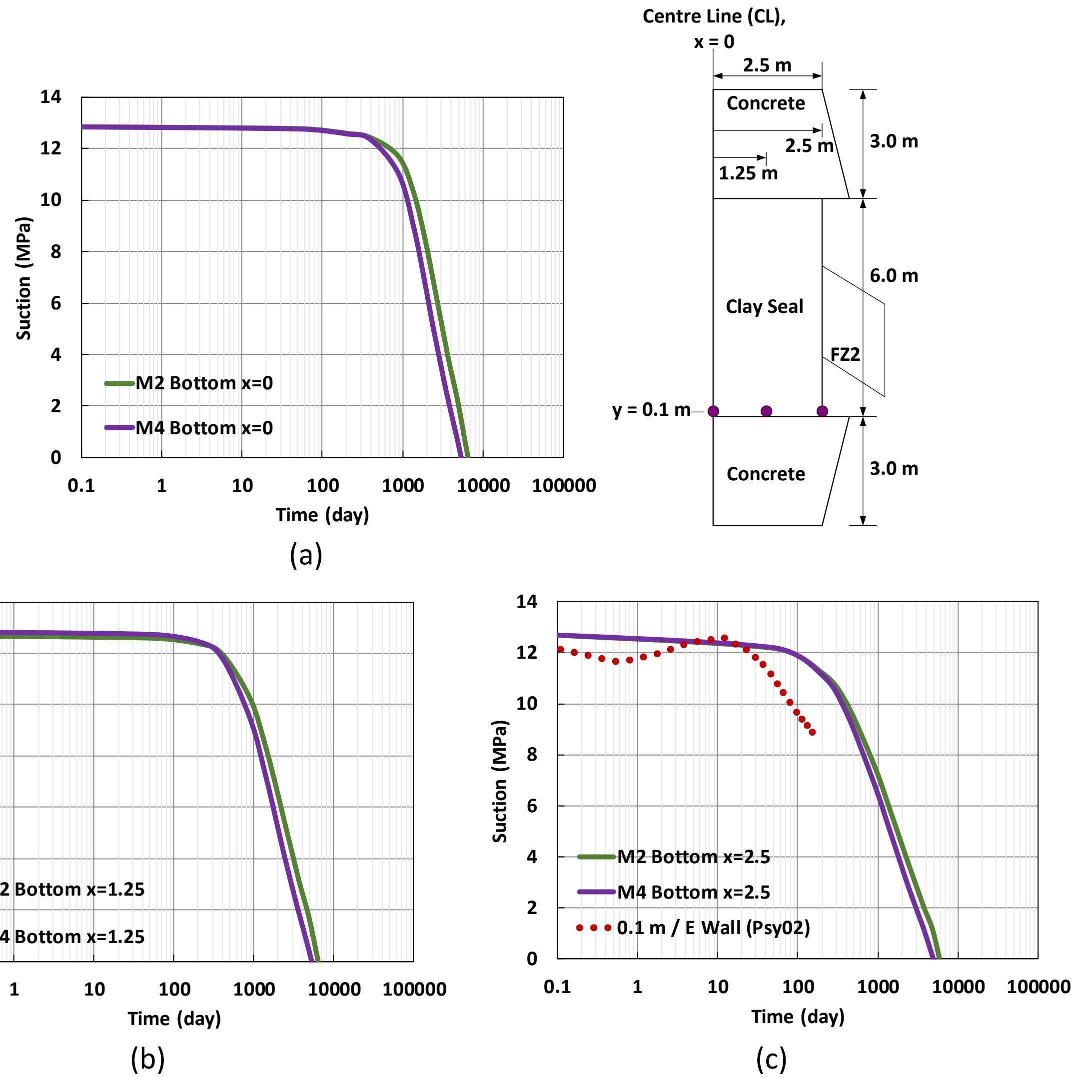

Figure 7-9. Comparison of changes in suction at the bottom of the clay (y = 0.1 m) between Model 2 and Model 4

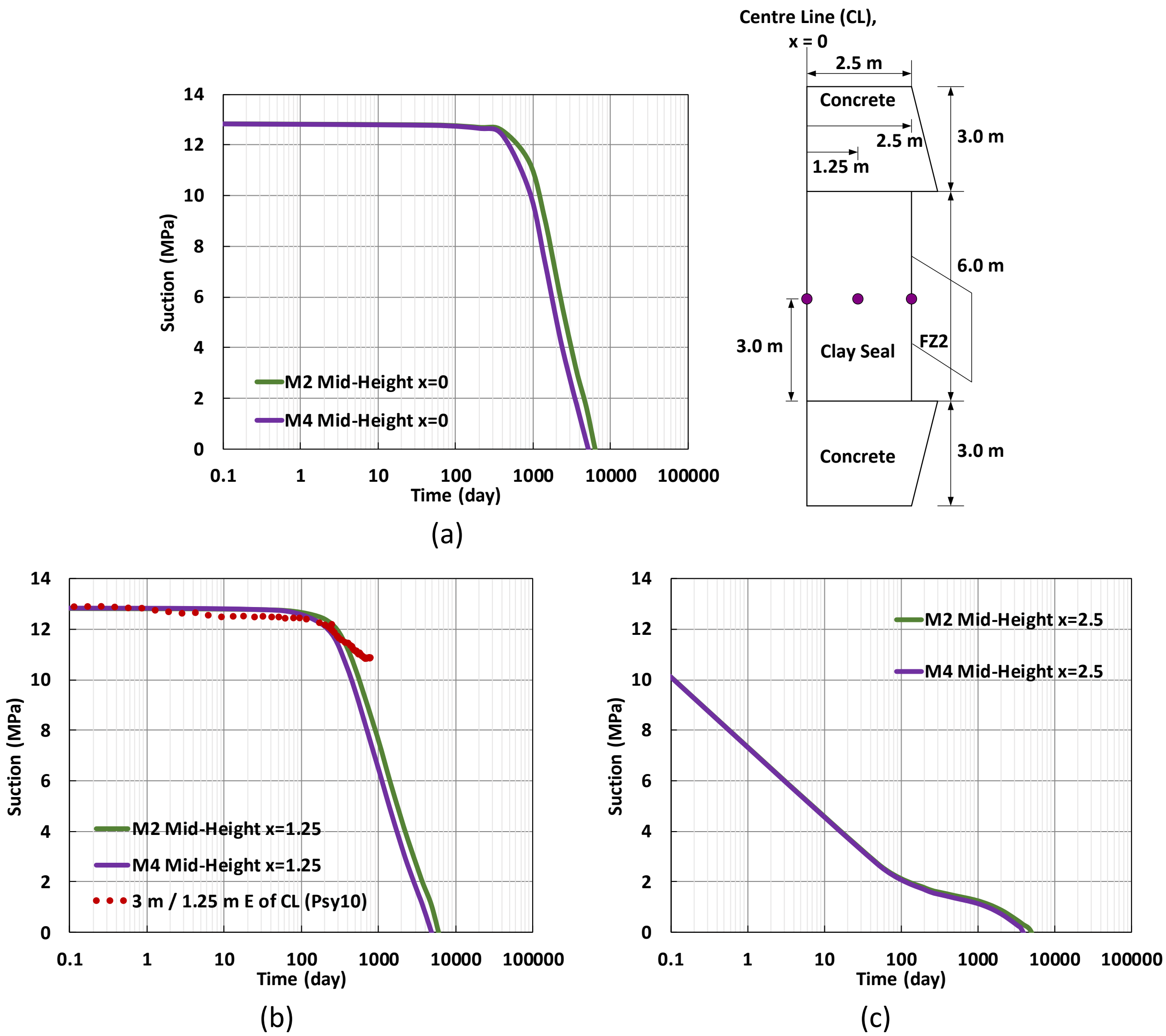

Figure 7-10. Comparison of changes in suction at the mid-height of the clay (y = 3 m) between Model 2 and Model 4

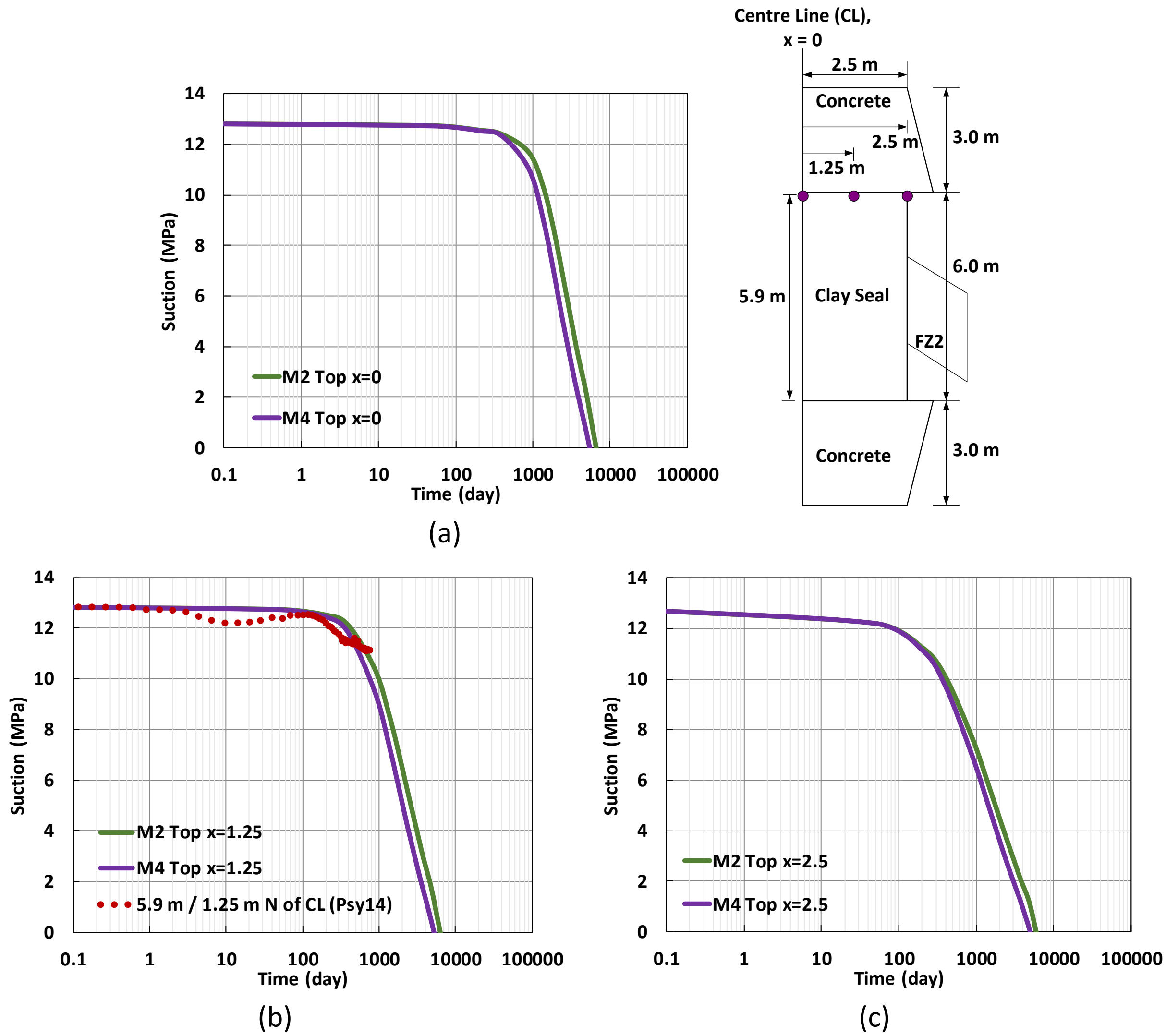

Figure 7-11. Comparison of changes in suction at the top of the clay (y=5.9 m) between Model 2 and Model 4

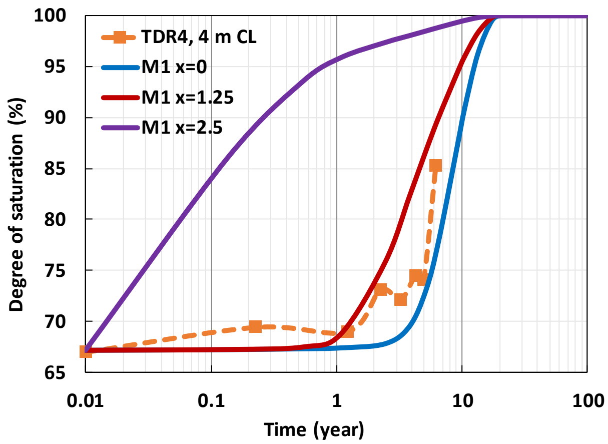

(a)

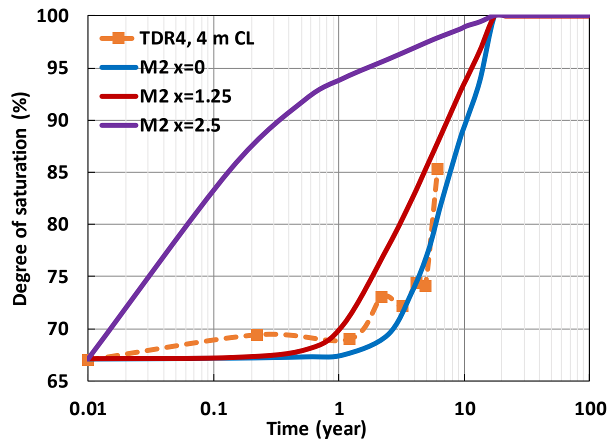

(b)

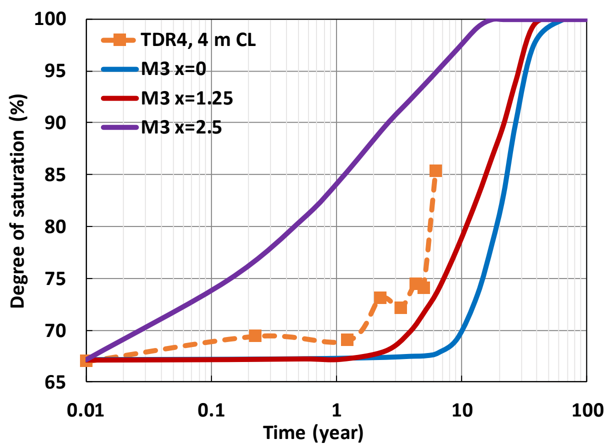

(c)

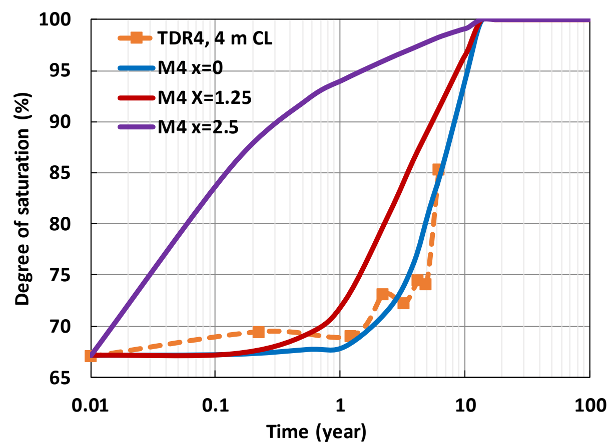

(d)

Figure 7-12. Comparison of changes in degree of saturation at 4 m from the bottom of the clay (y = 4 m) for all models

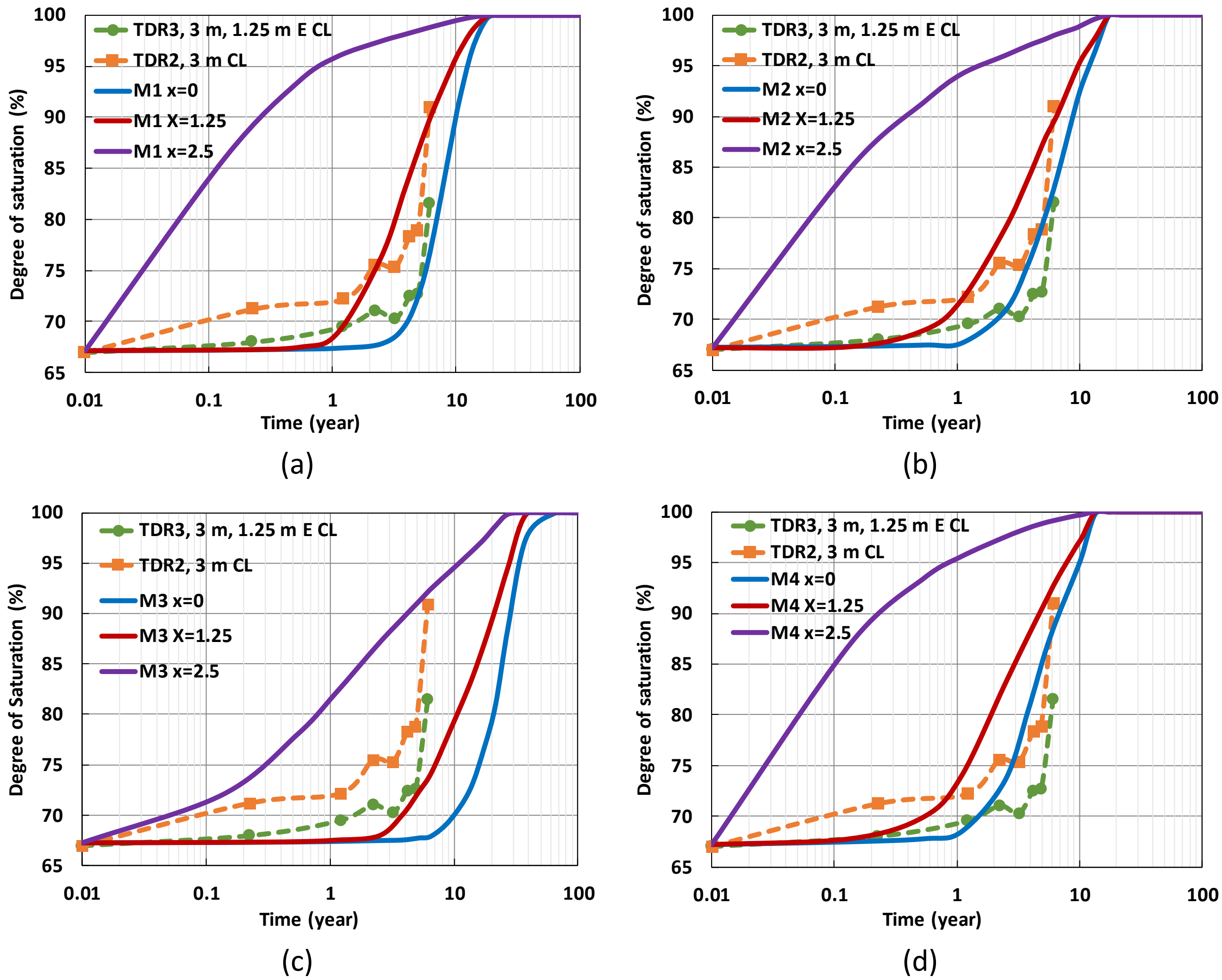

Figure 7-13. Comparison of changes in degree of saturation at 3 m from the bottom of the clay (y = 3 m) for all models

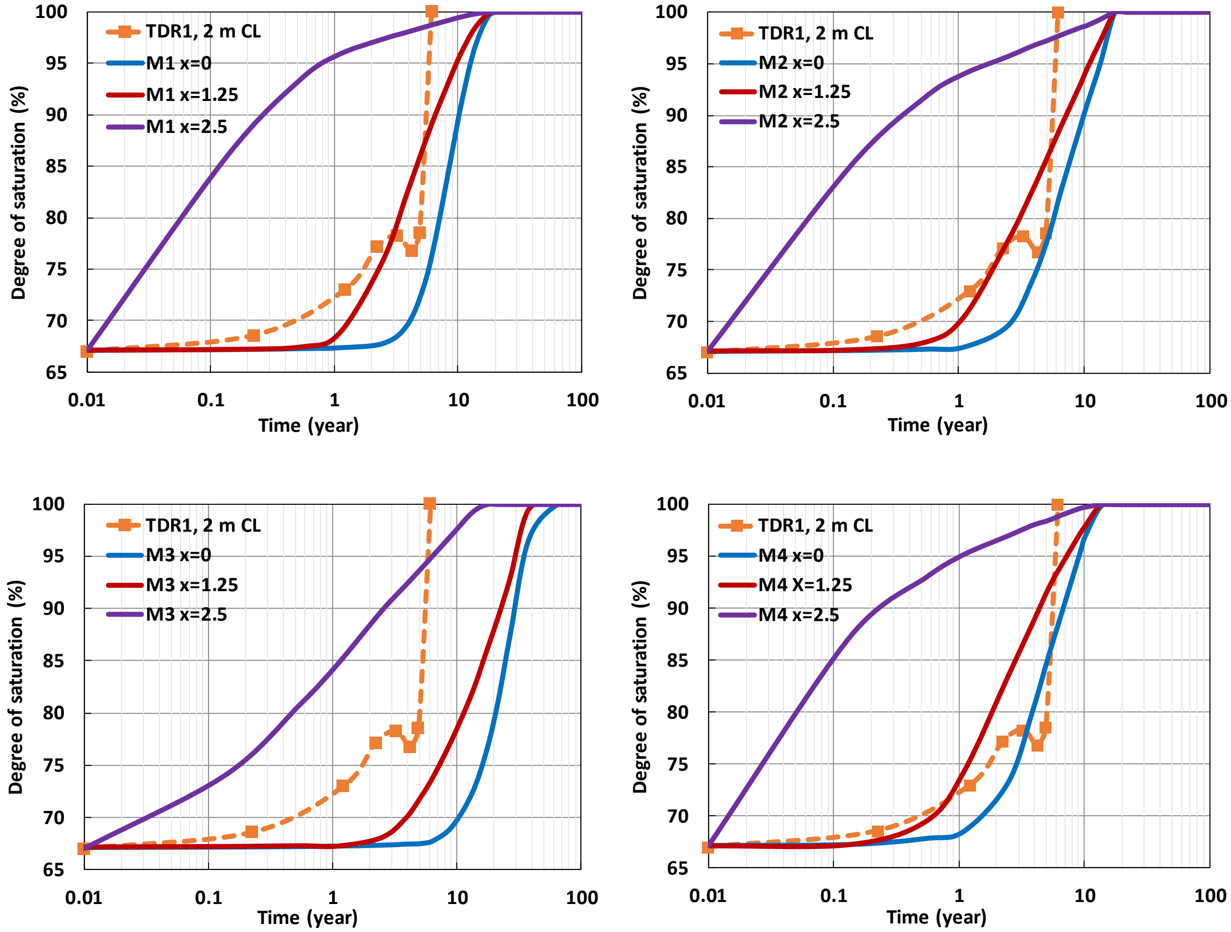

Figure 7-14. Comparison of changes in degree of saturation at 2 m from the bottom of the clay (y=2 m) for all models

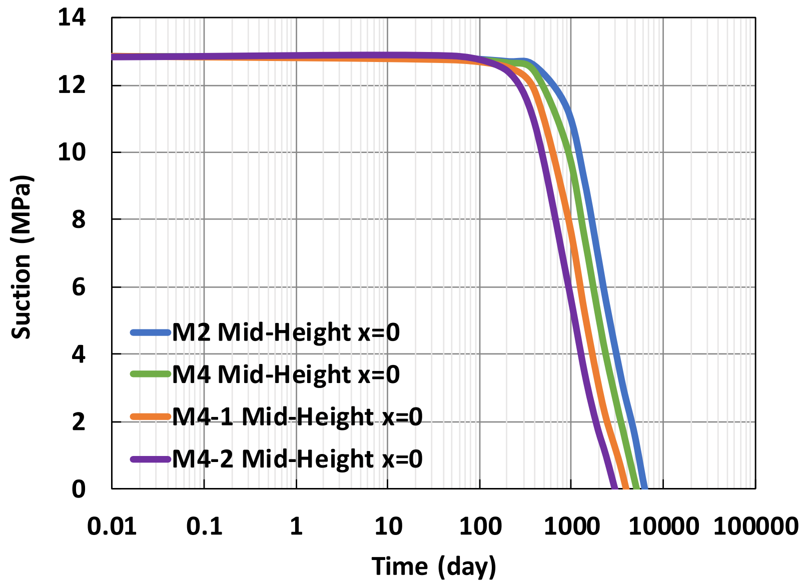

Figure 7-15. Comparison of suction changes with time for Model 2, Model 4, Model 4-1 and Model 4-2 at the mid-height of the clay seal

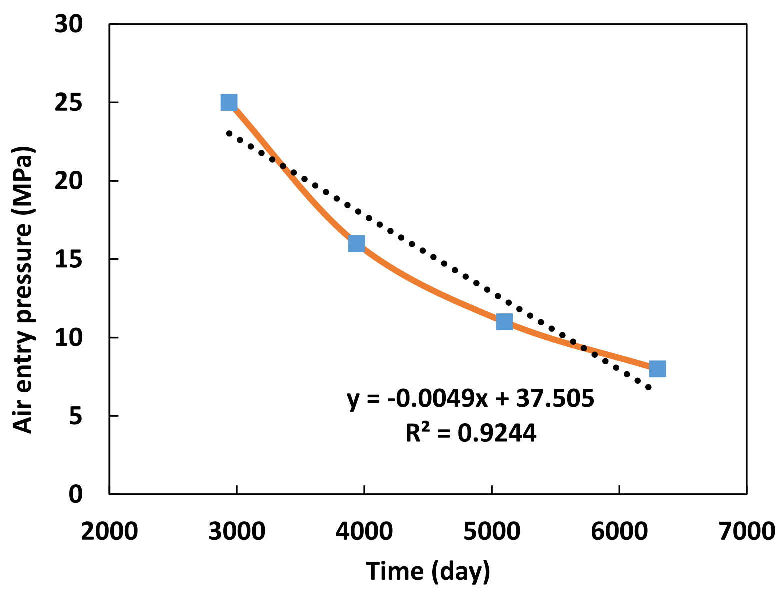

Figure 7-16. A relationship between hydration time and air entry pressure of the clay

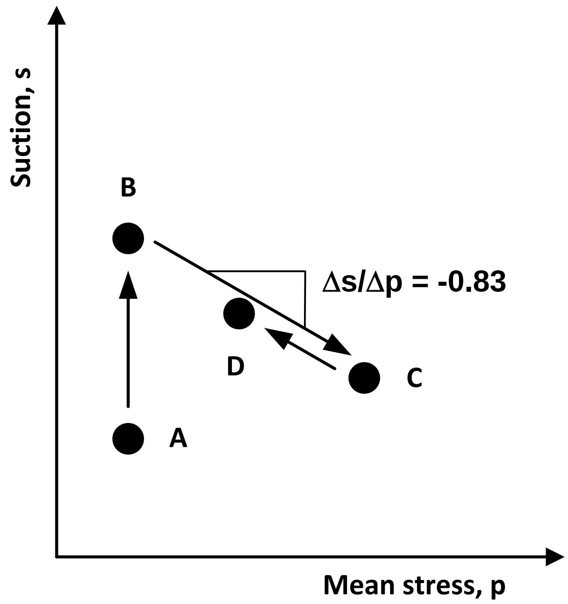

Figure 7-17. Stress path in a plot of mean stress (p) versus suction (s) (q=0) (after Blatz 2000)

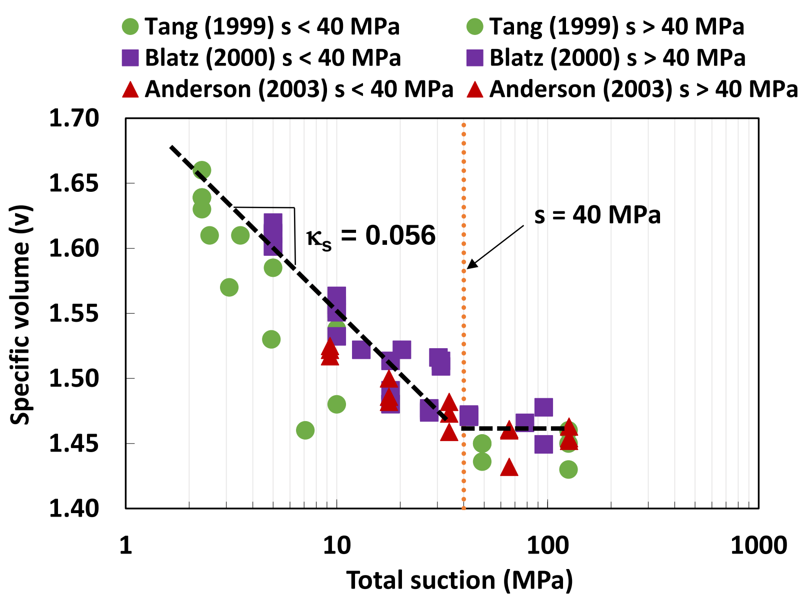

Figure 7-18. A plot of suction (s) versus specific volume (v) on unsaturated bentonite-sand (50%-50% dry mass) mixtures (Tang 1999, Blatz 2000 and Anderson 2003)

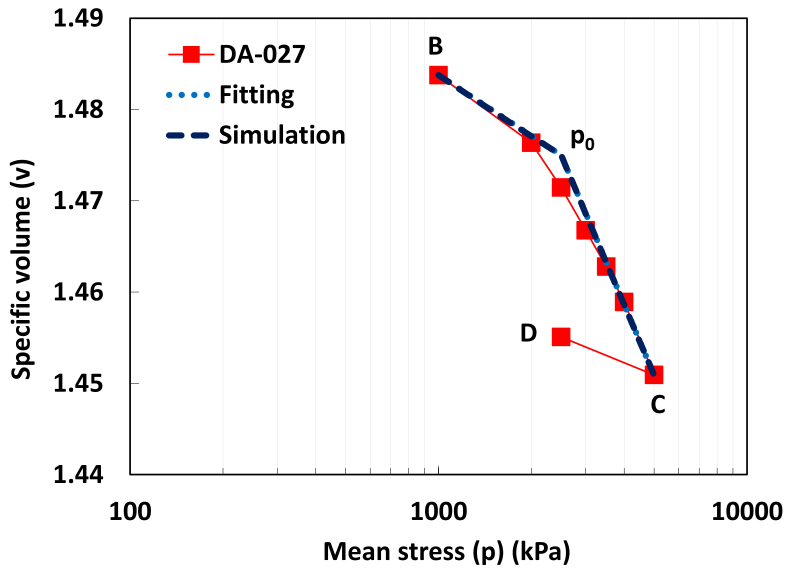

Figure 7-19. Results of isotropic loading and unloading on specimen DA-027 (Anderson 2003)

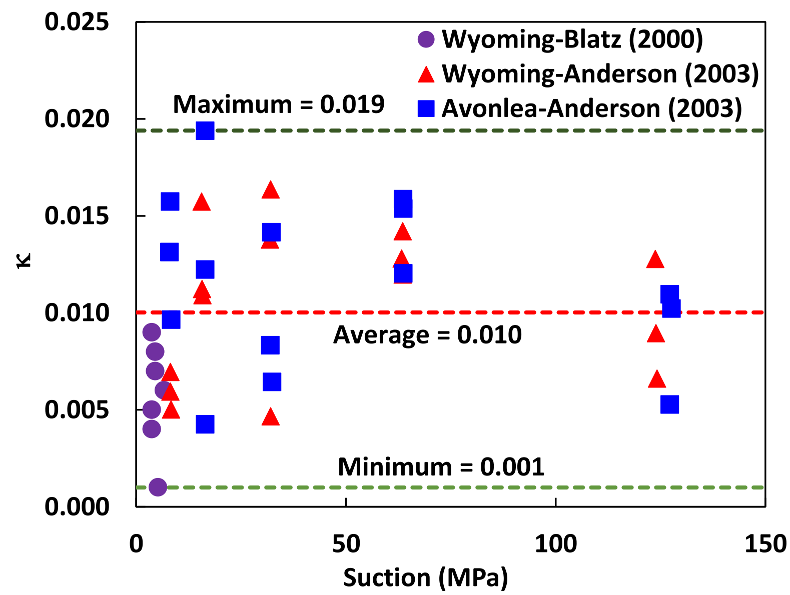

Figure 7-20. Distribution of parameter κ values plotted with suction

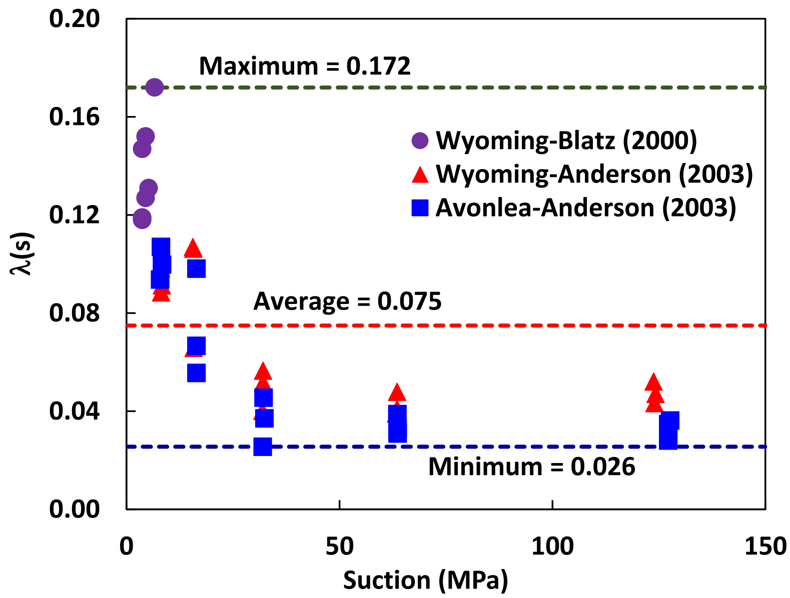

Figure 7-21. Distribution of parameter λ(s) values plotted with suction

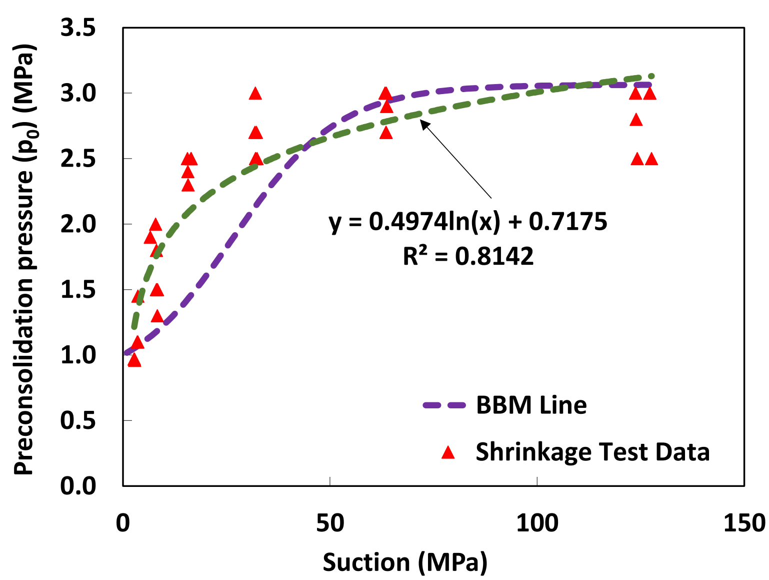

Figure 7-22. Distribution of the preconsolidation pressure (p_0) plotted versus suction

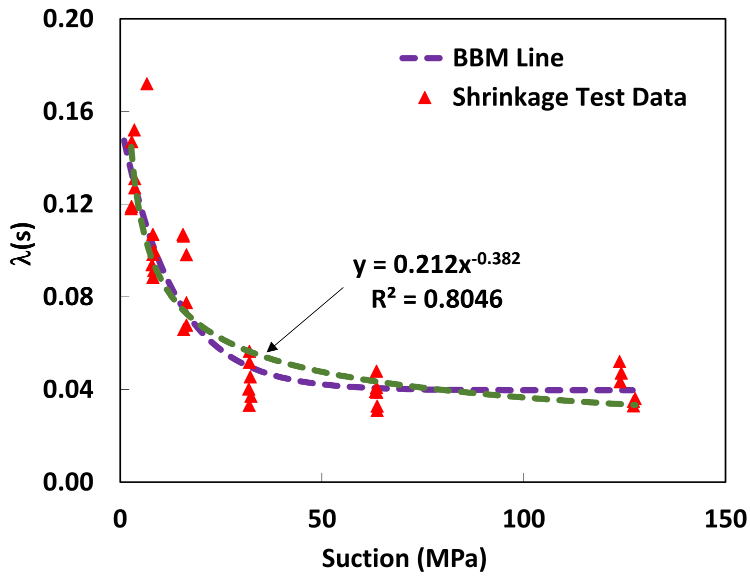

Figure 7-23. Distribution of the stiffness parameter λ(s) plotted versus suction

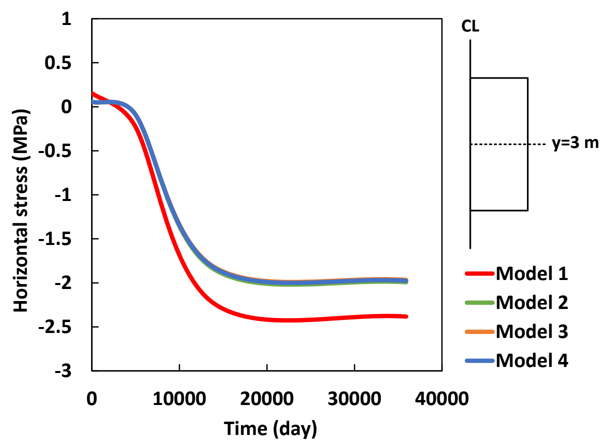

(a)

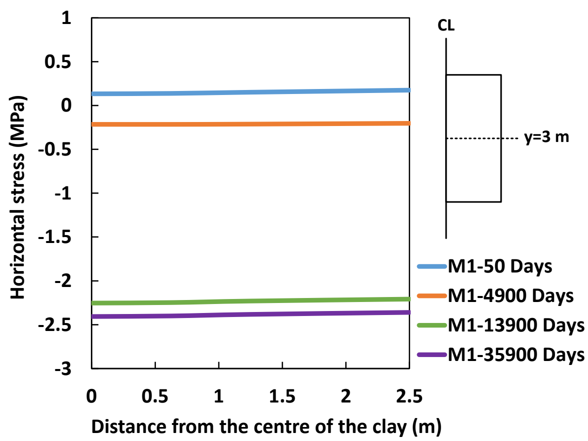

(b)

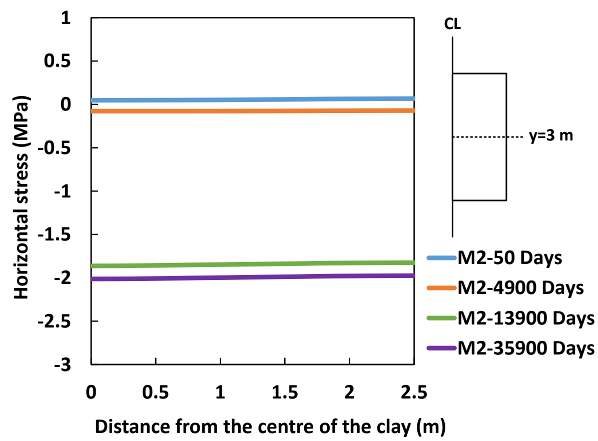

(c)

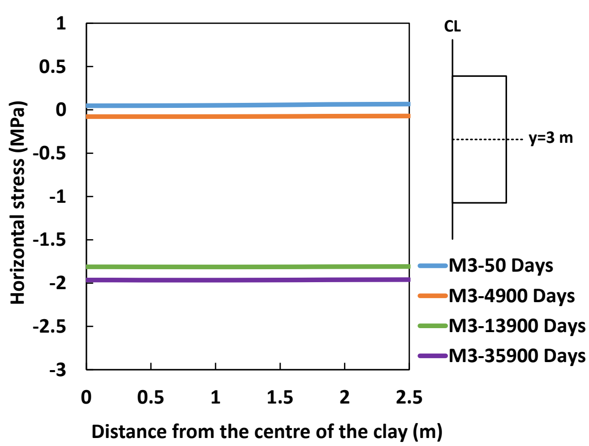

(d)

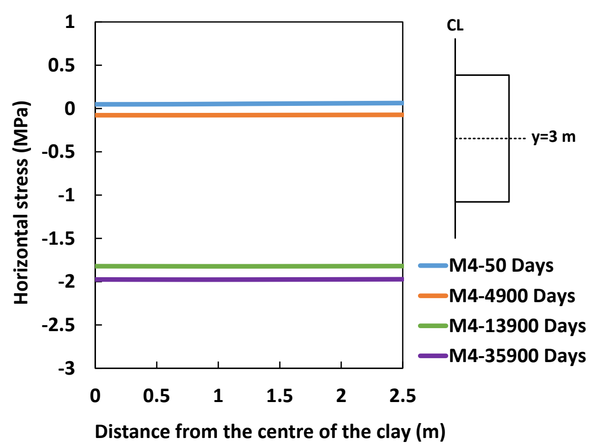

(e)

Figure 7-24. Distributions of horizontal (radial) stresses at the mid-height of the clay (y = 3 m) (note that negative stress is compressive)

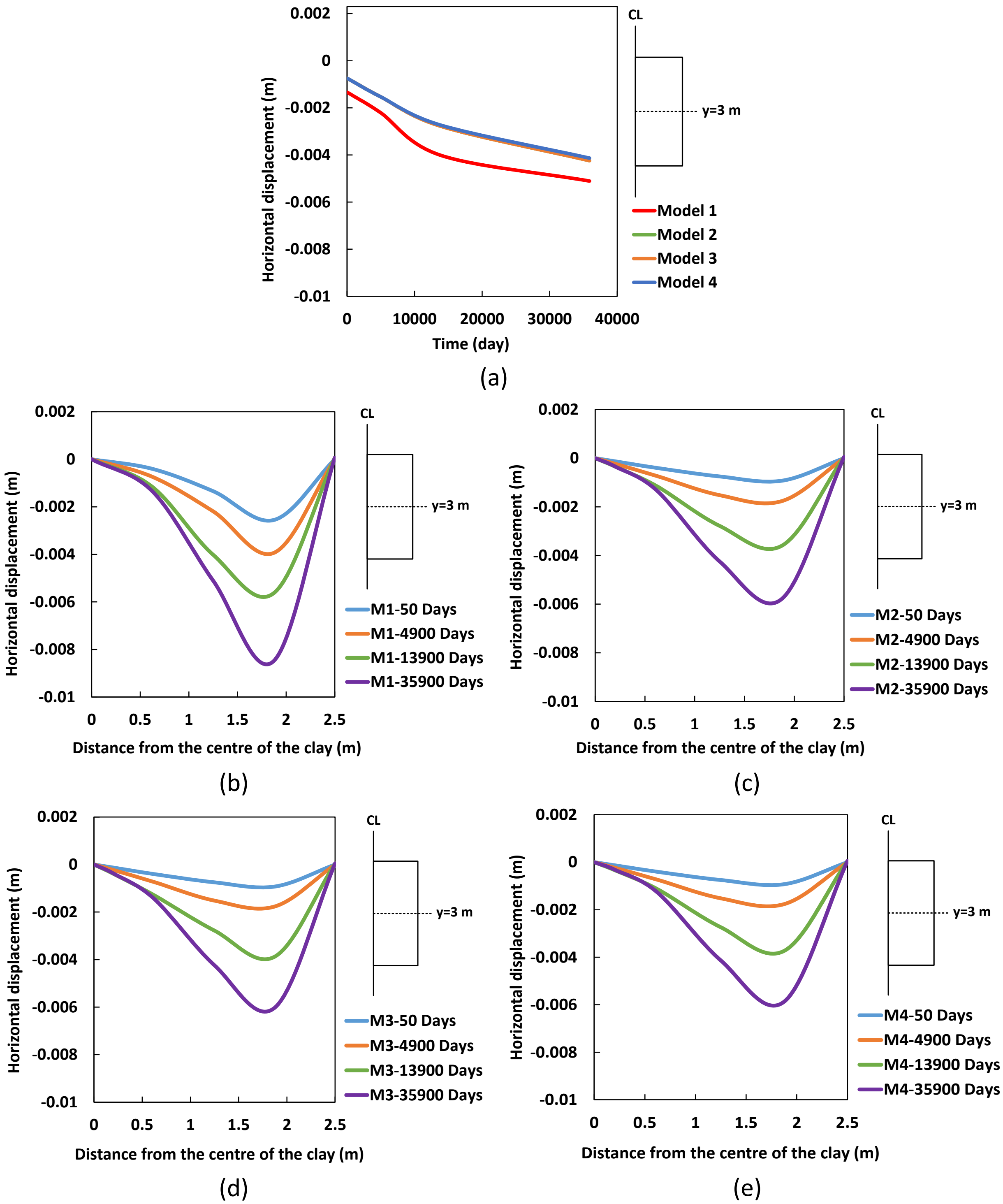

Figure 7-25. Distributions of horizontal (radial) displacements at the mid-height of the clay (y = 3 m)

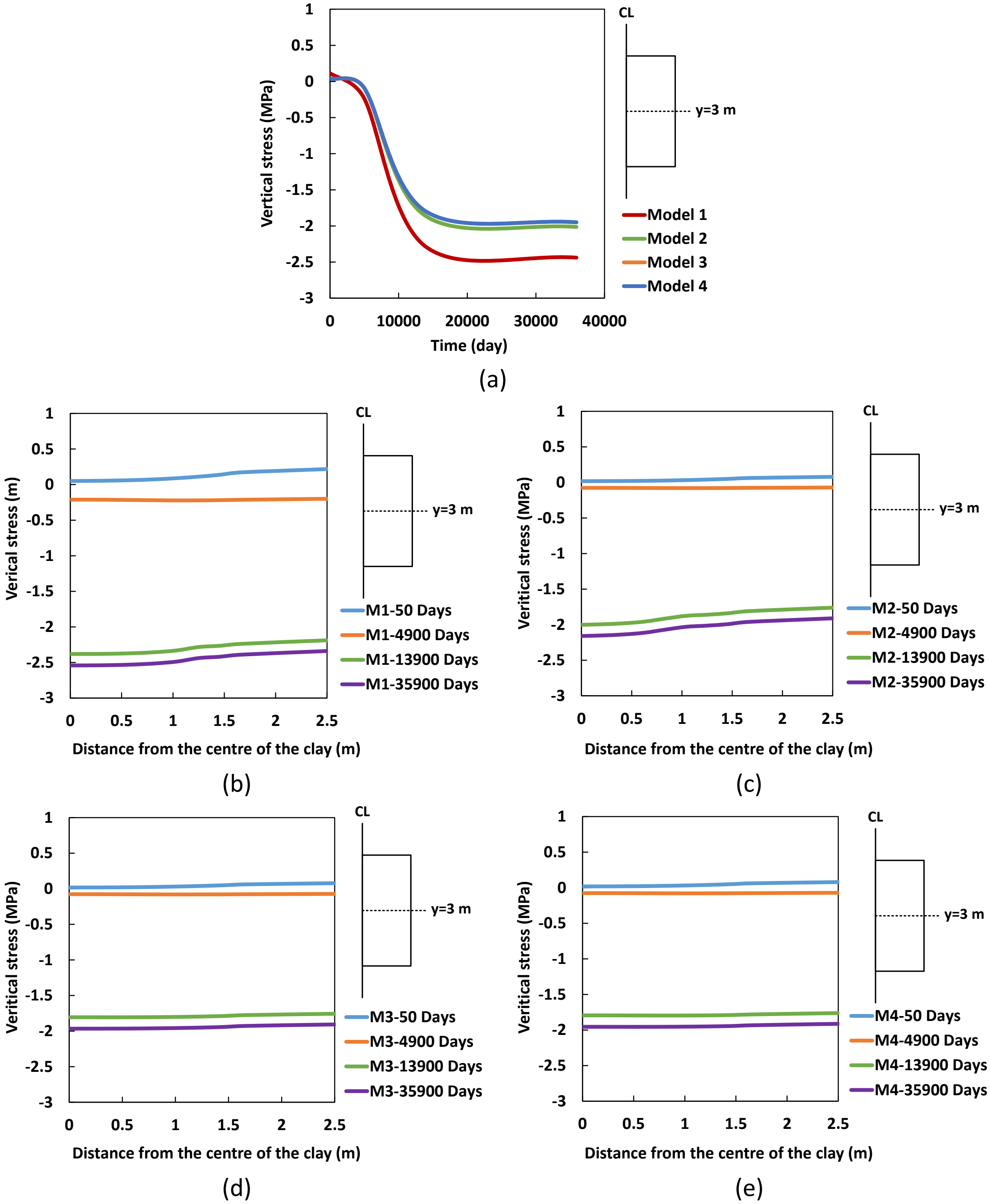

Figure 7-26. Distributions of vertical stresses at the mid-height of the clay (y = 3 m)

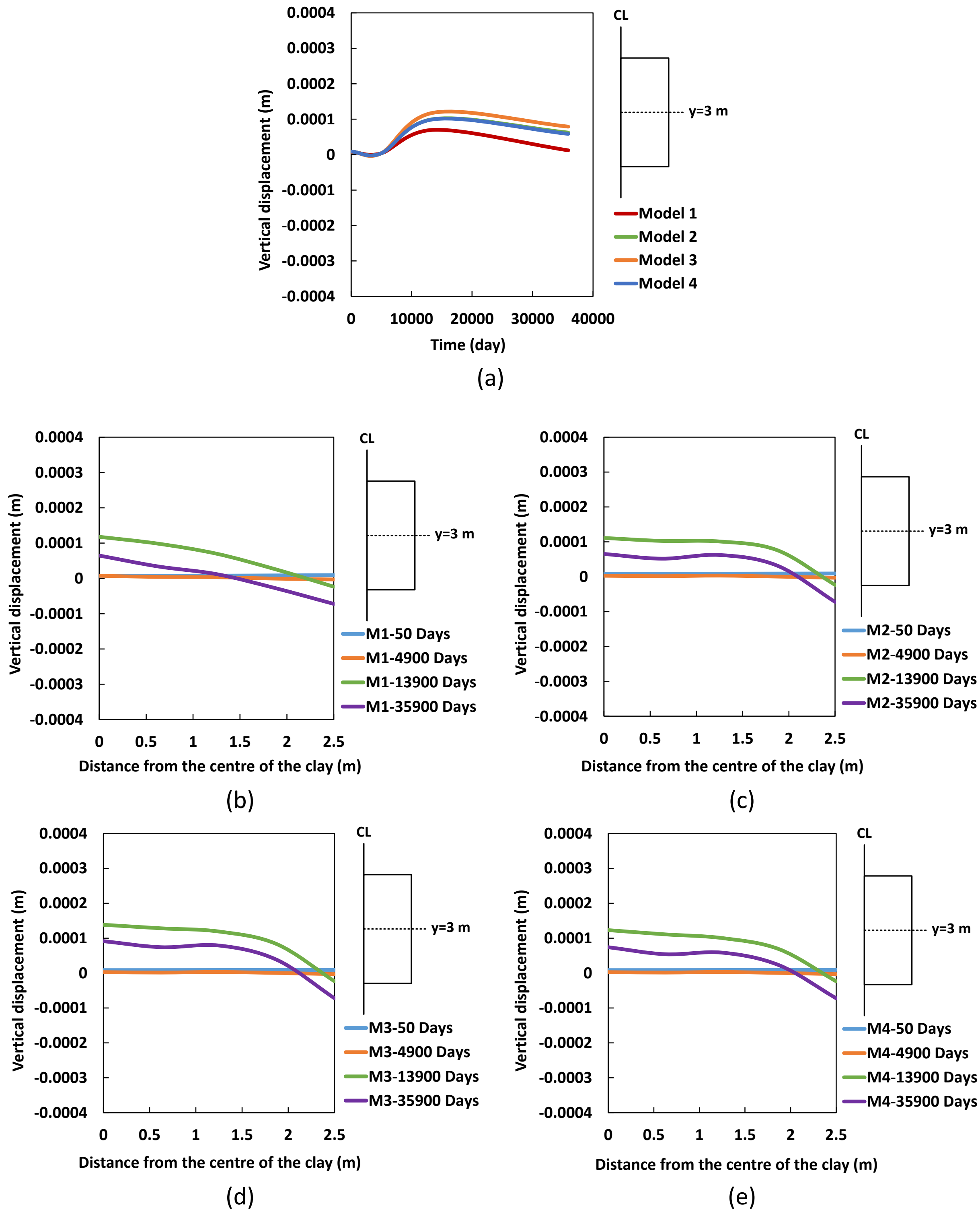

Figure 7-27. Distributions of vertical displacements at the mid-height of the clay (y = 3 m)

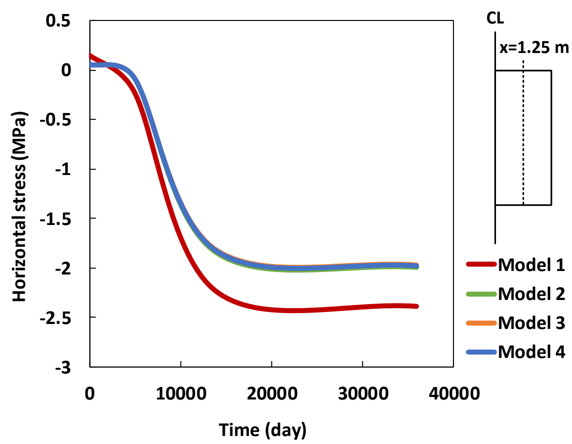

(a)

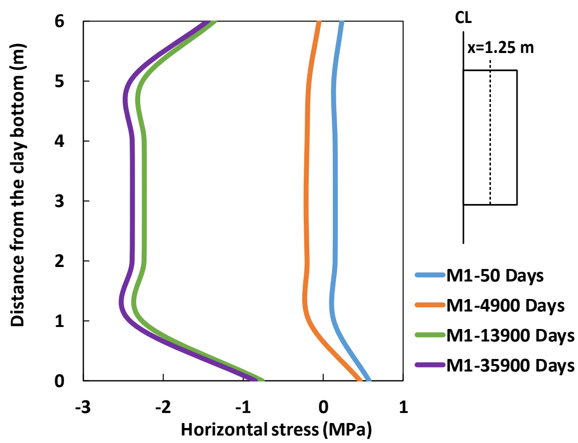

(b)

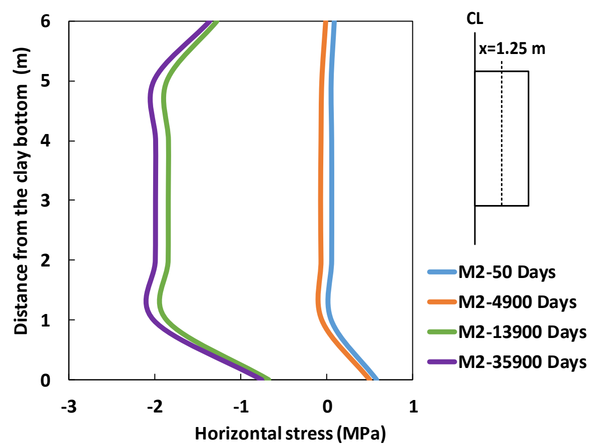

(c)

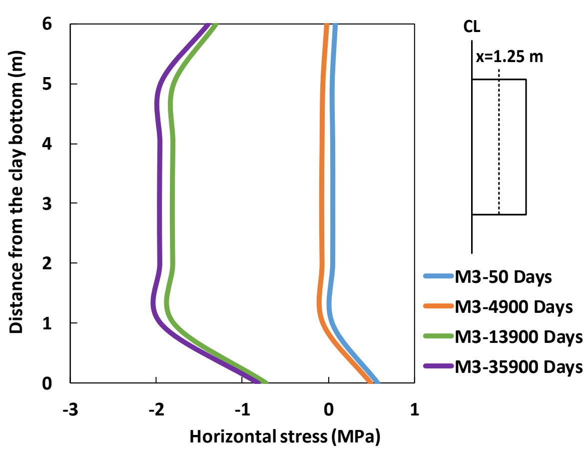

(d)

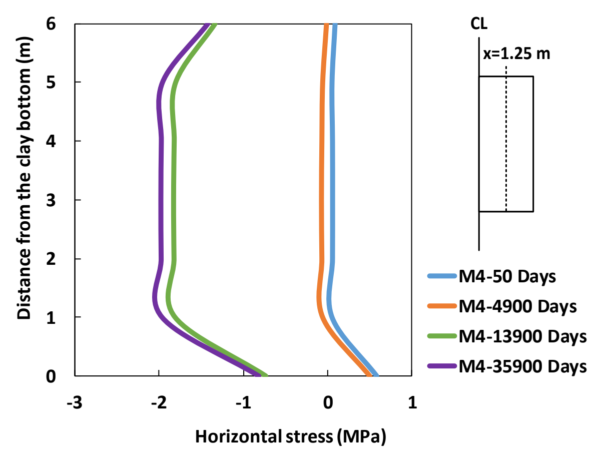

(e)

Figure 7-28. Predicted distributions of horizontal stresses at 1.25 m from the centre of the clay (x = 1.25 m)

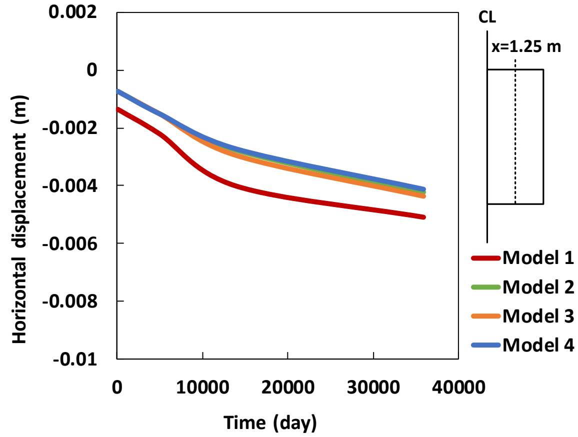

(a)

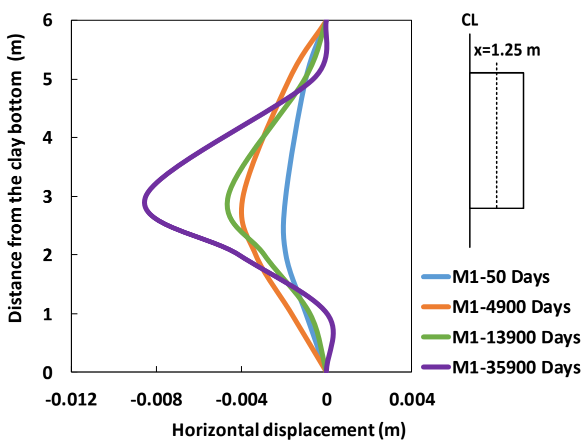

(b)

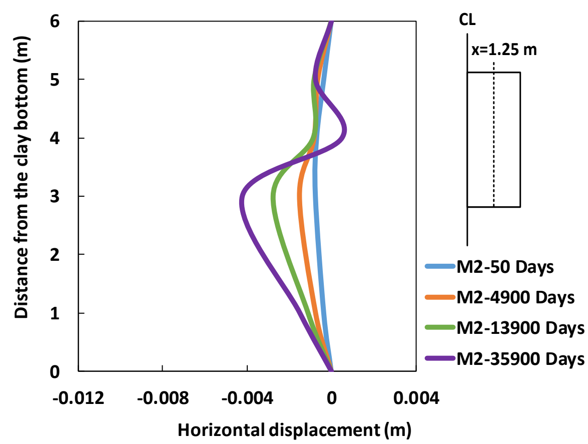

(c)

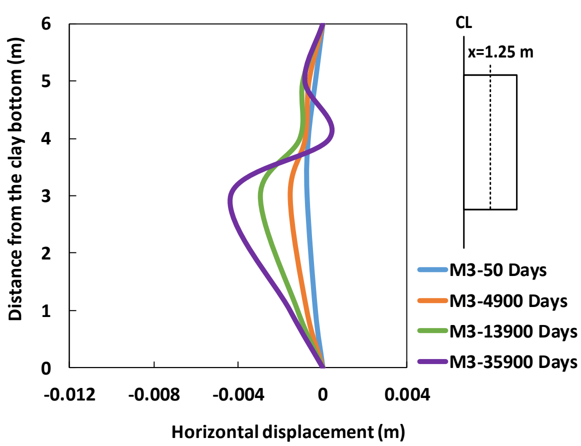

(d)

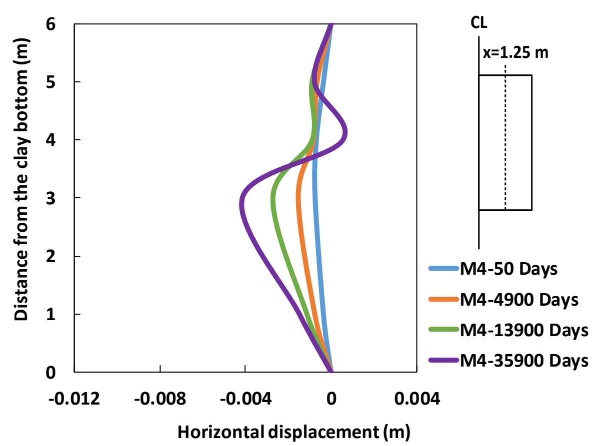

(e)

Figure 7-29. Predicted distributions of horizontal displacements at 1.25 m from the centre of the clay (x = 1.25 m)

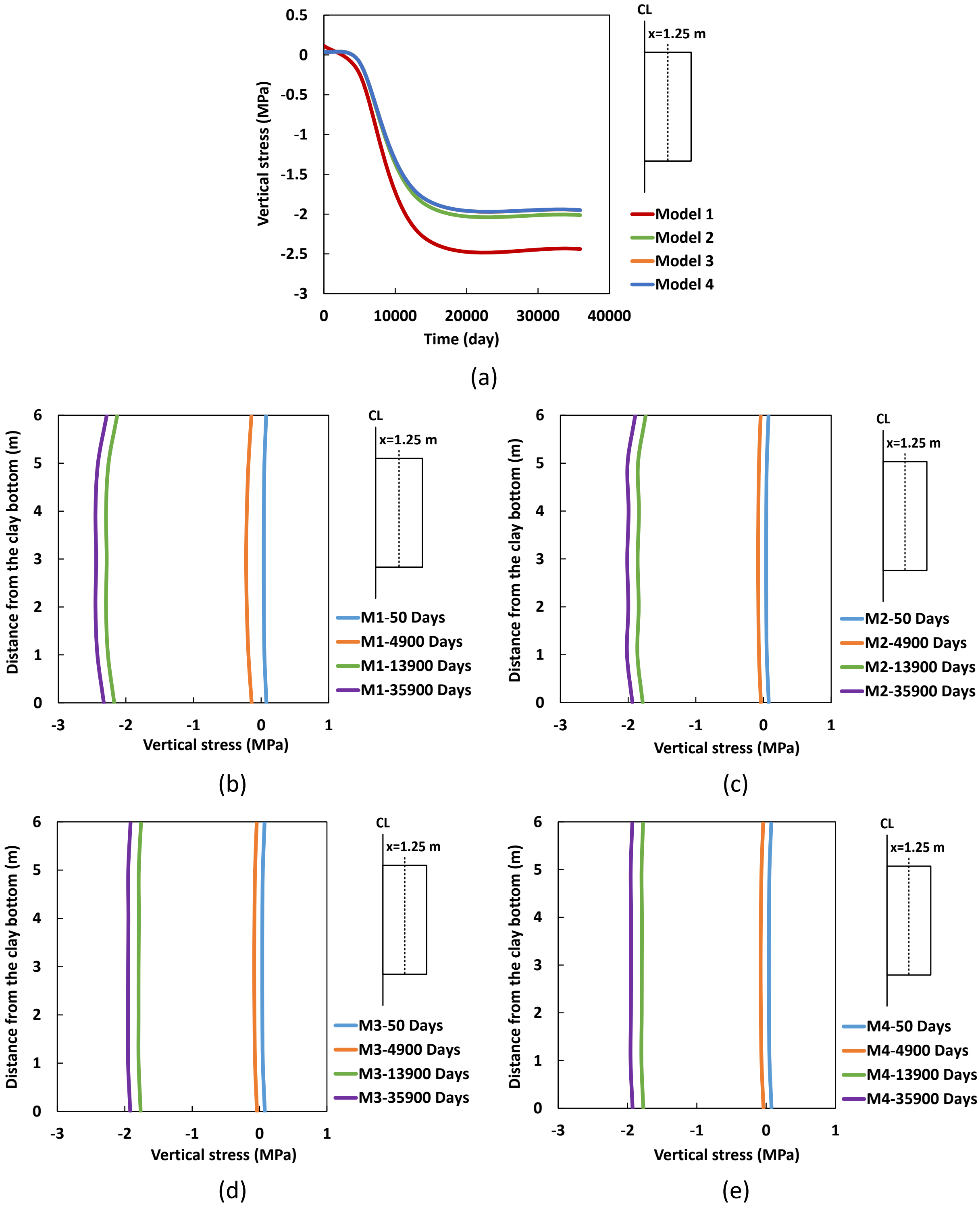

Figure 7-30. Predicted distributions of vertical stresses at 1.25 m from the centre of the clay (x = 1.25 m)

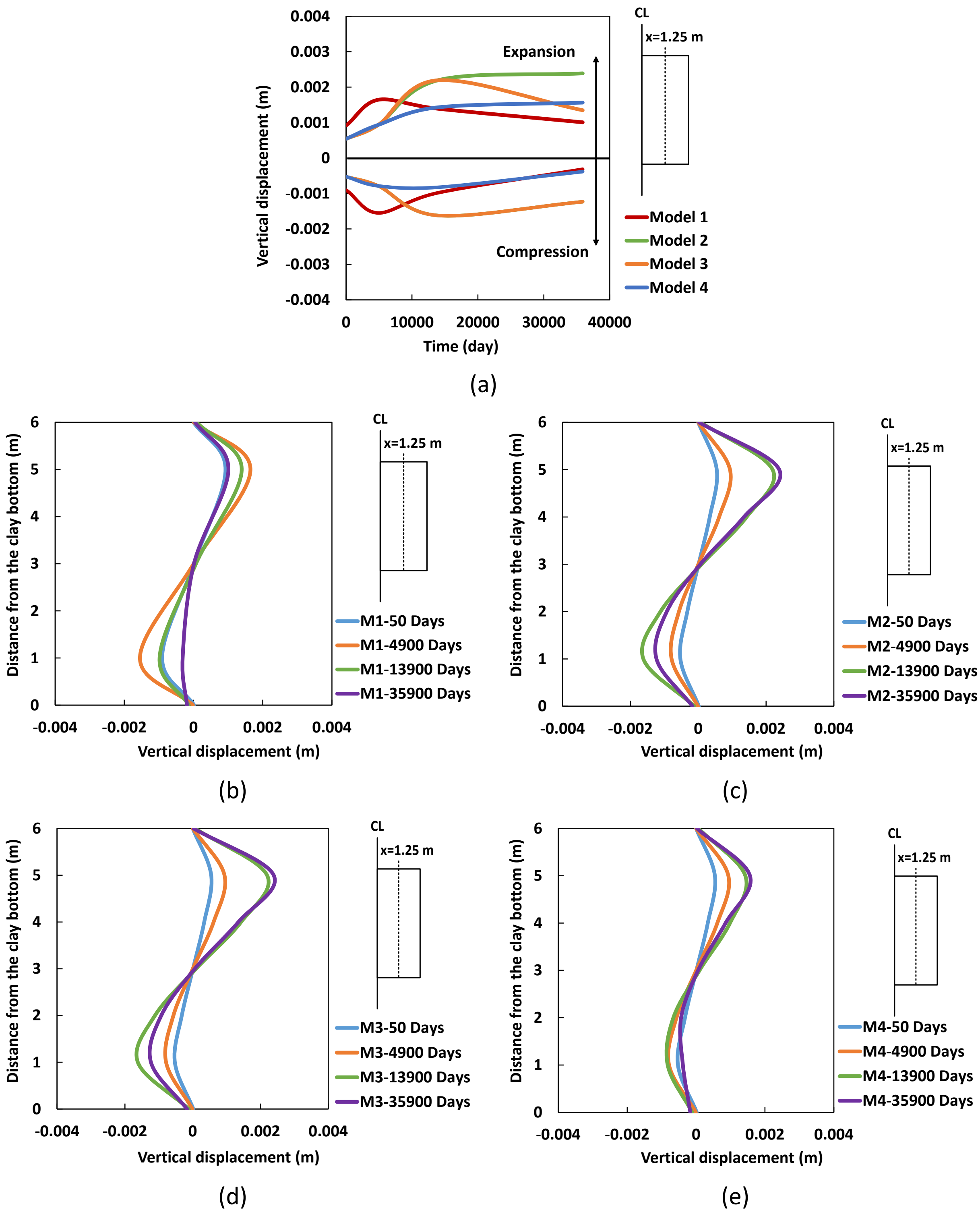

Figure 7-31. Predicted distributions of vertical displacements at 1.25 m from the centre of the clay (x = 1.25 m)

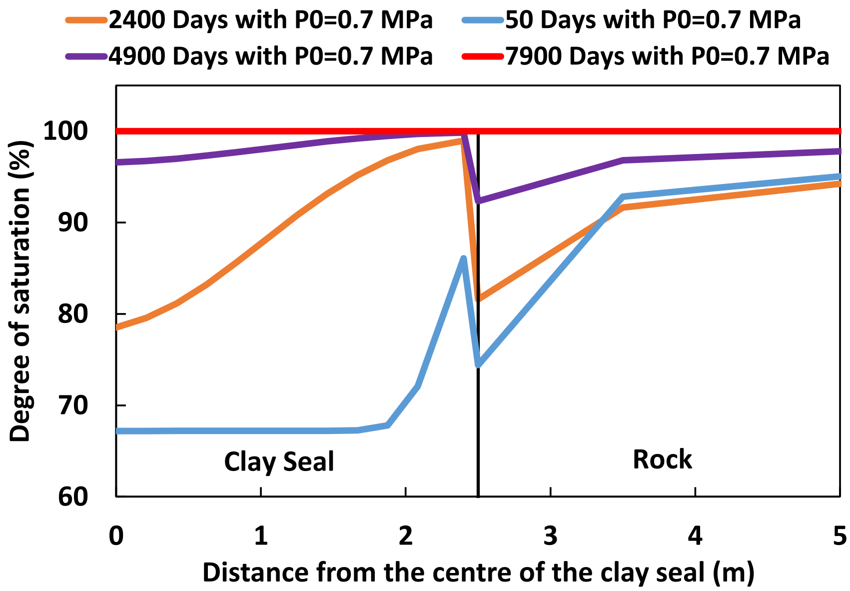

Figure 7-32. Distribution of degree of saturation at various times in the clay and rock for Model 1

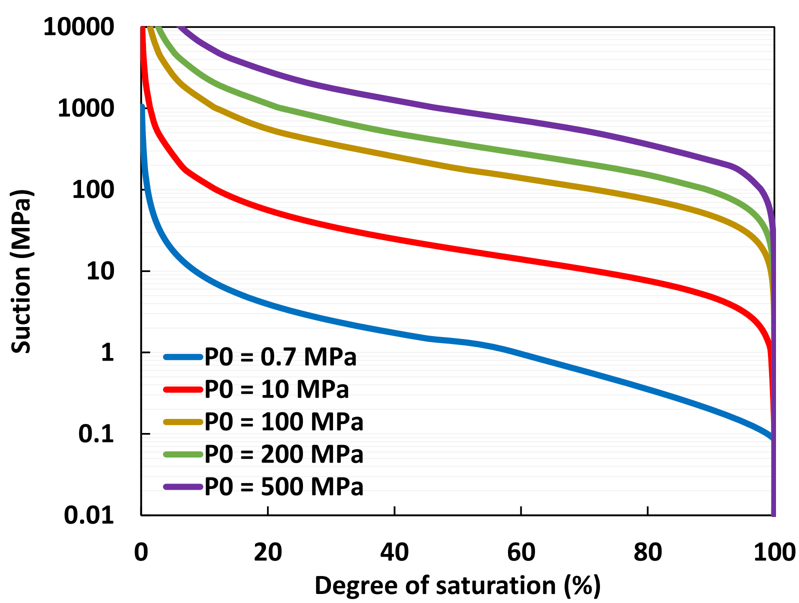

Figure 7-33. Water retention curves for the host rock with various air entry pressures

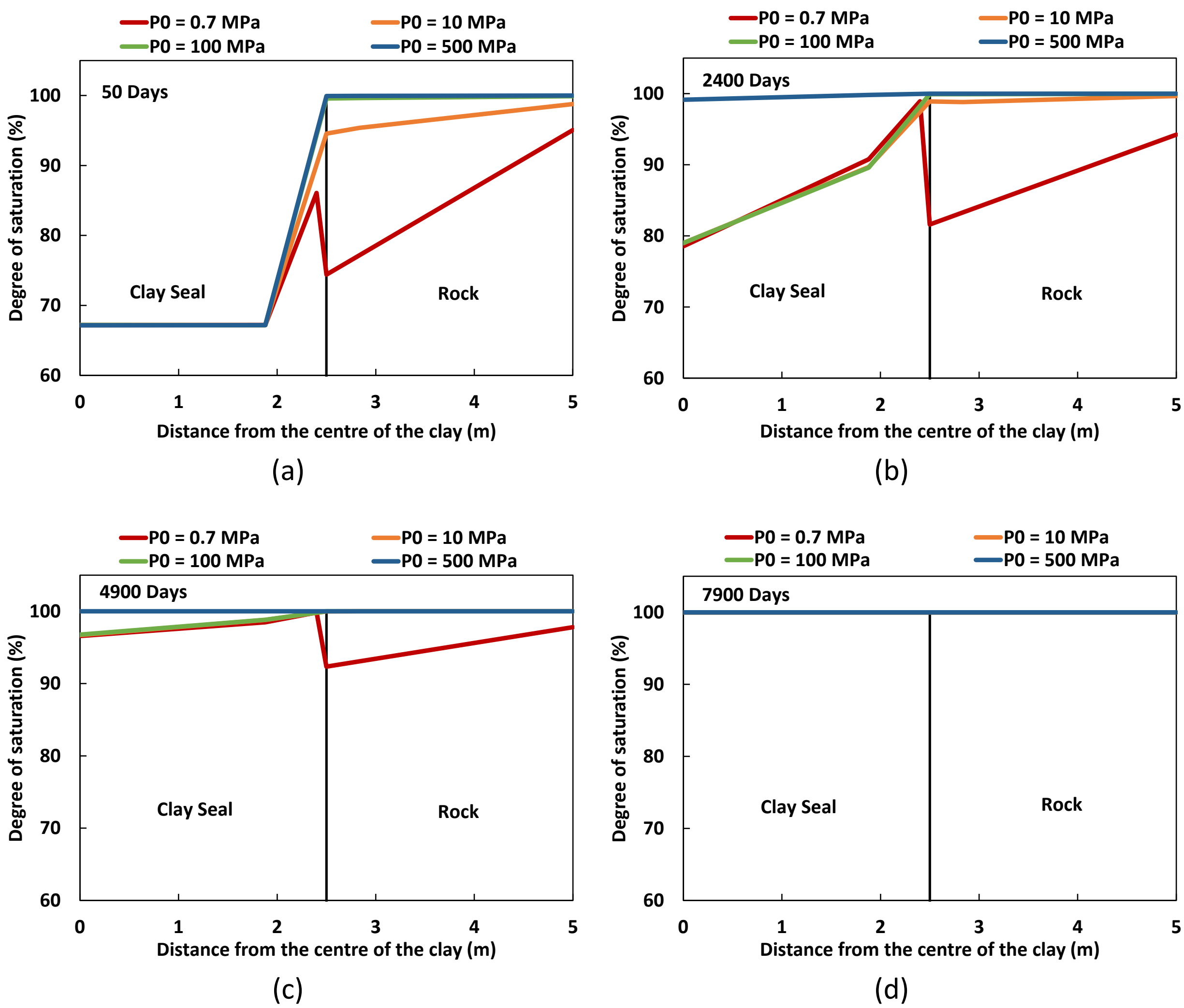

Figure 7-34. Predicted degrees of saturation with various air entry pressures of the host rock

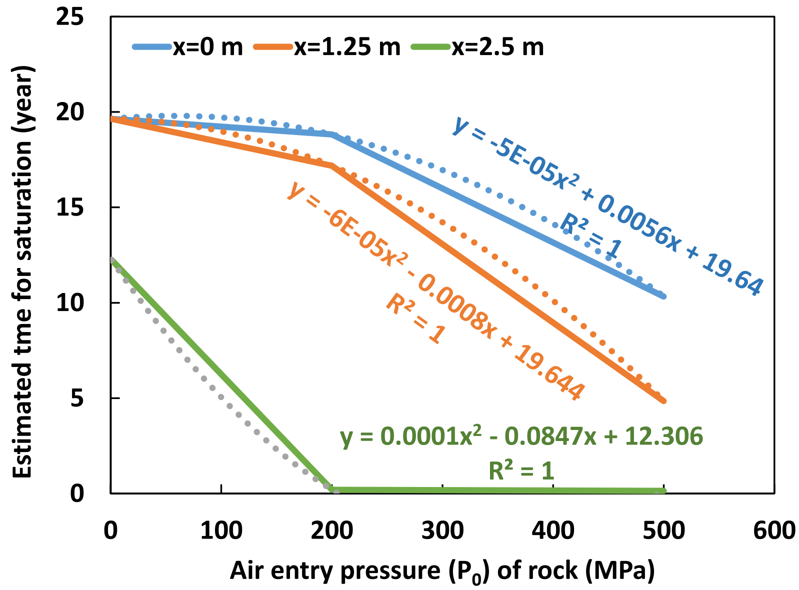

Figure 7-35. A relationship between the air entry pressure of the rock and hydration time of the clay

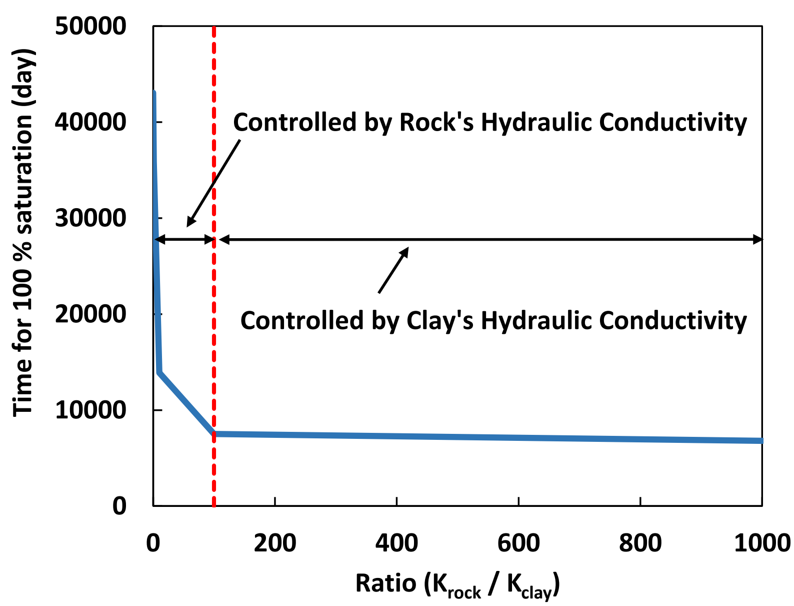

Figure 7-36. Hydration times of the clay by variations of hydraulic conductivity of the rock (x = 1.25 m and y = 3 m)

CHAPTER 8

REVIEW, CONCLUSIONS, CONTRIBUTIONS AND RECOMMENDATIONS FOR FUTURE WORK

8.1. Review and Summary

This research was intended to achieve following objectives: (1) determine representative hydraulic-mechanical parameters of the shaft sealing components such as clay seal and host rock and (2) develop numerical design tools to predict the performance of the shaft sealing system. The preceding chapters have described determination of H-M model parameters using extensive laboratory data, development of numerical models and comparisons of numerical predictions with field readings for the performance of the shaft sealing system. These chapters are reviewed and summarized as follows:

<u>Chapter 3: Interpretation of ESP field readings</u>

Based on monitoring data collected from 2009 to 2015, the data show that

(1) As of December 2015, hydration of the core of the clay component was still progressing and the core of the clay component was not fully saturated.

(2) Only a very gradual increase in the water content of the clay component occurred in the central portions of the clay component. During 2014, the four TDRs indicated only a small increase in the water content of the clay component. In 2015, all of the TDR sensors

started showing discernible increases in the water content of the clay component. The lowermost TDR1 showed 100% saturation and the other TDR sensors located at or above the mid-height of the clay component showed degree of saturation approximately from 75% to 90%.

(3) Based on laboratory data for swelling pressures in the same material, it is anticipated that on achieving saturation and complete flooding of the shaft, the swelling pressure component of total pressure will be of the order of 800 kPa and the pore water pressure component will be approximately 2500 kPa. This will result in a total pressure of approximately 3300 kPa that should be measured by the total pressure sensors (TPC) (Dixon et al. 2012). As of December 2015, under the existing hydraulic pressures, a saturated system would have been experiencing total pressures of the order of 2050 kPa at the lower concrete-clay interface. This was not observed by any of the sensors. This indicates that the clay component has not been saturated yet.

Chapters 4 and 5: Theoretical background and Numerical Modelling of Shaft Sealing System

Deviations of the governing balance equations that are adopted in CODE_BRIGHT (Vaunat and Olivella 2002) for mass balance, internal energy balance and momentum balance have been described. The constitutive laws selected for constitutive models are used for hydraulic-mechanical behaviour of the sealing components in both the saturated and unsaturated regimes.

Coupled H-M constitutive models have been developed using the CODE_BRIGHT program (Vaunat and Olivella 2002). The H-M parameters used in these models for the sealing components were calibrated using laboratory measurements. The hydraulic parameters of the sealing components were defined through use of van Genuchten's (1980) model and extensive laboratory test data related to the soil-water retention relationships. The Basic Barcelona Model (BBM), an elastoplastic constitutive model, (Alsonso et al. 1990) was used to describe the mechanical behaviour of the sealing system components.

Of the three cases that were used in the modelling, Case 3 with groundwater seepage applied in the bottom and outer regions shows a dramatic decrease in suction in the outer region in the initial stage of system wetting. However, the additional wetting process in the region affects only changes in suction at a very early stage of system wetting, but does not significantly affect the rate of decrease in suction after the early stage. The possible reason for this phenomenon is that once the edge regions become hydrated and start to swell, the swelling mechanism becomes dominant to control its hydraulic behaviour.

Numerical prediction shows a reasonable match with the field TDR readings for the water uptake trends of the clay seal component, although it slightly overpredicts the time required for the core of the clay component to achieve water saturation.

The predicted vertical pressures using CODE_BRIGHT (Vaunat and Olivella 2002) are in the range of 2.5 MPa to 2.7 MPa after 100 years, which are not far from the final vertical pressure of 3.3 MPa anticipated after the clay seal comes to equilibrium. Predicted distributions of the horizontal pressure and displacement along a vertical line, 1.25 m from the centre of the clay seal clearly indicate that horizontal pressures are dominantly developed along the location of FZ2.

Chapter 6: Evolution of Swelling Pressure of the Clay

Prediction of swelling pressure for the unsaturated clay component has been discussed in Chapter 6. Two models were introduced to estimate evolution of swelling pressure. The first model proposed by Liu (2013) using crystalline and osmotic swelling mechanisms estimates a swelling pressure of 0.86 MPa, which is close to what is expected in the field (0.8 MPa). The second model suggested by Dueck and Börgesson (2007) estimates a lower swelling pressure of 0.41 MPa for a confined condition. Considering the confined condition (that is, a constant volume condition) where the clay seal is sandwiched by the concrete segments and surrounded by the host rock, development of the swelling pressure can be affected by the confinement. The amount of infiltrated water can be minimized when swelling is restricted because volume change conditions significantly influence the hydraulic conductivity through microstructure changes.

The model predictions were verified in terms of the water retention capacity of the unsaturated clay seal. Suction predictions using the two models show reasonably good agreement with the measured data even though the first model shows slight deviation.

Chapter 7: Sensitivity Analysis of Hydraulic-Mechanical Parameters

The influence of critical hydraulic-mechanical parameters on the evolution of H-M behaviour of the sealing components have also been investigated. From different sets of the H-M parameters obtained through calibration processes, a series of numerical modelling exercises was performed.

By varying of the water retention parameters P_0 and β_1, numerical predictions have clearly demonstrated (1) the effect of hysteretic behaviour of the clay on it water uptake times of the clay, (2) the relationship between hydration process times and the water retention parameters P_0 and β_1, and (3) improvement in predicting the hydraulic behaviour of the clay.

Numerical prediction using the hydraulic parameters of P_0 and β_1 obtained for drying cycles indicates almost three times quicker hydration time for full saturation than those for wetting cycles. This comparison clearly shows the effect of hysteretic behaviour of the clay on its water uptake times. Different values of the water retention parameters of P_0 and β_1 can be determined from the same clay material and consequently result in different predictions of the clay's hydraulic behaviour. Therefore, selection of the water retention parameters is fundamentally important for numerical modelling to obtain qualitative and representative results.

Numerical prediction using different BBM mechanical parameters indicates that mechanical behaviour of the clay seal is not significantly sensitive to changes in the parameters within the range of their variations. That can be probably due to that the clay seal is confined by the sounding rock and concrete components.

The effects of desaturation of the rock on the hydraulic behaviour of the shaft sealing components have been investigated. The rock with a lower air entry pressure shows significant desaturation in the region adjacent to the clay and results in slower hydration process of the clay. On the other hand, rock with a greater air entry pressure remains fully saturated and much quicker hydration times are obtained with a greater air entry pressure of the rock. It is noted that desaturation of the EDZ was not observed in the actual field conditions of the ESP. The possible reason for no desaturation in the EDZ could be a relatively high initial degree of saturation (~67%) of the clay seal and therefore the suction corresponding to the degree of saturation was not high enough to withdraw water from the EDZ.

An analysis focusing on effects of changes in hydraulic conductivity of FZ2 on hydration times of the clay allows for distinguishing two hydraulic zones in which the hydration process is controlled by either the hydraulic conductivity of the rock or the hydraulic conductivity of the clay. When the ratio of the saturated hydraulic conductivity of the FZ2 to that of the clay (K_{FZ2} / K_{clay}) is higher than 100, hydration times are controlled by the clay's hydraulic conductivity. By contrast, when the ratio is lower than 100, hydration time of the clay is dominantly affected by the rock's hydraulic conductivity. In the ESP, the ratio of FZ2's hydraulic conductivity to the clay's hydraulic conductivity is 1000 and therefore, the clay's hydraulic conductivity controls the hydration time of the clay.

8.2. Conclusions

Chapter 1 presented four hypotheses that formed the basic of the work described in succeeding chapters. Conclusions related to these hypotheses can be made as follows:

Hypothesis 1*: Hydraulic-mechanical (H-M) model parameters calibrated from laboratory tests can improve prediction of the coupled H-M behaviour of the clay seal.*

Conclusions for hypothesis 1 can be drawn from Sections 7.2 and 7.3. These sections show that the parameter calibration using extensive laboratory test data on the same clay material allows for determining various sets of H-M parameters. Numerical simulations using the calibrated H-M parameters provide close matches to the field behaviour.

Hypothesis 2*: Numerical modeling can provide a better understanding of the evolution of swelling pressures generated by the clay seal.*

Referring to Chapter 6, two prediction models were introduced to estimate development of swelling pressure of the unsaturated clay seal during water uptake. Since numerical modelling using CODE_BRIGHT (Vaunat and Olivella 2002) was limited to provide evolution of swelling pressure of the clay seal, numerically computed porosity values obtained from CODE_BRIGHT (Vaunat and Olivella 2002) were used in two prediction models for estimating the evolution of swelling pressure of the unsaturated clay seal. The first model using crystalline and osmotic swelling mechanisms estimates the maximum swelling pressure of 0.86 MPa in the centre of the clay seal, while for a confined condition, the second model estimates the maximum swelling pressure of 0.41 MPa in the same region. The prediction models using the computed porosity provide good understanding of evolution of swelling pressure during water uptake.

Hypothesis 3*: Inclination of the fractured zone (FZ2) simulating field conditions can affect the H-M model performance of the clay seal, compared to more simplified use of horizontally-oriented FZ2.*

Conclusions for hypothesis 3 can be made from Section 5.3.3, which describes the effect of groundwater flow from an inclined FZ2 on the predicted total pressures. The numerical model with inclined FZ2 can have a relatively higher pressure gradient that can allow for more quantity of groundwater flowing to the clay seal than the model with perfectly horizontal FZ2. Consequently, an increase in quantity of groundwater toward the clay seal can increase the clay seal's hydration process rate. The phenomenon showing slightly greater total pressures in the prediction with inclined FZ2 can result from this different pressure gradient.

Hypothesis 4*: Available experimental methods have limitations in explaining the long-term H-M equilibrium processes, and so well-calibrated numerical modeling can provide better understanding of the long-term performance of clay seal component.*

One of the most critical aspects in the safety assessment of disposal facilities is how to explain their evolution for a long period on the basis of observations that are limited in time. Referring to Chapters 5, 6 and 7, numerical modelling using CODE_BRIGHT (Vaunat and Olivella 2002) allows simulation of complex coupled hydraulic-mechanical processes of the shaft sealing components, critical analysis of the H-M parameters, and examination of the development of total pressure, swelling pressure and displacement of the clay component for 100 years.

8.3. Contributions

The major contributions resulting from the research are summarized as follows:

1 The H-M behaviour of the in situ main shaft seal was numerically examined and numerical results were compared with monitoring data obtained from real field conditions. This main shaft seal was the first in situ shaft seal constructed as part of Canada's deep geological repository concept. Numerical predictions compared with the field readings provide valuable information on long-term performance of a repository seal system and show what environmental parameters are critical in hydration process (Chapters 3 and 5).

2 During water uptake, evolution of swelling pressure of the clay seal at the mid-height and centre region was assessed using two different approaches. This work has not been previously conducted by any other researchers in the field. The first approach suggested by Liu (2013) was a theoretical approach using mechanisms of crystalline swelling and osmotic swelling of the clay. The second approach suggested by Dueck and Börgesson (2007) was based on empirical relationships. These two approaches show reasonable evolution of swelling pressure during water uptake and provide detailed insights into the swelling mechanism of the partially saturated clay seal (Chapter 6).

3 This research has performed the first ever sensitivity analysis of H-M model parameters. Various sets of H-M parameters were determined through calibration processes using extensive laboratory test data on the same bentonite-sand mixtures. These H-M parameters affect the performance of the clay seal (Chapter 7).

4 This research has assessed the effects of desaturation of the rock on the hydraulic behaviour of the clay seal, and provided a relationship between the air entry pressure of the rock and hydration time of the clay. This relationship has not been previously proposed by any other researchers (Chapter 7).

5 This research has provided a unique relationship between hydration time of the clay seal and hydraulic conductivity of the rock. This relationship allows for estimating hydration time of the clay seal, depending on a value of hydraulic conductivity of the rock (Chapter 7).

8.4. Recommendations for Future Research

While the major objectives have been achieved, some suggestions have arisen for future research.

(1) A representative water retention curve of the rock near the clay seal needs to be determined.

As described in Section 7.4, the sensitivity study simplified the water retention curve of the rock near the clay. The rock in contact with the clay contains a considerable excavation damaged zone (EDZ) and this EDZ contacts both FZ2 and the water-filled upper and lower parts of the shaft. Under the condition where a hydraulic channel in the EDZ between the upper and lower parts of the shaft is closed, the water retention curve of the rock in this analysis may not be entirely representative of the actual conditions. In addition, the clay seal will seal the micro-cracks and pores in the EDZ during water uptake. For this reason, a representative water retention curve of the rock near the clay seal should be determined and the effects of the EDZ on both the "global" water retention curve and water supply to the clay should be examined.

(2) Swelling behaviour of unsaturated bentonite-sand mixtures during water uptake needs to be investigated.

In most large-scale experiments such as RESEAL in situ shaft-seal test in the Boom clay (Barnichon and Volckaert 2003), FEBEX test in granite (Gens et al. 1998), the Isothermal test in AECL's URL (Thomas et al. 2002) and the Tunnel Sealing Experiment (TSX) in AECL'S URL (Chandler et al 2002), there have been no evaluations of the total, swelling and hydraulic pressure components because these experiments were not run to full saturation and did not reach a stress or density equilibrium. Description of development of swelling pressure during water uptake is limited and therefore is required for further research. Some studies (Thomas et al. 2002, Ballie et al. 2006) only reported development of swelling pressure which was the same as development of total pressure. With time, it could be expected that a stress and density equilibrium will occur and a uniform hydraulic condition might develop that would allow for estimation of swelling, pore water and total pressure components separately. However, a further complication for estimating swelling pressure is the question of whether the distribution of hydraulic gradient across the clay is uniform.

(3) Unavoidable voids generated during installation of the clay seal component need to be considered in performance assessment.

During installation of the clay seal, the centre region achieved a relatively higher dry density than the other regions around the perimeter of the clay seal and near the instrument cables due to difficulties during compaction. In in situ compaction, the differences in dry density are unavoidable. Achieving different dry densities means that the regions around the perimeter of the clay seal and near the instrument cables contain higher void ratios. The resulting higher void ratios can affect the degree of swelling and consequently the hydro-mechanical behaviour of the clay seal. Therefore, a better understanding of the effects of the non-uniform compaction is required in examining the overall performance of the repository.

REFERENCES

Agus, S.S., Schanz, T., and Fredlund, G. 2010. Measurements of suction versus water content for bentonite-sand mixtures, Canadian Geotechnical Journal 47, pp. 583-594

Ahmed, S., Lovell C.W., and Diamonds, S. 1974. Pore sizes and strength of compacted clay, Journal of the Geotechnical Division, ASCE, Vol. 100, pp. 407-425.

Al-Mukhtar, M., Robinet, J. C., Liu, C. W., and Plas, F. 1993. Hydromechanical behaviour of partially saturated low porosity clays. Proceedings of the International Conference on Engineered Fills, Newcastle-Upon-Tyne, U.K., pp. 87–98.

Alonso, E.E., Gens, A., and Hight, D.W. 1987. General report special problem soils. Proc. 9th Eur. Conf. Soil Mech. Found. Eng. 3, pp. 1087-1146.

Alonso, E.E., Gens, A., and Josa, A. 1990. A constitutive model for partially saturated soils. Geotechnique 40, pp. 405-430.

Anderson, D.E.S. 2003. Evaluation and comparison of mechanical and hydraulic behaviour of two engineered clay sealing material. M.Sc. Thesis, Dept. Civil Engineering, University of Manitoba, Winnipeg, Manitoba.

Baille, W., Lang, L., Tripathy, S., and Schanz, T. 2016. Influence of effective stress on swelling pressure of expansive soils. E3S Web of Conferences Vol. 9, 3rd European Conference of Unsaturated Soils, article number 14016.

Barnichon, J.D. and Volckaert G. 2003. Observations and predictions of hydromechanical coupling effects in the boom clay, Mol Underground Research Laboratory, Belgium, Hydrogeology Journal 11 (1), 193-202.

Baroghel-Bouny, V., Mainguy, M., Lassabatere, T., and Coussy, O. 1999. Characterization and identification of equilibrium and transfer moisture properties for ordinary and high-performance cementitious materials, Cement and Concrete Research, 29, pp. 1225-1238.

Bear, J. and Bachmat Y. 1986. Macroscopic modelling of transport phenomena in porous media. 2: Application to mass, momentum and energy transport, Transport in Porous Media 1, pp. 241-269.

Bear, J., Bensabat J., and Nir A. 1991. Heat and mass transfer in unsaturated porous media at a hot boundary. One-dimensional analytical model. Transport in Porous Media 6, pp.281-298.

Blatz, J.A. 2000. Elastic-plastic modeling of unsaturated high-plastic clay using results from a new triaxial test with controlled suction. Ph.D. Thesis, Department of Civil Engineering, University of Manitoba.

Blatz, J.A., Anderson, D.E.S., and Siemens G. 2006. Evaluation of the transitional inelastic behaviour of unsaturated clay-sand mixtures. Canadian Geotechnical Journal 44, pp. 436-446.

Blatz, J.A. and Graham, J. 2003. Elastic-plastic modeling of unsaturated high-plastic clays using results from a new triaxial test with controlled suction. Geotechnique 53 (1), pp. 113-122.

Bock, H. 2001. Experiment Rock Mechanics Analyses and Synthesis: Data Report on Rock Mechanics. Mont Terri Tech. Rep. TR 2000-02.

Borgesson, L. and Heinlein, J. 2003. Hydraulic bentonite/rock interaction in FEBEX experiment. Proceedings of the international symposium on large scale field tests in granite, Sitges, Barcelona, Spain, Advances in understanding engineered clay barriers.

Bucher, F., Jedehauser, P., and Mayor, P.-A. 1986. Permeability and shrinkage tests for quarzsand-bentonite mixtures. Technical report 86-13, Nagra, Switzerland.

Chandler, N.A. 2000. Water inflow calculation for the Isothermal Buffer-Rock-Concrete Plug Interaction Test. Ontario Power Generation, Nuclear Waste Management Division Report No. 06819-REP-01200-10046-R00.

Chandler, N. A., Dixon, D.A., Fairhurst, C., Hansen, F., Gray, M., Hara, K., Ishijima, Y., Kozak, E., Martino, J., Masumoto, K., McCrank, G., Sugita, Y., Thompson, P., Tillerson, J., and Vignal, B. 2002. The five year report on the tunnel sealing experiment: an international project of AECL, JNC, ANDRA and WIPP. Atomic Energy of Canada Limited Report, AECL-12127, AECL.

Chen, B., Qian L.X., Ye W.M., Cui Y.J., and Wang J. 2006. Soil-water characteristic curves of 305 Gaomiaozi bentonite. Chinese Journal of Rock Mechanics and Engineering, Vo1.25(4), pp. 788-793.

CODE_BRIGHT User's Guide. 2015. https://www.etcg.upc.edu/recerca/webs/code_bright/code_bright.

Cui, Y. J., Loiseau, C., and Delage, P. 2002. Microstructure changes of a confined swelling soil due to suction controlled hydration. Proc. 3rd International Conference on Unsaturated Soils, Recife 2, pp. 593–598.

Cui, S.L., Zhang, H.Y., and Zhang, M. 2012. Swelling characteristics of compacted GMZ bentonite–sand mixtures as a buffer/backfill material in China, Engineering Geology 141–142, pp. 65–70.

Delage, P. and Graham, J. 1995. Understanding the behavior of unsaturated soils requires reliable conceptual model. State of the Art Report, Proceedings, 1st International Conference on Unsaturated Soils, Paris, France, pp. 1223-1256.

Derjaguin, B.V. and Landau, L.D. 1941. Theory of the stability of strongly charged lyphobic sols of the adhesion of strongly charged particles in solutions of electrolytes, Acta Physiochem. URSS 14, pp. 633–662.

Dixon, D.A., Gray, M.N., and Thomas, A.W. 1985. A study of the compaction properties of potential clay-sand buffer mixtures for use in nuclear fuel waste disposal, Eng. Geol. 21, pp 247-255, Amsterdam.

Dixon, D.A. and Miller, S.H. 1995. Comparison of the mineralogical composition, physical, swelling and hydraulic properties of bentonites from Canada, the United States and Japan. Atomic Energy of Canada Limited Report AECL-11303, COG-95-156.

Dixon, D.A. 2000. Pore water salinity and the development of swelling pressure in bentonite-based buffer and backfill materials. Helsinki, Posiva Report, POSIVA 2000-04 (ISBN 951-652-090-1).

Dixon, D.A., Chandler N.A., and Baumgartner P. 2002. The influence of groundwater salinity and interfaces on the performance of potential backfilling materials. In Proceedings of the 6th International Workshop on design and Construction of Final Repositories, Backfilling in Radioactive Waste Disposal, Brussels, ONDRAF/NIRAS, Brussels, Belgium. Transactions, Session IV, Paper 9.

Dixon, D.A., Martino, J., and Onagi, D. 2009. Enhanced Sealing Project (ESP): Design, construction and instrumentation plan. Nuclear Waste Management Organisation (NWMO) APM-REP-01601-0001, Toronto, Canada.

Dixon, D.A, Martino, J., Holowick, B., and Priyanto, D. 2011. Enhanced sealing project: monitoring the THM response of a full-scale shaft seal. Canadian Nuclear Society (CNS) Conference, Decommissioning and Environmental Restoration for Canada's Nuclear Activities, Toronto, Canada.

Dixon, D.A., Priyanto, D., and Martino, J. 2012. Enhanced sealing project: project status and data report for period ending 31 December 2011, Nuclear Waste Management Organisation (NWMO) APM-REP-01601-0005, Toronto, Canada.

Dixon, D.A., Martino, J., Priyanto, D., and Kim, C-S. 2012. Three Years of Monitoring a Full-Scale Shaft Seal in a Granitic Rock Formation. GeoManitoba, 65th Canadian Geotechnical Society (CGS) Conference, Winnipeg, Manitoba.

Dueck, A. 2004. Hydro-mechanical properties of a water unsaturated sodium bentonite, laboratory study and theoretical interpretation. PhD-thesis, Lund Institute of Technology, Sweden.

Dueck, A. and Börgesson, L. 2007. Model suggested for an important part of the hydro-mechanical behaviour of a water unsaturated bentonite. Engineering Geology 92, pp. 160-169.

Everitt, R.A., Brown, A., Davison, C.C., Gascoyne, M., and Martin, C.D. 1990. Regional and local setting of the Underground Research Laboratory. In Proceedings of the Symposium on Unique Underground Structures, Denver, Colorado, pp. 64-1 - 64-23.

Faust, C.R. and Mercer, J. W. 1979. Geothermal reservoir simulation: 1. Mathematical models for liquid-and vapour-dominated hydrothermal systems, Water Resour. Res. 15(1), pp. 23-30.

Ferrage, E., Lanson, B., Sakharov, B.A., and Drits, V.A. 2005. Investigation of smectite hydration properties by modeling experimental X-ray diffraction patterns. Part I. Montmorillonite hydration properties, Am. Mineral. 90, pp. 1358–1374.

Ferrage, E., Lanson, B., Sakharov, B.A., Geoffroy, N., Jacquot, E., and Drits, V.A. 2007. Investigation of dioctahedral smectite hydration properties by modeling of X-ray diffraction profiles: influence of layer charge and charge location, Am. Mineral. 92, pp. 1731–1743.

Fredlund, D.G. and Houston, S.L. 2013. Interpretation of soil-water characteristic curves when volume change occurs as soil suction is changed. Advances in Unsaturated Soils, London, ISBN 978-0-415-62095-6.

Fredlund, D G. and Rahardjo, H. 1993. Soil mechanics for unsaturated soils. John Wiley & Sons, Inc.

Fung, Y.-C. and Tong, P. 2001. Classical and computational solid mechanics. World Scientific.

Garcia-Sineriz, J L., and Barcena, I. 2003. Reliability of THM instrumentation for underground research laboritories. Advances in Understanding Engineered Clay Barriers: Proceedings of the International Symposium on Large Scale Field Tests in Granite. Sitges, Spain.

Gens, A. and Alonso, E.E. 1992. A framework for the behaviour of unsaturated expansive clays. Canadian Geotechnical Journal, 29, PP. 1013-1032.

Gens, A., Alonso, E.E., Suriol, J., and Lloret, A. 1995. Effect of structure on the volumetric behaviour of a compacted soil. 1st International Conference on Unsaturated Soils. Paris, Balkema. 1: 83-88.

Gens, A., Garcia-Molina, A.J., Olivella, S., Alonso, E.E., and Huertas, F. 1998. Analysis of a full scale in situ test simulating repository conditions. International Journal for Numerical and Analytical Methods in Geomechanics, Vol. 22, pp. 515-548.

Graham, J., Gray, M.N., Sun, B.C.-C., and Dixon, D.A. 1986. Strength and volume change characteristics of a sand-bentonite buffer. Proc. 2ND Int. Conf. Radioactive Waste Management, Winnipeg, Manitoba, pp. 188-194.

Graham, J., Saadat, F., Gray, M.N., Dixon, D.A., and Zhang, Q.-Y. 1989. Strength and volume change behaviour of a sand-bentonite mixture. Canadian Geotechnical Journal, Vol. 26, pp. 292-305.

Graham, J., Oswell, J.M., and Gray, M.N. 1992. The effective stress concept in saturated sand–clay buffer. Canadian Geotechnical Journal 29 (6), pp. 1033-1043

Graham, J., Chandler, N., Dixon, D.A., and Roach, T.T., and Wan, A.W.L. 1997. The Buffer/container experiment: results, synthesis, issues. Atomic Energy Canada Limited Report, AECL-11746, COG-97-46-I.

Gray, M. 1993. OECD/NEA International stripa project overview volume III. Stockholm, SKB.

Guo, R. and Dixon, D.A. 2005. Coupled hydro-mechanical modelling of AECL's Isothermal Test and comparison with measured data. Ontario Power Generation Nuclear Waste Management Division Report 06819-REP–01200–10153-R00.

Guvanasen, V. and Chan, T. 2000. A three-dimensional numerical model for thermos-hydro-mechanical deformation with hysteresis in a fractured rock mass, International Journal of Rock Mechanics and Mining Science 39, pp. 89-106.

Huertas, F., Fuentes-Cantillana, J.L., Jullien, F., Rivas, P., Linares, J., Farina, P., Ghoreychi, M., Jockwer, N., Kickmaier, W., Marinez, M.A., Samper, J., Alonso, E.E., and Elorza, F.J. 2000. Full-scale engineered barriers experiment for a geep geologic repository for high-level radioactive waste in crystalline host rock (FEBEX project). Final Report, EUR 19147 EN, European Commission, Nuclear Science and Technology.

Iravanian, A. and Bilsel, H. 2009. Characterization of compacted sand-bentonite mixtures as landfill barriers in North Cyprus Proceedings of the 2nd international conference of new developments in soil Mechanics and geotechnical engineering, Near East University, North Cyprus, pp. 472–479.

Itasca Consulting Group, Inc. 2000. FLAC Fast Lagrangian Analysis of Continua, FISH in FLAC. Minneapolis, Minnesota: Itasca Consulting Group, Inc.

Kelsall, P.C., Case, J.B., and Chabannes, C.R. 1984. Evaluation of excavation-induced change in rock permeability. International Journal of Rock Mechanics and Mining Sciences. Vol. 21(3), pp. 123-135.

Kim, C-S., Priyanto, D.G., Blatz, J.A., Siemens, G.S., Siddiqua, S, Peters, S.B., and Dixon, D.A. 2009. The effects of fluid composition on the one-dimensional consolidation behaviour of clay-based sealing materials (2006-2009). Nuclear Waste Management Organization (NWMO) Technical Memorandum.

Komine, H. and Ogata, N. 1996. Prediction for swelling characteristics of compacted bentonite, Canadian Geotechnical Journal 33, pp. 11–22

Laird, D.A. 2006. Influence of layer charge on swelling of smectites, Applied Clay Science 34, pp. 74–87.

Ledesma, A. and Chen, G.J. 2003. THM modelling of the Prototype Repository Experiment: comparison with current measurements. Proc. Of the International Symposium on Large Scale Field Tests in Granite, Sitges, Barcelona, Spain. Advances in Understanding Engineering Clay Barriers, pp. 339-346.

Lingnau, B.E., Graham, J., and Tanaka, N. 1995. Isothermal modelling of sand-bentonite mixtures at elevated temperatures. Canadian Geotechnical Journal 32, pp. 78-88.

Liu, L. 2013. Prediction of swelling pressures of different types of bentonite in dilute solutions. Colloids and Surfaces A: Physicochemical and Engineering Aspects 434, pp. 303-318.

Low, P.F. and Anderson, D.M. 1958. Osmotic pressure equations for determining thermodynamic properties of soil water. Soil Science 86, pp. 251–253.

Luukkonen, A. 2004. Prediction of geochemical changes in the Prototype Repository tunnel backfill. Proceedings from Task Forced-related meeting on Buffer & Backfill modelling. Lund, Sweden, International Progress Report IPR-04-23, pp. 103-110.

Madsen, F.T. and Muller-Vonmoos, M. 1989. The swelling behaviour of clay, Applied Clay Science 4, pp. 143–156.

Martino, J. 2008. The tunnel sealing experiment 10 year summary report. Atomic Energy of Canada Limited, URL-121550-REPT-001, AECL.

Martino, J. 2010. A review of excavation damage studies at the Underground Reserch Laboratory and the rsults of the excavtion damage zone study in the tunnel sealing experiment. Ontario Power Genration Report No. 06819-REP-01200-10018-R00.

Martino, J., Dixon, D.A., Holowick, B., and Kim, C-S. 2010. Construction of full scale shaft seals and enhanced sealing project (ESP) monitoring equipment installation. Nuculear Waste Management Organization, APM-REP-01601-0003.

Mitchell J.K. 1993. Fundamentals of Soil Behavior. 2nd Edition. John Wiley & Sons Inc., NY.

Mollins, L.H., Stewart, D.I, and Cousens, T.W. 1996. Predicting the properties of bentonite - sand mixtures, Clay Mineralogy. 31, pp. 243–252.

Nuclear Waste Management Organization(NWMO). 2005. Choosing a way forward. The Future Management of Canada’s Used Nuclear Fuel, Final Study.

Olivella, S., Gens, A., Carrera, J., and Alonso, E.E. 1996. Numerical modelling for a simulator (CODE_BRIGHT) for the coupled analysis of saline media. In Engineering Computations, Vol. 13, No. 7, pp. 87-112.

Olivella, S. and Gens, A. 2000. Vapour transport in low permeability unsaturated soils with capillary effects. Transport in Porous Media 40, pp. 219-241.

Pfeifle, T. W. 1987. Mechanical properties and consolidation of potential DHLW backfill materials: crushed salt and 70/30 bentonite/sand, SAND85-7208, Sandia National Laboratories, Albuquerque, NM.

Pinder, G.F. and Abriola L.M. 1986. On the simulation of nonaqueous phase organic compounds in the subsurface, Water Resour. Res. 22(9), pp. 109-119.

Priyanto, D. 2007. Development and application of new constitutive models to simulate the hydraulic-mechanical behaviour of unsaturated swelling clay. Ph.D. Thesis, Dept. Civil Engineering, University of Manitoba, Winnipeg, Manitoba.

Priyanto, D., Dixon, D.A., and Man, A. 2011. Interaction between clay-based sealing components and crystalline host rock. Clays in Natural & Engineering Barriers for Radioactive Waste Confinement, Vol. 36, pp. 1838-1847.

Priyanto, D., Dixon, D.A., and Martino, J. 2014. Enhanced Sealing Project (ESP): Project Status and Data Report for Period Ending 31 December 2014. Nuclear Waste Management Organization (NWMO) Technical Report APM-REP-01601-0005, Toronto, Canada.

Pruess, K. 1987. TOUGH User's Guide. Report LBL-20700, NUREG/CR-4640, pp.80

Pusch, R., Borgesson, L., and Ramqvist, G. 1987. Final report of the borehole, shaft and tunnel sealing test - Volume III: tunnel plugging. Stripa Project Technical Report, 87-03, SKB.

Pusch, R. 1989. Alteration of the hydraulic conductivity of rock by tunnel excavation. International Journal of Rock Mechanics and Mining Sciences, Vol.26, No.1, pp. 71-83.

Radhakrishna, H.S. and Chan, H.T. 1985. Strength and hydraulic conductivity of clay-based buffers for a deep underground nuclear fuel waste disposal vault. Ontario Hydro, TR-327

Ribó, R., Pasenau, M., Escolano, E., Ronda, JSP., and Sans, AC. 2000. GiD user manual, International Centre for Numerical Methods in Engineering (CIMNE), Barcelona

Richards, B G. 1965. Moisture equilibria and moisture changes in soils beneath covered areas, a symposium in print. Australia: Butterworths, pp. 39-46.

Roscoe, K.H. and Burland, J.B. 1968. On the generalised stress-strain behaviour of wet clay. Engineering Plasticity, Cambridge: Cambridge University Press, pp. 535-609.

Rutqvist, J., Börgesson, L., Chijimatsu, M., Kobayashi, A., L.Ling, Nguyen, T.S., Noorishad, J., and Tsang, C.-F. 2000. Thermohydromechanics of partially saturated geological media: governing equations and formulation of four finite element models. International Journal of Rock Mechanics and Mining Sciences, 38:105–127.

Saiyouri, N., Tessier, D., and Hicher, P.Y. 2000. Microstructural approach and transfer water modelling in highly compacted unsaturated swelling clays, Mech. Cohes. – Frict. Mater. 5, pp. 41–60.

Saiyouri, N., Tessier, D., and Hicher, P.Y. 2004. Experimental study of swelling in unsaturated compacted clays, Clay Mineralogy. 39, pp. 469–479.

Schneider, S., Mallants, D., and Jacques, D. 2012. Determining hydraulic properties of concrete and mortar by inverse modelling. Material Research Society Symposium Proceedings, Vol. 1475, pp. 367-372.

Seiphoori, A., Ferrari, A., and Laloui, L. 2014. Water retention behaviour and microstructural evolution of MX-80 bentonite during wetting and drying cycles. Géotechnique 64 (9), pp. 721–734.

Sposito, G. 1972. Thermodynamics of swelling clay–water systems. Soil Science 114, pp. 243–249.

Studds, P.G., Stewart, D.I., and Cousens, T.W. 1998. The effects of salt solutions on the properties of bentonite-sand mixtures, Clay Mineralogy, 33, pp. 651–660.

Sun, D.A., Cui, H., and Sun, W. 2009. Swelling of compacted sand-bentonite mixtures, Applied Clay Science, 43, pp. 485–492.

Tang, G.X. 1999. Suction characteristics and elastic-plastic modelling of unsaturated sand-bentonite mixture. Ph.D. Thesis, Dept. Civil Engineering, University of Manitoba, Winnipeg, Manitoba.

Tang, G.X., Graham, J., Blatz, J., Gray M., and Rajapakse, R. 2002. Suctions, stresses and strengths in unsaturated sand–bentonite. Engineering Geology. 64, pp. 147–156.

Thomas, H.R., Sansom, M.R., Volcaert, G., Jacobs, P., and Kumnan, M. 1994. An experimental and numerical investigation, Proceeding of the 3rd European Conference on Numerical Methods in Geotechnical Engineering Manchester, pp. 181 - 186.

Thomas, H.R., Cleall, P.J., and Melhuish, T.A. 2002. Simulation of the tunnel sealing experiment using THM modelling. Ontario Power Generation Inc., Nuclear Waste Management Division Report No. 06819-REP-01200-10112-R00.

van Genuchten, R. 1980. A closed-form equation for predicting the hydraulic conductivity of unsaturated soils, Soil Science Society of America Journal, pp. 892-898.

Van Olphen, H. 1977. An Introduction to Clay Colloid Chemistry: For Clay Technologists, Geologists, and Soil Scientists, John Wiley and Sons, New York.

Vanapalli, S., Lu, L., Infante Sedano, J. A., and Oh, W. T. 2012. Swelling characteristics of sand-bentonite mixtures. 2nd European Conference of Unsaturated Soils, Vol. 2, pp. 77-84.

Vaunat, J. and Olivella, S. 2002. CODE_BRIGHT-GiD User's Guide. A 3-D program for thermo-hydro-mechanical analysis in geological media. 1st Conference on Advances and Applications of GiD. Barcelona, Spain.

Verwey, E.J.W. and Overbeek, J.T.G. 1948. Theory of the Stability of Lyophobic Colloids: The Interaction of Sol Particles Having an Electric Double Layer, Elsevier, New York.

Villar, M V., Garcia-Sineriz, J L., Barcena, I., and Lloret, A. 2005. State of the bentonite barrier after five years operation of an in situ test simulating a high level radioactive waste repository. Engineering Geology 80, pp. 175-198.

Volckaert, G., Imbert, C., Thomas , H.R., and Alonso, E.E. 1996. Modelling and testing of the hydration of clay backfilling and sealing materials. End of Contract Report on CEC, Contract No. F12W-CT90-0033.

Wan, A.W.L., Graham, J., and Gray, M.N. 1990. Influence of soil structure on the stress-strain behaviour of sand-bentonite mixtures. Geotechnical Testing Journal, GTJODJ, 13(3), pp. 179-187.

Wan, A. W. L. 1996. The use of thermocoulpe psychrometers to measure in situ suctions and water contents in compacted clays. PhD Thesis, Winnipeg, Manitoba: University of Manitoba.

Wang, Q., Tang, A.M., Cui, Y.J., Delage, P., and Gatmiri, B. 2012. Experimental study on the swelling behavior of bentonite/claystone mixture, Eng. Geol., 124, pp. 59–66.

Westsik, J.H., Jr. and Harvey, C.O. 1978. Hydrothermal reactions of nuclear waste solids. PNL-2759, Pacific Northwest Laboratory, Richland, WA.

Wheeler, S.J. and Sivakumar, V. 1995. An-elasto-plastic critical state framework for unsaturated soil. Geotechnique, 45(1), pp. 35-53.

Wiebe, B.J. 1996. The effect of confining pressure, temperature, and suction on the strength and stiffness of unsaturated buffer. M.Sc. Thesis, Department of Civil and Geological Engineering, University of Manitoba, Winnipeg, Manitoba.

Yahia-Aissa, M., Delage, P., and Cui, Y.J. 2001. Suction–water relationship in swelling clays. Clay Science for Engineering. In: Adachi, K., Fukue, M. (Eds.), Proceedings of the IS-Shizuoka International Symposium on Suction, Swelling, Permeability and Structure of Clays. Shizuoka, Japan Balkema, pp. 65–68.

Ye, W.M., Cui, Y.J., Qian, L.X., and Chen., B., 2009. An experimental study of the water transfer through confined compacted gmz bentonite. Engineering Geology 108 (3–4), pp. 169–176.

Yong, R.N. and Mohamed, A.M.O. 1992. A study of particle interaction energies in wetting of unsaturated expansive clays, Canadian Geotechnical Journal 29, pp 1060–1070.

Yong, R.N. 1999. Soil suction and soil–water potentials in swelling clays in engineered clay barriers, Engineering Geology. 54, pp. 3–13.